UNIVERSITÉ D’ORLÉANS

Thèse réalisée à l’

INSTITUT VON KARMAN

ÉCOLE DOCTORALE ÉNERGIE, MATÉRIAUX, SCIENCE DE LA TERRE ET DE L’UNIVERS

LABORATOIRE de RECHERCHE : PRISME

THÈSE présentée par :

Boris CONAN

soutenue le : **12 décembre 2012**

pour obtenir le grade de : **Docteur de l’université d’Orléans**

Discipline/ Spécialite : **Genie Mécanique - Mécanique des fluides**

WIND RESOURCE ASSESSMENT IN COMPLEX TERRAIN BY WIND TUNNEL MODELLING

Thèse co-dirigée par :

Sandrine AUBRUN	HDR, Univ. d’Orléans, PRISME
J.P.A.J. van BEECK	Professeur, Institut von Karman, Belgique

Rapporteurs :

Fernando PORTÉ-AGEL	Professeur, EPFL, Suisse
Michel STANISLAS	Professeur, École Centrale de Lille

JURY :

Sandrine AUBRUN	HDR, Univ. d’Orléans, PRISME
Andreas BECHMANN	Senior Scientist, DTU, Danemark
Alvaro CUERVA	Professeur, UPM, Espagne
Philippe DEVINANT	Professeur, Univ. d’Orléans, PRISME
Laurent PERRET	MdC, École Centrale de Nantes
Fernando PORTÉ-AGEL	Professeur, EPFL, Suisse
Michel STANISLAS	Professeur, École Centrale de Lille
J.P.A.J. van BEECK	Professeur, Institut von Karman, Belgique

If one does not know to which port one is sailing,
no wind is favourable.

Lucius Annaeus Seneca (4 BC - AD 65)

Acknowledgements

That was not really planned when I arrived at VKI for the DC (Diploma Course) in 2008-2009 that I would stay for so long. But had I probably *felt under the spell* of experimental research already in 2007 when I performed for the first time wind tunnel testing at the NCR Canada for my master thesis. The enthusiasm of my supervisor at that time, Dr Bernard Tanguay transmitted me the *virus* of experimental research and the will to improve my theoretical and practical skills. Bernard, you have a great responsibility in this achievement! I am very in debt.

This thesis couldn't be so without the contribution of many people I met over the three years.

I am first very gratefully to my co-directors Sandrine Aubrun and Jeroen van Beeck for their very complementary support. Sandrine, Jeroen, you were my left and right side brain coaches over the thesis by helping me in having a more organized and structured work, and also by feeding me with ideas and visions. I am very grateful.

I would like to acknowledge the members of the jury and specially the two "rapporteur" for accepting to review my work, I'm very honored. I also appreciated their interesting and usefull comments.

This PhD work was performed with the financial support of the European Commission within the WAUDIT Initial Training Network (Wind resource assessment audit and standardization: www.waudit-itn.eu), a Marie-Curie action funded under FP7-People program. I provided me a perfect environment for research, trainning, and many opportunities to meet researchers and professionals from the wind industry sector. I'm very grateful.
I would like to thanks the people of the WAUDIT project, we had a very nice team for work and fun. Many thanks you to our dear coordinator Javier Sanz for building the network, organising us forefront seminars on wind energy and providing validation data of the Alaiz test case.
Francesco, Heather, Graciana, Nicolas, Thomas, Fernando, Christos, Georges, Venki, Nikolas, Patrick, Tilman, Cian, and Domingo, dear fellows, we had great times in Pamplona, Trondheim, Brussels (a couple of times), Hamburg, Amsterdam, Delft and Copenhagen!! Thanks to the EU Marie Curie program of the EU, we can now say that we master the inner of networking! It was a pleasure to work with you.

Going more in the work presented in this manuscript, I would like to thanks Tee Seong, Alvaro and Javier from UPM for designing and fabricating the Alaiz mock-up, for the Bolund wind tunnel data, and for the many fruitful exchanges on how to model and measure the wind.

All the experimental work was performed at the VKI, and couldn't be accomplished without the EA technical team: Guillaume, Didier, Michel, Alain, Carl, Momo and Dani, who built the set-ups, mock-ups and supported me with technical advices on a daily basis when preparing and running the wind tunnels.

I would like to thank the master students that contributed from near or far to this work, it was sometimes tedious but mainly a pleasure to work with them: Francesco, Dario, and Valeria. A special thanks is due to Sophia and Fernando who contributed the most to the content of this thesis.

During the PhD time, working at the VKI was always a pleasure, I want particularly to thanks Domingo for our discussions about wind (better in front of an ice-cream), Erik, Alessandro, Jésüs, Mickeal, Francesco, Antonino, Jayson, and Memo for sharing good moments in and out of the office.
I will certainly miss the numerous *lunch rides* to Alsemberg or Ixelles for having a "all you can eat" wok buffet or a bento with Delphine, Nico, Julien and Marcos. I could benefit during this time of personal courses on how to speak *properly* belgian ;)

I cannot miss a particular thanks that has to be attributed to professor C.S. who allowed me to turn my PhD plans *towards unexpected horizons...* Thanks to his *contribution* I had the opportunity to *put into perspective* the tests performed in the VKI-L1 wind tunnel for some time and I had to reoriented my PhD work towards the use of more modest wind tunnels. This was a very enriching experience to test how fast one can recover when its main tool is suddenly *unavailable*.

Finally, I would like to thanks my friends and my family that always supported me throughout my studies by encouraging me and visiting me. I'm finally done!!

Contents

Chapter 1.

Introduction

1.1. The wind energy sector in Europe in 2012

In the end of December 2011, the cumulative wind power installed in the EU reached almost 94 GW, a growth of 11% compare to the previous year. The wind energy sector has had a fast growth since 2000, with 15% per year in average. Wind farms represent 10% of the total EU installed power capacity, it was only 2% in 2000. Wind is covering 6.3% of the electricity consumption (Figure 1.1). Wind power is the second renewable energy source, closely following large hydraulic installations.
With 21% of the overall new installed power capacity in 2011, a 3.9% increase compare to 2010, the sector is still in very fast growth.

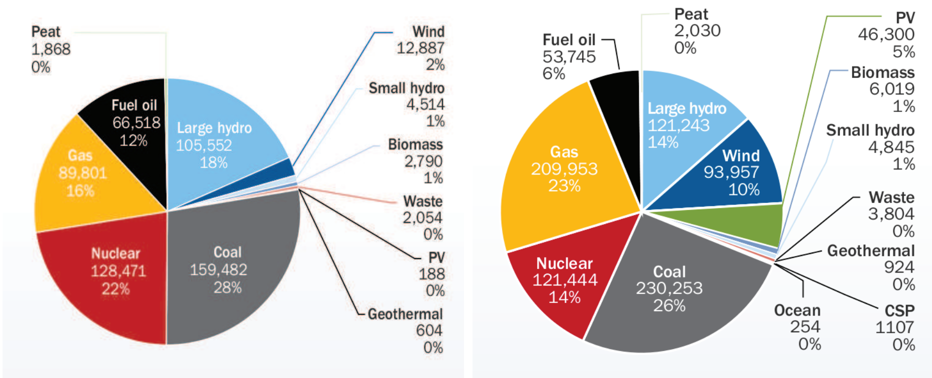

Figure 1.1.: EU power capacity mix in 2000 (left) and in 2011 (right).

Worldwide, Europe (mainly Germany and Spain) has the largest installed capacity in 2011, China and the USA are following. The Asian market is growing quickly, China constructed 44% of the new installation in 2011!
Numbers are accessible from the annual report of the GWEC[1] and the EWEA[2] organisations.

[1]Global Wind Energy Council: www.gwec.net
[2]European Wind Energy Association: www.ewea.org/

1.2. Wind resource assessment in complex terrains

Despite a very fast growth, the cost of the electricity produced from wind is still high compared to well established electricity sources. A multiplication of the wind farms and an increase of their profitability is necessary to attract more investors and to lower the energy production cost. One of the main drivers of the profitability is the accurate assessment of the wind resource because it directly determines the annual energy production.
The wind power, P_W, is the potential energy present in the wind, it is related to the cube of the wind velocity:

$$P_W = \frac{1}{2}\rho_{amb} S_R U^3 \tag{1.1}$$

where ρ_{amb} is the density of the ambient air, S_R is the rotor swept area and U the wind speed. Therefore, an accurate measurement or evaluation of the wind speed at the position of a turbine is of utmost importance for the assessment of the profitability of a wind farm.

Europe understood this key issue and set the target to decrease the uncertainty of the long term annual energy production forecasting and the local wind conditions forecasting to 3% regardless the site complexity by 2020 (source, TP Wind[3]). This objective is very optimistic, but the will to increase the confidence in the prediction exists and is driving the research across Europe.
In case of open fields with no topography, the evaluation of the wind speed can be realized by simple models extrapolating the wind at the wind farm location from close-by measurements masts. The wind potential assessment in these zones is already well known and precise, the work really starts when wind farms are installed in sloping terrain.
Despite the growing interest of going offshore to benefit from flat terrain with higher and more constant wind, still in 2011, most of the new wind power capacity is installed onshore (91%). Therefore, to take advantage of high winds, wind farms tend to be more and more placed in uneven topographies like hills, ridges or mountains. Gentle slopes, lower than 15° are often still manageable by simple linear models but for a more difficult topography, non-linear phenomena occurs, like flow separation. Another approach is then necessary for the wind resource assessment in complex terrain.
The way mainly foreseen for wind resource assessment in complex terrain is to perform a numerical modelling by CFD (Computational Fluid Dynamics) that include turbulent modelling schemes and is able to resolve complex flows. A lot of research is currently carried out on this topic to improve for example the reliability and the computation costs.
Field measurements are necessary to provide validation data but its cost, its lack

[3] www.windplatform.eu

of spacial resolution and its difficulty to measure 3D flows makes it challenging for complex terrains assessment. Its application to complex terrain and the increase of its spatial resolution are current research and development topics.
A third option, and also a complement to the two others, is to use a wind tunnel to reproduce the atmospheric flow and to measure the wind over a scaled model of the terrain. This approach has the advantage of being a real flow, with a low level of modelling, and controlled conditions. However, a lot of care and experience is needed to perform a proper modelling of atmospheric winds in wind tunnels. This is the topic of this work.

1.3. The challenge of wind tunnel testing

Wind tunnel modelling is an essential tool for most applications of fluid dynamics involving air like aerodynamic design of planes, ground vehicles or buildings, because it is able to reproduce closely the real behaviour of the air in a given situation. Wind tunnels remain a reference for validating numerical models.

Wind tunnel modelling is also called physical modelling. Indeed, contrary to CFD simulations that model a flow by equations (numerical modelling), in the wind tunnel the reality is modelled using a representative flow that is set to behave as the full scale flow. Nevertheless, wind tunnel modelling remains modelling, i.e. assumptions have to be made and a certain number of similarity criteria using dimensionless parameters have to be fulfilled for the modelling to be correct. In addition the initial conditions of the real flow (inflow conditions) have to be reproduced.
For atmospheric flow applications, wind tunnels are mainly used for pollutant dispersion studies, wind comfort assessment and wind load measurements. For all those studies, like for wind resource assessment, the area to simulate can be of the order of a part or even a small city.
For a proper modelling in a wind tunnel a number of items has to be consider and discussed:

- the matching of the dimensionless numbers: from the Navier-Stokes equations, a certain number of requirement have to be fulfil to simulate an atmospheric flow at full scale (dimensionless numbers).

- the reproduction of the wind inflow conditions: velocity and turbulence profiles at the inlet of the domain have to be matched to the full scale flow.

- the choice of the area to model and the scaling: the modelled area has to take into account enough surroundings around the area of interest to reproduce the wind, but stay small enough to be able to keep a reasonable scaling factor.

- the measurement technique relevance and accuracy: they have to be chosen according to the desired spatial and time resolution.

Most of the items listed, except measurement technique, are also a major concern for CFD modellers because they are facing the same questions as for numerical modelling.

All those topics are discussed in this work that aims at quantifying the relative importance of the modelling parameters and at contributing to increase the knowledge on wind tunnel modelling for atmospheric flows applied to wind resource assessment.

1.4. Objectives and structure of the thesis

The thesis has two main objectives:

- demonstrating the possibilities and the limitations of wind tunnel testing for wind resource assessment in complex terrain
- quantifying the most important parameters to be matched for a proper atmospheric flow physical modelling

Around the objectives, the manuscript is organised to go from a flat terrain simulation of atmospheric flows to the full study of very complex geometries.

Chapter 1 introduces the general context and objectives of the work. Chapter 2 describes the specificities of atmospheric flows and the way to model them it in a wind tunnel.
Chapter 3 is dedicated to the careful verification of the suitability of the two wind tunnels used and to the parametrization of the modelling of the Atmospheric Boundary Layer (ABL) in the test sections.
In Chapter 4, the study of simplified topographies is performed in order to understand the near and far wake of a topography. Results are compared to the literature. The goal is to quantify the downstream influence of a simple topography in order to help the modeller in choosing the right area to model.
In Chapter 5, two test cases are studied: the Bolund hill and the Alaiz mountain. Both are existing topographies equipped with measurement masts. The results obtained in the wind tunnel are compared to field measurements and other simulations, the goal is to assess the accuracy of the physical modelling in complex terrain. Parametric studies are also performed to quantify the impact of certain modelling parameters like the Reynolds number, the inflow conditions or the wind direction
Finally, Chapter 6 presents conclusions and perspectives.

Chapter 2.

Modelling atmospheric flows

2.1. The nature of wind

Solar energy is the main driver of the winds. Due to the diurnal cycle, the season or the latitude, the solar energy warms areas more than others and creates temperature differences on the ground. Air warmed by warmer surfaces rises up by buoyancy effect, travels in the atmosphere, and descends in area with cooler ground. The ground temperature difference is also linked to the capacity of the surface to accumulate heat.
For example, during the day the sun is providing equally energy to the coast and the sea, but the water has a very important inertia, therefore, the coastal surface is warmer than the water surface; this induces the rise of warm air on the ground and a sink of air above the sea leading to the so-called a sea breeze. At night, the temperature of the ground is decreasing quickly, however, thanks to its inertia, the water surface remains warm, therefore, warm air from the see will rise from the water surface and sink on the cooler ground; this is the night land breeze.
Additionally to the sun, at a large scale, the Coriolis effect is a very important parameter contributing to the global circulation of air on earth.
The solar energy and the Coriolis effect are leading the wind to blow over constant pressure lines.

One of the main characteristic of the wind is its variability in space and in time, at all scales. That makes its prediction challenging at a particular location because all scales have to be taken into account.
In space, at a given time, at the scale of the Earth, the global circulation of air is driven by the sun and the rotation of the Earth, at regional scale, the wind speed and direction are driven by the repartition of water, grounds and mountains chains. At a smaller scale the wind characteristics can change from a location to another due to the local topography and the presence of obstacles like forest, cities, hills. Going ever smaller, over a building, through a tree or over a ridge, the wind has different characteristics.

At a given location, the wind has a high variability in time. Over a year, a decade or more, the wind speed has low long-term variation, however, there is a lack of historical data to accurately predict it. This prediction is crucial for the

economic profitability of a wind farm. The wind also has a strong seasonality.
Below this time scale, the wind has a strong variability and presents a velocity correlation peak for approximately four days, this is the time for a large scale weather system to circulate over a given location. Another peak is at 12h, this is the diurnal peak. This scale is also called the synoptic scale. This time scale is important for the integration of a wind farms in the electricity network and for the prediction of the repartition of the electricity production between various sources.
Down to the order of a minute, a second or less, the wind speed varies continuously around a mean value. By convention, the meteorological mean value is usually a 10 min average. Those variations are called turbulence. It has a 3D nature. The assessment of the turbulence is of importance for the design of the wind turbine and the evaluation of its performance.

2.2. The nature of turbulence

The concept of turbulence refers to high frequency wind speed fluctuations. For atmospheric flows, it goes from the order of the minute to a fraction of a second. By convention, the mean wind speed is defined on a 10 minutes basis, and the turbulence can be described by the fluctuation of the wind speed around the mean wind speed.
Turbulence is a short-time random 3D fluctuations that is superimposed to larger scales. The phenomenon is mainly driven by the friction with the Earth surface, the boundary layer concept, and by the thermal effects resulting from temperature variations.
The concept of turbulence is often described as a chaotic phenomenon, meaning that small differences in the initial conditions can quickly result in large differences. This complex phenomenon is difficult solve by deterministic equations like the Navier-Stokes equations, the statistical approach is often chosen.
The Reynolds decomposition proposes to describe the instantaneous velocity of a fluid, u, by a time averaged speed, U and a fluctuation u'. So that the instantaneous velocity can be written as

$$u = U + u' \tag{2.1}$$

with $\bar{u}' = 0$. For atmospheric flows, 10 minutes if often taken as averaging time. The turbulence can be quantified in the three directions of space (i = u, v, w) with the turbulence intensity,

$$I_i = \frac{\sigma_i}{U} = \frac{RMS(i')}{U} \tag{2.2}$$

or with the turbulent kinetic energy (TKE),

$$k = \frac{1}{2}\left(\overline{u'^2} + \overline{v'^2} + \overline{w'^2}\right) = \frac{1}{2}\left({\sigma_u}^2 + {\sigma_v}^2 + {\sigma_w}^2\right) \tag{2.3}$$

with σ_i, the standard deviation of the i component.
The friction with the surface is the major source of turbulence and depends on the surface roughness, the wind will be affected differently if the terrain is a sea, a landscape, a city, a forest, or hills. The turbulence has a strong variation with height, it is high close to the ground, in the surface layer, and it is getting lower and lower until reaching the free atmosphere where the wind is not affected by the ground any more. The layer of influence of the surface is called the atmospheric boundary layer (ABL). The ABL is usually considered to be the first 1-2 km from the ground depending on the type of terrain. Out of the ABL, it can be considered that the influence of the ground is negligible, the wind is then mostly driven by the global circulation of air in the Earth, this is the geostrophic wind.

2.3. The neutral atmospheric boundary layer

2.3.1. Definition

The ABL is usually divided in two layers, the inner region and the outer region.
The turbulence intensity is the highest close to the ground and gradually decreases with height. In the lowest 10% of the ABL, (100 m to 200 m depending on the surface roughness, see figure 2.1) the gradient of velocity, turbulence, temperature and humidity is the highest, this layer is called the surface layer. From the surface layer to the top of the ABL (up to 1-2 km), the turbulence in the air keeps decreasing and the Coriolis forces become important. This is called the mixing or Eckman layer. Additionally, as mentioned previously, the pressure gradient is null along the wind direction.
In this study, only the neutral stratification is modelled, then, the temperature gradient is not considered and that means that inertia dominates buoyancy (more details in section 2.4.2). In reality, this is the case for most of the high wind conditions. Extensive information can be find in several reference books like Kaimal, Garratt or Wyngaard [51, 40, 90].

2.3.2. Velocity and turbulent intensity mean profiles and ABL classification

In neutral conditions, in the surface layer, with no pressure gradients, the vertical wind velocity profile can be described by the logarithmic law derived from the flux of momentum (see Kaimal [51]):

$$\frac{U}{u_*} = \frac{1}{\kappa}\, ln\left(\frac{z}{z_0}\right) \tag{2.4}$$

where u_* is the friction velocity and z_0 is the aerodynamic roughness length that is function of the real surface roughness. This parameter is used for the classification of the ABL types. The equation is valid well above the roughness elements,

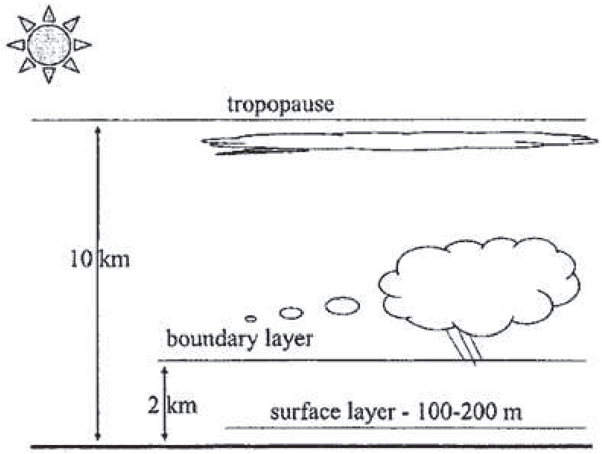

Figure 2.1.: The structure of the atmospheric boundary layer (ABL).

Roughness class	**Slightly rough**	**Moderately rough**	**Rough**	**Very rough**
Type of terrain	Ice, snow water surface	Grassland, farmland	park, suburban area	forest, inner-city area
z_0 in [m] VDI	10^{-5} to 5.10^{-3}	5.10^{-3} to 10^{-1}	0.1 to 0.5	0.5 to 2
α VDI	0.08 to 0.12	0.12 to 0.18	0.18 to 0.24	0.24 to 0.4
z_0 in [m] Eurocode	type 0 3.10^{-3}	type I and II 10^{-2} to 5.10^{-2}	type III 0.3	type IV 1
z_0 in [m] ESDU	10^{-3} to 3.10^{-3}	10^{-2} to 3.10^{-2}	10^{-1} to 3.10^{-1}	> 0.7

Table 2.1.: VDI guidelines, ESDU, and Eurocode ABL classifications [85, 35, 36].

from around two times the roughness element heigth. Table 2.1 presents the VDI, ESDU and the EUROCODE classifications [85, 35, 36].

Another way of describing the mean velocity profile inside the ABL is the power law, this is more a fitting law than a theoretically derived law:

$$\frac{U}{U_{ref}} = \left(\frac{z}{z_{ref}}\right)^{\alpha} \tag{2.5}$$

Ranges of power-law coefficient α are also defined in relation with the surface roughness (Table 2.1).

The friction velocity u_* in equation 2.4 can be defined by the surface stress τ_{wall},

$$u_*{}^2 = \frac{\tau_{wall}}{\rho} \tag{2.6}$$

which, in case of no longitudinal pressure gradient and no viscous stress, is limited to by the Reynolds stresses near the wall,

$$u_*{}^2 = -(\overline{u'w'})_{wall} \tag{2.7}$$

In the surface layer, the shear stress is considered constant with height. Above, it decreases with hight.

For each surface roughness classification, ESDU [35] proposes a turbulence intensity vertical profile of the three velocity components:

$$I_i = \frac{\sigma_i}{u_*}\frac{u_*}{U} \tag{2.8}$$

with

$$\frac{\sigma_u}{u_*} = \frac{7.5\mu[0.538 + 0.09\ ln(z/z_0)]^p}{1 + 0.156 ln(u_*/f_c z_0)} \tag{2.9}$$

$$\frac{U}{u_*} = 2.5\left[ln(\frac{z}{z_0}) + 34.5\ \frac{f_c z}{u_*}\right] \tag{2.10}$$

with $\mu = 1 - 6\, f_c z/u_*$, $p = \mu^{16}$ and f_c the Coriolis parameter depending on the latitude (λ), $f_c = 2\Omega sin \mid \lambda \mid$.

The transversal and vertical components are defined in the same way with:

$$\sigma_v = \sigma_u\left[1 - 0.22cos^4\left(\frac{\pi}{2}\frac{z}{u_*/6f_c}\right)\right] \tag{2.11}$$

$$\sigma_w = \sigma_u\left[1 - 0.45cos^4\left(\frac{\pi}{2}\frac{z}{u_*/6f_c}\right)\right] \tag{2.12}$$

An example is shown in figure 2.2.

2.3.3. The integral length scale

Another characteristic of turbulence in a flow is the turbulent integral length scale L_u. In theory, it is extracted from space correlation of the stream-wise velocity fluctuation but it is often deduced from a single point measurement on a long time. Indeed, the Taylor's frozen turbulence hypothesis makes the assumption that, while it is convected through a measurement point, an eddy is imperceptibly changed. Then, the time scale and the length scale at a certain height are simply related by:

$$L_u(z) = U(z).T_u(z) \tag{2.13}$$

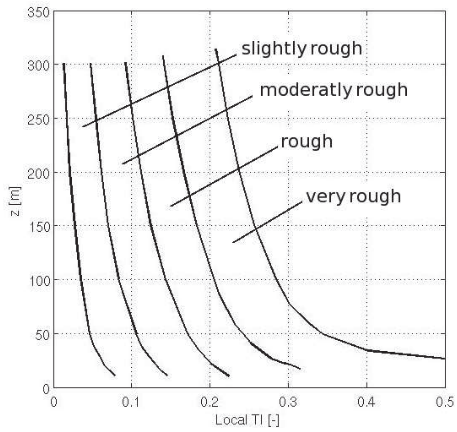

Figure 2.2.: The longitudinal turbulence intensity profile in function of the terrain roughness following the VDI guidelines.

So a good approximation of L_i is obtained by calculating the integral time scale T_i and then by computing the integral length scale by the equation 2.13.
T_i is calculated as the integral of the autocorrelation of the time signal of the velocity fluctuation. The integral is estimated with the *1/e* approximation taking the value for which the autocorrelation equals (1/e), see figure 2.3.

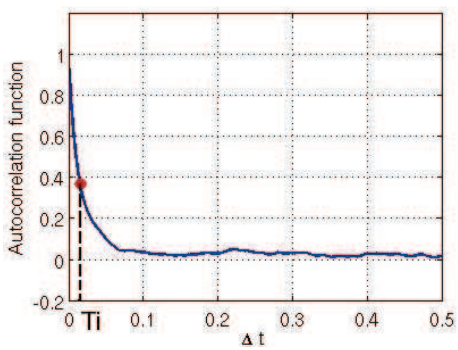

Figure 2.3.: Example of an autocorrelation function with the *1/e* technique.

Counihan [29], presents a fitting of a certain number of field observations and proposes turbulence length scale profiles associated to terrain roughness. Figure 2.4 presents the observations with the different profiles in function of the terrain roughness.

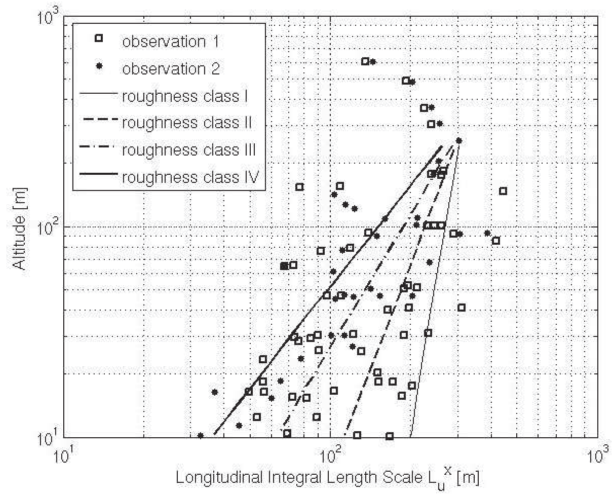

Figure 2.4.: Integral length scale profile observed in the field and approximation proposed by Counihan [29].

2.3.4. Spectral characteristics

The ABL is a turbulent flow and as such, it follows the Kolmogorov energy cascade process. Figure 2.5 describes the energy spectra of a typical flow, the spectra is divided in three areas: the energy containing range where the energy is produced (left), the inertial sub-range where the energy is transferred to smaller and smaller eddies (middle), and the dissipation range, where the kinetic energy is dissipated by viscosity into thermal energy (right). The inertial sub-range is the so called Kolmogorov cascade that presents a -5/3 slope.

A usual representation of the distribution of energy for atmospheric flows is the Kaimal [52] weighted spectrum. It consists in non-dimensionalizing the scalar energy spectrum by the square of the friction velocity and multiplying it by the frequency. This is plotted in figure 2.6 versus the dimensionless frequency scale n given by $n = f.z/U$. In this representation, the -5/3 slope turns into a -2/3 slope. From observations, the empirical relationships of the three components of the spectra are given by:

$$\frac{fS_i(f)}{{u_*}^2} = \frac{105n}{(1+33n)^{5/3}} \tag{2.14}$$

$$\frac{fS_i(f)}{{u_*}^2} = \frac{17n}{(1+9.5n)^{5/3}} \tag{2.15}$$

$$\frac{fS_i(f)}{{u_*}^2} = \frac{2.1n}{(1+5.3n^{5/3})} \tag{2.16}$$

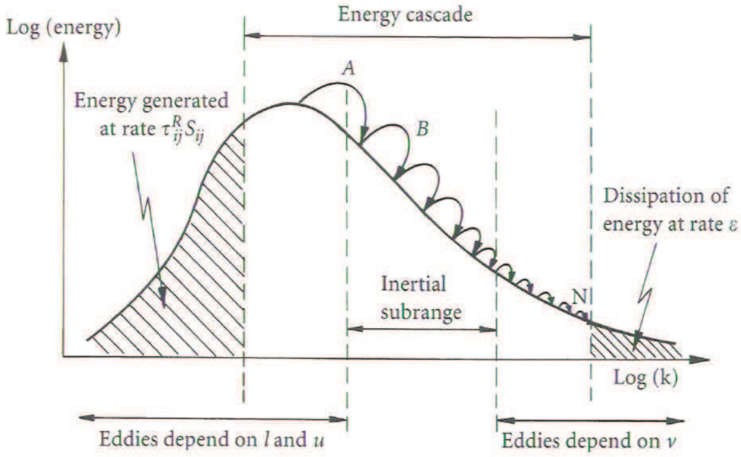

Figure 2.5.: The energy energy cascade (figure from Davidson [30]).

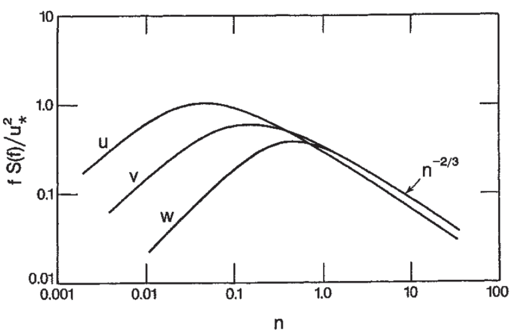

Figure 2.6.: Normalized neutral Kaimal spectra for u, v,and w in the surface layer [52].

2.4. Requirements for a laboratory simulation of atmospheric flows

All the challenge of physical modelling of atmospheric flows is to reproduce the characteristics of the wind in a test section of a wind tunnel. To ensure a similarity between the two flow systems, geometric similarity, kinematic similarity, dynamic similarity, thermal similarity and similarity of the boundary conditions have to be fulfilled. This section aims at defining the dimensionless numbers that scale the dimensionless governing equations of a fluid system, and at discussing the relaxations of the similarity requirements that are facing the reality of physical modelling.

2.4.1. Conservation of mass, energy and momentum

This part refers to the work of Cermak and Snyder [20, 76].
The first governing equation of a fluid system is the mass conservation:

$$\frac{\partial \rho}{\partial t} + \frac{\partial (\rho u_i)}{\partial x_i} = 0 \tag{2.17}$$

with i, j, and k, the longitudinal, transversal and vertical components, x_i, the distance in the i component, u_i the instantaneous velocity component, and ρ, the density.
The only requirement deduced from this equation is the geometrical similarity, the geometrical scaling factor has to be the same in all directions.

The conservation of momentum, the equation of motion, gives the criteria for dynamic similarity. The time averaged equation is here written with the variables represented by the mean and the fluctuating part:

$$\begin{aligned} \frac{\partial U_i}{\partial t} + U_j \frac{\partial U_i}{\partial x_j} + 2\epsilon_{ijk}\Omega_j U_k = -\frac{1}{\rho_0}\frac{\partial P}{\partial x_i} - \frac{\Delta T_0}{T_0} g\delta_{i3} + \nu_0 \frac{\partial^2 U_i}{\partial x_k \partial x_k} \\ + \frac{\partial < -u'_j u'_i >}{\partial x_j} \end{aligned} \tag{2.18}$$

where Ω is the angular rotation of the Earth, P the mean relative pressure compare to a neutral atmosphere, T is the mean temperature, with ΔT the temperature difference compare to a neutral atmosphere (T_0, ρ_0), g is the acceleration due to gravity, ν_0 the kinematic viscosity, ϵ_{ijk} the alternating tensor and δ_{i3} the Kronecker's delta.

The nondimensional form, is obtained by scaling the variables:

$$U_i{}^* = U_i/U_0 \; ; \; < u'_i >^* = u_i{}'/U_0 \; ; \; x_i^* = x_i/L_0 \tag{2.19}$$

$$t^* = tU_0/L_0 \; ; \; \Omega_i^* = \Omega_j/\Omega_0 \; ; \; \bar{P}^* = \bar{P}/(\rho_0 U_0^2) \tag{2.20}$$

$$\Delta T^* = \Delta T/(\Delta T)_0 \; ; \; g^* = g/g_0 \tag{2.21}$$

with L_0, U_0, ΔT_0, g_0 and Ω_0 the reference quantities given by the boundary conditions.

That gives the dimensionless equation of momentum conservation:

$$\frac{\partial {U_i}^*}{\partial t^*} + U_j^* \frac{\partial U_i^*}{\partial x_j^*} + \left[\frac{1}{Ro}\right] 2\epsilon_{ijk}\Omega_j^* U_k^* = -\frac{\partial P^*}{\partial x_i^*} - \left[\frac{1}{Fr^2}\right] \Delta T^* g^* \delta_{i3} + \left[\frac{1}{Re}\right] \frac{\partial^2 {U_i}^*}{\partial x_k^* \partial x_k^*} + \frac{\partial < -u_j' u_i' >^*}{\partial x_j^*} \tag{2.22}$$

Three dimensionless parameters are extracted from this formulation: the Reynolds number (Re) giving the ratio of advective to viscous terms, the Froude number (Fr), giving the ratio between inertial and convective forces, and the Rossby number (Ro), giving the ratio between the local acceleration and the Coriolis acceleration.
Notice that, often in atmospheric science, the Froude number is replaced by the bulk Richardson number (Rb) defined by

$$Rb = \frac{1}{Fr^2} \tag{2.23}$$

The third equation is the energy conservation:

$$\frac{\partial T}{\partial t} + U_i \frac{\partial T}{\partial x_i} = \left[\frac{k_0}{\rho_0 C_{p_0}}\right] \frac{\partial^2 T}{\partial x_k \partial x_k} + \frac{\partial < -\theta' u_i' >}{\partial x_i} + \frac{\phi}{\rho_0 C_{p_0}} \tag{2.24}$$

with θ' the instantaneous potential temperature and ϕ the dissipation function. That gives in its dimensionless form:

$$\frac{\partial T^*}{\partial t^*} + {U_i}^* \frac{\partial T^*}{\partial x_i^*} = \left[\frac{1}{Pr}\right] \left[\frac{1}{Re}\right] \frac{\partial^2 T^*}{\partial x_k^* \partial x_k^*} + \frac{\partial < -\theta' u_i' >^*}{\partial x_i^*} + \left[\frac{1}{Re}\right] [Ec]\, \phi^* \tag{2.25}$$

Two new dimensionless number are extracted, the Prandtl number (Pr), the ratio between the momentum diffusivity and the thermal diffusivity and the Eckert number (Ec), giving the ratio between kinetic energy and enthalpy.

So we have five dimensionless numbers to match for strictly fulfilling the similarity conditions:

$$\text{bulk Richardson number} \qquad Rb = \frac{(\Delta T)_0}{T_0} \frac{L_0}{{U_0}^2} g_0 \tag{2.26}$$

$$\text{Eckert number} \qquad Ec = \frac{{U_0}^2}{C_{p_0}(\Delta \bar{T})_0} \tag{2.27}$$

$$\text{Prandtl number} \qquad Pr = \frac{\nu_0}{k_0/(\rho_0 C_{p_0})} \tag{2.28}$$

$$\text{Rossby number} \qquad Ro = \frac{U_0}{L_0 \Omega_0} \tag{2.29}$$

$$\text{Reynolds number} \qquad Re = \frac{U_0 L_0}{\nu_0} \tag{2.30}$$

2.4.2. Discussion and relaxation of similarity parameters

The dimensionless numbers deduced from the governing equation are now considered one by one for wind tunnel physical modelling.

The Richardson number

As introduced in section 2.1, the sun is the driving force of the wind by inducting temperature differences. The Richardson number (Equation 2.26), the ratio between inertial and convective forces, defines the thermal stratification, so the stability of the atmosphere. The Richardson number is positive for stable stratification (Ri), equal to zero for neutral stratification, and negative for unstable stratification. Practically in a wind tunnel, it is very expensive and it needs a lots of expertise to reproduce a temperature gradient in the test section, in number of wind tunnels there is no temperature gradient and only neutral flows are simulated. In this study, only neutrally stratified flow are considered, this case is encountered the most for high winds conditions. Sometimes, the Froude number is used to determine the atmospheric stability.

The Eckert number

The Eckert number, equation 2.27, is also linked to temperature differences, it is defined by the ratio between the flow's kinetic energy and enthalpy, it characterizes the dissipation. As only neutrally stratified flows are modelled, there is no temperature difference considered, the Eckert number is zero.

The Prandtl number

The Prandtl number, equation 2.28, is an intrinsic characteristic of a fluid, this is the ratio between momentum and thermal diffusivity. In the wind tunnel, air is used, the criteria is then fulfilled.

The Rossby number

The Rossby number, equation 2.29, is linked to the rotation of the Earth, it is the ratio of the local acceleration of the fluid and the Coriolis acceleration. The Coriolis force has a major effect on the global circulation of air on Earth, however, at a local scale, its effect can be neglected. The maximum distance for relaxation of the Coriolis effect varies with the author, Snyder [76] reports from different sources a limit from 150 km to 5 km. It is usually assumed around 15 km in atmospheric dispersion. This limit can be reach in the wind tunnel if a very large area is simulated with a very large scaling factor.

The Reynolds number

The Reynolds number (Equation 2.30) is the ratio between inertial and viscous forces. This dimensionless number determines the flow regime, turbulent or laminar. L_0 is the characteristic length of the flow, it can be the boundary layer height or the hill height, and U_0 is the characteristic velocity of the wind. In the atmosphere typically, the Reynolds number is of the order of 10^8 (i.e. U_0 =10 m/s and $L_0 = 200$ m).
In the wind tunnel, because the major part of the experiments are done in air, the Reynolds number is directly affected by the scaling factor. A way to keep it would be to increase the wind tunnel speed. However, a simple calculation with $Re = 10^8$, and a commonly used 1/500 scale, one reaches the conclusion that the speed has to be 5 000 m/s. Two main things forbit such a test: the cost of operating a few m^2 test section at that speed and the incompressibility of the flow that becomes a predominant phenomena. Another way to reach the real Reynolds number is to increase the density of the fluid. Water can be used but the speed is often limited to a few m/s, the Reynolds numbers reached can be of the order of 10^7 (see Almeida or Yee [3, 91]) but not better.

In most of the cases, air is used and the Reynolds number similarity cannot be completed, depending on the scaling factor, $Re = 10^4$ to $Re = 10^5$ are reached. The assumption made is that the flow is Reynolds number independent. This assumption is based on the fact that in absence of thermal effect (neutral stratification) and Coriolis forces, the flow in the boundary layer is entirely turbulent. That leads to a constant C_D as function of the Reynolds number for sharp-edged bluff bodies such as buildings. Then, above a certain threshold, the flow is Reynolds number independent. The minimum Reynolds number to complete varies with the author but is usually accepted ([85, 76]) to be around

$$Re = \frac{LU}{\nu} > 10\,000 \tag{2.31}$$

This hypothesis fulfilled, problems may appear in the near wall region if the surface is too smooth, however, in atmospheric modelling, there is always a surface roughness to ensure turbulence until the very near wall. To verify this, a second criteria has to be addressed, the minimum roughness Reynolds number to avoid *relaminarization*:

$$Re_{\mu} = \frac{(z_0)_{wt} u_*}{\nu_0} > 5 \tag{2.32}$$

with $(z_0)_{wt}$ the aerodynamic roughness length at the wind tunnel scale.

Performing a verification of the Reynolds number independence assumption in the wind tunnel is nevertheless highly recommended for any test.
Sometimes, the surface roughness is exaggerated intentionally to ensure turbulence at the wall.

For the modelling to be complete, the boundary conditions have to be reproduced as closely as possible. The incoming profile in terms of velocity profile, turbulence intensity profile has to be matched, the integral length scale and the turbulent spectra are also important for a complete flow similarity.
Additionally, as in the atmosphere, the wind tunnel has to be adjusted to create a zero pressure gradient in the test section. The flow has also to be fully developed to ensure constant conditions over the test area. VDI guidelines and ESDU [35, 85] are providing norms for a proper reproduction of atmospheric flows in the wind tunnel.
The correct reproduction of the inflow conditions can be a very demanding task, it is the topic of the entire next chapter.

Chapter 3.

Atmospheric boundary layer modelling in the wind tunnel

3.1. Introduction

This chapter aims at introducing the wind tunnels, verifying their suitability for atmospheric flow reproduction and at getting knowledge on the reproduction of representative ABL flows.
The first part introduces the facilities and describes the ABL generation technique. Then, the next section goes through the requirements presented in the precedent chapter and compares them to the possibilities of the wind tunnels used.
The determination of the key characteristics of the ABL are discussed and compared to field data from the literature.
Finally, the influence of the BL generators is investigated with a parametric study using both wind tunnels and numerical tools. The goal is to determine and quantify the effect of each BL generator used in the wind tunnel to simulate an ABL flow.

3.2. The VKI-L1 wind tunnel

3.2.1. Wind tunnel characteristics

The von Karman Institute is equipped with a large low-speed closed-loop wind tunnel: VKI-L1 (Figure 3.1). The closed test section of the facility is 2 m high, 3 m wide and 15 m long. Two contra-rotating fans driven by a 580 kW DC motor allow a maximum speed of 60 m/s. In wind engineering applications, the velocity is often set around 20 m/s and all the length of the test section is used to model a neutral atmospheric boundary layer. To simulate the wind coming from all directions, the mock-ups can be placed on a 2.8 m diameter turn-table. If necessary, the ceiling of the wind tunnel can be adjusted to control the longitudinal pressure-loss over the tunnel test-section and to overcome blockage effects.

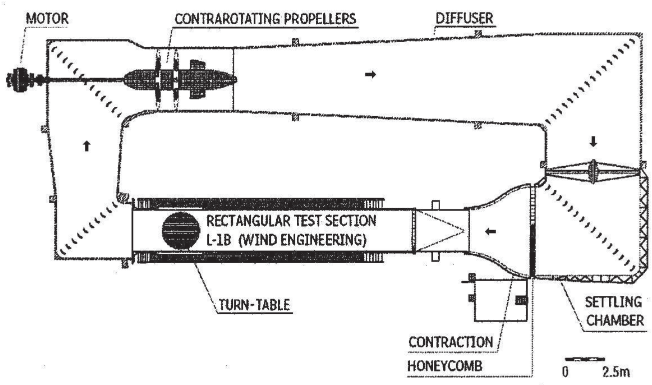

Figure 3.1.: VKI-L1 wind tunnel in wind engineering configuration.

3.2.2. Atmospheric boundary layer generation technique

To develop a BL representative of a neutral atmospheric boundary layer (NABL) in the test section, a set of obstacles is placed to create velocity and turbulence gradients. At the very beginning of the test section, a grid is placed together with a fence. These items are initiating the development of the BL by giving a strong initial perturbation. Then, over 14 m, roughness elements are distributed on the floor to develop the vertical velocity and turbulence profiles representative of the local surface roughness present in the field (Figure 3.2 and 3.3).

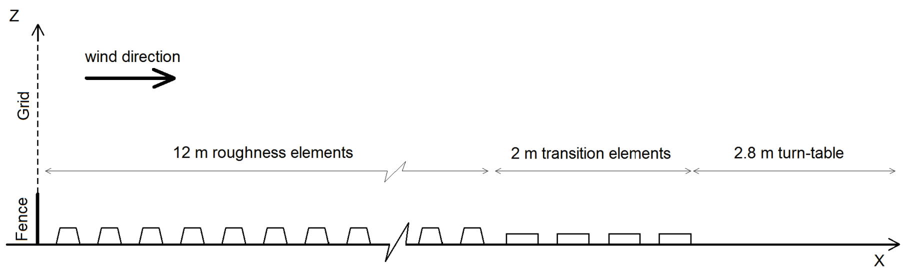

Figure 3.2.: Boundary layer generation set-up in VKI-L1 test section.

Roughness elements are spread on the test section on 29 cup rows. The density varies with the distance, first 6 rows of 24 elements are placed, followed by 23 rows of 12 elements. Their height can be adapted to the roughness classification of the ABL to simulate: offshore, landscape or city, and to the scale of the model (Figure 3.4). Roughness elements are conical, two height are available: 32 mm and 95

Figure 3.3.: Left: General view of the boundary layer generators: the grid, the fence (on the background) and the roughness elements. Right: Zoom on the cup dimensions (right)

mm. Finally, transition elements are placed in 7 rows of 12 elements. Table 3.1 details the ABL generator geometries used in the VKI-L1 wind tunnel.

Element	**Number**	**Description**	**Size (X . Y . Z) / (d-D.h) [mm]**
Fence	1	wooden board	10 . 3 000 . 150
Grid	1	metal mesh (83% porosity)	1.6 . 3 000 . 2 000
Roughness element: Cup 1	420	plastic, conical shape	30-40 . 32
Roughness element: Cup 2	420	plastic, conical shape	45-70 . 95
Transition elements	84	wooden cubes	50 . 120 . 20

Table 3.1.: Description of boundary layer generators used in the VKI-L1 test section.

The roughness distribution classification proposed by [37] defines the roughness density $\lambda = A_g/S_G$ and the frontal roughness density $\lambda_f = A_f/S_G$. A_g is the projected area of a roughness element to the ground, A_f the projected frontal area of a roughness element and S_G the ground area per roughness element. For a configuration with “Cup 1” as boundary layer generators, $S_G = (3 \times 12)/504m^2$ that gives a roughness distribution ratio of $\lambda = 1.71\%$ and $\lambda_f = 1.57\%$. With “Cup 2” elements, $\lambda = 4.5\%$ and $\lambda_f = 8\%$. As the density is not constant over the test section, the average density is given.
In the wind tunnel comparison table presented by [37], the density of the roughness elements in VKI-L1 wind tunnel is rather low for equivalent z_0.

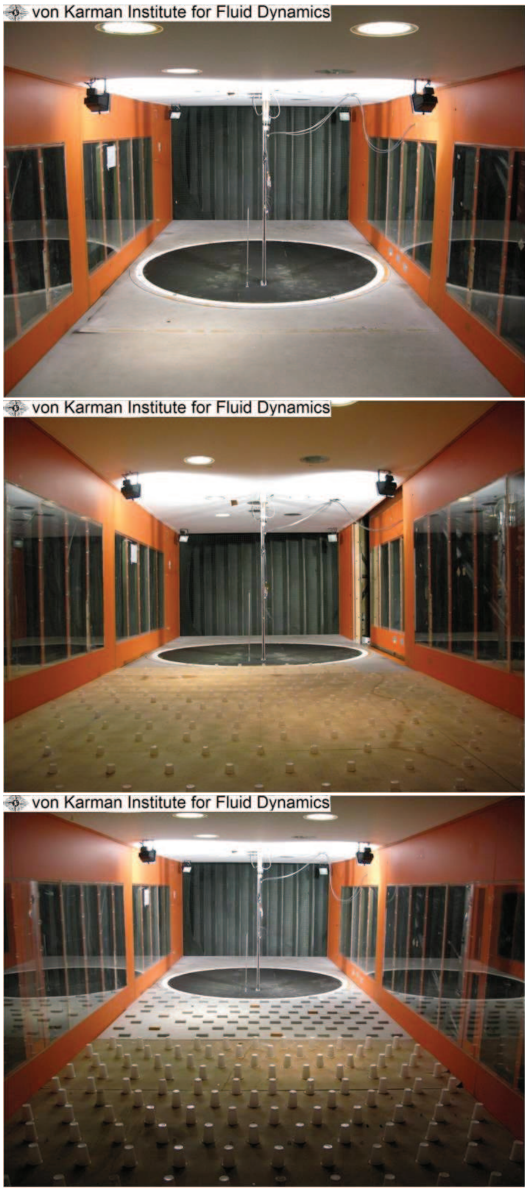

Figure 3.4.: View of the turntable of the wind tunnel with different boundary layer generators. Different terrain roughness can be simulated: offshore, rural or urban areas.

3.3. The VKI-L2 wind tunnel

3.3.1. Wind tunnel characteristics

The VKI-L2 wind-tunnel is a low-speed, open circuit wind-tunnel of suction type (Figure 3.5). The tunnel is equipped with a 0.35 m x 0.35 m closed test section and driven by a 4.4 kW variable-speed DC motor providing a maximum velocity of 35 m/s. The test section used for wind engineering is 2 m long and a set of boundary layer generators can be placed in the tunnel to simulate the different wind profiles.

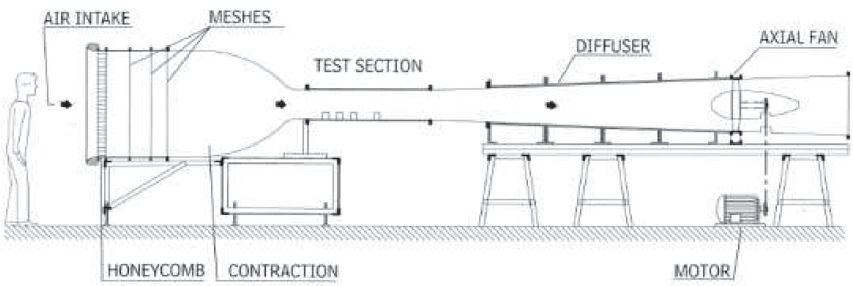

Figure 3.5.: VKI-L2 wind tunnel in the wind engineering configuration.

3.3.2. Atmospheric boundary layer generation technique

Several boundary layer generators are used in this tunnel: Lego® floor, Lego® blocks and two kind of Counihan wings [28]. The devices can be easily combined and adjusted to generate the appropriate velocity and turbulence profiles (Figure 3.6).

Element	Description	Size (X . Y . Z) [mm]
Fence	Legoblocks	16 . 350 . 10 (1 block height)
Roughness element	Lego blocks, plastic	16 . 16 . 10 (1 block height)
Rough surface	Lego plate, plastic	2000 . 350 . 2

Table 3.2.: Description of boundary layer generators available in VKI-L2 test section.

As for the large wind tunnel, the roughness distribution classification is computed. For a Lego® floor the roughness distribution ratio gives $\lambda = 30.7\%$ and $\lambda_f = 15.6\%$ and for 1 block roughness: $\lambda = 5.4\%$ and $\lambda_f = 3.4\%$.

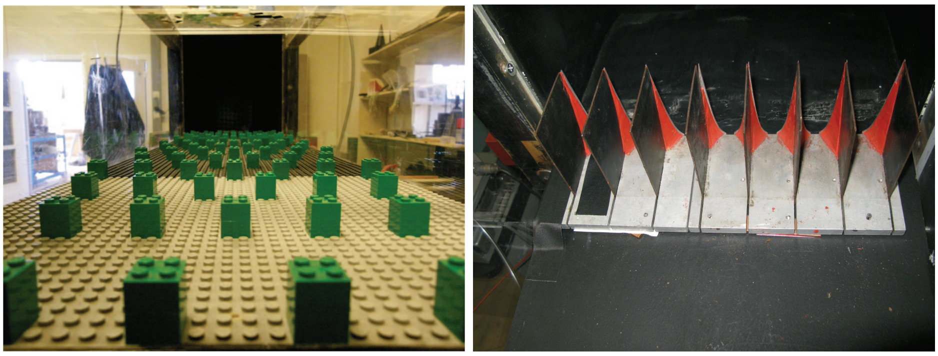

Figure 3.6.: View of the VKI-L2 wind tunnel test section with Lego floor, blocks and Counihan wings.

3.4. Verification of wind tunnels suitability for atmospheric flow modelling

The modelling of atmospheric flows in the wind tunnel requires the completion of the similarity criteria and the reproduction of the boundary conditions discussed in chapter 2. This section reviews the different requirements and discusses them for the case of both wind tunnels.

3.4.1. Reynolds number dependency

The Reynolds number is a key parameter of the flow system that ensures the same flow behaviour for equal value. For atmospheric applications, it cannot be fulfilled in the wind tunnel (section 2.4.2) then the equality of the Reynolds number is replaced by a minimum Reynolds number and a Reynolds number dependency study.
A study of the Reynolds number dependency in the two empty tests sections is performed using hot-wire anemometry (single wire in VKI-L2 and triple wire in VKI-L1 test sections).
In the VKI-L1 wind tunnel, velocity and turbulence profiles at $\mathrm{Re} = 1.5 \times 10^6$ and $\mathrm{Re} = 0.7 \times 10^6$ are recorded, figure 3.7 presents the results and table 3.3 quantifies the deviation from ideal case. In absence of obstacle, the Reynolds number is based on the boundary layer height δ ($U(\delta) = 0.99 U_{\text{free-stream}}$).

Looking at the comparison results (Table 3.3, details of the calculation of the numbers in Annexe B) for the range studied, the Reynolds number influence is very limited. The effect is higher on the turbulence level, with more scatter. The average difference is 2.5% for the mean velocity and 7.3 % for the turbulence intensity.

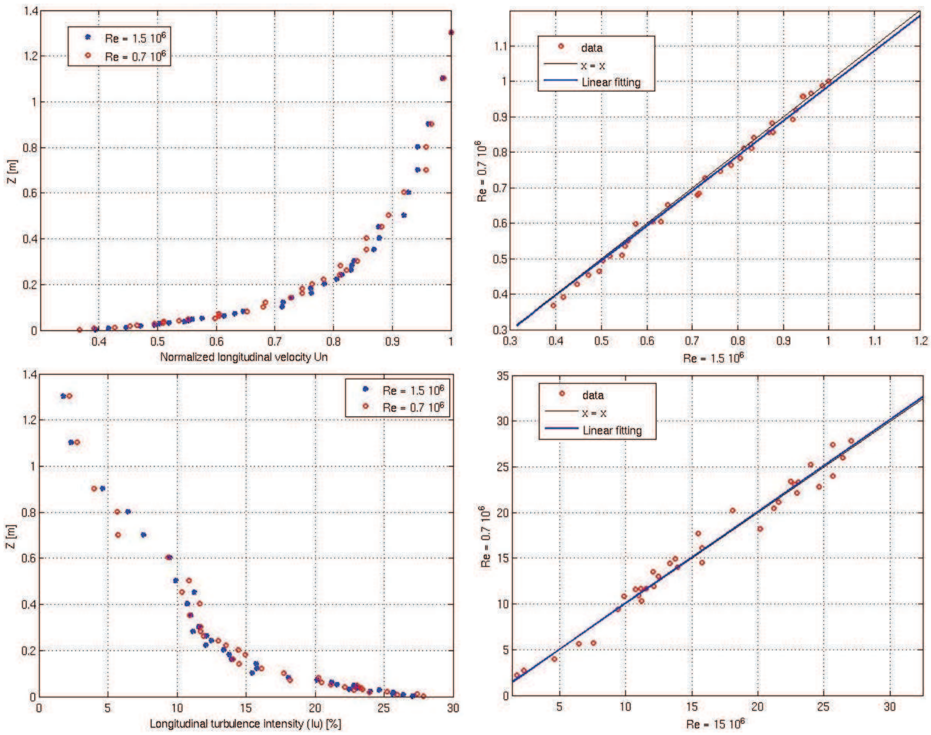

Figure 3.7.: Presentation of the Reynolds number dependency in VKI-L1 test section. Comparison of the normalized velocity profile (upper left) with the scatter plot (upper right) and of the turbulence profile (lower left) with scatter plot (lower right). The velocity profile is normalized at 1.3 m

Comparison Re = 0.7 $.10^6$ **and Re = 1.5** $.10^6$	U [-]	Iu [-]	Perfect match
Linear coefficient	0.987	1.005	1
Correlation coefficient	0.997	0.988	1
Fractional Bias	0.015	-0.007	0
Normalized Mean Square Error	0.001	0.005	0
Geometric mean	1.02	0.991	1
Geometric Variance	1.001	1.01	1
Average difference	0.025	0.073	0

Table 3.3.: Quantification of the Reynolds number dependency in VKI-L1 test section.

In the VKI-L2 wind tunnel, velocity and turbulence profiles are measured at

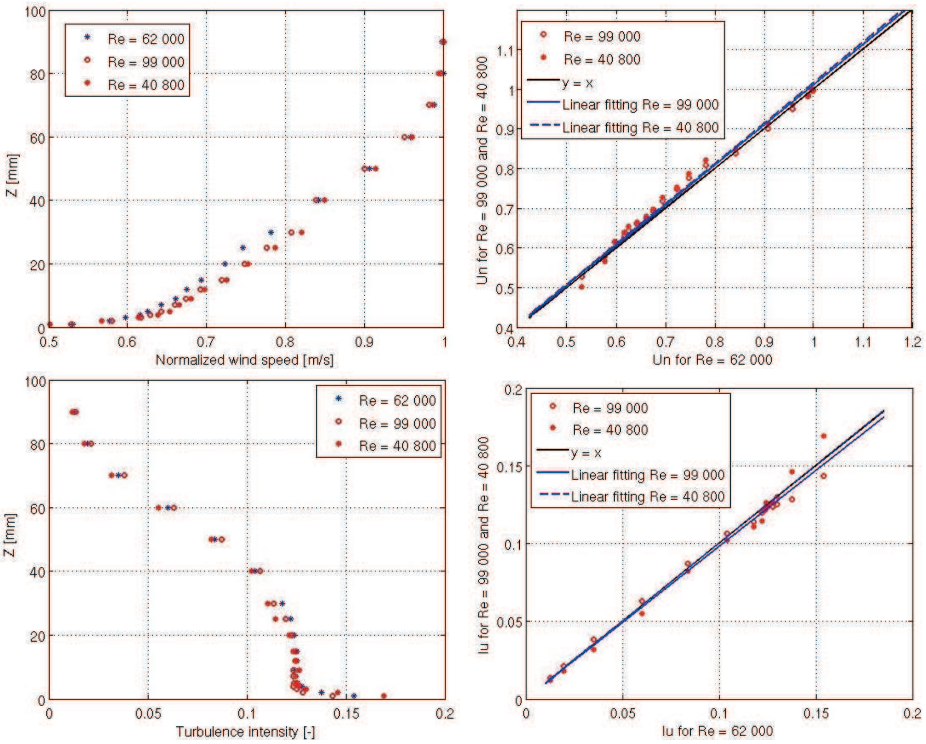

Figure 3.8.: Presentation of the Reynolds number dependency in VKI-L2 test section. Comparison of the normalized velocity profile (upper left) with the scatter plot (upper right) and of the turbulence profile (lower left) with scatter plot (lower right).

three free-stream velocities (8.01 m/s, 12.1 m/s, and 19.4 m/s) equivalent to Reynolds numbers of: 4.08×10^4, 6.2×10^4, and 9.9×10^4. Figure 3.8 and table 3.4 summarize and quantify the results taking as reference the lower Reynolds number.
In the range investigated, the Reynolds number has a limited influence on the velocity and turbulent profiles, the maximum difference is between $\mathrm{Re} = 4.08 \times 10^4$ and $\mathrm{Re} = 9.9 \times 10^4$ with an average difference of 2.8 % for the mean velocity and 4 % for the turbulence intensity.

The Reynolds number study compares completely independent measurements (performed on different days). It provides hence also a good evaluation of the repeatability of the measurement.

Comparison Re = 4 $.10^4$ **and Re = 6.2** $.10^4$	U [-]	Iu [-]	Perfect match
Linear coefficient	1.011	0.978	1
Correlation coefficient	0.997	0.997	1
Fractional Bias	-0.013	0.0155	0
Normalized Mean Square Error	0.001	0.002	0
Geometric mean	0.985	0.999	1
Geometric Variance	1.001	1.002	1
Average difference	0.019	0.037	0
Comparison Re = 4 $.10^4$ **and Re = 9.9** $.10^4$	U [-]	Iu [-]	Perfect match
Linear coefficient	1.017	1.001	1
Correlation coefficient	0.993	0.994	1
Fractional Bias	-0.018	0.006	0
Normalized Mean Square Error	0.001	0.002	0
Geometric mean	0.982	1.022	1
Geometric Variance	1.001	1.003	1
Average difference	0.028	0.040	0

Table 3.4.: Quantification of the Reynolds number influence in VKI-L2 wind tunnel.

3.4.2. Fully developed flow

To simulate the atmospheric wind, the flow has to be fully developed in the longitudinal direction, that means no longitudinal evolution of the averaged wind speed should be noticed. Two experiments are here compared: the first at the start of the turn-table (X = 0 m) and the other in its center (X = 1.4 m). Tests are performed at 15 m/s in the "Cup 2" configuration (see section 3.2.2). Results are presented in Figure 3.9 and comparison quantities are listed in table 3.5.

The results show a global similarity between the profiles but more scatter is observed near the surface where the velocity is low with high velocity gradient and high turbulence. The roughness elements on the floor stops at the start of the turn-table,(Figure 3.3) therefore, there is a zone without roughness between the two measurements, this implies the growth of a inner layer affecting the lower part of the wind profile by decreasing the turbulent level and increasing the velocity amplitude (Figure 3.9).

For the VKI-L2 wind tunnel the verification is performed in an empty test section, with no roughness elements. Two measurements distant from 0.05 m are taken at the area of the test. Figure 3.10 presents the velocity and longitudinal turbulence profile with the associated scatter plot and table 3.6 gives the quantitative data. For the distance measured, the development of the BL is negligible.

The distance used for the assessment of the fully developed state can be different from the one really used in the test section, a parameter can be easily defined to quantify the fully developed state in the region of the test:

$$\frac{\Delta U}{\Delta X} \times \frac{X_{\text{net area}}}{U_\delta} \tag{3.1}$$

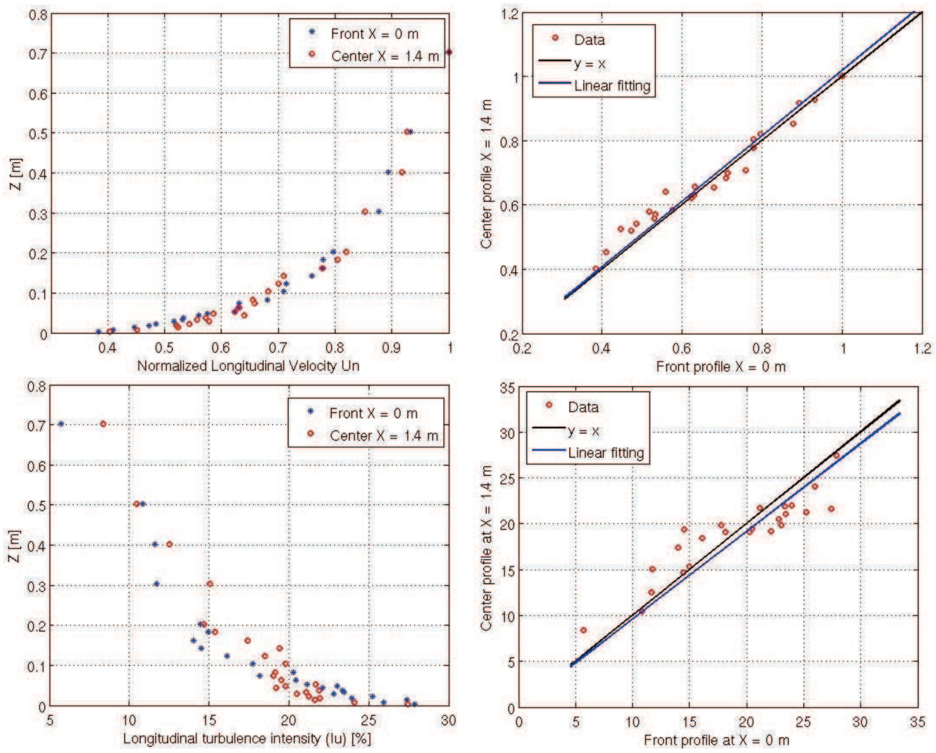

Figure 3.9.: Tests on the fully development state of the BL in VKI L1 test section. Comparison of the normalized velocity profile (upper left) with the scatter plot (upper right) and of the turbulence profile (lower left) with scatter plot (lower right).

with $X_{\text{net area}}$ the distance (in meter) used for the test. The number represents

Comparison X = 0 m / X = 1.4 m	U [-]	Iu [-]	Perfect match
Linear coefficient	1.017	0.958	1
Correlation coefficient	0.984	0.917	1
Fractional Bias	-0.026	0.016	0
Normalized Mean Square Error	0.003	0.018	0
Geometric mean	0.966	0.955	1
Geometric Variance	1.00	1.023	1
Average difference	0.054	0.125	0

Table 3.5.: Quantification of the fully developed state of the flow in VKI-L1 wind tunnel.

the percentage of velocity change inside the area used for the test. It is dependent

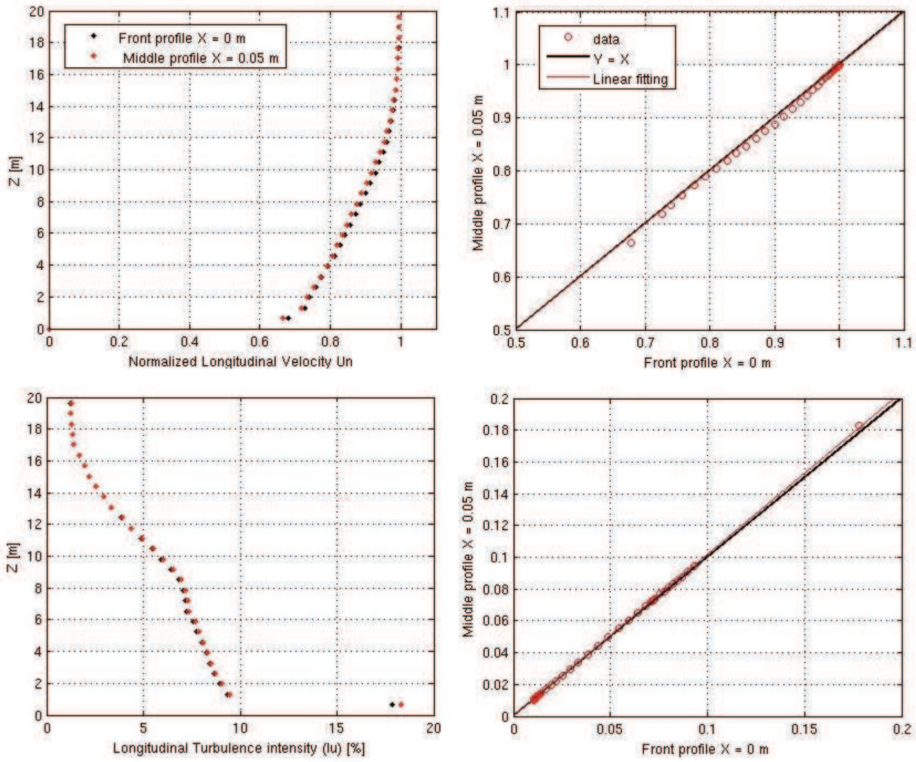

Figure 3.10.: Tests on the fully development state of the BL in VKI-L2 test section. Comparison of the normalized velocity profile (upper left) with the scatter plot (upper right) and of the turbulence profile (lower left) with scatter plot (lower right).

on the size of the mock-up used. For VKI-L1 wind tunnel, if the mock-up is 2 m long, it will be: (Average difference, from table 3.5) * $X_{\text{net area}}$ / ΔX = 0.054 * 2 / 1.4 = 0.077. That mean in average 7.7 % of change of the velocity profile.
For VKI-L2 wind tunnel, 1 m is used for the test in chapter 4, therefore, it will be: 0.003 * $X_{\text{net area}}$ / ΔX = 0.003 * 2 / 0.05 = 0.06.

Generally, the difference between the profiles are larger near the wall, this is the area where the velocity gradients are the most important so a small error in the vertical positioning can influence a lot the results. The calculations proves that the flows in both wind tunnels can be estimated fully developped.

Comparison X = 0 m / X = 0.05 m	U [-]	Iu [-]	Perfect match
Linear coefficient	1.035	1.0189	1
Correlation coefficient	0.999	1.000	1
Fractional Bias	0.002	0.011	0
Normalized Mean Square Error	0.000	0.001	0
Geometric mean	1.003	0.994	1
Geometric Variance	1.000	1.000	1
Average difference	0.003	0.0064	0

Table 3.6.: Quantification of the fully developed state of the flow in VKI-L2 wind tunnel.

3.4.3. Longitudinal pressure gradient

For a laboratory simulation of the ABL, a zero pressure gradient has to be developed in the mean flow direction. The VDI guidelines [85] propose to verify a maximum dimensionless pressure gradient criteria as:

$$\frac{(\frac{dP}{dX} \cdot \delta)}{(\frac{\rho_0}{2} \cdot {U_\delta}^2)} \leq 5\% \tag{3.2}$$

where δ is the BL height determined at 99% of the free-stream and U_δ the velocity at the BL height and.

The ceiling of the L1 wind tunnel test section is adaptable. The pressure gradient is calculated over 10 m at two free-stream velocities. The pressure difference is 12.9 Pa at 15 m/s and 2.2 Pa at 7 m/s. The dimensionless pressure gradients criteria is fulfilled for both cases with respectively 1.27% and 1%.
In the L2 wind tunnel, the highest dimensionless pressure gradient appears to be with the Counihan wings with a pressure difference of 17 Pa over 1.6 m, that gives 3.6%
For both wind tunnels, the longitudinal pressure gradient criteria is fulfilled.

3.4.4. Homogeneity of the flow

In both wind tunnels, measurements are carried out to assess the homogeneity of the wind velocity and turbulence in the lateral direction.

In L1 wind tunnel, a transversal profile is performed with a triple hot-wire probe (see annexe A.2.2) at h = 0.785 m above the turn-table center.
Results are plotted in figure 3.11.
The transversal variation of the longitudinal velocity component (U) is below 1% (0.7%) in the central part (0 m < Y < -0.9 m). The closest point measured at the side wall (Y = -1.2 m) is 7% lower than the middle velocity. This point is reaching the boundary layer of the side wall, that explains the decrease of the velocity and the increase of the turbulence intensity.

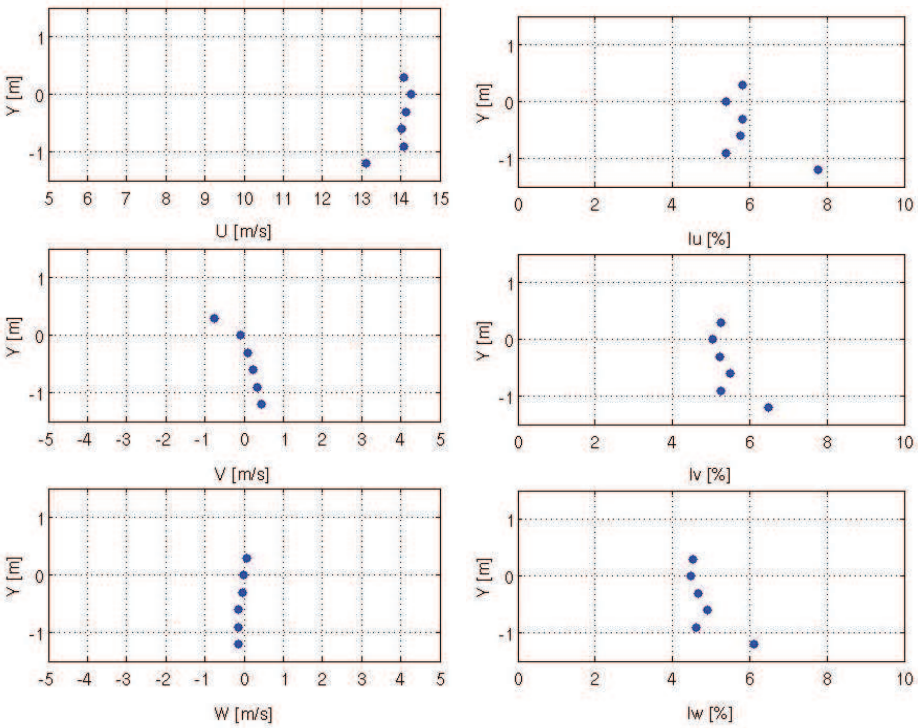

Figure 3.11.: Three velocity and turbulence intensity components of the test section transversal profile at h = 0.785 m above the turn-table of the VKI-L1 wind tunnel.

In the L2 wind tunnel, PIV measurements are performed and the transversal variation is quantified by comparing the velocity and turbulence profiles in the central PIV plane (Y = 0 m) to three parallel planes in the transversal direction (Y = 0.02 m, Y = -0.02 m and Y = -0.05 m). In the central zone measured (+/- 0.05 m), the maximum deviation is below 1% for both the velocity and the turbulence intensity.
Similarly to the fully developed flow, a parameter can be set:

$$\frac{dU}{dY} \times \frac{Y_{\text{net area}}}{U_\delta} \tag{3.3}$$

We here have, for VKI-L1, with a two meter wide mock-up: 0.007*2/1.8 = 0.8%. In VKI-L2, for a 0.1 m mock-up, it gives 0.01*0.1/0.1 = 1%

3.4.5. Conclusions

This section verifies the quality of the wind tunnels flow by checking one by one the requirements necessary to reproduce a fully developed turbulent boundary layer. Precise quantities of the bias in each test section are provided.
This section is a mandatory first step before going further in the study. It proves that the test sections can be suitable to perform atmospheric flows studies.

3.5. Determination of flow characteristics and comparison with literature field data

Once the reliability of the test section is verified, flow characteristics measured in the wind tunnels are compared to the real atmospheric wind. The first part aims at validating the tools for computing the ABL properties. Then, the mean and fluctuating velocity profiles simulated in the tunnels are compared to empirical data of real atmospheric flows.

3.5.1. Determination of ABL properties

The extraction of the properties of the modelled ABL, like the aerodynamic roughness length, the friction velocity (z_0 and u_* in equation2.4) or the power coefficient (α in equation 2.5) is not a straightforward task but it is of utmost importance because it is the link with the real atmospheric flow.
Few authors discuss this issue, like Farell, Iyengar and Karimpour [37, 44, 53]. Iyengar [44] presents a well documented comparison of the different ways to estimate the flow properties, especially the friction velocity for several boundary layers.
Traditionally, two approaches are possible to estimate the ABL properties: indirect procedures (curve fitting) or direct measurement. The direct measurement is only applicable for u_* and can be performed by measuring the Reynolds stresses near the wall or by measuring the wall shear stress τ_{wall} (equation 2.7) with an aerodynamic balance. The determination of z_0 and α results anyway from a curve fitting.
Usually, indirect methods are preferred to direct measurements because it can be simply extracted from a time averaged velocity profile, however, some important errors can be found if some precautions are not considered: the flow has to be fully developed, present an asymptotic state, and the fitting should be performed only using measurement in the logarithmic part of the profile.
Iyengar [44] presents two indirect methods, the first is to fit the velocity profile with a Hama's [41] profile and find the least error. The second is to fit both a log-law and power-law and to look for the best common fit. The indirect approach applied is not always satisfactory and can results in rather inaccurate values (factor of two).

Another result of this work is that the measurement of the Reynolds shear stress (eq. 2.7) with a X-wire probe can lead to an over estimation of the friction velocity by 15% compare to the aerodynamic balance measurement.
In his paper from 2001, Karimpour [53] is one of the only author to precisely describes and evaluate the precision of the indirect method used and to compare to direct and other indirect methods. He uses the fitting of a natural logarithmic curve, (equation similar to equation 2.4) to the mean velocity profile considering the right zone of the velocity profile. In figure 3.12, on the left side, the velocity profile plotted in semi-log clearly shows different parts and not all the profile has to be fitted to a logarithmic law. The velocity profile can be separated in three zones: the roughness sub layer, the logarithmic layer and the outer layer. In this particular case, the roughness sub layer extends until $z_r = 0.04$ m this is a little below the commonly estimated height $\mathrm{Z}_r = 2 \times \mathrm{H}_R$ ([37, 68]). The logarithmic part vanishes starting from $Z_1 = 0.3$ m, this upper limit that distinguishes the log zone from the outer zone is generally not very clear.

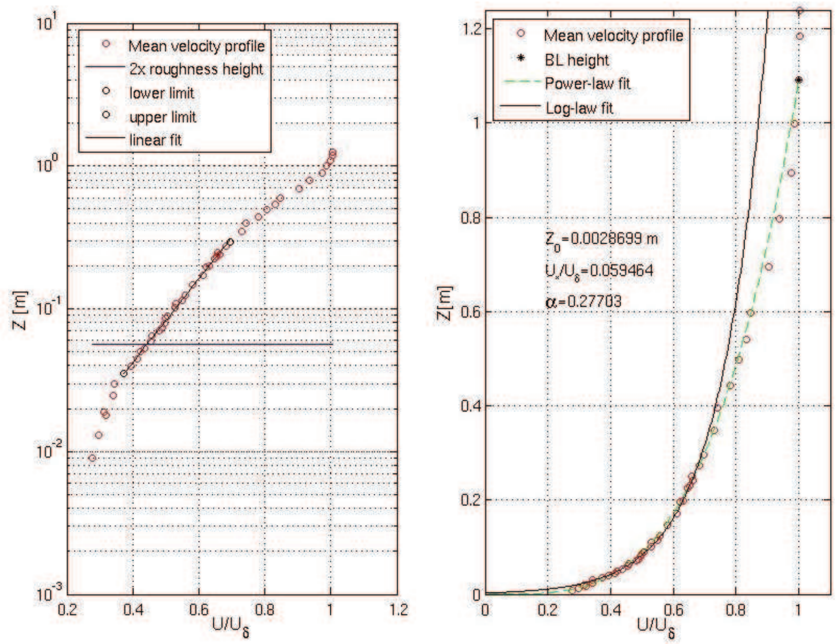

Figure 3.12.: Determination of ABL parameters of the BL proposed by Iyengar [44] with the present method.

In the present work, the determination of the parameters is performed by a

semi-automatic procedure with an indirect method consisting in fitting the mean velocity profile to the logarithmic equation 2.4. First, the mean velocity profile is displayed in a semi log plot (Fig. 3.12). The logarithmic part of the measured profile appears as a line and the user can choose the first and last point to account in the fitting. As the logarithmic law applies only above the roughness elements, an horizontal line is plotted at two times the roughness height (see Jimenez [47]). The trend of the linear fit a is linked to the friction velocity by: $u_* = \frac{\kappa}{a}$ and the aerodynamic roughness length z_0 is the intersection of the linear fit with the vertical axis ($z = z_0$ at $U = 0$).
For the power coefficient, α (in equation 2.5), it is deduced from fitting a power law to the measurements on the entire BL height, until $z = \delta$.

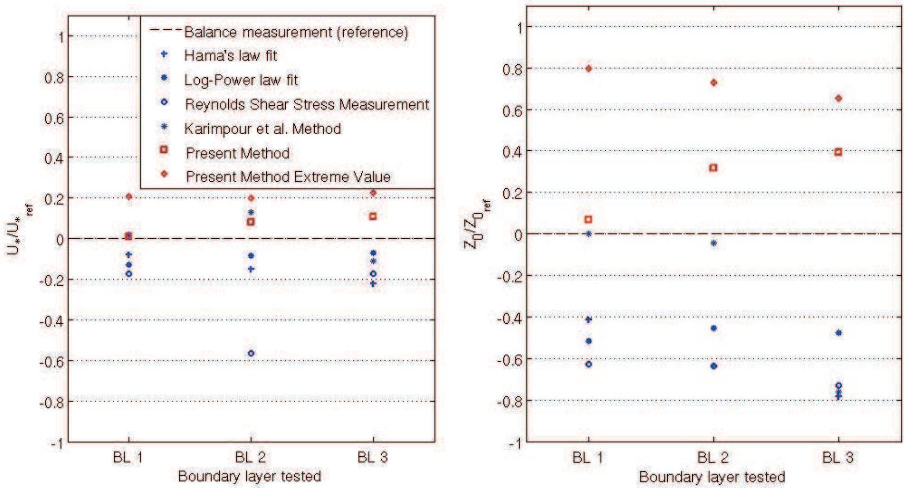

Figure 3.13.: Comparison of friction velocity u_* and aerodynamic roughness length z_0 determined by different methods.

To assess the accuracy of the procedure used, all methods described by Iyengar and Karimpour [44, 53] and the one used in this work are compared on the same boundary layers BL1, BL2 and BL3 available in Iyengar [44] and using $H_R = 0.028$ m cubic elements. Figure 3.13 summarises the results of the different approaches, the reference value is the one calculated by drag measurements. The "Extrem Values" in the figure are giving an estimation of the maximum freedom of the user.
The present indirect method is quite competitive in estimating the friction velocity, +6% in average. Notice that this method is always giving an overestimation. The degree of freedom of the user can give up to +22%, this is what other methods give in average.
For the aerodynamic roughness length, in general, results are much more spread.

The proposed method gives less scatter and equivalent results to the method proposed by Karimpour [53]: +26% in average compare to 27%. The proposed methods is also overestimating z_0.
The evaluation of the power coefficient α is very comparable to the estimation given by Iyengar [44], the method gives less than 1.5% of difference with a maximum of 3.5%.

Another check is performed by calculating the friction velocity by the in-house method and by the wall shear stress method (equation 2.7) thanks to the use of a triple hot-wire probe (see appendix A.2.2). This is performed only for one configuration and the proposed method gives u_*= 0.69 m/s instead of u_*= 0.71 m/s with the wall shear stress method. The mean velocity profile and the fluctuating information reach approximately the same estimation for the friction velocity. That confirms the good quality of the method proposed and gives confidence in the flow development.

The indirect methods used for this work works well in estimating the characteristics of the ABL: α, z_0 and u_* compare to the literature. This technique is applied to both experimental and numerical mean velocity profiles. Those parameters are important in the comparison with a real flow, but further verifications, such as for the turbulence are necessary.

3.5.2. Roughness element height (H_R), element density(λ) and aerodynamic roughness height (z_0) relationship

In the literature, several authors tried to relate the roughness element height to the aerodynamic roughness length. For example, Jimenez, Raupach and Farell [47, 68, 37] compute the ratio $\frac{\mathrm{Z}_0}{\mathrm{H}_R}$, compare it to the roughness density λ_f and shows that experimental data are following an empirical relationship.
The ratios are calculated for both wind tunnels and presented in figure 3.14. +/- 25 % uncertainty is added for the determination of the aerodynamic roughness length in the wind tunnel. The present data are also following this rule.

3.5.3. Aerodynamic roughness height (z_0) and power coefficient (α) relationship

Both the aerodynamic roughness length z_0 and the power coefficient α are reflecting the terrain roughness. Counihan [29] presents an empirical relationship between z_0 and α fitted to a series of field experiments details in the paper. Figure 3.15 presents the Counihan data and the fitting he proposes.

In the wind tunnel, z_0 and α can be determined independently and as α is not linked to a scaling factor (only a shape parameter), figure 3.15 can be use to determine a range of possible scaling factors for each configuration. Figure 3.16

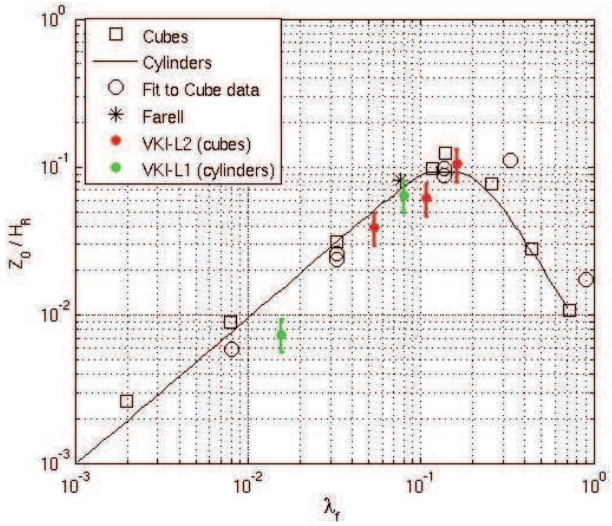

Figure 3.14.: Dimensionless roughness length z_0/H_R as a function of λ_f. "Cubes" and "Spheres" are taken from a compilation by Raupach [68], Farell is taken from Farell [37]. Notice that VKI-L1 roughness elements are cylinders and VKI-L2 roughness elements are cubic.

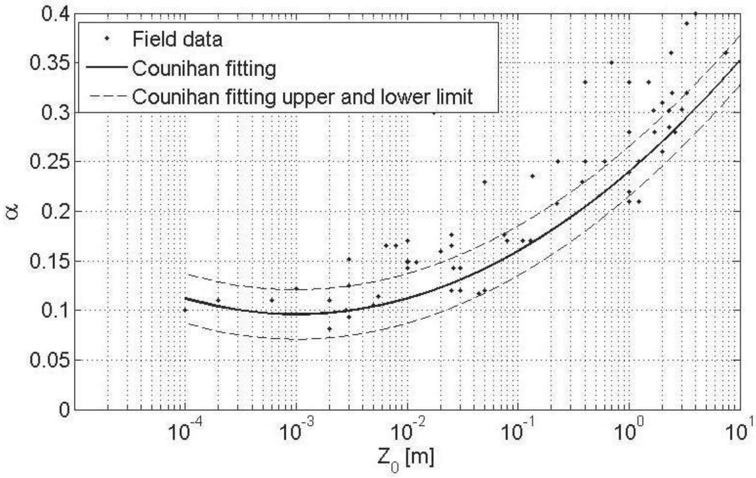

Figure 3.15.: Counihan [29] fitting of field data relating z_0 and α.

presents the wind tunnel measurements at the wind tunnel scale (blue and red dots) with Counihan results. For a given α there is a range of possible z_0, between the maximum and minimum curves proposed by Counihan. It also means a range of possible scaling factors. This is shown with an horizontal line in the graph. This is performed taking into account a potential 10 % error in the determination of the power coefficient. Due to the shape of the curve, for too low power coefficient, only the maximum scaling factor is possible to compute.
It is also visible that, the wind tunnel data have a trend very similar to the fitting of Counihan.
Results of scaling factors are summarized in table 3.7.

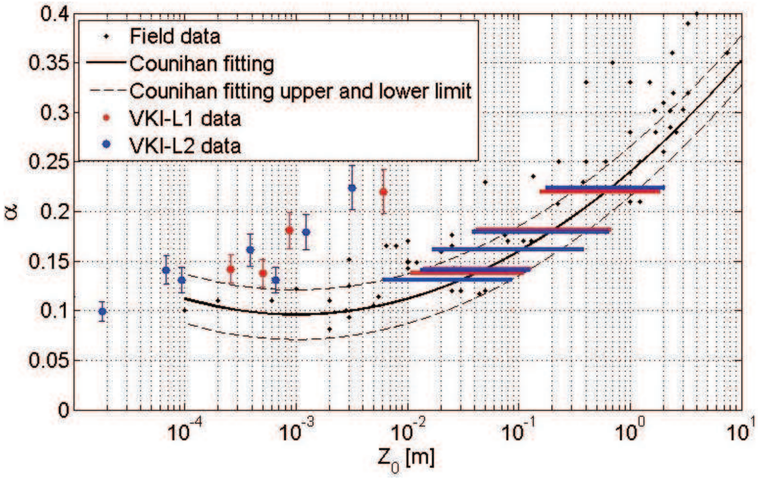

Figure 3.16.: Wind tunnel data added to the graph relating z_0 and α, the red and blue points are the wind tunnel data without scaling and the red and blue lines are the possible scalings to fulfil Counihan fitting.

Configuration	α	Min scaling factor	Max scaling factor
VKI-L1 no cups	0.112	-	6 600
VKI-L1 32 mm cups	0.18	50	770
VKI-L1 95 mm cups	0.22	25	300
VKI-L2 no roughness	0.12	-	14 000
VKI-L2 Lego floor	0.13	65	920
VKI-L2 11 mm block roughness	0.16	45	970
VKI-L2 21 mm blocks roughness	0.18	30	520
VKI-L2 31 mm blocks roughness	0.224	55	650

Table 3.7.: Estimation of the maximum possible scaling factors according to Counihan [29] relationship in both wind tunnels.

This is one way of estimating possible scaling factors in the wind tunnels, but other parameters enter into consideration like the turbulence properties of the wind tunnel flow. Next sections consider this aspects.

3.5.4. Turbulence intensity and turbulence scale profiles

According to the norms [85, 35], the turbulent intensity vertical profile depends on the terrain roughness (see equations 2.8 to 2.12). In the wind tunnel the modelled profile has to fall in the norms.
The scaling of a wind tunnel flow can then be performed by fitting the turbulence intensity profile to the VDI [85] norms presented in figure 2.2.
An example is presented in figure 3.17 with three profiles and at a possible scaling factor. The wind tunnel profile can fit a range of scales. Table 3.8 gives an idea of the possible range to fit the complete profile up to 350 m. Notice that higher and lower scaling factors are still possible but only a portion of the profile will fit the guideline.

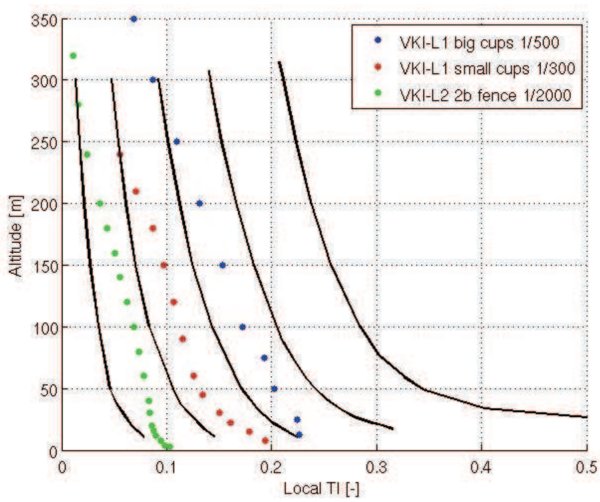

Figure 3.17.: Turbulence intensity profile in the wind tunnels. Possible scales for different configurations.

Additionally, the integral length scale information can be used to find a range of possible scaling factors following Counihan [29] classification introduced in figure 2.4. Figure 3.18 presents an example of a possible scaling for the same profiles as 3.17.

For three wind tunnel configurations presented as examples in figures 3.17 and

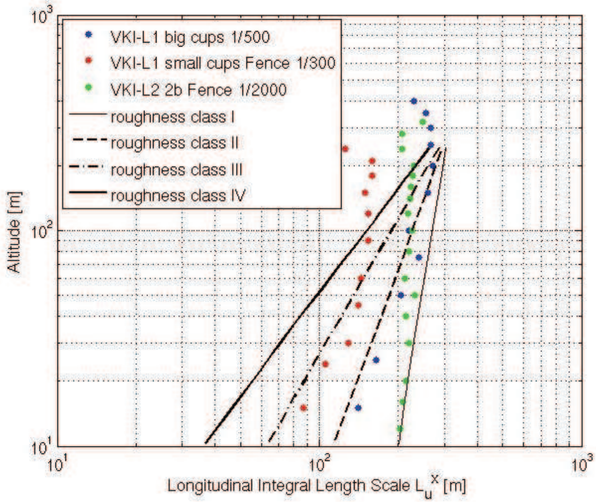

Figure 3.18.: Integral length scale profile in the wind tunnels.

3.18, the profiles are well following different terrain roughness. For example, the *VKI-L2 2b fence 1/2000* case is fitting well to a terrain category I for on the turbulent intensity profile. And turbulence length scale side, the profile is also coherent with a *slightly rough* terrain roughness.
For the *VKI-L1 95mm cups 1/500* configuration, the turbulent profile follows a *rough* terrain category. However, in figure 3.18 the integral length scale is too high compare to the terrain roughness found in figure 3.18 (130 m instead of 210 m at 50 m and 180 m instead of 210 m at 100m). That means that the characteristic length of the turbulence generated in the wind tunnel is a little too high for this scale. The scaling factor may be diminished to fit better the turbulence scale.
For each case, the scaling factor can be optimised to have the best desired turbulent reproduction in the wind tunnel.

3.5.5. Spectral information

In addition to the time-averaged data, the fluctuation of the wind velocity should also reflect the real ABL flow. The turbulent spectra is computed from triple hot-wire measurements realised in the VKI-L1 wind tunnel at a frequency of 3 kHz with a cut-off frequency of 300 Hz (Figure 3.19).
The turbulent spectra measured is compared with the Kaimal spectra [51] introduced in section 2.3.4 that comes from the fitting of field measurements from the KANSAS experiment [52]. The general shape reproduces well the Kaimal profile

Configuration	Possible range based on Iu	Possible range based on L_u
VKI-L1 no cups	200 - 5 000	250 - 700
VKI-L1 32 mm cups	100 - 3 000	200 - 650
VKI-L1 95 mm cups	300 - 1 000	150 - 650
VKI-L2 no roughness	4 000 - 20 000	—
VKI-L2 Lego floor	3 000 - 20 000	—-
VKI-L2 21 mm blocks roughness	- - 5000	1 000 - 2 500
VKI-L2 21 mm blocks fence	500 - 5 000	—

Table 3.8.: Estimation of the minimum and maximum possible scaling factors according to the turbulence intensity and the integral length scale information taking into account the complete profile up to 350 m.

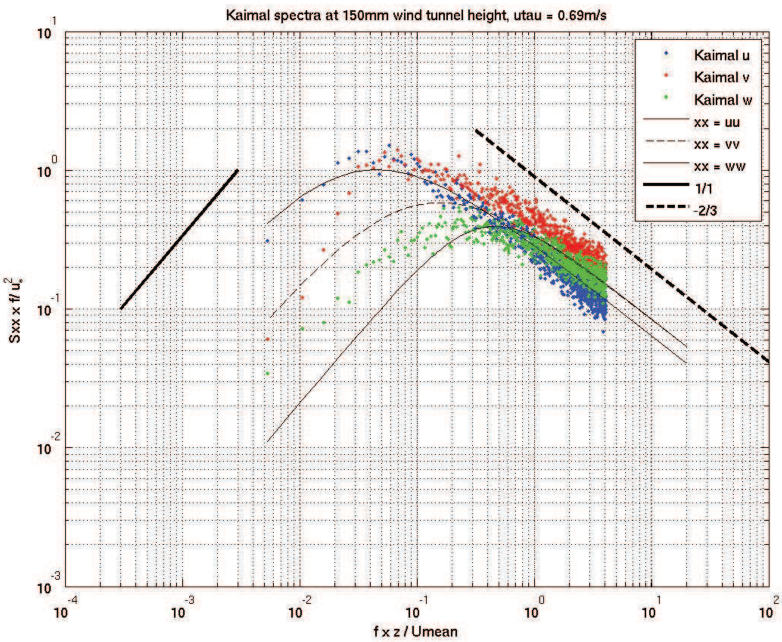

Figure 3.19.: Velocity spectra in the VKI-L1 wind tunnel performed at an altitude of Z = 0.15 m compared with Kaimal [52].

for the three components. The amplitude of the peak is a little overestimated for the longitudinal and the lateral component and it presents a little shift. This is also the case for the vertical component, but the amplitude is better reproduced. Generally, there is an over production of turbulence in the lateral and vertical direction especially for large structures,but the general shape reproduces reasonably well the ABL turbulence.

3.5.6. Conclusions

This section describes and validates the methodology for determining the time averaged properties of the BL.
Additionally, it compares successfully the wind tunnel BL properties with empirical laws extracted from field atmospheric data and underlines the similarities and limitations of the reproduction of atmospheric flows in both wind tunnels.
Both wind tunnels show their abilities in modelling atmospheric flows both for the mean and fluctuating information.

3.6. Parametric study of the BL generators

In order to reproduce given inflow conditions in the wind tunnel, and to prevent traditional time consuming trial and error tests, it is interesting to rationalize the approach by studying the effect of BL generators on the BL characteristics. To do so, a parametric study involving two wind tunnel tests and CFD computations is carried out.
Measurements and simulations aim at describing the effect of individual and combined BL generators, like roughness elements, fences and grids, on the BL characteristics: BL height, aerodynamic roughness length, turbulence level...
Results are presented and discussed in this section.

3.6.1. Test matrix

In the VKI-L1 wind tunnel, 7 configurations are tested to study the influence of the grid, the fence, and the roughness element height.
The numerical simulation is set to reproduce the VKI-L1 wind tunnel configuration. 11 configurations are tested to study the influence of the fence, the roughness element height and density.
In the VKI-L2 wind tunnel, 19 configurations are tested to investigate mainly the rule of the fence height and number, the roughness height and the Counihan wings. Table 3.9 summarises the configuration tested.

Number of configurations tested	grid	fence height	number of fence	roughness element height	roughness element density	transition blocks	Counihan wings
VKI-L1 Exp	1	1	1	3	1	3	-
VKI-L1 CFD	-	3	1	6	3	-	-
VKI-L2 Exp	-	6	5	5	1	-	1

Table 3.9.: Configuration tested for the parametric study.

Measurements are performed at the position of future tests and at a given free-stream velocity: table 3.10.

Configuration	Distance from start [m]	Free-stream velocity [m/s]
VKI-L1 Exp	15.4	15
VKI-L1 CFD	11	10
VKI-L2 Exp	1.5	25

Table 3.10.: Settings for the measurements in the wind tunnels and for the numerical simulation.

All those data are forming an important database for interpretation of the relative influence of each BL generator.

3.6.2. The numerical modelling

To support the experimental investigations, numerical computations are added to the global database. The numerical simulations are reproducing the VKI-L1 wind tunnel at full scale in different configurations that are not implemented in the wind tunnel. The Fluent software is used with a k-ϵ RANS model.
The numerical simulations are part of a previous work performed at VKI. More details can be found in [31].

Due to the difficulty to model the front grid numerically, only the effect of fences and roughness elements is investigated, specially changing the density. The numerical simulation includes the study of 5 different roughness heights, three different roughness densities and two fences.

3.6.3. The influence of the grid

In the ABL generation set-up in VKI-L1, a grid is placed at the entrance of the test section. Its effect is studied experimentally with 35 mm cups on the floor. Figure 3.20 presents the velocity profile, the Reynolds stress profile and the turbulence profiles of the wind with and without the grid at the inlet.
The grid has a direct effect on the boundary layer height that is almost doubling from around 0.3 m to around 0.6 m. With the grid, the wall friction velocity is almost not affected (+ 7.5 %) neither the aerodynamic roughness length (0.0026 m instead of 0.0015 m). The power coefficient is slightly affected (0.16 instead of 0.173)).
On the turbulence side, in the three directions very weak effect is observed: the free-stream turbulence is slightly increased and the near-wall turbulent level a little decreased. Those fluctuations are of the order of +/- 2 %.

3.6.4. The influence of the fence

Contrary to the grid, the fence has a dramatic impact on turbulence levels. Figure 3.21 compares two experiments carried out in the VKI-L1 wind tunnel with and without a $H_F = 0.15$ m fence. Both configurations include a grid and 35 mm cups elements.
The fence induces an increase of more than 5.5 % (absolute increase) of the turbulence level in average. All three components of turbulence are affected, this represents a multiplication by 9 of the TKE (also written k in equ. 2.3). The turbulence level is increased mostly between Z = 0.2 m and Z = 0.6 m. There, the TKE is multiplied by more than 15 in average. The influence of the fence is weaker under Z = 0.2 m.
The fence also provides a constant value of Reynolds stress up to Z = 0.5 m, the friction velocity can then be deduced from the equation 2.7 by taking the friction velocity where it is independent of height.

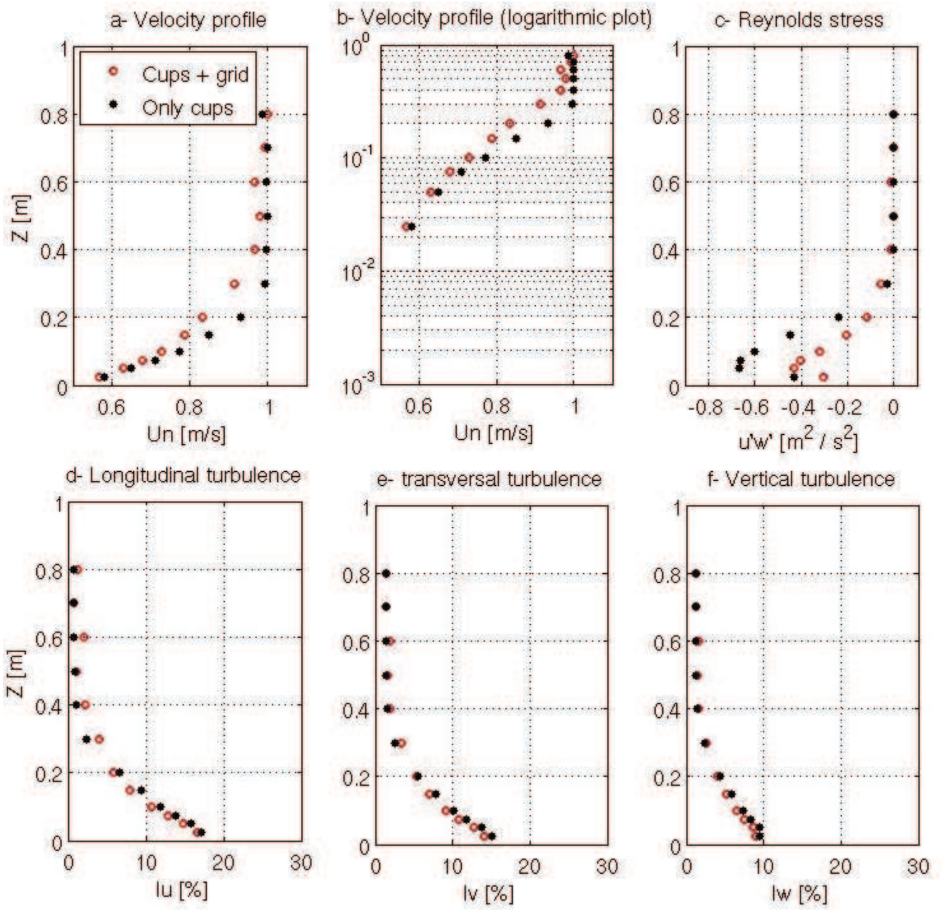

Figure 3.20.: Effect of the presence of the grid in VKI-L1 wind tunnel. Tree components measurements performed with a triple hot-wire A.2.2

Three configurations, no fence, $H_F = 0.05$ m and $H_F = 0.10$ m are tested numerically in a configuration with 35 mm cups roughness and no grid (Figure 3.22). Observations are similar to the experiment, the increase of the fence height affects directly the boundary layer height and drastically the turbulence level. The influence is mainly visible above a certain height, here Z = 0.1 m.

A more detailed study is performed in the VKI-L2 wind tunnel (see description

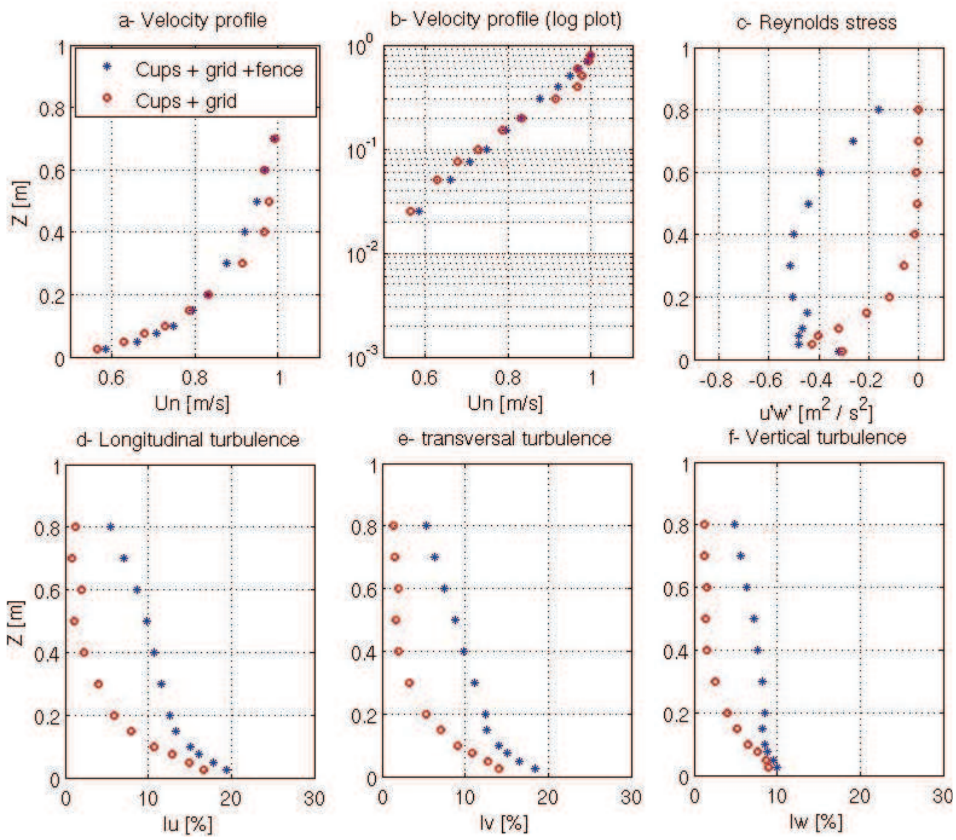

Figure 3.21.: Effect of the 0.15 m fence on the three components of the velocity and the turbulence. Study in VKI-L1 wind tunnel.

in section 5.3.3) with five fences: H_F = 0.01 m, 0.02 m, 0.03 m, 0.04 m and 0.06 m in a test section equipped with Lego floor surface. Results presented in figure 3.23 are once again showing the increase of the boundary layer height and the progressive increase of the turbulence level when the fence's height increases. The higher number of available data would allow the building of empirical relationship.

The effect the number of fences of the same height is also investigated by placing 1, 2, 3 and 4 fences of H_F = 0.01 m height in the test section. The fences are arranged at 35 H_F from each other along the test section. Figure 3.24 presents the results together with the case without fence. The general remark is that the number of fences has a very weak effect on both the velocity and the turbulence profile. With 2 fences, the velocity deficit induced is less than 1% and the turbu-

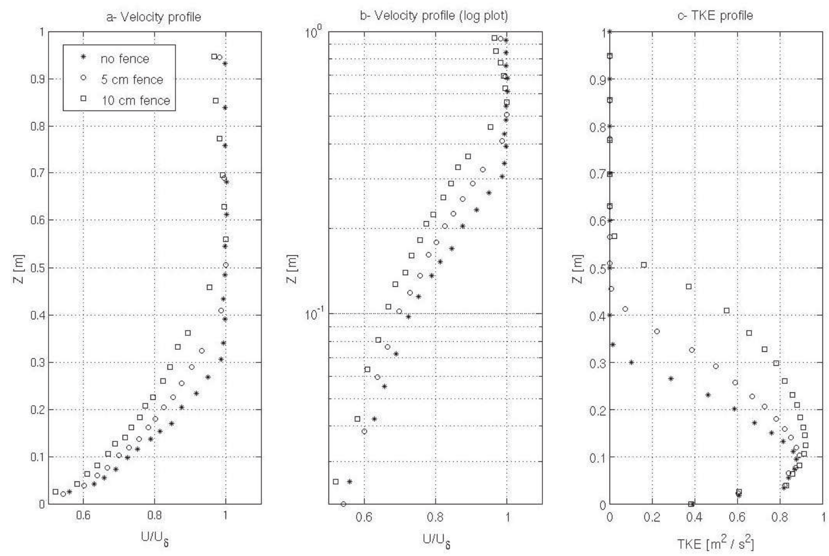

Figure 3.22.: Effect of the fence height studied by CFD for three heights.

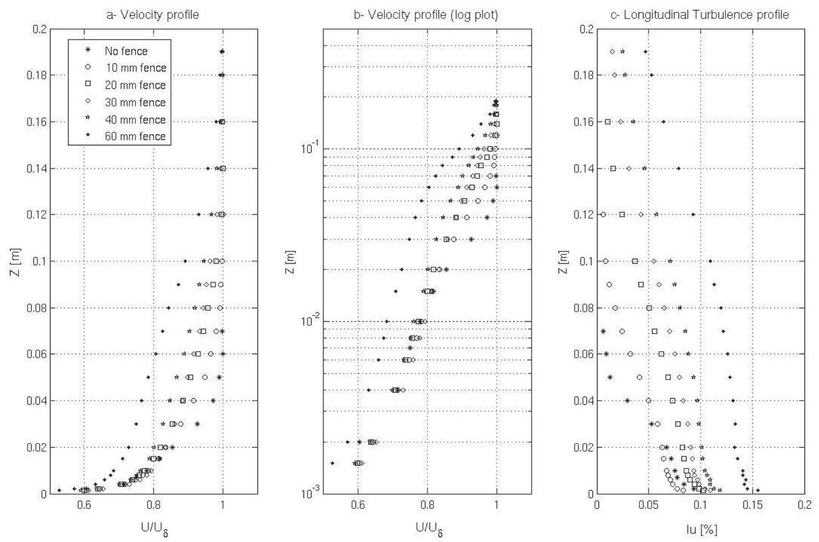

Figure 3.23.: Effect of the fence height studied in VKI-L2 wind tunnel with a Lego floor at 5 different heights.

lence increase of the order of +0.2% compare to the case with only one fence and with 4 fences, the velocity deficit is below 3% and the turbulence increase around +0.5 %.
Increasing the number of fences has almost no effect on the velocity and turbulence profile.

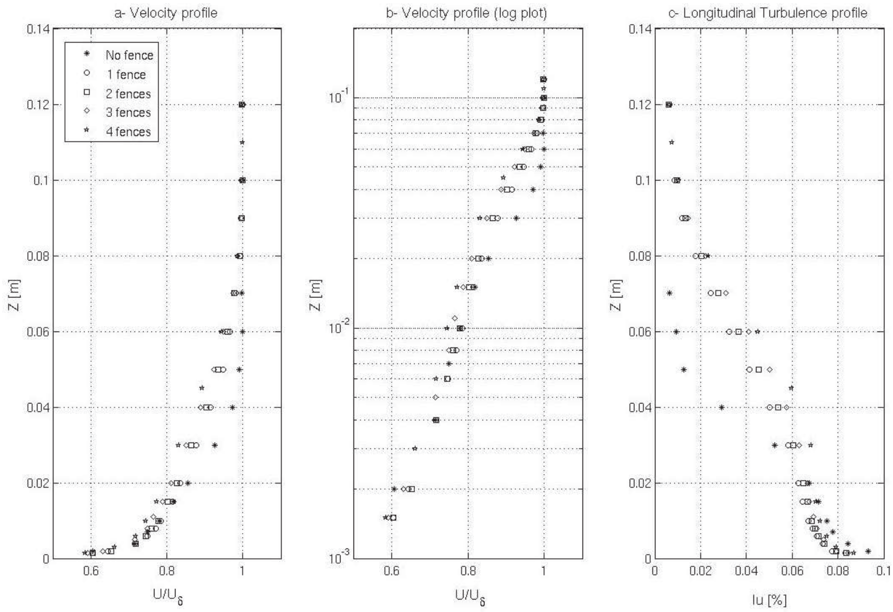

Figure 3.24.: Effect of the number of fences studied in VKI-L2 wind tunnel.

3.6.5. The influence of the roughness elements

With the same three supports (2 wind tunnels and a CFD simulation), a study of the influence of the wall roughness is performed.
In VKI-L1 wind tunnel three roughness heights are tested, all of them also include a 15 mm fence and a grid, roughness heights are: $H_R = 0$ mm, 35 mm and 95 mm.
As the surface roughness increases the boundary layer height and the turbulence level increases as well (Figure 3.25). However, contrary to the effect of the fence, the roughness influences much more the lower part of the BL, the effect is vanishing in the highest part of the profile. In VKI-L1, the turbulence intensity increase due to the roughness disappears for altitudes higher than 0.4 m in the case of 35 mm cups and 0.55 m for 95 mm roughness elements.

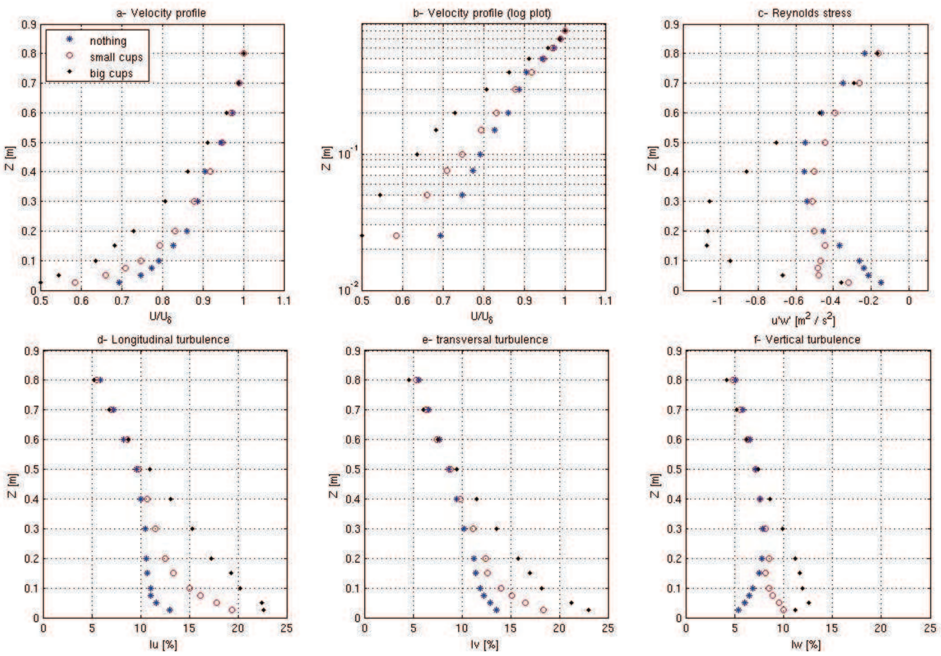

Figure 3.25.: Effect of the roughness height in the three components, study with a triple hot-wire in VKI-L1 wind tunnel.

As no fence was used, this phenomena is more visible in the numerical simulation, in figure 3.26 c-, the effect of the roughness is limited to a certain hight lower than the fence influence. It is also clearly noticeable from the log plot in figure 3.26 b-, that the aerodynamic roughness length is influenced very much by the roughness height, $z_0 = 3.3\ 10^{-4}$ m for 10 mm roughness and $z_0 = 1.2\ 10^{-2}$ m for 95 mm roughness height.

The last measurement, in the VKI-L2 wind tunnel, is consistent with the other results: increase of the boundary layer height, increase of the aerodynamic roughness length and increase of the turbulence level in the lower part of the BL. (Figure 3.27).

The effect of the roughness element density is also investigated by CFD computation. Three densities are tested, $\lambda_1 = 8.64$ %, $\lambda_2 = 6.48$ % and $\lambda_3 = 4.32$ % (definition of λ in section 3.2.2). The higher density is the reference one used for all other tests. Figure 3.28 shows that a higher density increases the turbulent level and the boundary layer height. In the range tested, the influence of the roughness

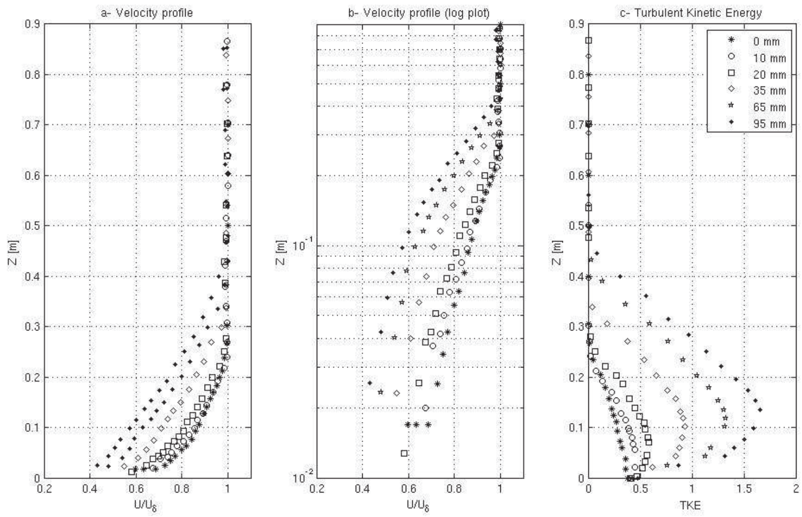

Figure 3.26.: Effect of the roughness height modelled by CFD.

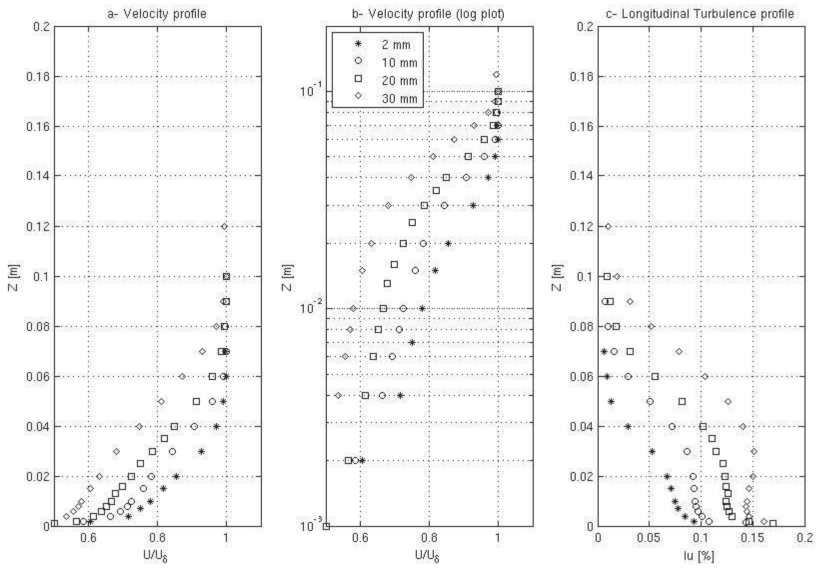

Figure 3.27.: Effect of the roughness height studied in VKI-L2 wind tunnel.

element density is of the order of 5 % for the velocity profile and related quantities and of the order of 20% for the TKE. This is limited compared to the influence of the roughness height or the fence height (often of the order of 100%).

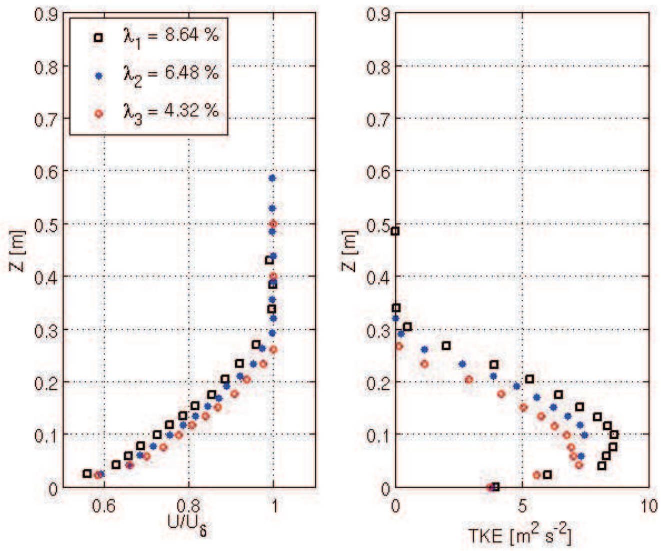

Figure 3.28.: Effect of the roughness density by CFD.

The fence height and the roughness element height are the two main drivers of the BL.

3.6.6. Modelling and parametrization of the fence and roughness element

The goal of this section is to try to extract general trends from all the test performed to find laws linking the BL generators dimensions to the BL characteristics (aerodynamic roughness lenght, BL height, turbulence level...). As the previous section show the predominance of the fence height and the roughness element height, the work is focused on the study of both parameters H_F and H_R.
Figure 3.29, compares the effect of the fence height and the roughness height on the BL height (δ) and the aerodynamic roughness length (z_0). It can be seen that the fence height drives mainly δ and the roughness element height drives z_0. Those dimensions and their link to the properties of the BL are deeper investigated in this section.

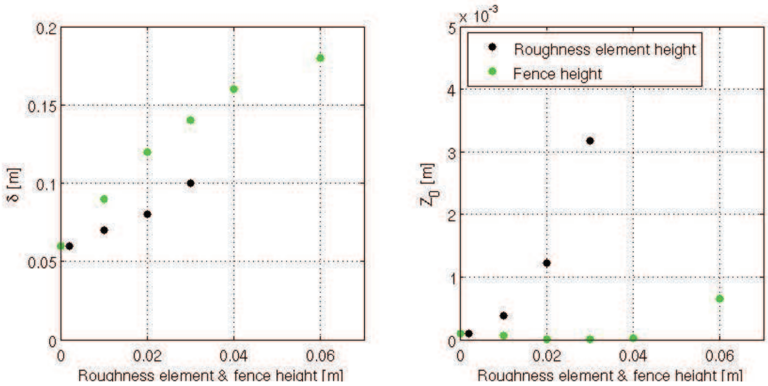

Figure 3.29.: Comparison of the effect of the fence height H_F and the roughness element height H_R on the BL height (left) and on the aerodynamic roughness length (right).

3.6.6.1. The fence height

Tests performed in the VKI-L2 wind tunnel are the most appropriate to study the fence effect as 6 configurations are tested. To extract a tendency, figure 3.30

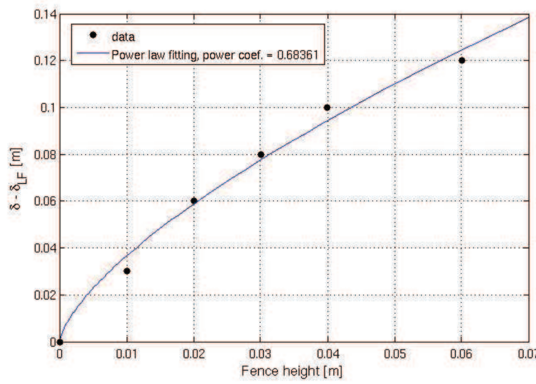

Figure 3.30.: Evolution of the boundary layer height ($\delta - \delta_{LF}$) with the fence height H_F.

shows the boundary layer height (δ) in function of the fence height (H_F). A simple power law can be fitted to this graph:

$$\delta(H_F) = 0.85 {H_F}^{0.68} + \delta_{LF} \tag{3.4}$$

with δ_{LF} the boundary layer height with the rough surface floor and no fence.

The increase of turbulence can also be estimated. Figure 3.31 (left) presents the evolution of the longitudinal turbulence level (Iu-Iu$_{H_F=0}$) in function of the fence height (H_F) for all the available altitudes (Z). From the data, (black dots in the figure) for a given altitude, the longitudinal turbulence level is increasing linearly with H_F following two slopes in function of the fence height. We have:

$$\text{for } H_F \leq 0.02 \text{ m:} \qquad \text{Iu} = \text{C}_1.H_F + \text{Iu}_{H_F=0} \tag{3.5}$$

$$\text{for } H_F > 0.02 \text{ m:} \qquad \text{Iu} = \text{C}_2.H_F + \text{Iu}_{H_F=0} \tag{3.6}$$

The coefficient of the slopes are changing with the altitude (Z), and figure 3.31

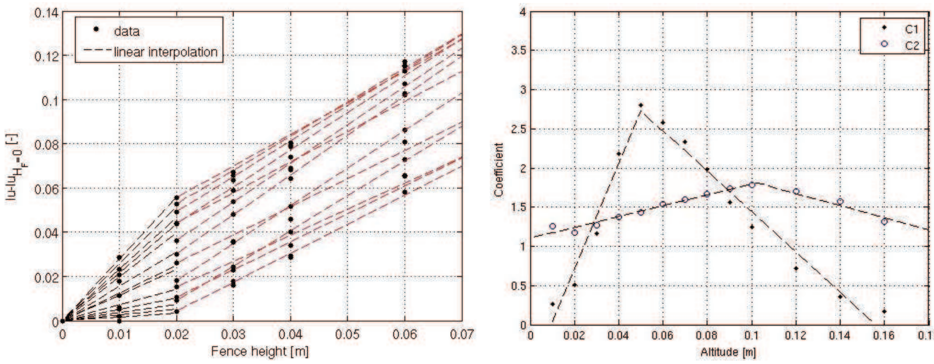

Figure 3.31.: Evolution of the longitudinal turbulence level (Iu-Iu$_{\text{H}_F=0}$) with the fence height H_F with a linear interpolation (left), and evolution of the linear interpolation coefficient with height (right).

(right) presents their evolution. It appears that they have a linear trend and two fitting can be build up in function of the altitude:

$$\text{for Z} \leq 0.05 \text{ m:} \qquad \text{C}_1 = 67.42 * Z - 0.639 \tag{3.7}$$

$$\text{for Z} > 0.05 \text{ m:} \qquad \text{C}_1 = -25.77 * Z + 4.018 \tag{3.8}$$

and

$$\text{for Z} \leq 0.1 \text{ m:} \qquad \text{C}_2 = 6.94 * Z + 1.103 \tag{3.9}$$

$$\text{for Z} > 0.1 \text{ m:} \qquad \text{C}_2 = -7.75 * Z + 2.6 \tag{3.10}$$

Thanks to this interpolation, a contour map of the longitudinal turbulence level can be drawn in function of the fence height and the altitude. Figure 3.32 presents

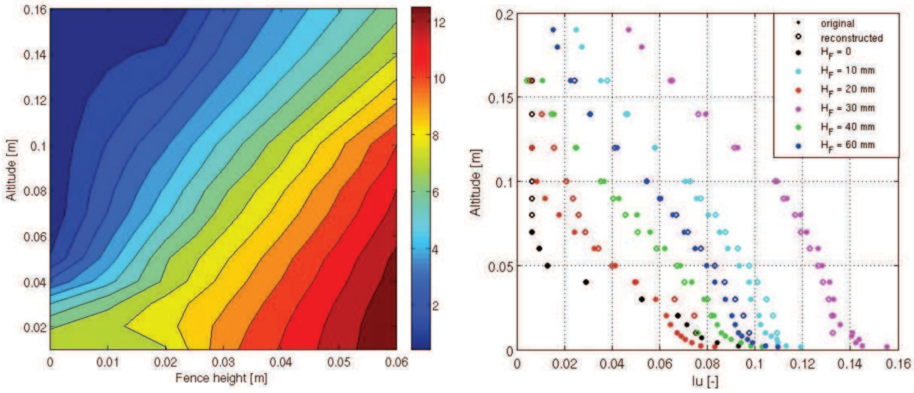

Figure 3.32.: Contour map of the longitudinal turbulence level in function of the altitude and the fence height [%] (left). Comparison between the original and reconstructed turbulence intensity profiles (right).

the contour map (left) and the comparison between the reconstructed turbulence profiles and the original data (right). The scatter observed between measured values and interpolation is 4.3 % in average except for H_F=0.01 m where the scatter in of the order 12 %. The interpolation shows clearly that influence of the fence reaches high altitudes.
Thanks to the interpolation, the effect on turbulence of any fence below H_F = 0.06 mm can be foreseen in VKI-L2. A similar behaviour can be expected from the VKI-L1 test section but too few data was gathered to confirm it.

This work allows a better understanding of the influence of the fence height on the properties of the BL and facilitates the decision process in choosing the fence height needed.

3.6.6.2. The roughness elements height

Similarly to the study performed for the fence height, a deeper investigation of the results is performed to understand and model the effect of the roughness height (H_R).
The roughness length is mainly influencing the aerodynamic roughness length z_0, and all wind tunnels and CFD data are falling in the same tendency. Figure 3.33 shows the aerodynamic roughness length in function of the roughness height in a log-log plot, the tendency see is a linear evolution of the logarithmic profile:

$$log(z_0) = 0.51\ log(H_R) - 0.42 \tag{3.11}$$

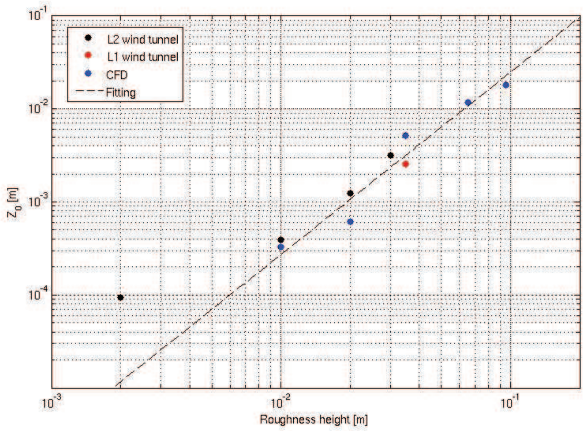

Figure 3.33.: Evolution of the aerodynamic roughness length z_0 with the roughness height H_R.

This empirical fitting works for a roughness height (H_R) between 0.01 m and 0.1 m. Notice that from the tests in VKI-L1 wind tunnel only one point is reported in this graph, this is because it is the only comparable measurement, others are performed with a grid.
This empirical relationship is strong because it is the same for both wind tunnels and for the numerical modelling.
Such a "universal" law is possible for the determination of the aerodynamic roughness because the aerodynamic roughness length (z_0) does not depend on the distance (after the profile is fully developed) neither on the velocity, this is a property of the surface. In contrary, the boundary layer height is dependent on distance and free-stream velocity.

The influence of the roughness element height on the turbulence profile is investigated using the same methodology as for the fence height in section 3.6.6.1.

As for the fence height, the linear fitting is divided in two (figure 3.34, left):

$$\text{for } H_R \leq 0.02 \text{ m:} \qquad \text{Iu} = \text{C}_1.H_R \tag{3.12}$$

$$\text{for } H_R > 0.02 \text{ m:} \qquad \text{Iu} = \text{C}_2.H_R \tag{3.13}$$

The coefficient of the slopes are changing with the altitude (Z), and figure 3.34

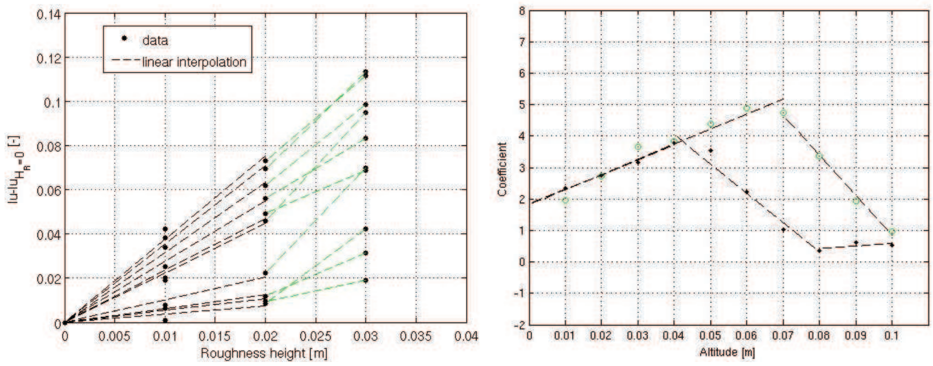

Figure 3.34.: Evolution of the longitudinal turbulence level (Iu) with the roughness element height H_R with a linear interpolation (left), and evolution of the linear interpolation coefficient with height (right)

(right) presents their evolution.The coefficients are also fitted linearly:

for Z $\leq$ 0.04 m:	$C_1 = 46.48 * Z + 1.844$	(3.14)
for 0.04 $\leq$ Z $\leq$ 0.08 m:	$C_1 = -93.22 * Z + 7.78$	(3.15)
for Z > 0.08 m:	$C_1 = 8.4 * Z - 0.24$	(3.16)
and		
for Z $\leq$ 0.07 m:	$C_2 = 47.9 * Z + 1.82$	(3.17)
for Z > 0.07 m:	$C_2 = -127 * Z + 13.54$	(3.18)

Like for the fence, a contour map of the longitudinal turbulence level can be drawn in function of the roughness element height and the altitude. Figure 3.35 presents the contour map and the comparison between the reconstructed turbulence profiles and the original data. In this case, due to the low number of data, the scatter observed is 1 % in average. The contour map clearly shows the very high influence of the roughness elements near the surface but the quick vanishing of its effect with height.

3.6.6.3. Relative effect of the roughness element height compare to the fence height

Figure 3.36, compares at the same scale the contour plot of the influence of the fence (left) height with the influence of the roughness element height (right) on the longitudinal turbulence intensity.
This confirms that the fence influences the BL profile up to a high altitude, and, at the contrary, the roughness elements are mainly influencing the lowest part of

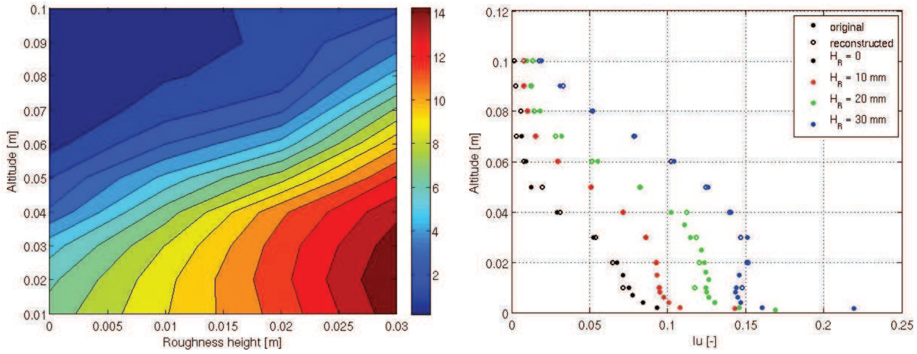

Figure 3.35.: Contour map of the longitudinal turbulence level in function of the altitude and the roughness height [%] (left). Comparison between the original and reconstructed turbulence intensity profiles (right).

the BL but in a stronger way. For instance, at Z = 0.1 m, a 0.03 m fence induces a turbulence level of 5.5 % where, with 0.03 m roughness, the turbulent level is close to 2 %. At the contrary, at Z = 0.04 m the same fence induces 8.2 % of turbulence where the same height roughness element gives 14 %.

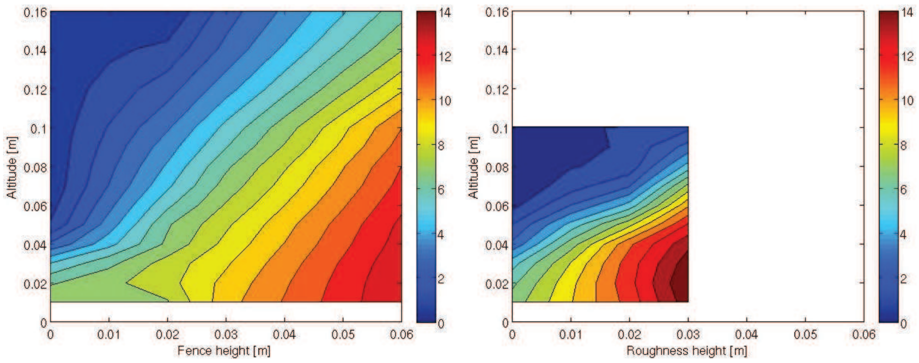

Figure 3.36.: Influence of the fence height (left) and of the roughness element height (right) on the longitudinal turbulence level.

3.6.7. Conclusions

This parametric study performed with two wind tunnels and a numerical simulation quantifies the effect of individual BL generators. The study demonstrates the

very limited effect of increasing the number of fences or changing the roughness elements density (in the range tested).
The section points out that the fence is the main driver of the BL height and the turbulence profile at high altitude whereas the surface roughness elements are driving the lower turbulence profile and the aerodynamic roughness length. The fence and the roughness elements are found to dominate the BL generation strategy. They have to be adjusted to reproduce the desired BL.

This study is defining simple relationships relating the BL generators to the BL characteristics. This work is of great help for quickly finding the right strategy to reproduce a given wind profile. It is performed for the VKI wind tunnels but may be adapted to any wind tunnel. Some of the relationship, like between the aerodynamic roughness length and the roughness element height are universals and the tendencies of others are expected to be the same.

3.7. Summary and conclusions

In this chapter a number of fundamental work is performed to build a strong basis allowing to go further in the physical modelling of atmospheric flows.
After the detailed description of the wind tunnels and the BL generation tools, the validity of performing atmospheric flows studies in the wind tunnel is discussed and verified through a number of verifications: Reynolds number, fully developed state, pressure gradient and homogeneity of the flow. The detailed study quantifies the properties of the fully turbulent boundary layers developed in both test sections.
Then, an extensive comparison with field atmospheric measurements and empirical relationships is carried out. The time average and the fluctuating properties of the ABL simulated in the wind tunnels are checked against field measurements and literature data. This part validates that VKI-L1 and VKI-L2 wind tunnels are suitable for atmospheric flows simulations.
The methodology used for determining the BL characteristics from time-average profile is verified by comparison to literature data.
After those verifications, the reproduction of ABL flows is studied in details by a parametric study quantifying the BL generators influence on the BL properties. It is found that the fence height and the roughness element height are the two major parameters influencing the BL. The fence height drives the BL height and the turbulence level at high altitude and the roughness element height drives the aerodynamic roughness length and the turbulent level closer to the wall. The two have to be combined to reproduce a given inflow condition.
Now that the modelling of atmospheric flows and the reproduction of inflow conditions are mastered in the wind tunnels test sections, terrain complexity can be added with more confidence.

Chapter 4.

Flow over simple geometries

4.1. Introduction

The modelling of the wind over a complex terrain brings a lot of questions to tackle. In the last chapter, the reproduction of the inflow conditions in the wind tunnel was discussed as well as the validity of using wind tunnels for atmospheric flow modelling. Now in front of a site to evaluate, a major question is the choice of the area to model. Especially in the case of a complex site, it can be surrounded by hills, mountains or cliffs. The question can be: what's the size of the area around a site of interest that has to be modelled to properly simulate the flow?
On one side, the area to model in the wind tunnel should be large enough to include the surrounding terrain. This way, the effect of the surrounding relief is modelled. On the other side, the test section has given dimensions that could lead to a very high scaling factor. In this case, a very carefully verification of the validity of the similarity criteria, especially for the Reynolds number is necessary. Additionally, it penalizes the spatial resolution of the measurements.
The final choice of the area to model around a site of interest results from a compromise between the complexity of the site and the feasibility of using a high scaling factor.
Numerical modellers also have this choice to make, their limitation is not the test section dimension but, for example, the available CPU time.

To give some insight, this chapter studies simple geometries and their far wake. The goal is to define and to quantify the extension of the disturbed area after of a single topography to try to estimate its downstream influence. This aims at estimating if an upstream relief affects the site of interest. If not, it can be removed from the simulation, if yes, its effect has to be modelled.
This study is also of interest from a pure wind energy point of view for the determination of the best positioning of a wind turbine near a topography. The quantification of the flow around and after a ridge allows to find the most appropriate location for the turbine near a hill: out of the wake or in the speed-up region of the hill.
Literature and norms are giving estimations of the speed-up on hill tops but not on the wake effect. This section aims at contributing to this knowledge.

After a short theoretical introduction reviewing the literature, this chapter presents a detailed wind tunnel study performed in the near wake of two different hills to explain the difference in the nature of the wake behind hills with and without flow separation. Tests are performed on 2D models of simplified hills and ERCOFTAC data are added to the results to complement the study. The flow properties like the velocity deficit and the turbulence increase are then measured in the far wake to quantify their evolution with distance. Contrary to many available studies, the very far wake, up to 50 times the hill heigh, is investigated to try to include all the downstream perturbations. Thanks to the use of Particle Image Velocimetry (PIV), a good space resolution is possible.

4.2. Flow over two-dimensional hills

The Askervein hill project is maybe the most well known with field test campaign on a hill, number of numerical and experimental studies are comparing their results to the available field data [81, 82].

In the literature, a great quantity of authors investigated the behaviour of flow over hills. Since the 70's, scientists started investigating the effect of ridges or hills in an ABL. There exists numerous field studies, analytical analysis and wind tunnel tests from this time. At that time, the interest was mainly the study of gas dispersion but Meroney [62] already in 1978 was aiming at evaluating the hill speed-up for wind energy applications. The growth of the wind energy sector is one of the driving force for the science to progress since this time.
In 1975, Jackson and Hunt [45], (J-H) proposed a full analytical solution for wind over low hills, many authors since then added modifications and improvement [79, 60, 14, 43, 58, 88], it remains a very strong basis for many studies. From the mid 80's to now, the use of computer models became increasingly popular but, over the years, wind tunnels remain used in numerous applications due to the difficulty to model flow separation and flow recovery by numerical models. Both modelling are now used.

Some characteristics are common to the flow over any isolated hill: it presents an upstream speed-down due to the presence of the hill, a speed-up at the hill top and a speed-down with a wake region in the downstream part. Usually the evolution of the wind speed is described by its ratio of change, the fractional speed-up ratio (FSR):

$$\Delta S = \frac{U(z) - U_0(z)}{U_0(z)} \tag{4.1}$$

with U the wind speed at the height z above local ground and U_0 the upstream speed before the influence of the hill at the same height z.

Hills can be of different shapes: triangles, sinus, Gaussian. They are usually

categorized by their slope. Low slopes can be solved by analytical solutions but for higher slopes, due to flow separation in the downwind side and even sometimes in the upwind side, the flow cannot be solved simply analytically.
The slope of a hill is defined by the ratio

$$s = \frac{H}{2.L_i} \tag{4.2}$$

H is the height of the hill and L_i is the horizontal length from the center of the hill to the length where $z = H/2$ (see figure 4.2).

4.2.1. Gentle slope or Low hills

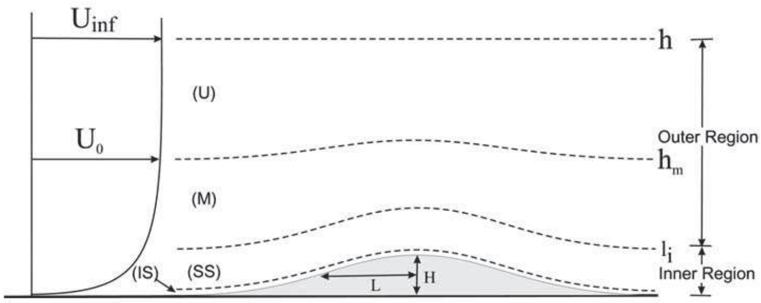

Figure 4.1.: Flow over two-dimensional low hill. Figure from [6]

Finnigan, [38], from a compilation of wind tunnels and field studies determined that separation never occurs before an angle of 15° and always occurs for slopes over 18°. We here define a *low* hill a hill with a gentle slope below 15° in opposition to the *steep* hill that has a slope steeper than 18°.
Upstream a *low* hill, the flow is slowed down by the presence of the hill, at the hill top a speed-up is created together with a turbulence decrease. In the down wind part, for gentle slopes, no flow separation occurs, however, the flow experiences a velocity deficit and a turbulence increase. For *low* hills, analytical models have been developed and improved over the years to estimate the velocity speed-up at the top of a hill.
The J-H model, improved mainly by Britter [14], Mason[60], Hunt [43] and Weng [88] is the most well known. In this analysis, the flow over the hill is divided in two regions, the inner layer and the outer layer (Figure 4.1). The lower part of the inner region is called the viscous layer (also called inner surface layer, IS) where viscosity dominates and where velocity goes to zero in very steep gradients. The shear stress layer (SS) extends from the top of the viscous layer to the top of the inner layer l_i. In this region, the mean flow is affected by the shear stress. Above, the outer region starts, there the flow is considered inviscid. This part is divided

in a middle and an outer region. This division is presented in figure 4.1. The inner region height is defined by:

$$l_i.\ln\left(\frac{l_i}{z_0}\right) = 2.\kappa^2.L_i \tag{4.3}$$

Mason [60] proposed l^* as an alternative approximation of the inner layer depth.

$$l^*.\ln^2\left(\frac{l^*}{z_0}\right) = 2.\kappa^2.L_i \tag{4.4}$$

the middle (M) and the upper region (U) height are defined by:

$$h_m = L_i.\left(\ln\frac{L_i}{z_0}\right)^{-1/2} = 2.\kappa^2.L_i \tag{4.5}$$

The J-H theory is rather complex to apply to any hill, simplifications from Taylor following the same approach with empirical constants give an estimation of the speed-up at the top of the hill:

$$\Delta S = \Delta S_{max}\exp\left(\frac{-A.z}{L_i}\right) \tag{4.6}$$

with

$$\Delta S_{max} = \frac{B.H}{L_i} \tag{4.7}$$

with A, B empirical constant function of the hill shape.
Taylor and Lee [80] also proposed a simple estimation of the maximum speed-up deduced from J-H:

$$\Delta S_{max} \approx 0.8\ H/L_i \qquad \text{for 2-D escarpments} \tag{4.8}$$

$$\Delta S_{max} \approx 2.0\ H/L_i \qquad \text{for 2-D ridges} \tag{4.9}$$

Following [38], this is a good approximation that compares by ± 15% to wind tunnel and field data.

As reminded by Ayotte [5], it is well known that the validity of the linear theory vanishes when considering steeper hills. Indeed, for higher angles, the flow may separate and induce non-linear phenomena that doesn't find simple analytical solution.

4.2.2. Steep slope hills

For topographies with higher slopes (> 18°), analytical solutions are no longer valid, then a numerical or a wind tunnel modelling is necessary to estimate the speed-up and the characteristics of the wake. Many authors studied a broad panel of shapes: triangles, sinusoid, half-sinusoid, Gaussian.

The general behaviour of the flow around a *steep* hill is first an upwind deceleration close to the ground due to the blockage created by the hill, in some cases a recirculation area is present depending on the upstream slope. Then a speed-up zone can be observed around the hill crest and, finally, on the lee side, a wake area with a recirculation region and a recovery zone that can extend very far down-stream. The recirculation region generates very high turbulence, and a strong velocity deficit. The turbulence is convected downstream, diffused in all directions and dissipated with the distance. The flow can take tens of times the height of the hill before recovering its original velocity profile and much more to recover the initial turbulence level.
The size of the recirculation varies with the shape of the hill and the surface roughness. Costa [27] and Pearse [65], by comparing different shapes, found out that a triangle shape induces a much stronger perturbation with a longer recirculation and a wake that extends higher and further. In [18] (sinus shape) the reattachment point is between x/H = 5.4 and 6.5, the larger recirculation area corresponds to the rougher surface. In this paper, the velocity is still not recovered after x/H = 7.5. In [3] (inverse 4^{th} polynomial) , experimenting in a water channel, the reattachment point is at x/H = 4.8 with a smooth surface. The vertical component of the velocity is recovered within less than x/H = 10 and the longitudinal component at around x/H = 15. At the contrary, the velocity fluctuations in both directions are still higher at the last measurement point at about x/H = 15.
In [55], the reattachment point is around x/H = 5.3, the experimental determination of l_i appears to be higher than predicted by the JacksonHunt theory and lower than the alternative l^* proposed by Mason [60]. The reattachment point is function of number of parameters: hill shape, surface roughness... and therefore difficult to predict accurately. A more detailed comparison is performed in section 4.6.3.

Most of the studies mentioned are describing the speed-up at the hill top and studying the near wake. Indeed, the speed-up ratio is very important for determining the best position to install a wind turbine. However, the recovery of the flow after a hill is poorly documented. This is also important to determine the area to model around a point of interest but also to estimate the impact of an upstream topography on the available wind power and the turbulence level.

4.3. Test cases

The investigation of flow over simple 2D shapes is performed using a combination of wind tunnel experiments performed in the VKI-L2 test section and existing experimental data, available in the ERCOFTAC database. The near and far wake are investigated.

4.3.1. The ERCOFTAC case

There are numbers of studies investigating the flow around hills (see section 4.2). Among them, the ERCOFTAC[1] database is chosen for this study because data are easily accessible. ERCOFTAC is a European community gathering academic institutions and industrial partner for sharing experience and improving the state-of-the-art in flow turbulence and combustion. The “case 69” investigating the flow over a 2D hill with different slopes is chosen.
The shape of the hill is given parametrically by:

$$x = \frac{1}{2}\xi\left[1 + \frac{a^2}{\xi^2 + m^2(a^2 - \xi^2)}\right] \tag{4.10}$$

$$z = \frac{1}{2}m\sqrt{a^2 - \xi^2}\left[1 - \frac{a^2}{\xi^2 + m^2(a^2 - \xi^2)}\right] \tag{4.11}$$

$$\text{with } |\xi| \leqslant a \ , \ a = L \ , \ m = n + \sqrt{n^2 + 1} \ , \text{ and } n = \frac{H}{L}$$

With H the hill height and L the half hill length. This parametric shape gives a hill close to a sine function as presented in figure 4.2. The length L_i is, the length at which the hill height is $H/2$.

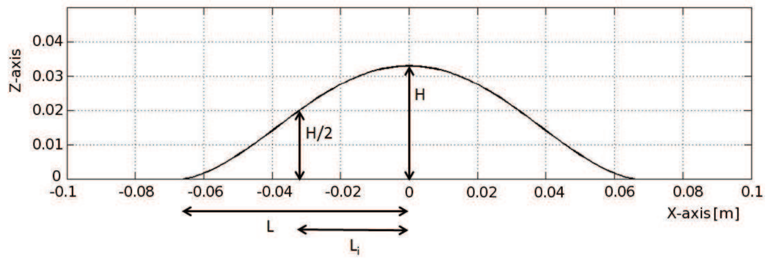

Figure 4.2.: Example of the hill shape obtained from the parametric equations (equation 4.11) with $H = 33$ mm and $L/H = 2$.

A set of three hills is available in the ERCOFTAC database, E-3, E-5 and E-8, they have the same height ($H = 0.107$ m) but the aspect ratio is changing: $L = 3H$, $L = 5H$ and $L = 8H$. The first hill as a mean slope of 23°, then a recirculation is likely to happen. The two others have mean slopes of 12° and 10° so no separation is expected. Table 4.1 summarises the hills tested with the conditions (the Reynolds number is based on the height of the hill).
Data are from experiments performed by Khurshudyan et al [54] with hot wire anemometry at 4 m/s. The longitudinal velocity (U), the flow angle (ϕ), the longitudinal and vertical standard deviation (σ_U and δ_W) and the Reynolds shear

[1]European Research Community On Flow Turbulence And Combustion

stress $-\overline{u'w'}$ are available. Measurements are performed at 16 locations upstream and downstream the hill. An example of the data is plotted in figure 4.3.

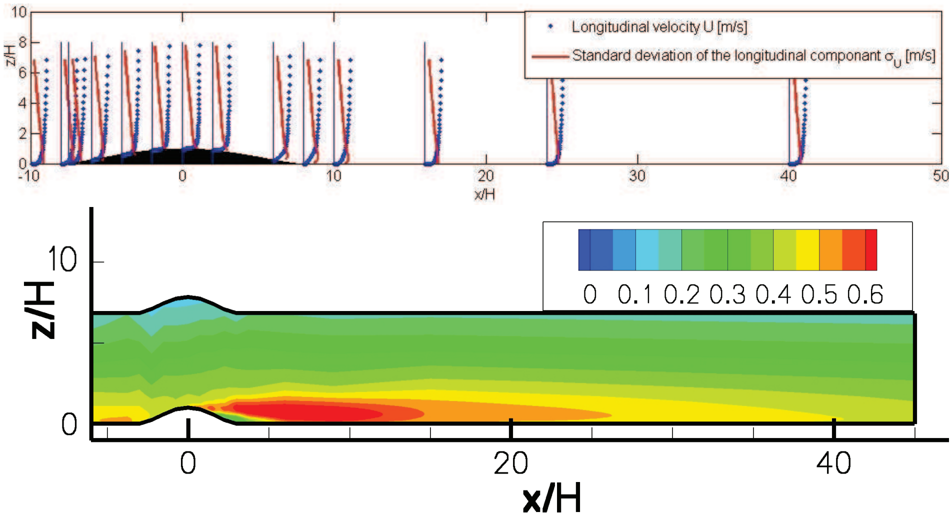

Figure 4.3.: Example of available data from an ERCOFTAC case [54]. Top: longitudinal velocity and longitudinal standard deviation component for a L = 8H hill. Bottom: contour line of the longitudinal standard deviation [m/s] for the L = 3H case obtained by linear interpolation.

4.3.2. Wind tunnel tests

Tests are performed in the VKI-L2 wind tunnel described in section 5.3.3 in the 0.35 x 0.35 x 2 m test section. Three hills with ERCOFTAC shapes are tested with L/H ratio of 2 and 4: V-2, V-2b and V-4. All hills are summarized in table 4.1 and figure 4.5.

Wind tunnel mock-ups are 0.35 m wide extrusions of the shape described. The three models tested are made out of wood and painted black for the PIV measurements. The ratio L/H gives an idea of the steepness of the hill, the higher the ratio, the flatter the hill. In the table 4.1, only the three first cases are expected to induce flow separation (angle above 18°).

The blockage is maximum with the second hill (V-2b) but it stays below 10%. This is the limit of use of this test section.

The hill is positioned at x = 0.5 m from the start of the test section. For this study, no BL generators are placed on the floor, the inlet velocity and turbulent profiles are given in figure 4.4. The BL height is around $\delta = 0.03$m. Both the floor and the model have a surface roughness around 10 μm.

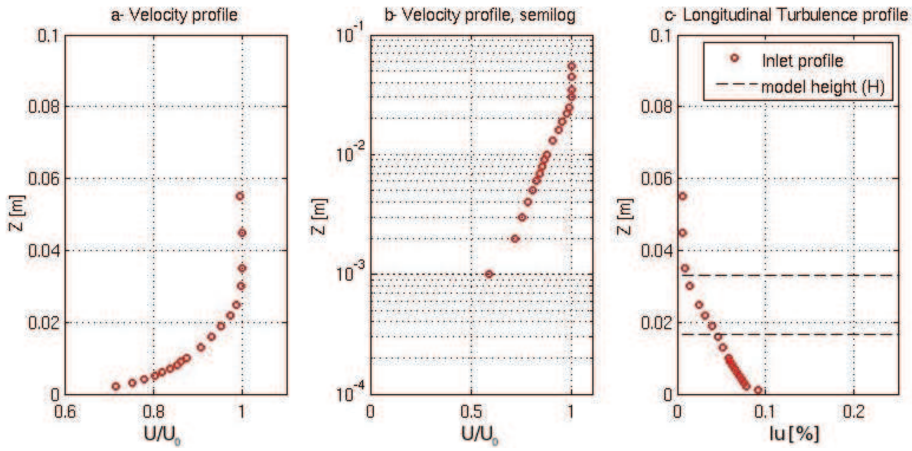

Figure 4.4.: Inlet velocity and longitudinal turbulence profile at the position of the hill. $z_0 = 3.7210^{-6}$ m and $u_* = 1.1$ m/s. U_0 is the speed at the BL height δ.

All tests are performed at 15 m/s, the velocity is measured by a Pitot probe at the entrance of the test section, where it is not affected by the hill. The Reynolds number computed with the height of the hill is Re = 31 500 for the highest hill and Re = 16 250 for the lowest, both Reynolds numbers are above 10 000 that is set as the minimum value in section 2.4.

Particle Image Velocimetry measurements are performed around the hills in vertical planes located in the center line of the test section. One PIV plane is around 150 mm long and about 100 mm height. The juxtaposition of successive overlapping planes and the length of the test section allow to measure up to a distance of $x/H = 50$ for the lowest hills and around $x/H = 25$ for the highest one. All PIV successive planes recorded are joined together after averaging the 1 000 instantaneous images per plane and form a continuous set of information. The velocity in the longitudinal and the vertical direction are recorded, from this, the mean wind speed can be computed but also statistics from the velocity fluctuations: like the turbulence level, the vorticity and the Reynolds shear stress. When comparing to the inlet flow conditions, the velocity deficit and the turbulence increase can be computed.

4.4. The near flow of a low hill

This section, presents results of measurements in the near wake for the hill with a high L/H ratio (V-4).

Hills		L/H	L [m]	H [m]	L_i/H	s (angle)	U [m/s]	Re_H	H/δ
Steep	V-2	2	0.033	0.018	0.877	0.57 (30°)	15	17 200	0.6
	V-2b	2	0.067	0.033	0.97	0.51 (27°)	15	31 500	1.1
	E-3	3	0.351	0.117	1.171	0.42 (23°)	4	29 800	3.9
Low	V-4	4	0.066	0.017	2.35	0.21 (12°)	15	16 200	0.58
	E-5	5	0.585	0.117	2.925	0.17 (12°)	4	29 800	3.9
	E-8	8	0.936	0.117	4.75	0.10 (10°)	4	29 800	3.9

Table 4.1.: Description of the ERCOFTAC cases (E-#) and hills tested in the VKI-L2 test section (V-#). The three first hills are considered as *steep* hills and the three others as *low* hills.

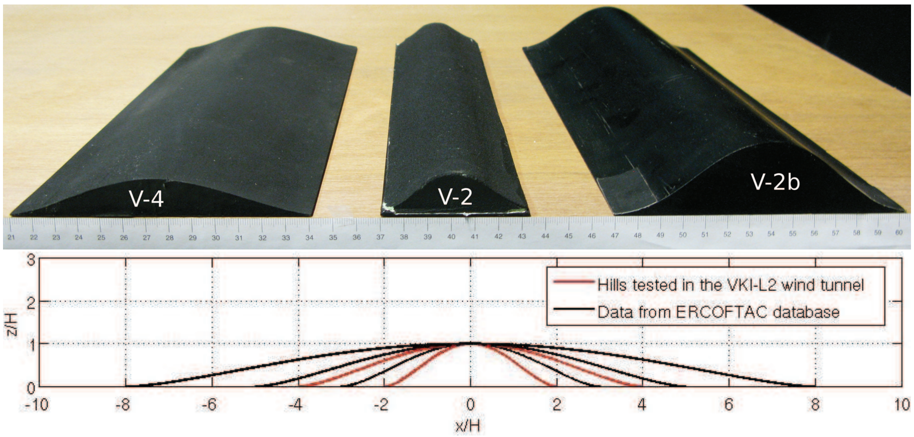

Figure 4.5.: Top: picture of the three hills tested in the VKI-L2 wind tunnel. Bottom: hill shapes investigated in this study, red contours are the hills tested in the wind tunnel, the data of the black contours hills are extracted from the ERCOFTAC database.

Plots are presented with axis normalized by the hill height (H). In the PIV measurements, there is sometimes a blanked part next to the surface, this is due to the laser reflection, no measurements are available in this area.

4.4.1. Instantaneous characteristics

In the instantaneous vector field presented in figure 4.4.1, the non uniformity of the vectors at x/H = -5 is the result of the turbulence in the inlet BL, this is more visible near the ground. Until the middle of the hill, $x/H = 0$, the instantaneous velocity vector field shows a deviation to the top. This deviation is due to the hill and still visible until far from the surface ($z/H > 2.5$). At the hill top, velocity vectors are back horizontal and their amplitude is clearly increased. On the lee

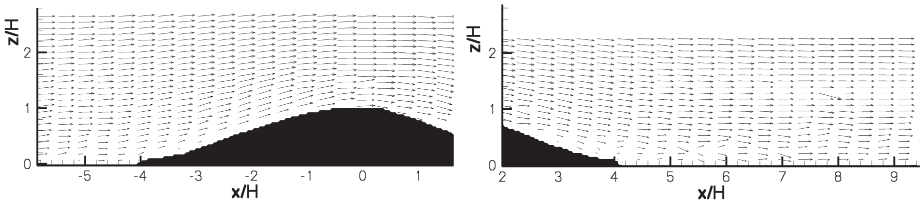

Figure 4.6.: The instantaneous velocity field around a *low* hill (V-4).

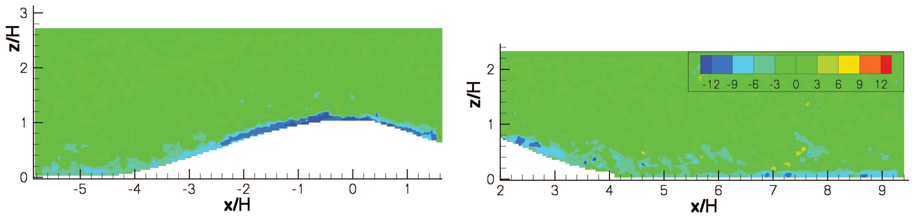

Figure 4.7.: Vorticity field (ω_Y) (flood) in the near wake of a *low* hill (V-4).

side of the hill, velocity vectors are mainly pointing downwards. After the hill, the amplitude of the velocity is lower and fluctuations are more important than at the inlet. Over the hill, velocity vectors are affected by the presence of the hill but remain parallel to each other, no sign of a detachment is visible.
The vorticity field (ω_Y) plotted in figure 4.7 reaches the same conclusion that no separation phenomena occurs on the lee side of the hill. Nevertheless, the vorticity is increased and a wake zone is present after the hill.

4.4.2. Mean flow distribution

The streamlines plotted with the time averaged longitudinal velocity field, figure 4.8, enlighten the fully attached state of the flow around the hill. At the top of the hill, the streamlines are *compressed* creating the speed-up. The flow streamlines in the downstream part of the hill are not affected a lot by its presence. The speed-up zone at the hill top is clearly visible. Figure 4.9, shows the time average velocity vector field, on the downstream part, a velocity speed down is measured but no separation occurs.
In figure 4.10, the vertical velocity is represented. As expected, $W = 0$ at the inlet, $W > 0$ at the wind side of the hill and $W < 0$ on the lee side. The maxima of the vertical component is reached near the surface at around $x/H =$ -1.75 and $x/H =$ 1.75. The distribution of vertical velocity is rather symmetric in amplitude and in geometry on both side of $x/H = 0$. The hill influence on the vertical component is visible above $z/H = 2.5$. In the longitudinal direction, after $x/H \approx 5$, the vertical velocity is back to the inlet conditions.

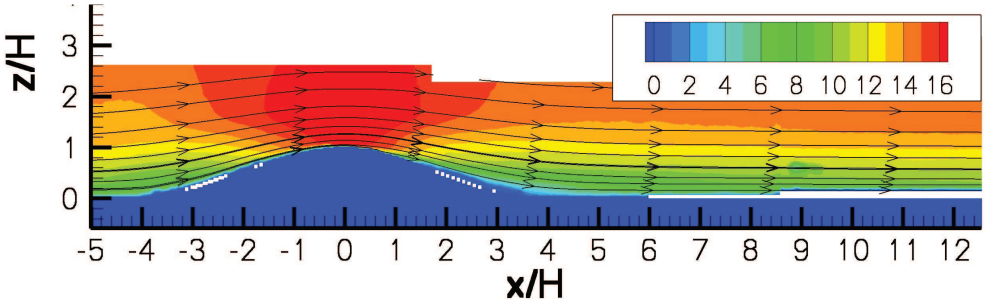

Figure 4.8.: The longitudinal wind velocity component U [m/s] and the streamlines over a *low* hill. $Re \approx 16000$.

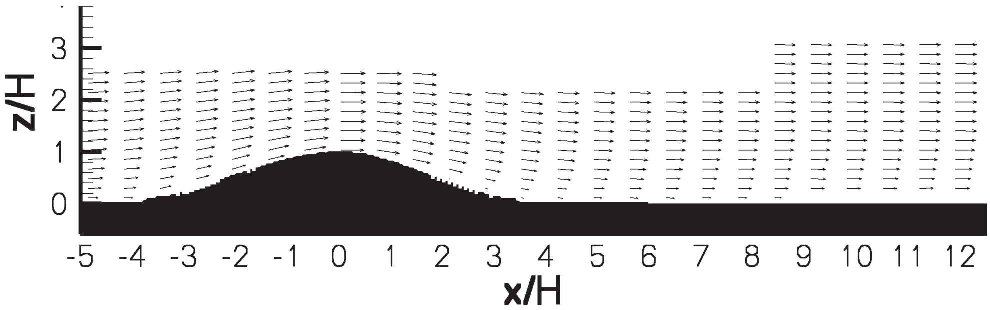

Figure 4.9.: The velocity vector field over a *low* hill.

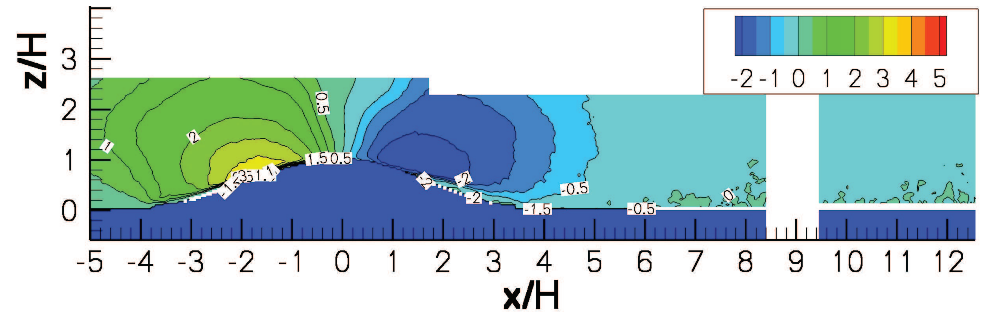

Figure 4.10.: The vertical wind velocity component W [m/s] over a *low* hill.

4.4.3. Turbulence characteristics

Even if there is no separation, the *low* hill has an influence on the turbulence characteristics on the lee side. Figures 4.11 and 4.12 present the standard deviation in the longitudinal and the vertical direction in the close wake of the hill. The maximum fluctuation is located around $z/H= 0.4$. After the hill, around

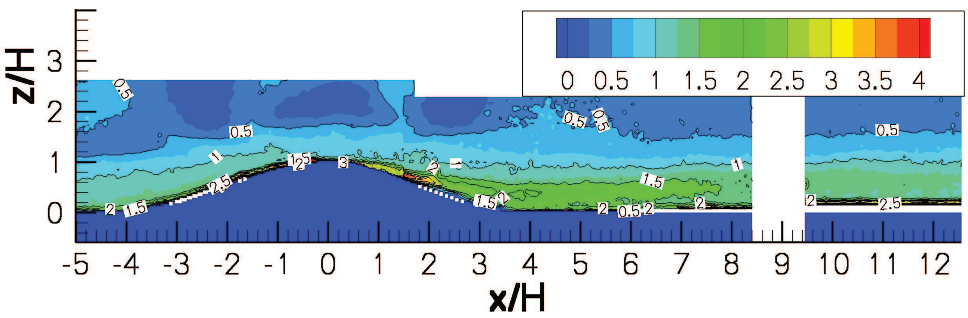

Figure 4.11.: The horizontal standard deviation of the velocity σ_U [m/s] over a *low* hill.

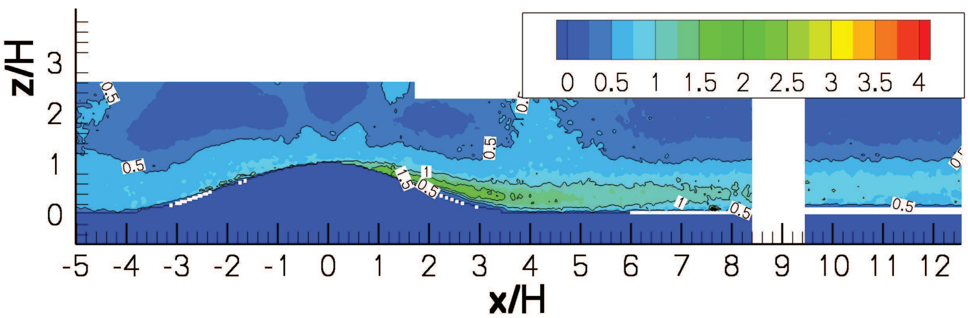

Figure 4.12.: The vertical standard deviation of the velocity σ_W [m/s] over a *low* hill.

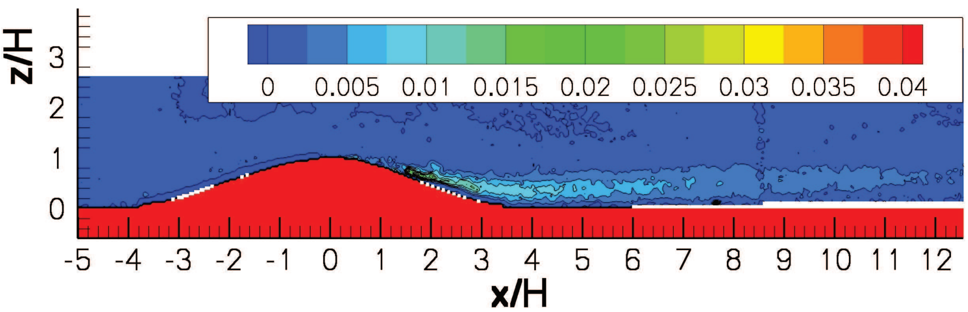

Figure 4.13.: The normalized Reynolds shear stress $-\overline{u'w'}/U_0^2$ [-] over a *low* hill.

x/H = 1.75, the longitudinal component experiences a maximum above σ_U = 3 m/s. Further downstream, due to dissipation and diffusion in the other directions, the maximum fluctuation is lower, around 2 m/s. Going further in the wake, the longitudinal and the vertical fluctuations are getting lower and lower but, at x/H = 12, both are still affected by the presence of the hill. A full study of the wake recovery needs to measure further downstream.

As the longitudinal and vertical velocity fluctuations are affected, the Reynolds stress, $-\overline{u'w'}/U_0^2$, is also increasing (figure 4.13). The Reynolds stress, normalised by the velocity at the height of the hill in the undisturbed flow, has its peak value at around $x/H = 2$ and $z/H = 0.4$. This is the same area as the maximum for σ_U and σ_W. From this point, it is decreasing with the distance. Its effect is still visible at $x/H = 12$.

4.4.4. Summary

Over the *low* slope hill, ($< 12°$) no separation is observed, the streamlines are weakly affected and the vertical velocity distribution is symmetrical over the hill. However, the hill is significantly slowing down the flow on the lee side. The turbulent properties are also modified. After $x/H = 12$ all the components of the velocity fluctuation are still affected.

4.5. The near flow of a steep hill

In the following paragraphs, results are presented for the two hills having the lowest L/H ratio, so the steepest slope (V-2 and V-2b). The instantaneous and time averaged features are presented as well as the turbulence characteristics.
Plots are presented with axis normalized by the hill height (H).

4.5.1. Instantaneous characteristics

The instantaneous velocity field, presented in figure 4.14 is composed by a high velocity region above $z/H = 1$ and a very low velocity region downstream the hill and below $z/H = 1$, the wake of the hill. In between, the velocity shear is very important and the flow experiences very strong velocity gradients. In this region, clockwise vortices can be distinguished from the instantaneous velocity vector field. For more precision, the vorticity ω_Y and the λ_2 criteria [67, 46] are calculated. The vorticity gives the high *curl* (*curl* as the mathematical transformation) locations and the direction of rotation ($\omega_Y > 0$ for counter clockwise rotation and $\omega_Y < 0$ for clockwise rotation). As high shear regions have a high curl, they are also detected. To distinguish between a shear and a vortex, the λ_2 criteria is computed. Figure 4.15 shows the superposition of the vorticity and the vortex detection criteria which utility is demonstrated at the crest of the hill: the shear is very high, but there is no vortex. Around the height of the hill, a series of vortices are detected enlightening a vortex shedding emanating from the hill crest and forming clockwise vortices. Vortices are breaking down with distance but some strong vortices remain at $x/H = 3$. Weaker counter clockwise vortices are present in the wake but they are in minority.

The large coherent span-wise structures described reveal a Kelvin-Helmoltz (K-H) type instability generated at the crest of the hill. This is typical from two dimensional shapes, like the backward facing step [1, 2, 70]. The K-H-like instability detected is one of the instabilities of a detached flow after a 2D shape. Other instabilities are also typical from a detached shear layer, like the low-frequency oscillation of the reattachment zone of the recirculation area, more details can be find in [56, 77].

4.5.2. Mean flow distribution

The mean distribution of the velocity flow is calculated over 1 000 images and shows the time averaged flow evolution over the hill. Figure 4.16 presents the longitudinal velocity component in the near wake with the velocity streamlines. The mean velocity information differs from instantaneous measurements, here the vortices are averaged. The velocity information clearly shows a speed-up at the top of the hill and a wake region with a large recirculation bubble.
With the velocity streamlines, the size of the recirculation can be estimated between $x/H = 3.5$ and $x/H = 4.5$. In figure 4.17,the velocity vector field is presented and a reverse flow area is visible on the lee side of the hill. The figure also shows the high deficit in longitudinal velocity in the wake.
The hill is affecting the vertical velocity (figure 4.18). In the upstream flow $W = 0$. On the wind side, the wind is accelerated upwards by the presence of the hill. The vertical motion starts almost at x/H = -4 and is visible at several hill heights. On the lee side, in average, the downwards motion is weaker than the upwards motion but more extended in the stream-wise direction. It is still visible a few tens of times the hill height downstream. Contrary to the gentle slope, the vertical velocity component is not symmetric.

4.5.3. Turbulence characteristics

The turbulent characteristics of the flow are determined by statistics thanks to the 1 000 images recorded per PIV plane.
In the inlet flow, the turbulence is low. Then, due to the separation occurring at the hill crest, the disturbance induced by the hill is very high. Figures 4.19 and 4.20 are presenting the longitudinal and vertical standard deviations of the velocity components with the same scale as presented in section 4.4. The longitudinal component of the turbulence, is the most affected (maximum value $\sigma_U =$ 4.1 m/s compare to $\sigma_W = 2.75$ m/s), the peak is reached at the top of the hill. At $x/H = 13$, the turbulence is still very high compared to the undisturbed flow. Notice that, contrary to the longitudinal one, the vertical standard deviation has its maximum at around $x/H = 3$ and then decreases.
The Reynolds stress $-\overline{u'w'}/U_0^2$ is computed and normalized by the mean undisturbed incoming flow at the height of the hill in figure 4.21. Similarly to the

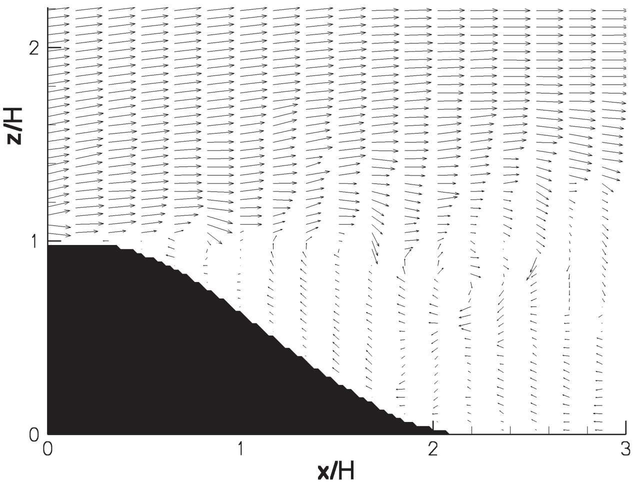

Figure 4.14.: The instantaneous velocity field in the near wake of the *steep* hill. Several vortices can be distinguished.

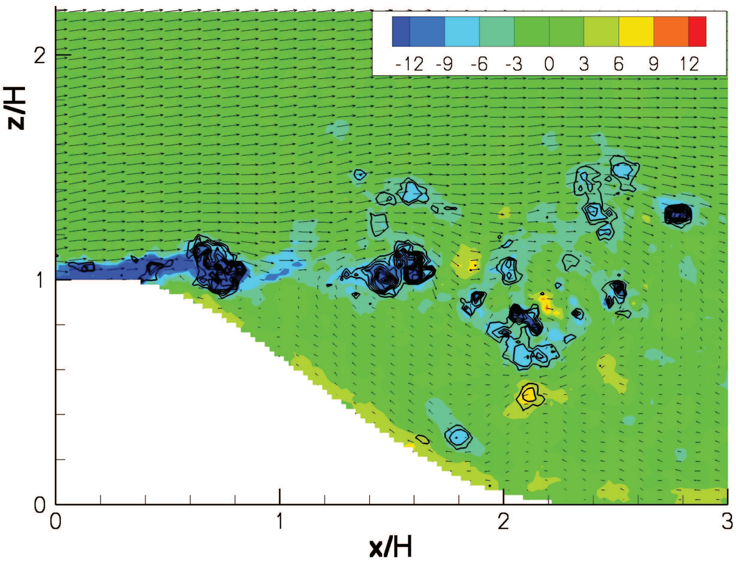

Figure 4.15.: Vortex detection in the near wake of the *steep* hill thanks to the vorticity field (ω_Y) (flood), the λ_2 criteria (lines) and the instantaneous velocity field (vectors).

longitudinal standard deviation, the Reynolds stress has its maximum at the hill top and decreases after $x/H = 4$.

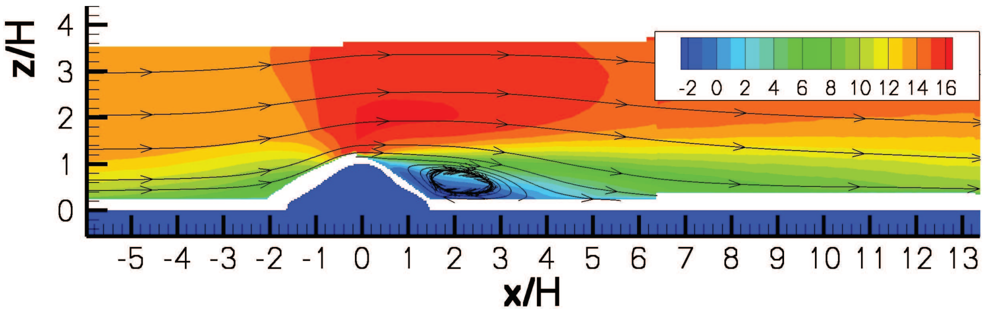

Figure 4.16.: The mean longitudinal velocity U [m/s] and the streamlines over the *steep* hill. $Re \approx 17000$.

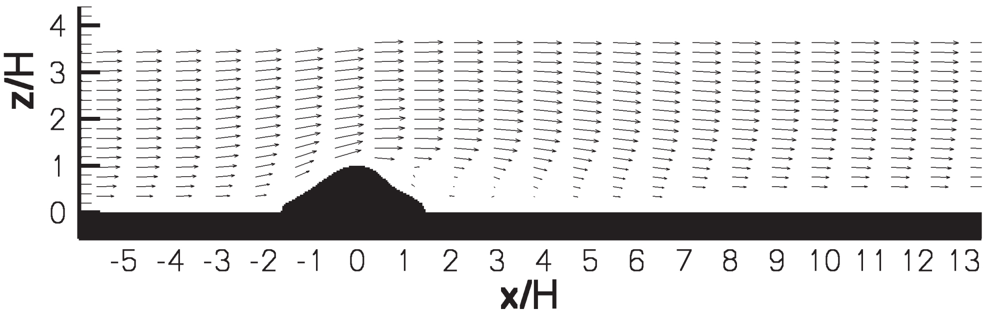

Figure 4.17.: The velocity vector field over the *steep* hill.

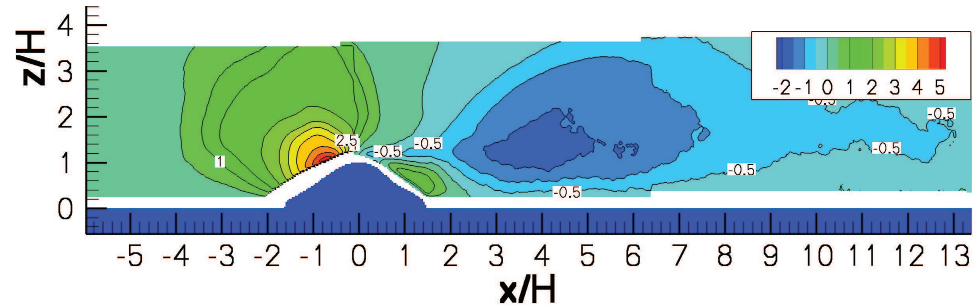

Figure 4.18.: The vertical wind velocity component W [m/s] over the *steep* hill.

4.5.4. Summary

Over the *steep* hill, the time averaged velocity field shows a recirculation bubble. In fact, this is an average feature due to a vortex shedding from the separation area at the hill crest. The two-dimensionality of the model used induces Kelvin-Helmholtz type vortex shedding emanating from the hill crest. This explains the

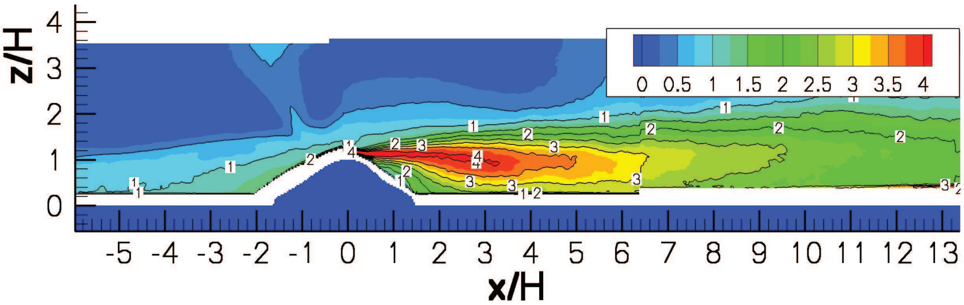

Figure 4.19.: The longitudinal standard deviation of the wind velocity σ_U [m/s] around the *steep* hill.

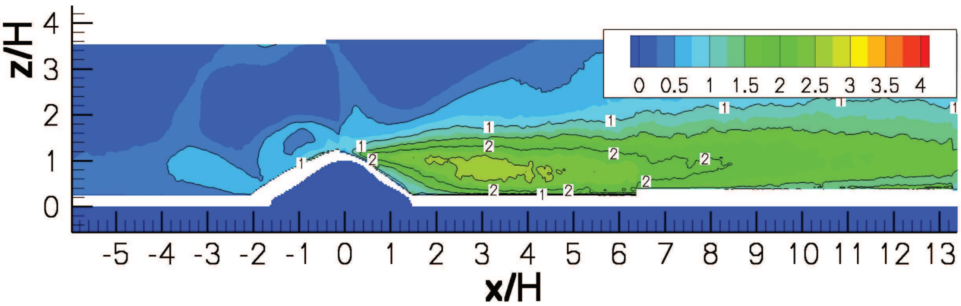

Figure 4.20.: The vertical standard deviation of the wind velocity σ_W [m/s] around the *steep* hill.

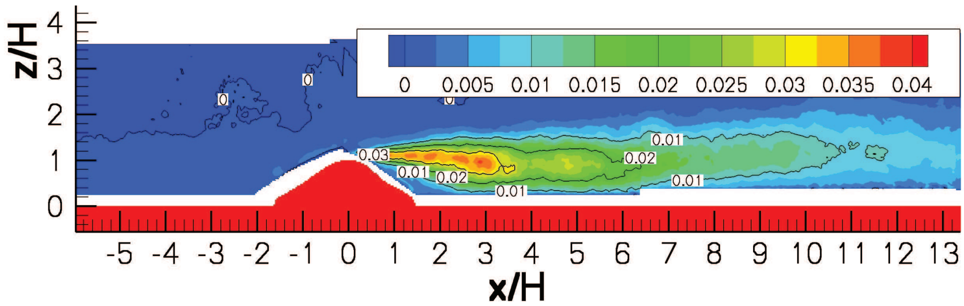

Figure 4.21.: The Reynolds shear stress $-\overline{u'w'}/U_0^2$ [-] around the *steep* hill.

high turbulence level and its anisotropy. The velocity deficit and the increase in turbulence induced by the separation at the crest of the hill persists a long distance downstream.

Contrary to the flow around the *low* hill presented in section 4.4 the flow over a *steep* hill is detached and the nature of the wake is very different close to the hill.

Further investigations are carried out in the far wake in order to determine the downwind effect of a simple hill (see section 4.6.4 and 4.6.5).

4.6. Quantification of the hill effect and comparison with literature

As described in the two precedent sections, on any hill there is a speed-up zone at its top and a disturbed zone in its downstream part. Depending on the slope of the hill, the flow separates or not after the hill top. If a separation occurs, the nature of the near wake is different leading to very a high perturbation.
To go further in the study, some basic features of the near hill are investigated and compared to the literature: the size of the recirculation bubble and the speed-up ratio.
Then, the far downstream effect of the hills is quantified to define a perturbation zone downstream the hill. This study aims at quantifying, for a simplified hill, a speed-up area favourable for a wind turbine siting and a perturbed zone downstream that is not favourable.
This study also aims at helping a physical modeller in estimating whether or not an upstream topography influences the site of interest and if it has to be included or not in the modelling.

4.6.1. Variables describing the flow

The Fractional Speed-up Ratio ΔS (equation 4.1) is a very broadly used variable. It describes the percentage of change of the velocity profile at one position compared to the inlet profile. A positive value gives a speed-up and a negative value a speed-down. It enlightens the positive or negative evolution of the flow velocity. In the wake of the hill the velocity deficit, U_w, can be defined as:

$$U_w(z) = U(z) - U_0(z) \tag{4.12}$$

This is also the numerator of the FSR. From this, an interesting thing to quantify is the wake depth, $h_w(x)$. It can be defined as the height for which the velocity deficit reaches 5% of the inlet velocity: $U_w(h_w) = -0.05 * U_0(h_w)$ or also $U(h_w) = 0.95 * U_0(h_w)$. In other words, $h_w(x)$ is the contour where $\Delta S = -0.05$. Similarly, the longitudinal extension of the wake can be defined by $l_w(x)$, the maximum stream-wise distance for which $\Delta S = -0.05$.

For steep slope hills with separation, the size of the recirculation area is estimated with the line defined by $U(x, z) = 0$. This line reaches zero at the reattachment point.
On the turbulence side, the turbulence increase due to the hill can be defined by the residual turbulence intensity computed as the local increase of turbulence

intensity:

$$Iu_w(z) = \frac{\sigma_U(z) - \sigma_{U_0}(z)}{U(z)} = I_U(z) - I_{U_0}(z) \tag{4.13}$$

Additionally, the maximum standard deviation, or Reynolds stress can be extracted for every x/H position, this is a good indicator of the extension and the persistence of the downstream wake.

Figure 4.22 presents an example of the wake depth h_w, the reverse flow area and the height of the maximum Reynolds stress over the *steep* hill measured in the wind tunnel.

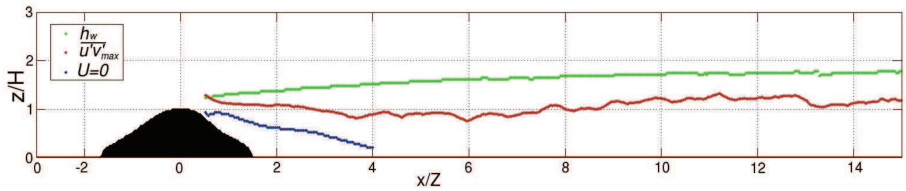

Figure 4.22.: Measurement of the recirculation area (blue), the wake height (green) and the height of the maximum Reynolds stress (red) after a *steep* hill in function of the distance.

4.6.2. Speed-up area

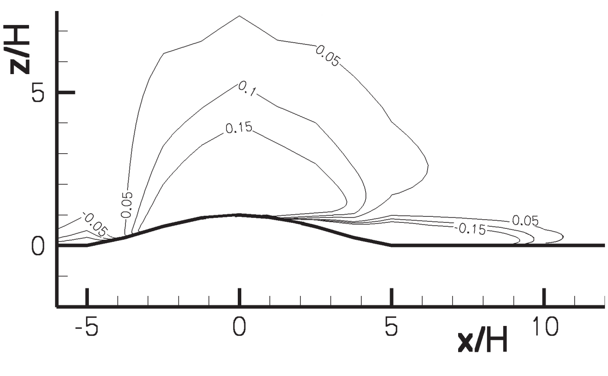

Figure 4.23.: Example of the velocity speed-up (ΔS) on the top of the L=5H hill.

This paragraph focuses on the speed-up region at the top of the hill.
Following [55], the maximum of the speed-up is situated close to the surface, at the

height of the inner layer l_i. From this altitude going up, the speed-up is decreasing in intensity (figure 4.23). The speed-up gradient is in opposite direction than the ABL velocity gradient. As a result, the velocity profile at the top of the hill tends to be more uniform. A wind turbine situated in this area, in addition of having a higher speed at the hub height, will experience smaller vertical velocity gradient along the rotor diameter.
The theoretical values of ΔS, l_i and the modification l^* proposed by [60] are computed with equations 4.5 to 4.9.
The maximum speed-up value and the inner layer height are determined from the experimental results and from the ERCOFTAC data.
Results are summarised in table 4.2 and in figure 4.24. Like for [55], the measured l_i is most of the time falling in between the two proposed approximations, however, it is much closer to l_i, from the theory proposed by J-H. An average difference is around 15% from Jackson-Hunt theory.

	Observations		Theory from J-H		
Hills	ΔS_{max}	l_i [m]	ΔS_{max}	l_i [m]	l^* [m]
V-4	1.05	1.8 e^{-3}	0.85	2.03 e^{-3}	0.52 e^{-3}
E-5	0.74	10.1 e^{-3}	0.68	13.7 e^{-3}	2.6 e^{-3}
E-8	0.33	23 e^{-3}	0.42	20.9 e^{-3}	3.7 e^{-3}

Table 4.2.: Comparison between the maximum speed-up and its position predicted by the J-H linear theory and the results obtained by the measurement data and the ERCOFTAC cases.

For the maximum speed-up, its evolution with the hill ratio follows the trend proposed by the simplified linearised theory but the experiments are +/- 20% around the predicted value. Finnigan [38] found +/- 15 % agreement. Even if the order of magnitude is conserved, differences are quite large, results are crossing the simplified theoretical curve (figure 4.24).

4.6.3. Recirculation area - reattachment length

After the top of the hill, for high slopes, the flow detaches and forms a recirculation area on the lee side. The separation phenomenon is already described in details in section 4.5: a vortex shedding emanating from the hill crest is creating a time-averaged recirculation area. This happens here for $L = 2H$ and $L = 3H$. Experiments are conducted on two hills of $L = 2H$ for $H = 17$ mm (hill V-2) and $H = 33$ mm (hill V-2b), the configuration $L = 3H$ comes from ERCOFTAC database.
The position of the reattachment point X_r is computed by following the line $U = 0$ when it reaches the ground. A double checked is performed by plotting the veloc-

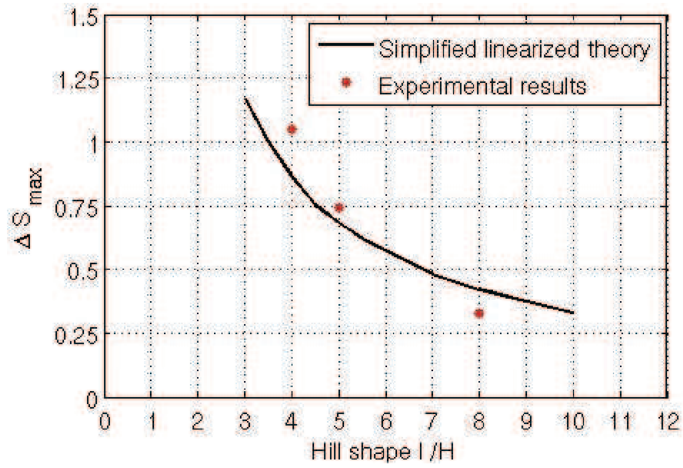

Figure 4.24.: Comparison between the maximum FSR (ΔS) of the hills studied with the linearised theory from J-H, equation 4.7. Values are reported in table 4.2.

ity streamlines and looking at the position where they diverge near the surface. Reattachment lengths are reported in table 4.3.

For the experiments, for the same shape, at a given speed, the reattachment

Configuration	L	H [m]	s ($H/(2L_i)$)	U [m/s]	Re$_H$	X_r/H
E-3	3H	0.117	0.29	4	31 200	7.5
V-2	2H	0.018	0.52	15	17 200	4.5
V-2b	2H	0.033	0.57	15	31 200	5.8
Kim et al. "S5H4"	2H	0.04	0.5	7	18 000	5.85
Kim et al. "S5H7"	2H	0.07	0.5	7	31 200	4.30
Arya et al.	3H	0.110	0.29	4	28 000	5.5

Table 4.3.: Details of the comparison between the measurement of the reattachment point for the three experimental cases with the literature from [55] and [4].

point varies from $x/H = 4.5$ to $x/H = 5.8$ if the height is doubled (cases V2 and V2-b). Kim [55] reports a decrease of the distance X_r with increasing height but indicates that this may be due to a limitation of the set-up. From the article of Jovic [50] that gathers experiments on a Backward-Facing-Step, two cases with the same velocity but different heights give an increase of the reattachment point for a higher step. From the available data, the parameters H, L and U are not enough to parametrize the reattachment point. In Bradshaw [13] study, many geometries are tested, (cube, BFS, plate, fence) and it is reminded that the reattachment

zone is also linked to the ratio between the height of the BL and the height of the obstacle. Other authors like [18] enlighten that the wake also depends on the roughness height.
From the literature, the geometry of the hill “V-2b” tested is very close to the “S5H4” case from Kim [55] and Arya [4] (table 4.3) and the position of the reattachment point is very similar, within around 5% of difference.

4.6.4. Wake - Velocity deficit

This section describes the wake formed on the lee side of the hill. The wake is different in nature if a flow separation occurs or not but, there exists a velocity deficit and a turbulence level increase on the lee side of any hill. The goal is to try to evaluate the horizontal and vertical extension of the wake.

The wake is here defined by a velocity deficit lower than 5 % of the reference speed at the same height ($-U_w < 0.05.U_0$). Figure 4.25 presents the horizontal and vertical extension of the wake, for different criteria: $\Delta S = -0.05$, $\Delta S = -0.10$ and $\Delta S = -0.15$. For the two cases with flow separation (two upper figures), the wake region extends very far downstream the hill top. For $L/H = 2$, the length of the wake is found to be even longer than 50 H. For $L/H = 3$, the wake is shorter and extends up to around 17 H. For hills with separation, the wake is found to be shorter with lower slope (higher L/H).
For the cases without recirculation, the wake is generally smaller but, contrary to the recirculation cases, its longitudinal extension is increasing with a lower slope (higher L/H).
Figure 4.26 summarises the evolution of the length and the depth of the wake for the different hills. It can be observed a significant difference from the case with separation ($L/H < 3.5$) and the case without separation ($L/H > 3.5$). For the non-separation cases, the wake length l_w/H seems to increase linearly with the ratio L/H. This means that the wake region depends directly on the half length of the hill (L), we have: $l_w/H = f(L/H)$.

For *low* hills, a simple conservative formulation would be that the velocity is recovered at 95% after a distance $l_w = 2L$.
For *steep* hills, the relation is not so clear. From the same figure 4.26 (top), the contours $\Delta S = -0.15$, $\Delta S = -0.10$ and $\Delta S = -0.05$ seems to be proportional to each other. The results show approximately that $l_w/H(\Delta S = -0.15) = 0.92 \times l_w/H(\Delta S = -0.10) = 0.92 \times 0.90 \times l_w/H(\Delta S = -0.05)$.

The depth of the wake varies much less with the hill ratio. The maximum height observed is $h_w \approx 1.65$ for $L/H = 8$. Like for the wake length, there is a discontinuity of behaviour between the *low* and *steep* hills.

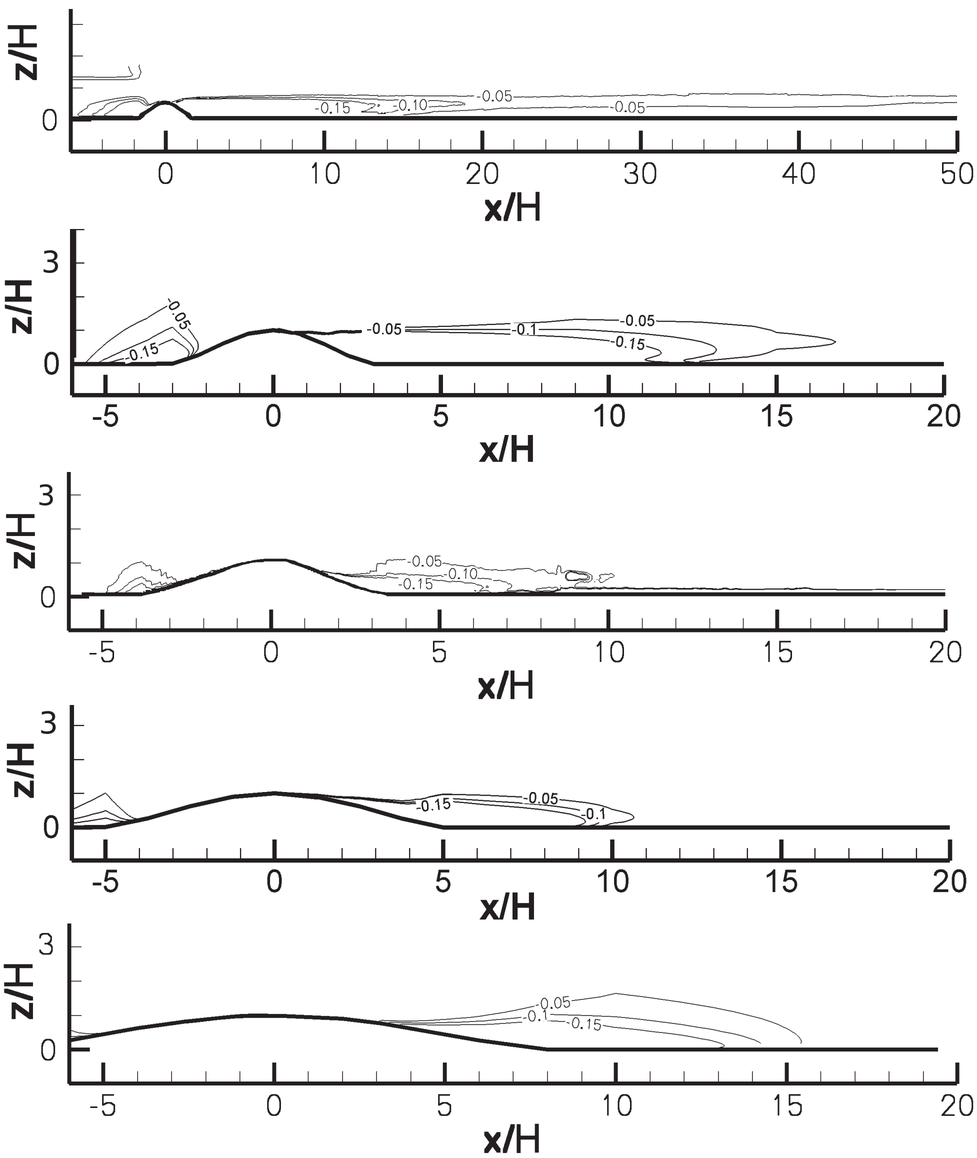

Figure 4.25.: Contours of the wake calculated from the FSR (ΔS) with the criteria: $\Delta S = -0.15$, $\Delta S = -0.10$ and $\Delta S = -0.05$ for the five hills (from top to bottom): $L = 2H$, $L = 3H$, $L = 4H$, $L = 5H$ and $L = 8H$.

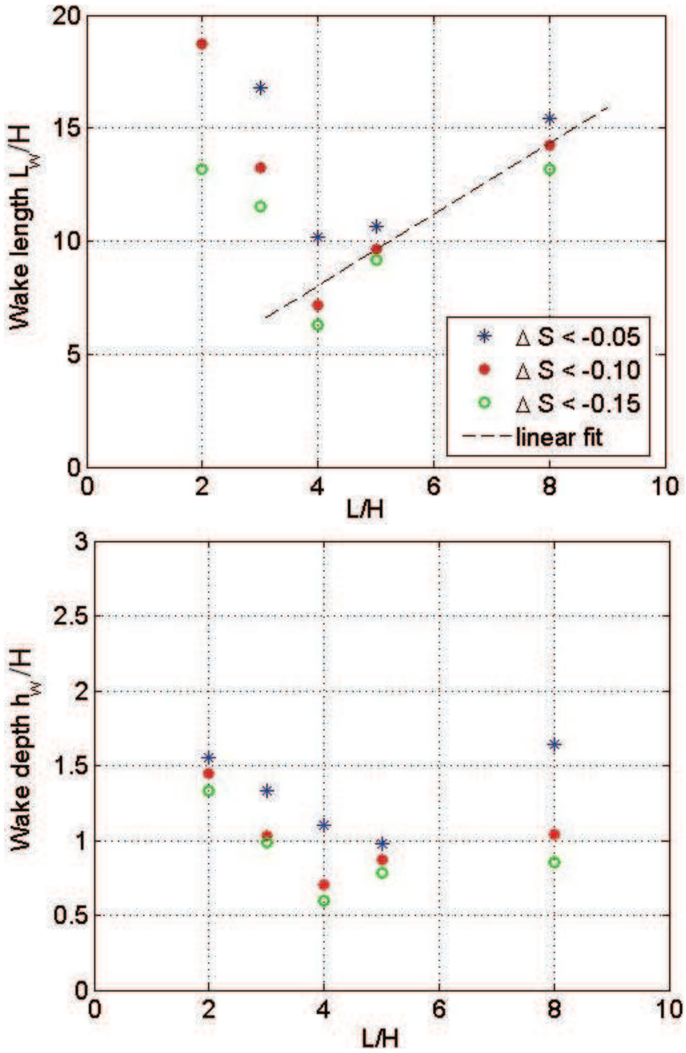

Figure 4.26.: The wake size is approximated by the distance where $\Delta S = -0.15$, $\Delta S = -0.10$ or $\Delta S = -0.05$. Top: wake longitudinal extension (l_w) in function of the hill aspect ratio (L/H). Bottom wake depth (h_w) in function of the hill aspect ratio (L/H).

4.6.5. Wake - Turbulence increase

The wake of a hill, whether there is a recirculation or not, is also associated to a turbulence increase. Similarly to the velocity deficit, the turbulence increase can

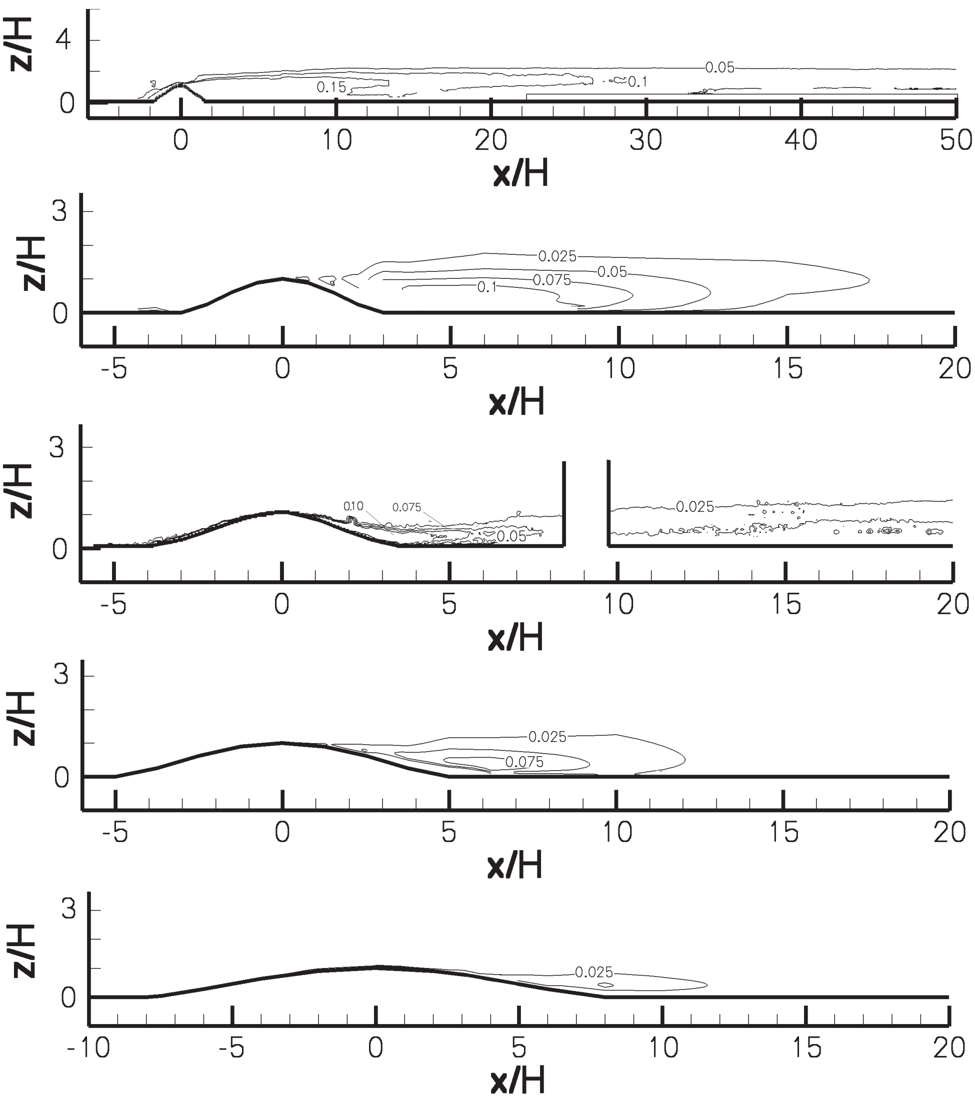

Figure 4.27.: Contours of the residual turbulence intensity Iu_w from equation 4.13. $Iu_w = 0.05$ means that the local turbulence is increased like $Iu(z) = Iu_0(z) + 0.05$. Results are shown for five hills (from top to bottom): $L = 2H$, $L = 3H$, $L = 4H$, $L = 5H$ and $L = 8H$.

be visible far after the hill, often further than the velocity perturbation. This sec-

tion aims at quantifying the perturbed zone downstream a hill and at modelling the turbulence decrease in the wake.
To define the extension of the disturbed area, a simple variable is calculated, here called "remaining turbulence intensity" Iu_w, defined in equation 4.13.
It is difficult to set a clear limit to define the wake area with the turbulent information. A criteria of $Iu_w = 2.5$ % is chosen as the limit for the definition of the wake.
Figure 4.27 presents, for the five cases studied, the longitudinal and vertical extension of the wake. Several contours are plotted from $Iu_w = 0.15$ down to $Iu_w = 0.025$. For the first case, $L = 2H$, a great separation occurs and, even after 50 H, the turbulence is greatly increased, + 0.05 compare to the inlet turbulence level. The low turbulence of the inlet and the steepness of the hill explain such a situation for which the wake extends extremely far from the hill top. For $L = 3H$, a separation occurs as well and the wake extends more than 17 times the hill height. For the hill $L = 4H$, even if no separation occurs, Iu_w is still over 2.5% at 20 times the hill height, however, the $Iu_w = 0.05$ contour is closer to the hill than for the $L = 3H$ case. The far extension of the wake in this case may be due to a convergence problem in the statistical data coming from the PIV experiments. For the two last cases ($L = 5H$ and $L = 8H$), the longitudinal extension of the wake is getting weaker and weaker.
All results are plotted in figure 4.28. A general tendency is difficult to extract, but the wake longitudinal extension l_w computed from the turbulence level is generally of the same order than the wake computed from the velocity information. l_w seems to be constant after $L/H = 5$.

The velocity fluctuation is maximum after a hill with separation. Then it decreases with the distance. If a turbulence level at an iso-height is considered, the lower the altitude, the stronger the perturbation. Going upwards, the effect of the hill is weaker and weaker. At any height, after experimenting a peak, the turbulence is decreasing by dissipation and diffusion and tends to come back to the inlet turbulence level, before the perturbation. This effect is presented in figure 4.29. For the FSR at iso-height $z = 0.7H$, (figure 4.29, top), the turbulence level is abruptly reaching 300% at $x/H \approx 2$. This extreme value is reached in the recirculation area that combines high velocity fluctuations and low speed. Going downstream, the turbulence level drops and then, tends in an asymptotic manner to the inlet turbulence level. For $z = 1.5H$, (lower plot in figure 4.29) the turbulence level is slowly increasing starting at $x/H \approx 2$ and until $x/H \approx 8$ to reach $Iu \approx 20\%$. The turbulence level is then decreasing to the inlet value.
In Arya [4] some flow features are compared to the 1/x function, this approach is tested for the turbulence intensity at iso-height. For this, several iso-height profiles of the turbulence level Iu are extracted, like shown in figure 4.29, and plotted like:

$$Iu = C_1.(x/H)^{-1} + C_2 \tag{4.14}$$

with C_1 and C_2 constant to be determined.

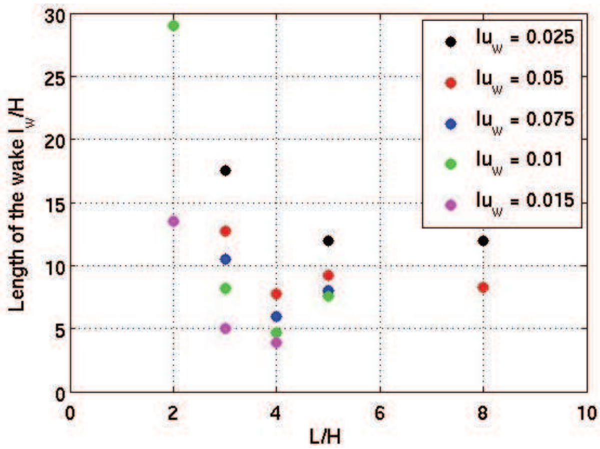

Figure 4.28.: The wake longitudinal extension (l_w/H) in function of the hill aspect ratio (L/H). The wake size is approximated by the distance where the turbulence increase compare to the inlet turbulence, Iu_w is 2.5%, 5%, 7.5%, 10% and 15%.

In figure 4.30, the plot on the left shows that the 1/x decrease of the turbulence level Iu is valid for all the heights starting around $x/H = 7$. The evolution of constants C_1 and C_2 is reported on the right side of figure 4.30. It is clear that the slope C_1 of the fitting depends directly on the altitude (z/H) above the local height. A linear evolution can be fitted. We have $C_1 = -1.6(z/H) + 3.3$.
The constant C_2 shows very weak evolution with altitude.

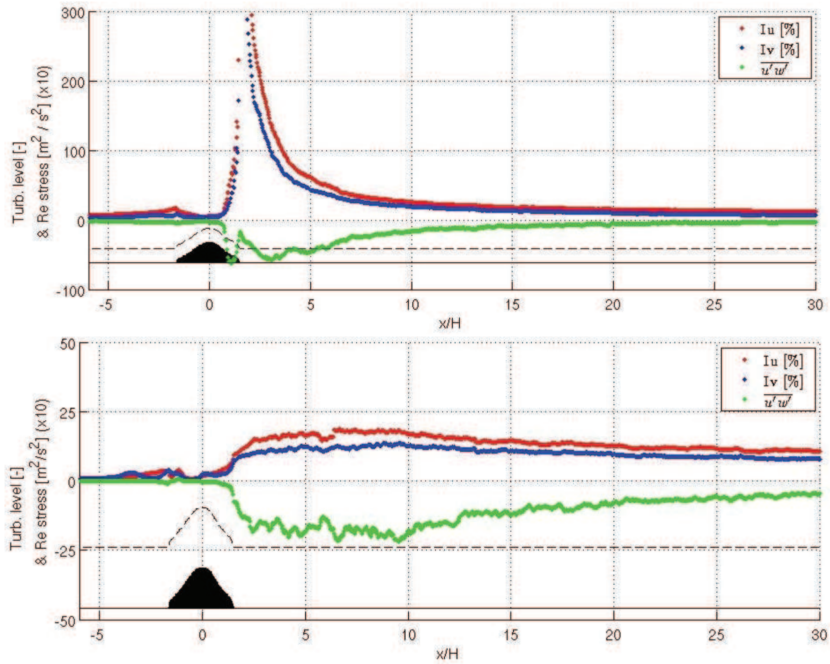

Figure 4.29.: Flow behaviour at $z/H = 0.7$ iso-height above the ground (top). The mean and fluctuating quantities near the surface are very much influenced by the presence of the hill (case V-2) in the near and far wake. Flow behaviour at $z/H = 1.5$ iso-height above the ground (bottom). At a higher altitude, the flow is weakly influenced by the presence of the hill.

4.7. Summary and conclusion

This chapter has two main goals. The first is about wind tunnel modelling of a complex terrain, to help the experimentalist in evaluating the influence of the area surrounding a site of interest. Thanks to the determination of the effect of an upwind topography, the experimentalist can decide which surrounding relief to include in the simulation. The second goal is related to the determination of favourable and unfavourable zones for wind turbine siting near a hill.
To complete both objectives, the quantification of the near and far wake of simplified hills is performed. Experiments are carried out in the VKI-L2 wind tunnel and completed with the ERCOFTAC database. In total five hills with different length to height ratios (L/H) are investigated including cases with and without flow separation at the hill top. The presence of a separation changes the nature of the near wake and its intensity.

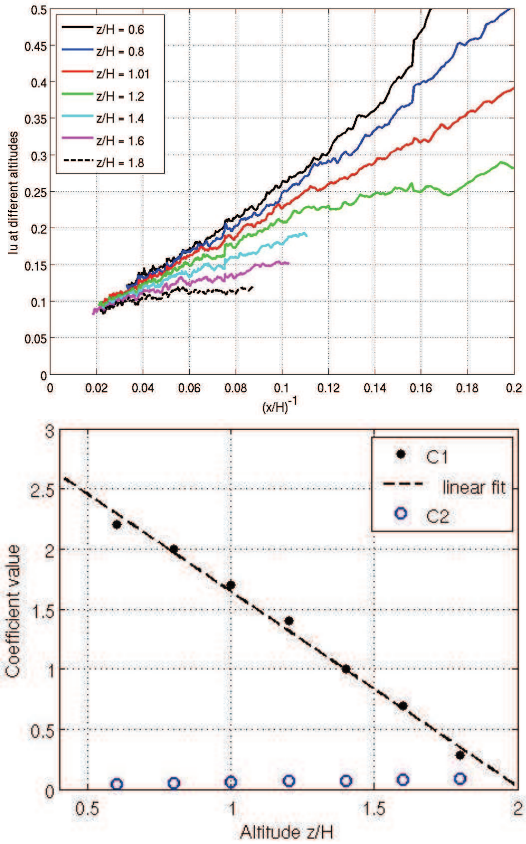

Figure 4.30.: Top: the turbulence level Iu evolution with the inverse of the distance for different height (hill "V-2"). Bottom: the evolution of the coefficients of the 1/x fitting with altitude.

For gentle slopes, the length of the wake generated by the hill (l_w) depends on the length of the hill L and can be roughly estimated by $l_w = 2.L$. The results over gentle slopes generally follows the linearised theory described by J-H.
For steep slopes, a vortex shedding is emanating from the hill top and forms a time-averaged recirculation area creating very high turbulence level and velocity deficit. Contrary to the gentle slope, l_w is increasing for lower L/H.
The turbulence created in the wake of a hill is vanishing by diffusion and dissipation with distance. The decay law of the turbulence is following the 1/x function with a multiplying function linearly decreasing with altitude.
All this study quantifies the vertical h_w and horizontal l_w extension of the wake of a single hill. This is of interest for a wise choice of the location of a wind turbine:

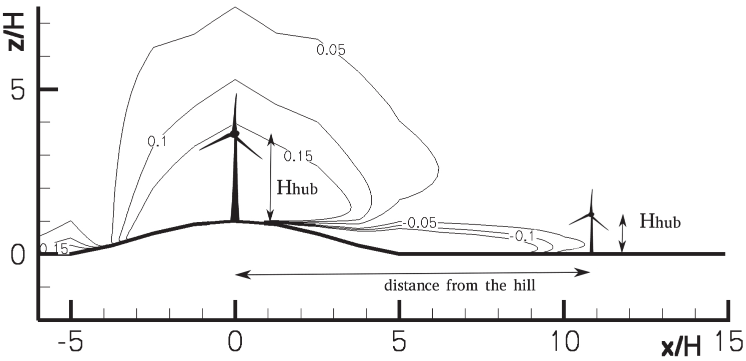

Figure 4.31.: Summary of a typical FSR (ΔS) over a hill and the positioning of wind turbines.

the hub height H_{hub} and the distance from the hill top to the wind turbine have to be compared to the wake size h_w and l_w (Figure 4.31). For instance, for *low* hills, the minimum distance between the hill top and the position of the turbine to have less than 5% velocity deficit is $D = 2L$.

Another important aspect of this work is linked to wind tunnel modelling. The knowledge of the downstream influence of a relief is of utmost importance to decide the area to model around a given site. For gentle slopes, the $l_w = 2L$ rule can be applied but, for steeper slopes with separation, the downstream wake can extend to more than $x/H = 50$ with still 5% velocity deficit and 5% additional turbulence. This is not negligible for wind resources assessment. Then a case to case study is necessary to decide the inclusion or not in the model of the hill is encouraged. It has to be mentioned that a lot of parameters influence the wake after a hill like the BL height and the upstream turbulence intensity. The results presented may be a conservative approach for sinus shaped-hills.

Chapter 5.

Wind tunnel study of two complex terrain test cases

5.1. Introduction

To benefit from stronger winds, wind turbines tend to be more and more placed in sloppy terrain, cliffs or mountainous terrains. One of the counterpart is that a complex topography can induce very complex flow fields like flow separation and reverse flows. Even without flow separation, the wind can experience high velocity deficit and turbulence (see chapter 4). One of the challenges of placing wind turbines in a complex terrain is the wind resource assessment.
After studying simplified hills, this chapter confronts wind tunnel modelling to two real cases. The first test case is the Bolund island, a relatively small rock (12 m height) in a Danish fjord with well defined boundary conditions and numbers of measurement masts. The second test case is the Alaiz mountain in Spain, a very big and complex topography (620 m height). Both sites are equipped with field measurements to compare to the wind tunnel results.
In addition to the comparison with field data, several parametric studies are performed in order to quantify the impact of modelling parameters such as the reproduction of inflow conditions, the choice of the area to model, the Reynolds number or the wind direction.
The goal of this chapter is to assess the validity of wind tunnel testing in complex terrain and to assess the influence of modelling parameters on a real geometry.

5.2. Wind tunnel modelling in complex terrain

The wind over complex topography has been investigated since the early 80's for pollution dispersion studies but also for wind turbine siting. A complex topography often means a large terrain to model and then a very small scale, below 1/1 000. Wind tunnel investigations are still now taking a subsequent part of the studies. Indeed, if properly performed, a wind tunnel study is versatile and can be cheaper than a numerical simulation that also need a reference for validation.
In 1980, Meroney [62], studied the wind over hills and complex terrain for wind power application in the Southern Alps in New-Zealand using a mock-up at 1/5000 scale. Comparisons with field measurements at 10 m gave, in average, a correlation

coefficient of around 0.8. In 1981, Neal [64], also in New-Zealand, investigated the wind over a 1/4 000 terraced model of a peninsula. In both cases, the comparison is limited to low altitudes (10m). In 1984, Cermak [21], in a review, made the statement that, for high scaling factors, the front fetch should be long enough to have fully developed flow, the reproduction of the real terrain is important and that wind tunnel modelling can be used at scaling factors up to 1/ 10 000.
In 1987, Teunissen [82] presents the famous Askervein hill tested at three scales in two different wind tunnels: 1/800, 1/1 200,and 1/2 500. The conclusions are that the wind tunnel is giving satisfactory results compared to field data for the speed-up (around 20%) but the turbulence is nevertheless giving more scatter (50%). The scatter observed is higher in the wake and weaker at the maximum speed-up. The comparison between the different wind tunnels gives a good reproducibility. It has to be noticed that the Askervein hill has rather gentle slopes and is only 116 m high.
In 2003, Bowen [11], recommended to keep a scaling ratio above 1/6 000 in order to properly simulate the turbulence. Some experiments have been carried out since then with very variable scaling factors: Chock [22], over Hawaii: 1/6 000, Veiga-Rodrigues [86] over Askervein hill in UK: 1/7 000, Derickson [32] over Lantau Island in USA and with an interesting coupling with meso-scale simulations to define the inflow profile: 1/4 000, Siddiqui [75] over Honk-Kong area: 1/3 000, Shiau [74] over Keelung harbour in Taiwan: 1/2 000, or Mac Auliffe [61] over a part of Gaspésie in Canada, 1/1 500.
Most of the modellings are compared with field data at low altitude. Many of them, because of the high scaling factor, use terraced model, in order to generate enough turbulence at the surface. With this technique, the near flow may be not simulated correctly but for wind resource assessment, only the flow above 30 to 50 m is of interest.

In this chapter, high scaling factors are also used to simulate the wind in very complex terrains and results are compared to well instrumented hills with high masts (up to 150m). To gain experience on the modelling, parametric studies are also carried out to try to asses the importance of the some modelling parameters.

5.3. The Bolund hill (Dk)

This section presents the wind tunnel test in the VKI-L2 wind tunnel of a model of the Bolund hill, results are compared to field and other wind tunnel measurements. With numerous field, CFD and wind tunnel data, well defined inlet condition and a small size, the Bolund hill is a good first validation test case. Additionally, its reduced size allows to perform experiments in a small wind tunnel that makes parametric studies easier. To quantify the importance of modelling parameters onto the experimental results, a parametric study is performed with parameters like the inflow angle, the Reynolds number, and the inflow conditions. The effect of the reference height for the calculation is also quantified.

5.3.1. Topography and instrumentation

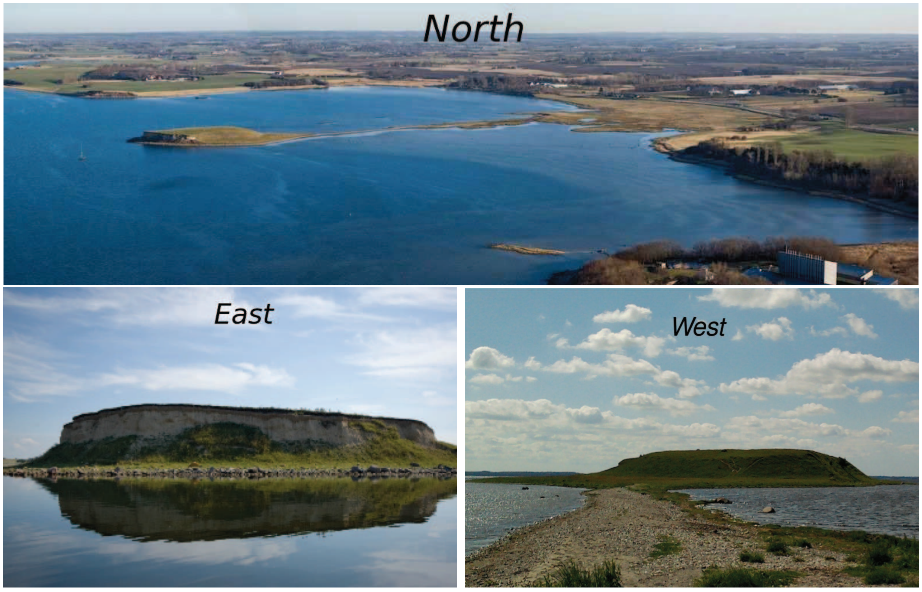

Figure 5.1.: Views of the Bolund hill in Roskilde Fjord, Denmark. Top: top view from the South, bottom left: western steep escarpment, and bottom right: eastern slope (images from [7]).

The Bolund hill [9, 8] is a small natural peninsula located in the Roskilde Fjord in Denmark. The hill is surrounded by water except on its East side where a narrow path links it to the land. The hill is relatively small, 12 m high, 130 m long in the W-E direction and 75 m wide in the N-S direction. It presents a steep cliff on its west side, facing the fjord (figure 5.1 bottom left) the top of the hill is rather flat, it does like a *plateau* and the slopes on the northern, southern and eastern sides are reaching up to 40°. The western wind is particularly of interest because of the very long area of sea upstream and the very steep escarpment of the hill that provide well defined inflow conditions and a great challenge to model the behaviour of the flow around a complex topography. Additionally, the small dimensions of the hill gives the advantage to be in the surface layer, therefore, the flow can be modelled to be neutrally stratified [9].
A field measurement campaign was realized by DTU-Wind [1] in collaboration with

[1]Denmark Technical University, Roskilde, Denmark

Vestas using a set of ten masts (M0 to M9 in Figure 5.2) spread on the hill and its surroundings. The masts are defining two lines, “line A” (239°) and “line B” (270°). Cup anemometers and three component sonic anemometers were placed at 2 m and 5 m above the local ground. The measurement campaign took place in winter 2007-2008.

Results presented in the following sections are extracted from three components

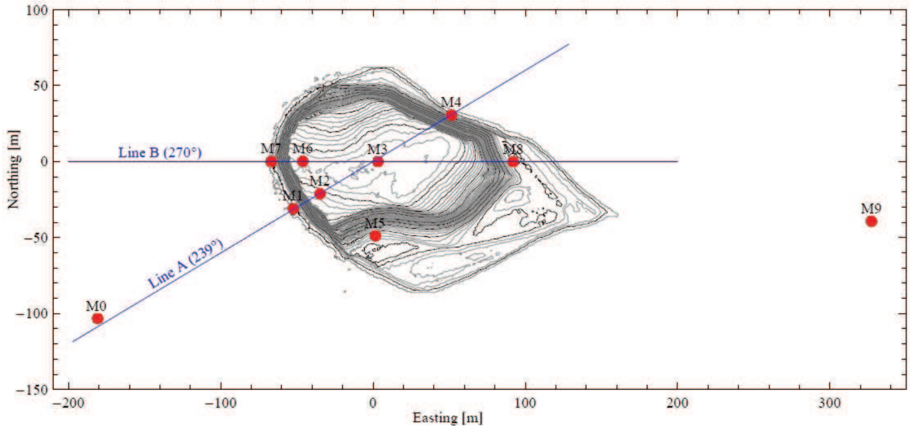

Figure 5.2.: Elevation contours and repartition of the measurement masts over the topography (figure from [7]).

Figure 5.3.: A mast at the western ridge of the hill and on the *plateau* of the hill equipped with sonic anemometers (images from [7]).

sonic anemometers acquiring at 20 Hz. 10 min average are then computed from the signal ([7]).
Following the random error analysis procedure used in the wind tunnel and presented in appendix A.2.4, mathematically, only independent samples can be averaged to compute a mean or a standard deviation. Then typically for an atmospheric flow with a mean wind speed of 10 m/s and a an integral length scale of 200 m, there are only 15 independent samples in a 10 min acquisition (counting only samples separated by two times the typical time of the process). That leads to a poor accuracy in the determination of the mean and standard deviation: ±10% at 95 % CL for the mean and ±50% at 95% CL for the variance. It has to be pointed out that the measurement in the field is very different than in the wind tunnel. A 10 min acquisition in the field is set (arbitrarily) to distinguish between the turbulent fluctuations of the wind and the weather variability, in the wind tunnel, constant wind direction and mean value can be imposed leading to a more accurate determination of the averaged properties.

5.3.2. The Bolund blind comparison

A blind comparison gathering a large number of researchers and comparing many possible approaches to predict the wind over the Bolund hill was organized at DTU Wind, Dk. The comparison includes simple linear models (like WAsP), numerical models: RANS and LES, a wind tunnel and a water channel simulation. Modellers were given the topography, the roughness, and the inlet conditions and were asked to estimate the speed-up and the turbulence level. Part of the results is shown in figure 5.4 and 5.5 from [8].

The compared parameters are the velocity magnitude increase ΔS and the turbulence increase Δk with:

$$\Delta S = \frac{S - S_{ref}}{S_{ref}} \tag{5.1}$$

with

$$S = \frac{1}{3}\sqrt{U^2 + V^2 + W^2} \tag{5.2}$$

and

$$\Delta k = \frac{k - k_{ref}}{{S_{ref}}^2} \tag{5.3}$$

The first thing to notice from figure 5.4 is the very high scatter of the results found, especially close to the ground, at 2 m: ± 50% on the *plateau* and 50% in the wake. For that height, in general, models are coherent in the first part of the hill, until $X \approx -25m$. From this point, much more scatter is observed, the modelling of the wake gives the most different results. The last measurement point $M4$ is almost never simulated successfully at 2 m a.g.l. Results are more successful

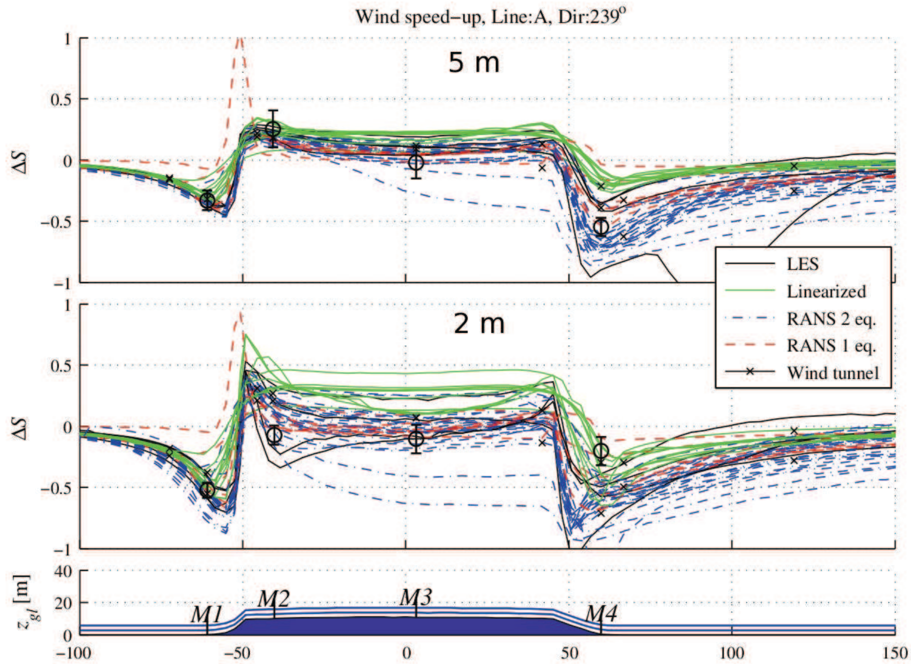

Figure 5.4.: Comparison of the FSR (ΔS) computed by linearised models, CFD, measured by wind tunnel experiments and measured in the fields (black dots) at 2 m and 5 m on the "line A". From [8].

at 5 m a.g.l. with 25% scatter on the *plateau*.
On the turbulent side in figure 5.5, the scatter observed is also very important, specially near the front cliff of the hill ($M2$). The turbulence increase (Δk) is mostly underestimated in the simulations.
This blind comparison enlighten the margin of improvement before reaching a good and universal prediction of the wind resource in complex terrain.
According to the authors of the blind comparison [8], the RANS simulations with one closure equation appeared to be the most successful in modelling the flow around the hill.

5.3.3. Experimental configurations

The dimensions of the island allows to keep the scaling factor relatively low, even in a small test section. For this experiment, the VKI-L2 wind tunnel is used with a 0.35 x 0.35 x 2 m closed test section (see its description in section). A scaling factor of 500 is chosen, that gives a blockage ratio below 5%,

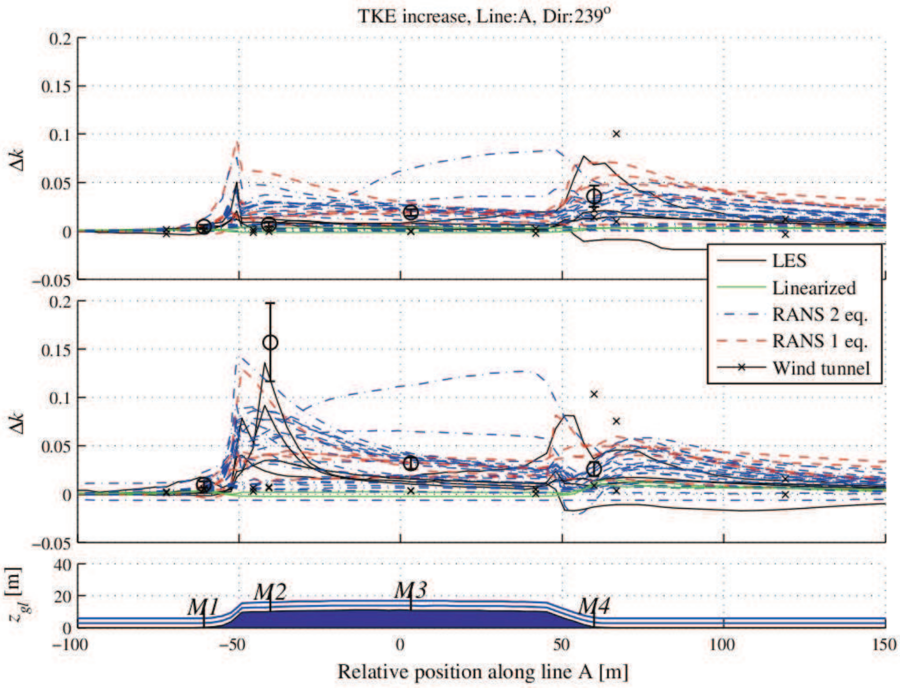

Figure 5.5.: Comparison of the turbulence increase Δk computed by linearised models, CFD, measured by wind tunnel experiments and measured in the fields (black dots) at 2 m and 5 m on the "line A". From [8].

$B_R = (0.024 \times 0.2)/(0.35 \times 0.35) \approx 4\%$.

Figure 5.6.: Terraced model of the Bolund hill at 1/500 scale.

The model installed in the test section is fabricated from 12 layers of 2 *mm* wood plates cut according to the contour of the hill shape every 1 *m*. The result is a terraced model with 2 *mm* steps. This technique is preferred to real hill contours to ensure a rough surface that keeps enough turbulence production at the surface. The technique is also simple, cheap and fast. The model, figure 5.6, is painted black to limit the light reflections from the Particle Image Velocimetry (PIV) illumination during the measurements.

Tests are performed at a free-stream velocity from 5 m/s to 15 m/s monitored by a Pitot probe situated at the entrance of the test section. Four PIV planes are recorded to cover the inflow and the entire model. At each PIV plane, a set of 1000 images is acquired. From the separated planes, the reconstruction of the time averaged field over the complete hill is realized from reference images taken at the different camera positions before each test. The recomposed averaged field is continuous but instantaneous acquisitions are not correlated from a plane to another.

The test section is set to reproduce the real inflow condition: offshore wind (cat. I in VDI guidelines). With the work of chapter 3, the best configuration is found using a 20 mm fence and a 2 mm rough floor. The modelled aerodynamic roughness length at full scale is $z_{0_{wt}} = 4.9 \times 10^{-3}$ m compare to $z_{0_{field}} = 6 \times 10^{-3}$ m estimated in the field [9]. Figure 5.7 compares the measured inflow conditions in the field to the profile developed in the wind tunnel. The velocity profiles are normalized at $z = 10$ m. Both velocity profile and turbulence intensity profile in the wind tunnel are well reproducing the real inflow conditions.

5.3.4. The flow around the Bolund hill

The flow over the Bolund hill is presented along the “line B” (figure 5.2) with a West wind (270°). Results of the velocity components over the Bolund hill are presented at the real scale in figures 5.8 to 5.13.
A velocity decrease is observed at the foot of the hill due to the escarpment. Then, a velocity speed-up is observed at the hill top, the presence of a high velocity zone at the ridge of the hill and the velocity streamlines convergence enlighten this phenomena.
The longitudinal velocity speed-up is closely followed by a low speed area close to the surface. No recirculation bubble is visible on the averaged field.
The vertical velocity (figure 5.10) is largely influenced by the frontal escarpment leading to a great upwards velocity increase near the ridge top. Its effect is visible up to almost 50 m both upwind and in altitude. A small downwards velocity area is present right after the speed-up, it may be due to a separation area. However, no averaged reverse flow is recorded in this experiment.
The velocity decrease at the hill’s foot is associated to a longitudinal turbulence

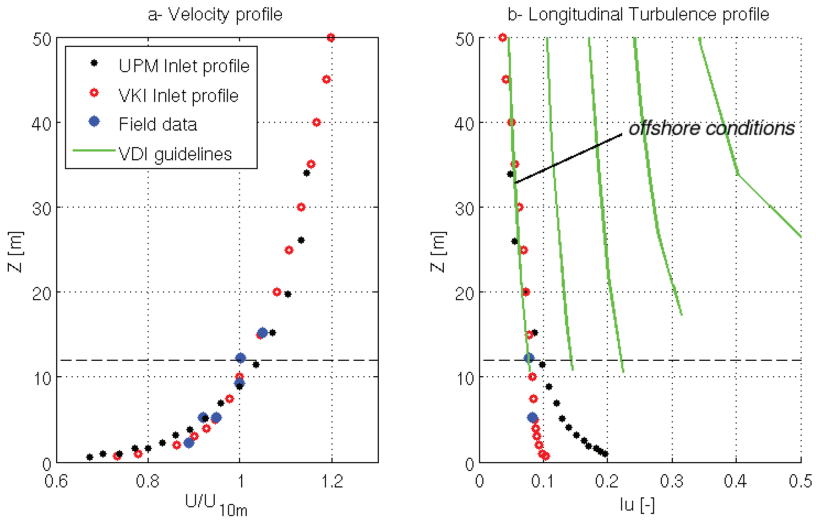

Figure 5.7.: Bolund inlet conditions: velocity (left), longitudinal turbulence profile (right), comparison with VDI guidelines (green), field measurements (blue), and inlet conditions in the UPM wind tunnel (black).

increase. At the crest of the escarpment, below the velocity speed-up, the low speed area is combined to a great increase of the longitudinal velocity fluctuation. It extends in altitude up to $z \approx 4$ m that is 1/3 of the escarpment height (figure 5.12). In the stream-wise direction, the high turbulence zone extends until $x \approx 76$ m, this is around 6 times Bolund height.

After the escarpment crest, the longitudinal and vertical velocity components remain almost constant until the back slope of the hill, this is where a wake region starts ($X \approx$50). There, the vertical component of the velocity experiments a downward motion and the longitudinal velocity component is significantly reduced. The wake region and its velocity deficit is clearly visible in the velocity vector field in figure 5.11 but no recirculation is recorded. A high turbulence area is emanating from the top of the hill, right where the downwind slope starts. The wake of the hill extends further downstream than the measurement area.
The downstream slope, at the position of the measurement, is around $s = 0.15$ ($\approx 9°$) and no separation occurs, this is in line with the theory and experiments conducted in chapter 4.

In the work performed at the UPM[2] [92] and [93] on a 1/115 scale Bolund hill

[2]Universidad Politécnica de Madrid, Spain

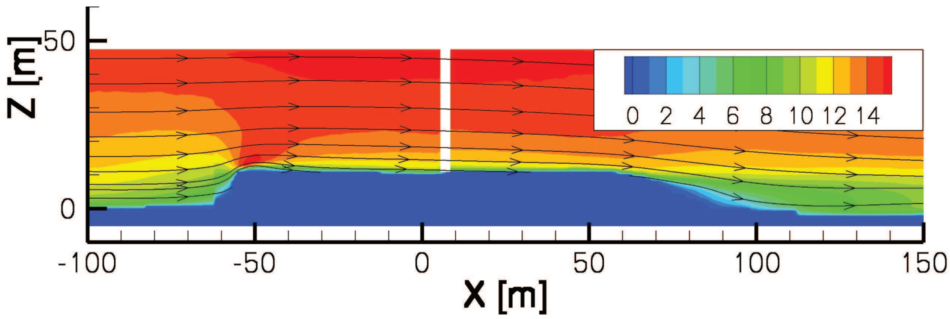

Figure 5.8.: Velocity field around Bolund hill. Velocity magnitude M [m/s] and velocity streamlines.

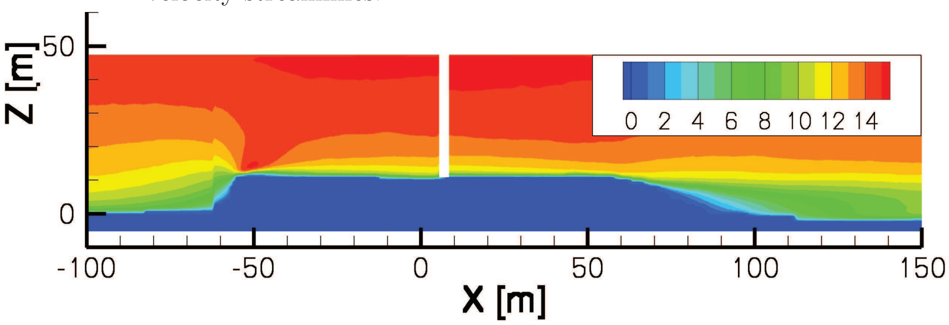

Figure 5.9.: Longitudinal wind speed U [m/s].

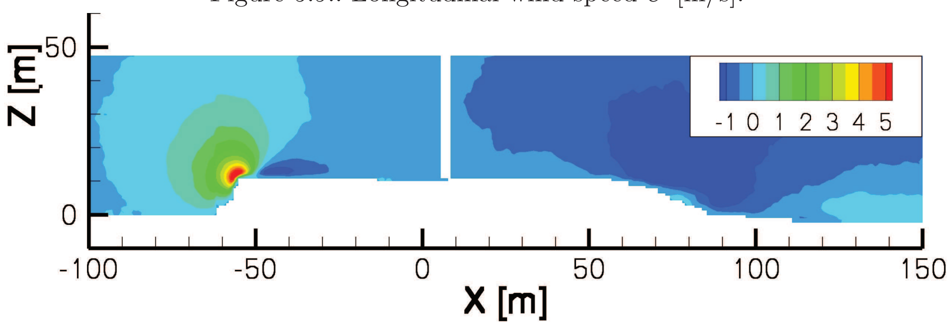

Figure 5.10.: Vertical wind speed W [m/s].

(2% blockage), the PIV spatial resolution is much higher close to the crest of the Bolund escarpment, however, the time averaged field doesn't show a reverse flow, only instantaneous frames can, sometimes present a reverse flow. The pressure measurements carried out on the same model shows a great drop of the surface pressure at the hill crest that would suggest a flow separation.

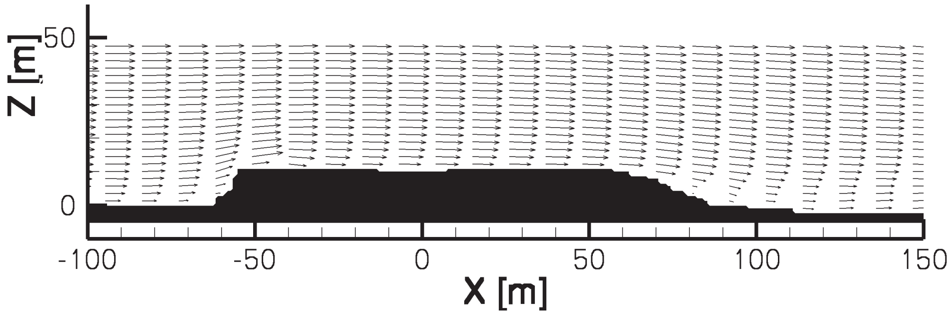

Figure 5.11.: Velocity vector field around the hill.

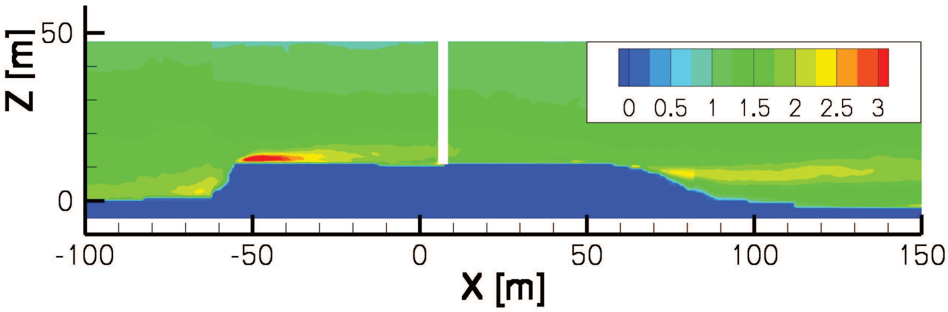

Figure 5.12.: Standard deviation of the longitudinal velocity component σ_U [m/s] around the hill.

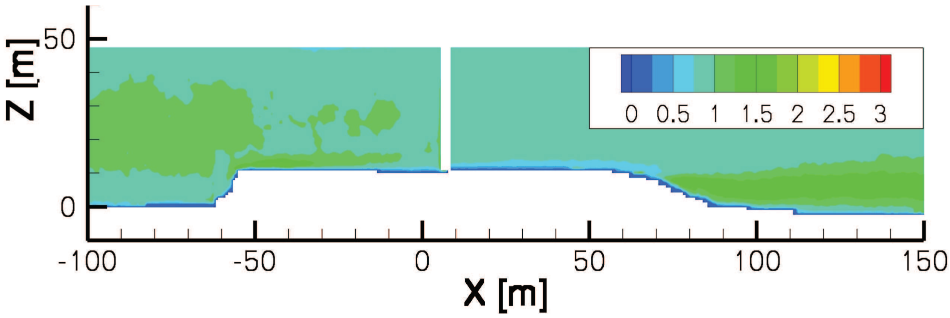

Figure 5.13.: Standard deviation of the vertical velocity component σ_W [m/s] around the hill.

Compared to 2D forward facing step (FFS) for which a clear separation occurs at the crest of the escarpment, the Bolund hill is three dimensional, the flow can go around it. Additionally, the crest is not very sharp. Then, the separation, if existent, may be much weaker than expected from a 2D escarpment. However, a vortex shedding is likely to happen, and there is a large velocity deficit and an important turbulence increase.

5.3.5. Comparison with field data and modellings

Results of the FSR (ΔS) and the turbulent kinetic energy increase (Δk) at 5 m a.g.l. are presented in this section for the West wind ("line B" or 270°). Field data are from sonic anemometer monitored by DTU-Wind, the 1/500 scale results are from 2D2C-PIV performed at VKI and the 1/115 results are performed by UPM with a three-component hot-wire.
For the wind tunnel data extracted from PIV, the calculation of the FSR (ΔS), only the longitudinal and vertical components are taken into account. For the turbulence increase Δk, the transversal turbulence level is estimated following the ABL relationship (see chapter 2): $\sigma_v = 0.75 \times \sigma_u$.
The FSR measured at the 1/500 and 1/115 scales (figure 5.14) are in general, in the errorbar of the four available field measurements. The speed-up at the top of the hill (M7, X = -67.3 m) is specially well reproduced in both tunnels. The two experiments are very well correlated along the hill *plateau* but both are forecasting a speed-up of nearly 25% where the field measurements are not measuring any speed increase (mast $M3$). It is noticeable that some of the results presented in the blind comparison are similarly predicting a speed-up where nothing is measured in the field. This over prediction is somehow independent on the modelling (RANS, LES, wind tunnel...), wind tunnel experiments are all overestimating it. A possible influence of the inflow conditions is discussed in section 5.4.2.
In the down slope of the hill, the 1/500 experiment is modelling a greater velocity deficit, down to less than $\Delta S = -50\%$, which matches with the measurements. The experiment at 1/115 scale presents a weaker velocity deficit ($\Delta S = -25\%$) in this area (near M8: X = 91.46m). This may be due to the higher inlet turbulence intensity near the ground simulated at UPM that may lead to a quicker wake recovery.

On the turbulent side, in figure 5.15, both experiments are predicting a weak increase of the turbulent kinetic energy along the hill and a final increase in the down slope region. Available measurements are somehow showing a regular increase with the distance and none of the wind tunnel simulations is able to reproduce this effect. The surface roughness is modelled in none of the mock-ups so it may be that not enough turbulence is generated at the surface to perfectly reproduce the turbulence increase. The down slope part (near M8) is the area with the most scatter.

Figure 5.16 and table 5.1 are comparing quantitatively the two experiments and the field data. As described before, the 1/500 scale simulation is the closest to the measurements for the FSR with 8.8% average error and only one measurement with more than 4.5% difference. The 1/115 is also performing quite well but with an average error of 34%, mainly due to the poor reproduction of the wake. For

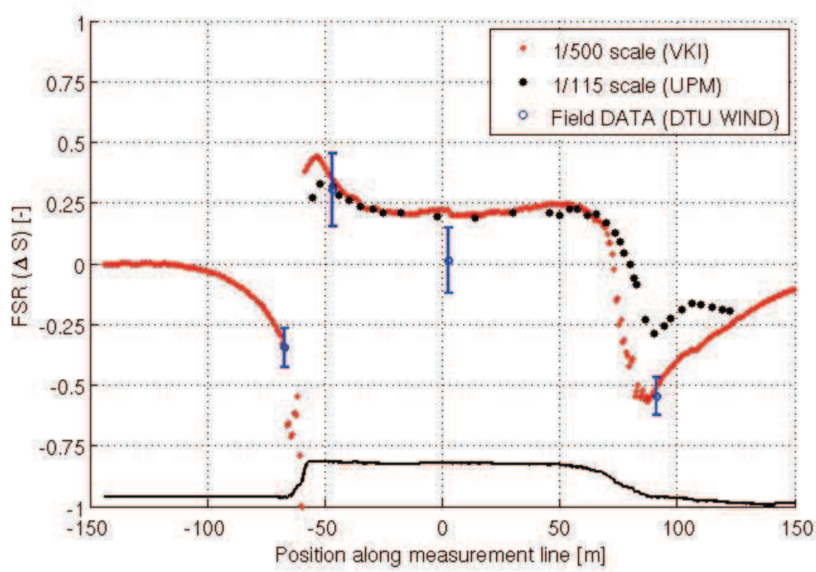

Figure 5.14.: FSR (ΔS) at 5 m a.g.l. along *Line B*,comparison of field data with wind tunnel experiment.

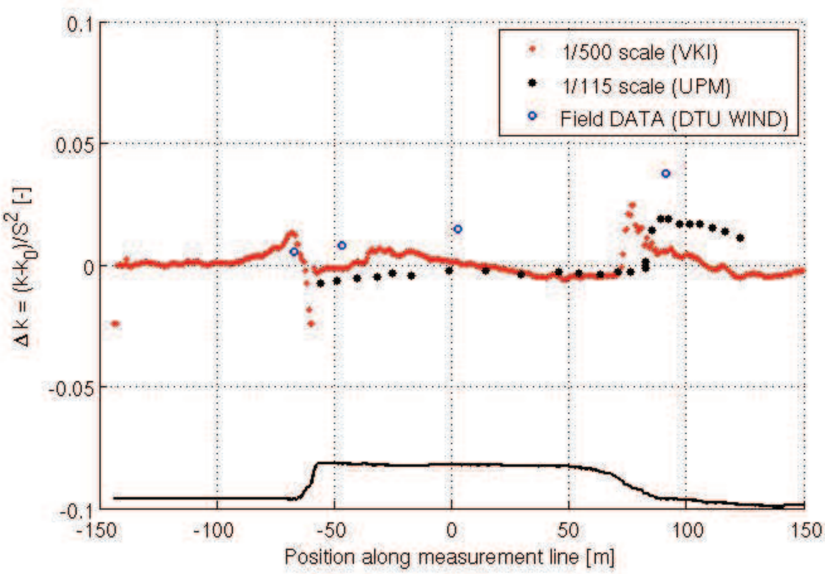

Figure 5.15.: Increase of turbulent kinetic energy at 5 m a.g.l. along *Line B*, comparison of field data with wind tunnel experiment.

Δk, both models are underestimating the measurements on site, an average error of more than 100% is recorded but this is mainly due to the value that is close to zero. Compare to the scatter of the results of the blind comparison, the results are in the scatter observed. Results of the 1/115 scale experiment are somehow showing more coherence with a correlation coefficient close to 0.93.

The modelling in the wind tunnel at 1/500 scale of the Bolund hill gives sat-

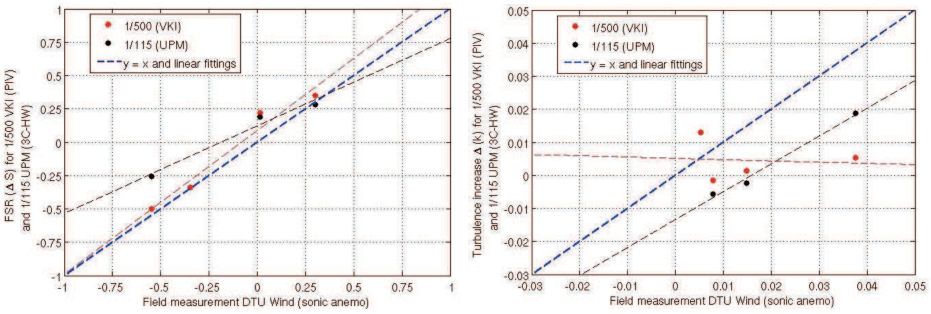

Figure 5.16.: Scatter plot of the FSR (ΔS) (left) and the turbulent kinetic energy increase (Δk) (right) for the two wind tunnel experiments compare to the field measurements by sonic anemometers.

Comparison field data with 1/500 (VKI)	ΔS	Δk	Perfect match
Linear coefficient	1.081	-0.0367	1
Correlation coefficient	0.981	0.0855	1
Fractional Bias	-0.086	1.130	0
Normalized Mean Square Error	0.015	4.594	0
Geometric mean	0.921	3.55	1
Geometric Variance	1.011	25.88	1
Average difference [-]	0.088	1.12	0
Comparison field data with 1/115 (UPM)	ΔS	Δk	Perfect match
Linear coefficient	0.608	0.689	1
Correlation coefficient	0.9631	0.929	1
Fractional Bias	-0.208	1.435	0
Normalized Mean Square Error	0.066	4.87	0
Geometric mean	0.765	-	1
Geometric Variance	1.120	-	1
Average difference [-]	0.34	1.09	0

Table 5.1.: Comparison of 1/115 and 1/500 scale wind tunnel experiment with field measurements, quantitative comparison.

isfactory results in predicting the FSR at 5 m, the difference observed compared to the field data is 8% in average but only one measurement out of four gives an overestimation above 4.5%. On the turbulent side, much more scatter is observed with a mean difference of more than 100% compared to the field data.

Many parameters can be involved in these discrepancies. A parametric study is performed to try to quantify the influence of several parameters.

5.4. Parametric study

Like mentioned in the chapter 2, the modelling of atmospheric flows in the wind tunnel involves lots of parameters to reproduce. This section aims at quantifying the influence of different modelling parameters on the flow field and at quantifying their relative importance on a real experiment. This approach is similar to an uncertainty quantification of the modelling parameters, the final effect of fluctuating parameters is studied. The goal is to better understand what are the most important parameters to fit.
Three modelling parameters are chosen for the parametric study: the Reynolds number, the inlet conditions and the flow angle. Table 5.2 summarises the configuration tested. The effect of the reference height is also investigated.

Configurations	Re_H	θ [°]	Inlet conditions
Test 1 (reference)	8 000	0	LF
-	24 000	0	LF
Test 2	40 000	0	LF
Test 3	24 000	0	FP
Test 4	24 000	0	CW
Test 5	24 000	-5	LF
Test 6	24 000	-15	LF
-	24 000	+5	LF
Test 7	24 000	+15	LF

Table 5.2.: Parametric study test matrix. Two tests are not presented because results are unreliable. θ is the wind direction, *CW*, *LF* and *FP* are the three inlet conditions tested: with Counihan wings, with a Lego floor and only the flat plate (see section 5.4.2).

To quantify the influence of each parameter, two quantities are defined:

$$\epsilon_{FSR} = \Delta S_2 - \Delta S_1 \tag{5.4}$$

and

$$\epsilon_{TKE} = \frac{k_2 - (k_2)ref}{(k_2)_{ref}} - \frac{k_1 - (k_1)ref}{(k_1)_{ref}} \tag{5.5}$$

with ΔS_i and Δk_i the FSR and the TKE in configuration (i).

5.4.1. Influence of the Reynolds number Re_H

At first, the Reynolds number is investigated in the test section. The same experiment as in section 5.3 is performed with a free-stream velocity of 5 m/s and 25 m/s. This is multiplying the Reynolds number by 5 from 8 000 to 40 000 (test 1 and 2).

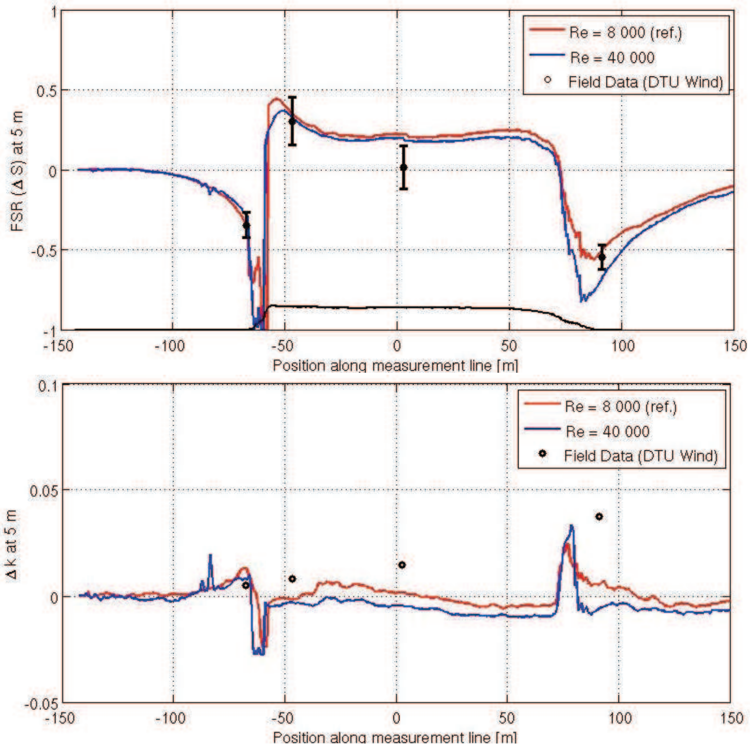

Figure 5.17.: ΔS and Δk for two different Reynolds numbers.

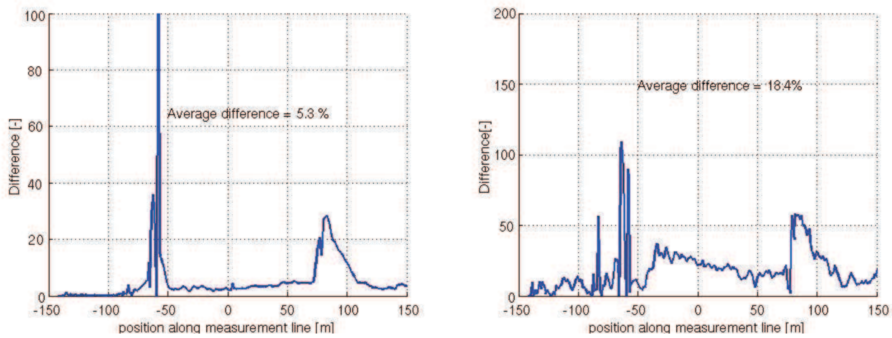

Figure 5.18.: Quantification of the Reynolds number effect on the FSR at 5 m. Percentage of error along the terrain for the FSR (left) and the turbulence kinetic energy increase Δk (right).

The test at 5 m/s gives, if defined with the model height, a Reynolds number below the symbolic limit of $\mathrm{Re}_H = 10\ 000$ defined in section 2.4.2 of Chapter 2 for the fully turbulent state of the flow. If defined with the model width or length, it gives $\mathrm{Re}_W = 50\ 000$ and $\mathrm{Re}_L = 100\ 000$. The second test performed at $\mathrm{Re}_H = 40\ 000$ gives similar results in terms of FSR and turbulent kinetic energy (Figures 5.17 and 5.18). An average difference of 5.3% is observed for the FSR and 18.4% for the turbulence increase. There are two locations where the difference between the two tests is above 5%, before the speed-up area and in the wake. Both areas are very steep gradient zones, therefore, a small error in the longitudinal positioning leads to large differences. The maximum speed-up error is around 10% and a shift of a few meters can be recorded. The second difference maximum is in the down slope of the hill, there, a peak difference of 30% is observed. Further downstream, the difference is decreasing and both simulations are converging to less than 5% . The difference observed for the TKE increase (Figures 5.17 and 5.18) is following the same trend as the FSR with an average difference close to 18%. The two same areas of higher difference are present.
A greater Reynolds number is increasing the intensity of the speed-up and of the wake but results are generally similar when multiplying the Reynolds number by 5. The terraced model is reaching his goal of providing close to Reynolds number independent flow.

5.4.2. Influence of the inlet conditions

When simulating any atmospheric flow, the reproduction of the boundary conditions is a major concern. Indeed, it makes sense that whether the terrain is the sea or a city center, the behaviour of the wind will be different. In the wind tunnel, the inflow conditions are reproduced thanks to BL generators, their arrangement is determining the wind velocity and turbulence profiles. Chapter 3 is dedicated to the wind tunnel reproduction of the wind speed and turbulent profile reproduction.
This section aims at determining the influence of small variation of the inlet conditions on the flow over a complex topography. It is chosen to model slight changes of the velocity and turbulence profile to underline the sensibility of the inlet conditions. Three inlet profiles are tested, the one reproducing as closely as possible the field data, see section 5.3.3 (called LF for "Lego floor"), another one using Counihan wings and providing similar conditions but with a smaller BL height and steeper turbulence gradient (called CW for "Counihan wings"). The third profile is the test section profile without any BL generator, the BL height is of the order of the hill height and the free-stream turbulence is very small (called FP for "Flate Plate"). The LF and CW configurations are close to the classification "I", *slightly rough* of the VDI guideline [85], set for offshore conditions. Figure 5.20 and table 5.3 presents the three BLs tested and their characteristics.

From figures 5.20 and 5.21, the influence of the inlet conditions is clearly visible

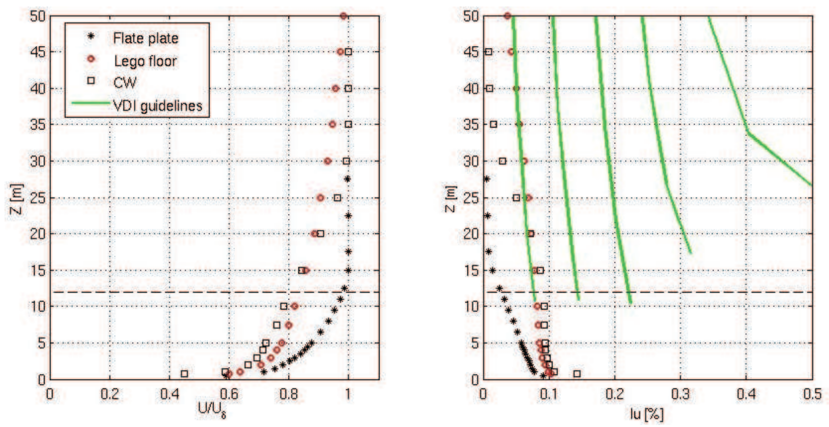

Figure 5.19.: The three different inlet conditions tested.

Configurations	LF	FP	CW
δ [m]	60	12.5	30
z_0 [m]	0.0048	0.0018	0.015
I_u [%]	8 %	3%	9%
δ/H	5	1	2.5

Table 5.3.: Characteristics of the three inlet boundary layers tested. Dimensions are at the real scale.

on both the FSR and the TKE.
Like for the Reynolds number effect, the area before the hill is weakly affected but this time, all the downstream part after the FSR maximum is influenced by the inlet condition changes. At the position of the maximum FSR ($X \approx -55$), both FP and CW configurations are experimenting a close but lower FSR of 37.5% and 41.3% respectively, that is a difference of -6.9% and -3.1%. The ratio between the BL height and the hill height may explain this difference.
On the Bolund *plateau*, the CW inlet condition leads to an increase of the FSR by around 10% compare to the reference case and the FP configuration leads to a decrease of 10%. Inlet conditions have a high influence on the *plateau* speed-up and this may explain the discrepancies observed compared to field measurements (section 5.3.5). The speed-up at the *plateau* is overestimated for the LF configuration that reproduces the best the available field measurements (Figure 5.7) but results at the *plateau* are improved by with a lower BL. An explanation may be find in the ratio between the hill height and the BL height (δ/h). A low δ/h ratio would lead to a lower speed-up when a high ratio will increase the velocity speed-up. Higher measurements of the inlet profile may give more information

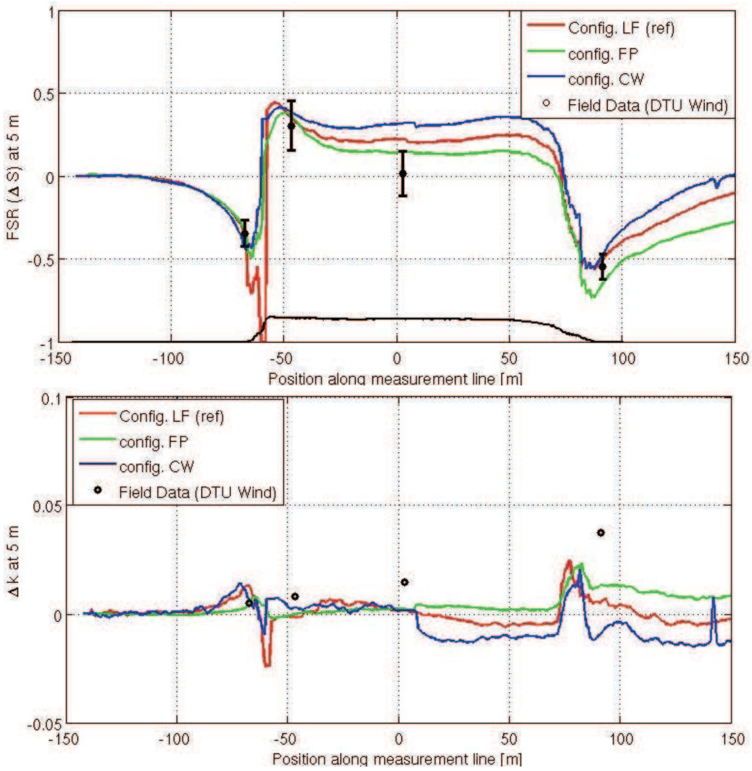

Figure 5.20.: ΔS and Δk for three different inlet conditions.

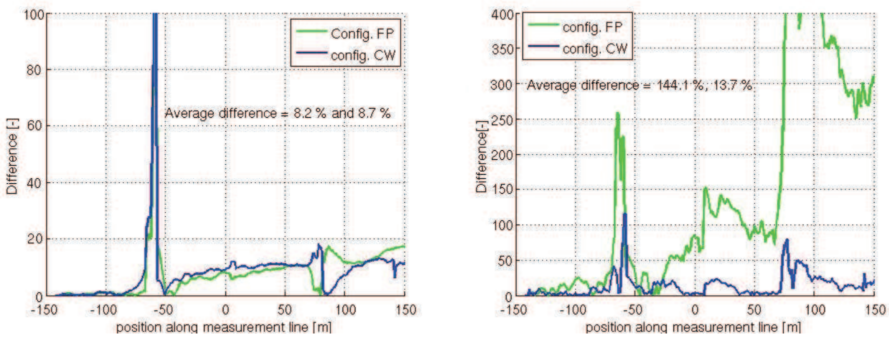

Figure 5.21.: Quantification of the effect of the inlet conditions. Percentage of error along the terrain for the FSR (left) and the turbulence kinetic energyΔk increase (right).

about this hypothesis. Form [73] the δ/h ratio certainly has an influence on the size of a recirculation area on a Forward Facing Step. A deeper investigation may be necessary to understand the possible influence of the δ/h ratio on the speed-up.

On the TKE side, the CW configuration leads to a TKE level 8% lower than the reference case. 100% increase is observed for the FP configuration. At the position X $\approx$ 80, the velocity deficit for the CW case is the same as the reference case but the FP configuration experiments 18% lower value. At that position, the TKE level of the FP case experiences an important increase, up to more than 400% compare to the LF configuration. Further in the wake, the CW inlet conditions keep implying higher FSR and lower TKE where the FP inlet condition gives lower FSR and higher TKE.
In the FP configuration, the inlet turbulence level is 3% instead of around 8% for the two other cases, this low inlet level explains the much higher increase of the turbulence level experienced for this configuration. The diffusion phenomena is weaker and the turbulence stays longer downstream. This configuration presents always a lower FSR than the reference case.
For the CW configuration, it is the other way around, the inlet turbulence level is higher, then a weaker turbulence increase is noticed compared to the reference case. The FSR is mainly higher than the reference case.

5.4.3. Influence of the flow angle

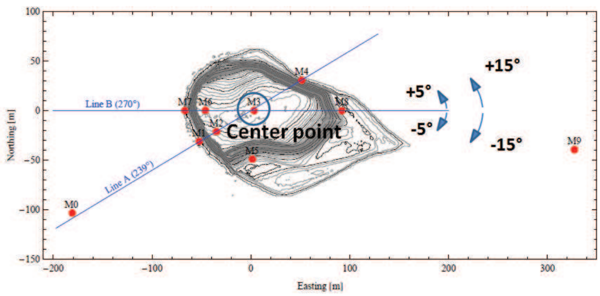

Figure 5.22.: The three different inlet conditions tested.

In the field, the wind direction is fluctuating a lot. For computing a directional average, a range of angle is selected. When changing the incoming flow angle, the section of the hill changes and the results can be affected. To estimate the influence of the angle of the Bolund hill on the velocity and the turbulent level, a set of experiments is proposed by changing the incoming flow angle from -15° to +15°. The mast $M3$ is roughly at the center of the hill, it is set as the center of rotation and the angles are defined in figure 5.22. Results are presented in figure

5.23 and 5.24.

In this parametric study, the shape of the hill seen by the flow differs from

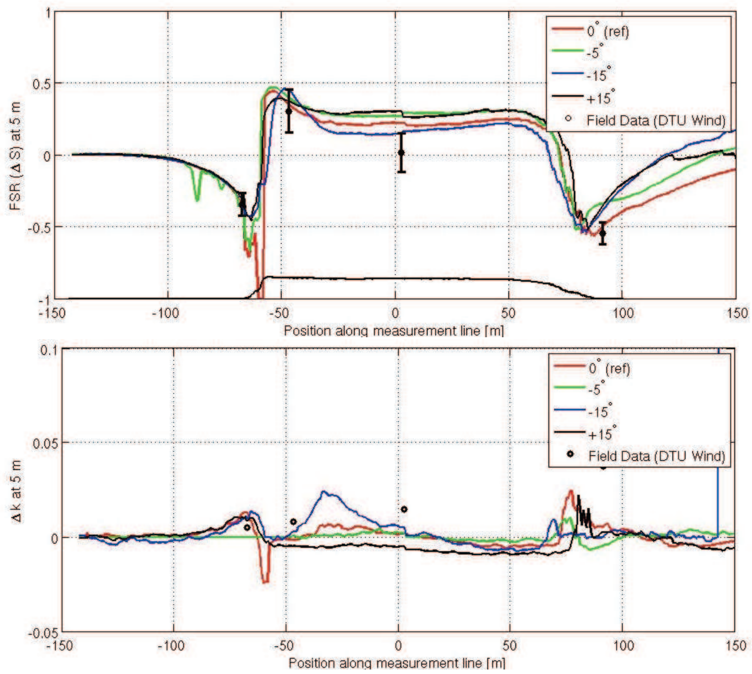

Figure 5.23.: ΔS and Δk for different flow angles.

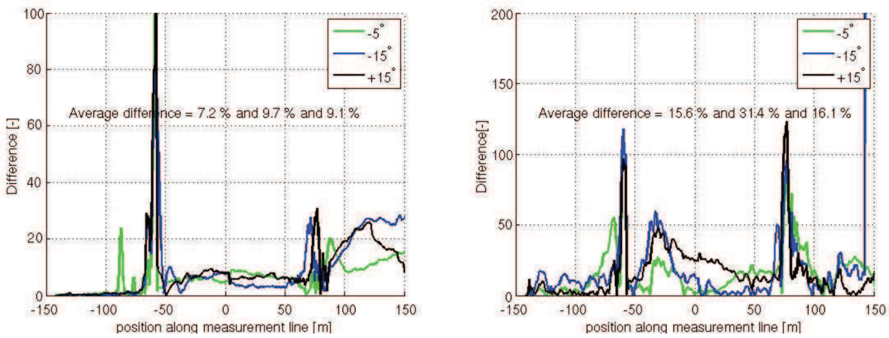

Figure 5.24.: Quantification of the effect of the flow angle. Percentage of error along the terrain for the FSR (left) and the turbulence kinetic energy increase Δk (right).

an angle to the other, this is the main explanation of the differences observed.

In general, maximum differences are observed as previously before the maximum FSR and in the wake. For the angles -15° and +15°, the geometry is shorter in the X direction leading to a faster recover of the FSR, the profile of the hill following -15° angle has a earlier and smoother down slope.
Maximum FSR differences are around 9.5% on the *plateau* and can reach more than 25% in the wake. The average FSR difference is below 10%.
On the turbulent side, the average difference is between 15% and 30% with local peaks over 50%.

5.4.4. Influence of the reference height

Additionally to the modelling parameters, the exact position of the measurement may be a source of uncertainties. In the wind tunnel, at a scale of 1/500, 5 m in the real scale is equivalent to 1 cm. A parametric study is here performed by changing the reference height by +/- 20 %. That corresponds to 2 mm change at the wind tunnel scale.
Like the other parameters, the change of the reference height is mainly affecting the maximum FSR and the wake area (figures 5.25 and 5.26. In average, the difference is limited to around 2.8 % for 4 m and 2 % for 6 m but the maximum FSR is increased by 9 % at 4 m and decreased by 6.5 % at 6 m. On the turbulence side, the higher the altitude, the lower the turbulence, in average, the turbulence is increased by 2.4 % at 4 m and deceased by 2.4 % at 6 m.

5.4.5. Discussion of the relative influence of the parameters tested

The parameters studied and their influence on the final results are summarised in table 5.4.

Configurations	Variation	FSR	$\Delta k/k$
Angle	$\pm 15°$	8.67 %	21 %
Inlet profile	see tab. 5.3	8.5 %	78.8 %
Reynolds number	$(\times 5)$	5.3 %	18.4 %
Reference height	± 20 %	2.65 %	2.5 %

Table 5.4.: Average difference of FSR and TKE compare to the reference test.

The first parameter influencing the flow over the Bolund island is the inlet conditions, even with the rather limited change of the inlet velocity profile, the final FSR is modified by 8.5% in average and the turbulence by almost 80%. The inlet profile is definitely the most important parameter to reproduce for this test case. Second in the ranking of the most important parameter, the wind direction. This result is for sure case dependant. Indeed, the change of the geometry due to the wind direction depends on the topography studied. In any case, field data are

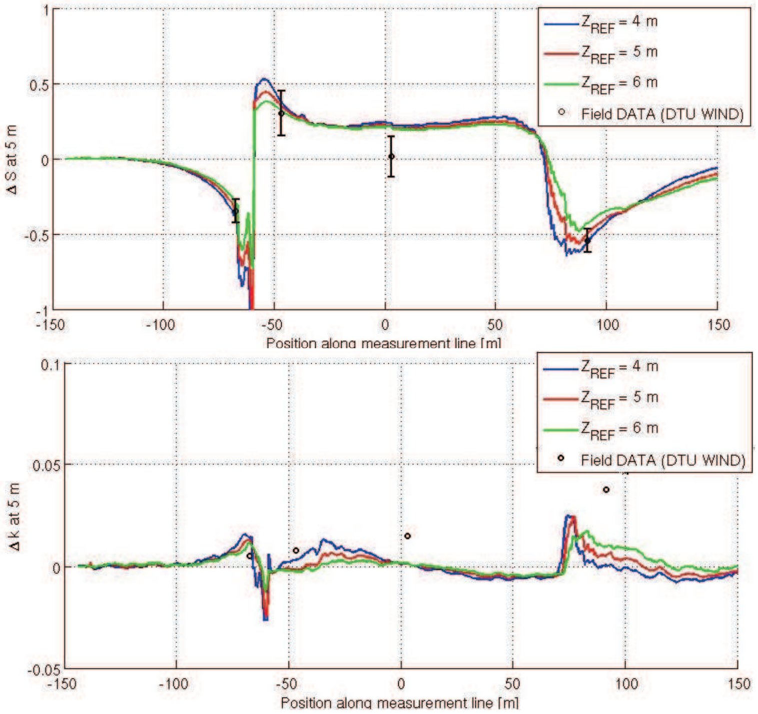

Figure 5.25.: ΔS and Δk for different heights.

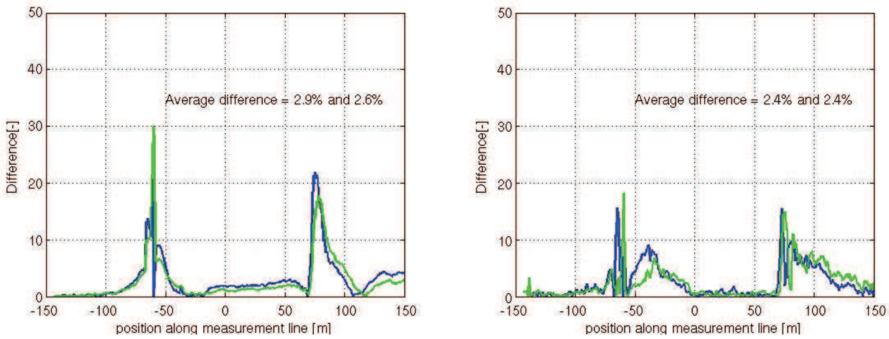

Figure 5.26.: Quantification of the effect of the reference height. Percentage of error along the terrain for the FSR (left) and the turbulence kinetic energy increase Δk (right).

often averaged with a band of +/-5° so the assessment of the influence of this

parameter can be important.
The Reynolds number dependency study and the study of the influence of the reference height can be assimilated to the determination of an uncertainty range. The Reynolds number study is also a check of the validity of the simulation.
It has to be mentioned that the model roughness also can have an effect on the velocity speed-up. This is not investigated in this study, various effects are reported in [18, 19, 61, 86].

5.5. The Alaiz mountain (Sp)

The Bolund hill is a real hill with complex topography but, unlike many complex cases, it is small, isolated and with well defined boundary conditions. To move one step further, and to face more complex cases, the simulation of the Alaiz site is undertaken.
The Alaiz mountain has all the characteristics of a complex test case for wind resources assessment: altitude, geographic extension, complex surroundings and no measurements of the boundary conditions.

The goal of this study is to investigate the Alaiz mountain in the wind tunnel. Results are compared to field measurements for validation and to CFD computations for more details comparison. Additionally, similarly to the study performed on the Bolund test, a parametric study of the most important modelling parameters is performed to try to quantify their importance.

5.5.1. Description of the topography and the site instrumentation

Figure 5.27.: Global view of the Alaiz mountain with the front ridge and the city of Pamplona.

The Alaiz mountain (Figure 5.27 and 5.28) is a very complex terrain with steep slopes situated in Navarra, South from Pamplona, in the North of Spain [17, 16, 24, 26]. The terrain is a 1130 m high mountain surrounded by slopping

terrain in the North and very complex topography in the South. The mountain is extending 15 km in the South and is more than 12 km long in the W-E direction. Number of wind turbine farms are already installed on site (figure 5.28).
Five measurement masts are placed on the mountain *plateau*, around the position (UTM30-X = 618 000m, UTM30-Y = 4 728 000m) in the elevation map of figure 5.28. Masts are 120 m height and equipped with cup and sonic anemometers. At least 4 levels per mast are instrumented with wind vanes, cup anemometers and temperature and humidity sensors. Measurement masts are placed near the position of future wind turbines. The local wind rose has two dominant wind directions: North and South (figure 5.29).

At the position of the masts, the mountain is like a *plateau* at 1 120 m altitude (a.s.l.). To the North, the terrain is an even plain with a mean elevation of 500 m (a.s.l.). Several kilometres North from the Alaiz mountain, a 600 m to 750 m height *ridge* extends on more than 6 km in the West-East direction and less than 1 800 m wide in the North-South direction. If the altitude of the plain is deduced, the altitude of the Alaiz *plateau* is 620 m and the ridge is between 120 m and 250 m. The distance between the ridge top and the mountain *plateau* is around 6 km.
The North face of the mountain is divided in two slopes, a very steep slope of around 25°, from the foot of the hill to a height of 300 m and a 14° slope from 300 m to the *plateau* at 620 m.
South of the *plateau*, a slightly lower valley extends from UTM30-Y = 4 728 000m to a second peak around UTM30-Y = 4 726 500m where a row of wind turbines is installed. Further South, the mountain presents very complex topographies with escarpments aligned to the North-South direction.

5.5.2. Choice of the area to model and the scaling factor

Giving the wind rose presented in figure 5.29, and the positioning of the area instrumented, the wind tunnel test is chosen to be performed for a North wind. In this configuration, the *ridge* is an upstream obstacle of $h = 250m$ for the wind and it may affect the wind reaching the Alaiz mountain ($H_{Alaiz} = 620m$). The wind tunnel test section is 3 m wide and 2 m high, a compromise has to be found to decide the area to model around the position of the measurement masts.

Upstream the middle of the *plateau*, along the UTM30-X = 618 000m line, the front ridge presents a upwind slope of $L/H \approx 4.5$ (11°) and a downwind slope of $L/H \approx 2.8$ (19°). According to the precedent tests performed on simplified geometries in chapter 4, the downwind slope is over the limit of separation, a flow separation is to be expected. The foot of the Alaiz mountain is situated at 4 km from the ridge top, this is equivalent to 16 times the ridge height ($D = 16h$). From figures 4.26 and 4.28 in chapter 4, for $L/H \approx 2.8$, the FSR is still below $\Delta S < -5\%$ and the turbulence intensity increase is above 2.5% ($I_w > 2.5\%$) at

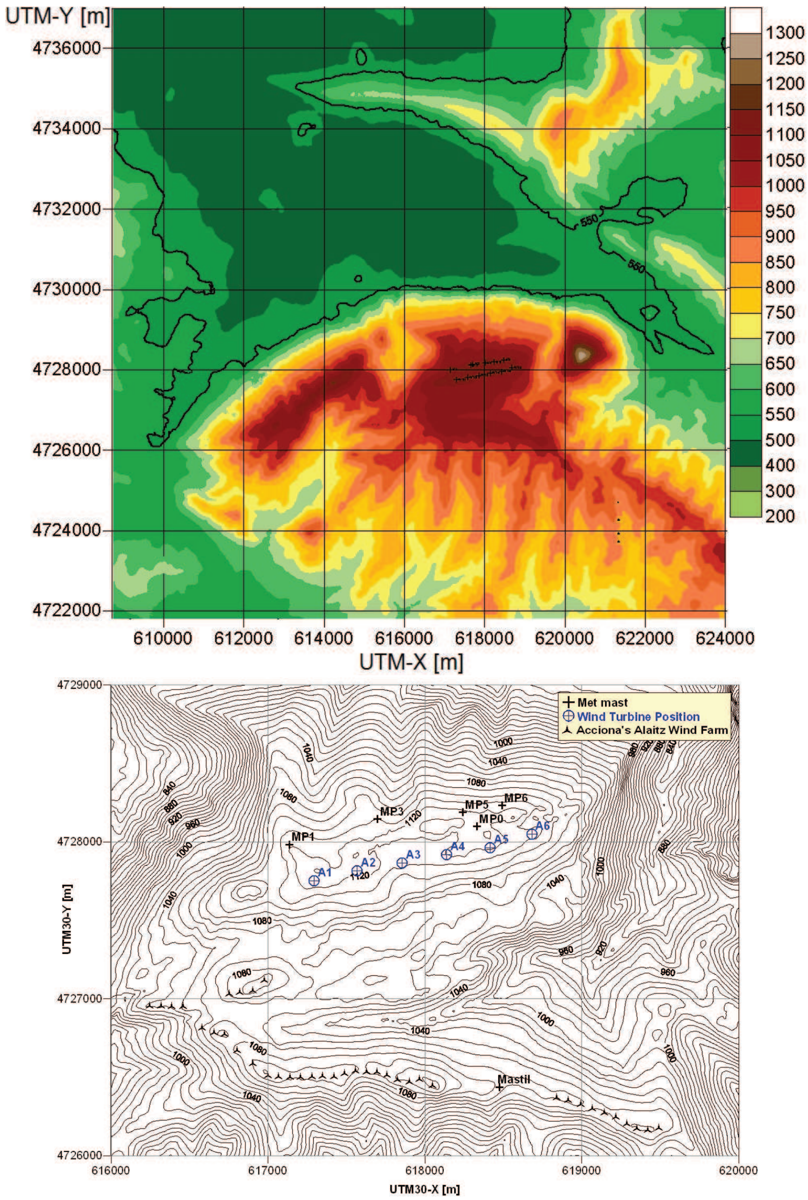

Figure 5.28.: Elevation map of the Alaiz mountain (top) and zoom on the Alaiz *plateau* with the measurement masts (bottom).

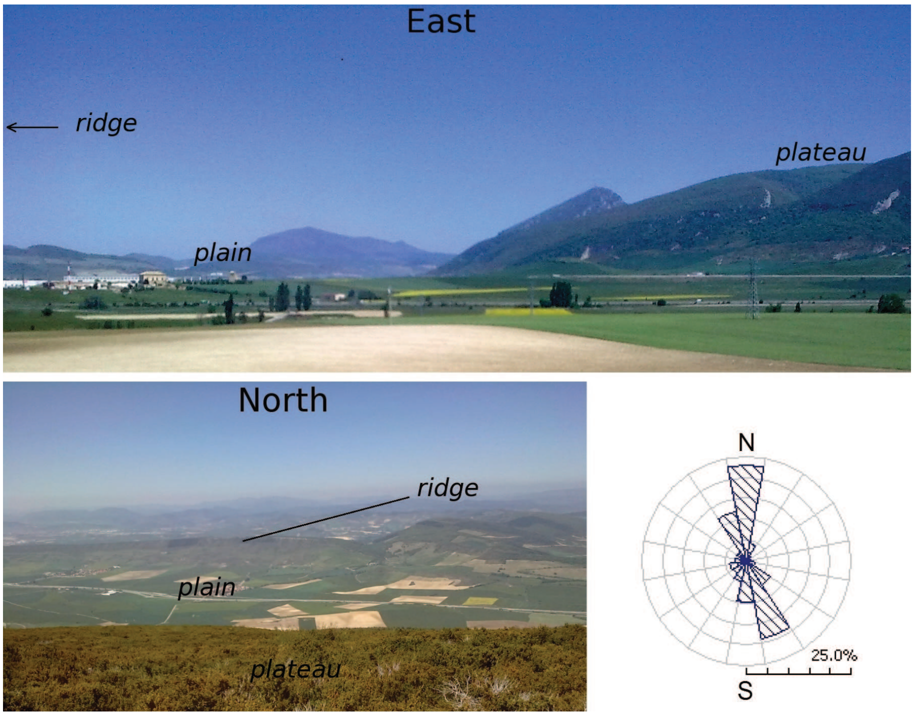

Figure 5.29.: Views of the test site looking to the East (top picture) and view from the top of the mountain looking to the North (bottom left). The ridge is visible on this picture. Bottom right: the wind rose at the Noain airport, North from the mountain (Fig 5.27).

the foot of the Alaiz mountain. This estimation of the influence of the inlet ridge is made taking into account an ERCOFTAC type hill, the real ridge is more a triangle-like shape. From Pearse, [65], who studied hills of different shapes, at the same ratio s, the triangle shape induces a stronger perturbation in the near wake than a bell shaped hill. This effect is also enlighten by DaCosta [27] comparing a 2D triangle and Gaussian shape. Then the downstream influence of the Alaiz upstream ridge can be expected to present a higher perturbation remaining longer downstream than the estimation from chapter 4. Additionally, with a triangle shape, the downstream flow is affected at a much higher altitude [65, 27].
Given the assumed influence of the front *ridge*, it is logical to include it in the wind tunnel mock-up. The total modelled area is 16 km long in the wind direction (N-S) and 15 km in the W-E direction (figure 5.30 and 5.31). That gives a scaling factor of 5357. The blockage in the wind tunnel is approximately 6.7%.

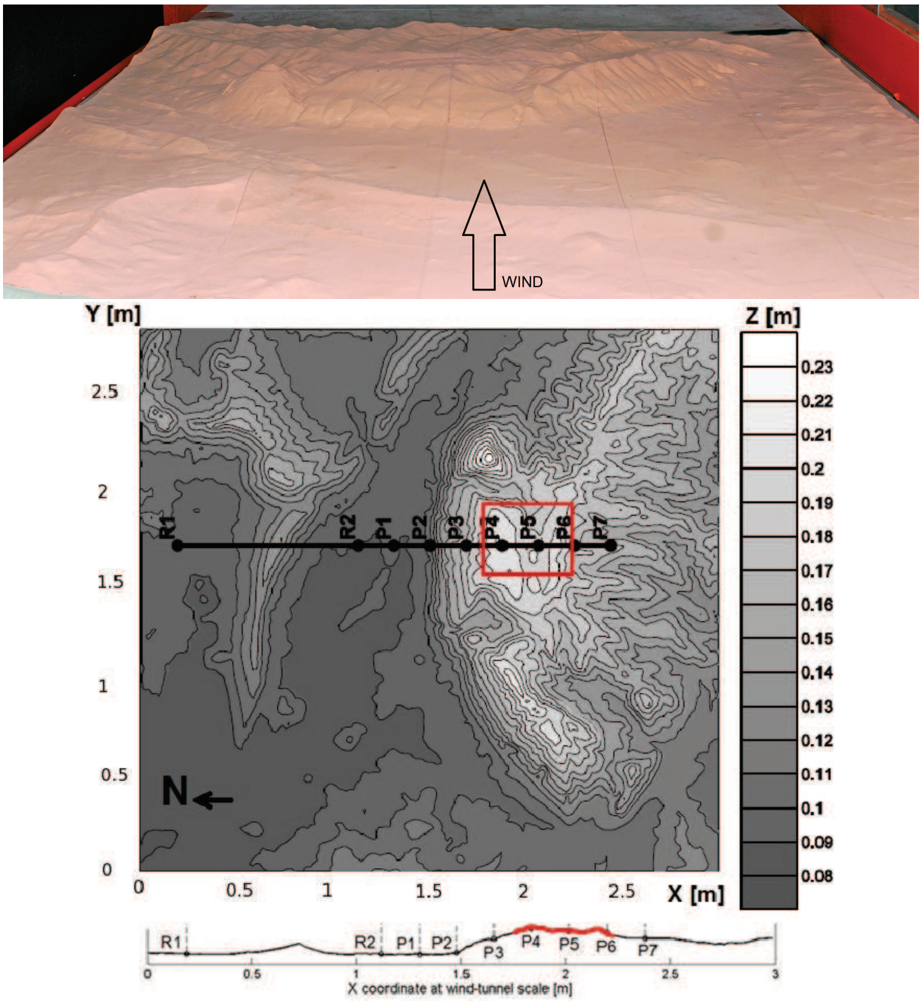

Figure 5.30.: View of the mock-up (top) and the area modelled at wind tunnel scale with the measurement plane (bottom).

5.5.3. Experimental configurations

The mock-up is made out of blocks of Necuron directly drilled from the 3D numerical mesh provided by CENER[3] and also used by numerical modellers. The model was fabricated at UPM[4] on a numerical drilling tool with 1/10 mm precision. The

[3]National Center for Renewable Energy, Spain
[4]Universidad Politecnica de Madrid, Spain

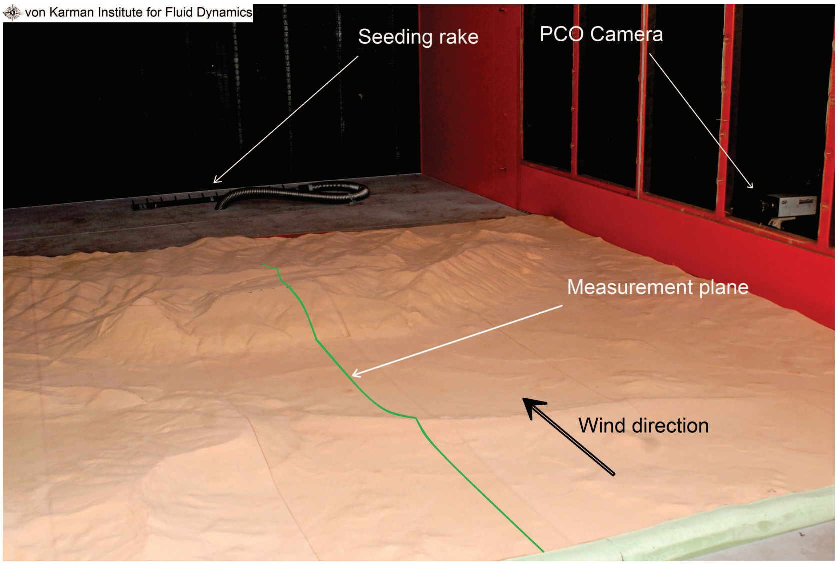

Figure 5.31.: The Alaiz mock-up in the test section with the PIV set-up.

final surface roughness is approximately $R = 10\ \mu m$. This mock-up doesn't take into account the real surface roughness neither the roughness changes of the terrain. The surface finishing can be considered smooth.
Hot-wire (HW) and PIV measurements are carried out along the measurement plane defined in figure 5.31. The model is painted black around the PIV measurement position. The laser is placed on the ceiling of the test section with an optical path bringing a laser sheet to the model. The smoke seeding is placed downstream of the model and, after a few minutes, thanks to the closed-loop wind tunnel, the whole test section is homogeneously filled with smoke. This technique prevents any upstream disturbance from a seeding rake. PIV data are recorded in six overlapping planes along the measurement line between points $R2$ and $P6$ (figure 5.30 and table 5.5). Average fields of 500 images are then recomposed to form a continuous data set. The processing of the images is performed with an in-house code called *WIDIM* [72] that performs cross-correlation and windows refinement (see appendix A.1). The final resolution of the PIV measurements is about 1.78 mm/vect in the vertical and the horizontal directions.
Single HW measurements are carried out at positions $R1$ to $P6$. The HW acquisition parameters are described in table 5.6. More details can be found in appendix A.2.

The experiments are carried out at 15 m/s, the Reynolds number based on the mountain height is $Re = 110000$.

Reference point	UTM30-Y [m]
R1	4 737 000
R2	4 732 000
P1	4 731 000
P2	4 730 000
P3	4 729 000
P4	4 728 000
P5	4 727 000
P6	4 726 000
P7	4 725 000
P8	4 724 000

Table 5.5.: Position of the reference points along UTM30-X = 618 000 m.

Acquisition parameters	Values
Acqu. frequency [Hz]	750
Filter frequency [Hz]	300
Number of point	90 000
Acqu. time [s]	120

Table 5.6.: Acquisition parameters for the HW measurements.

On the field, there is no measurement of the inlet conditions. Seeing the map in

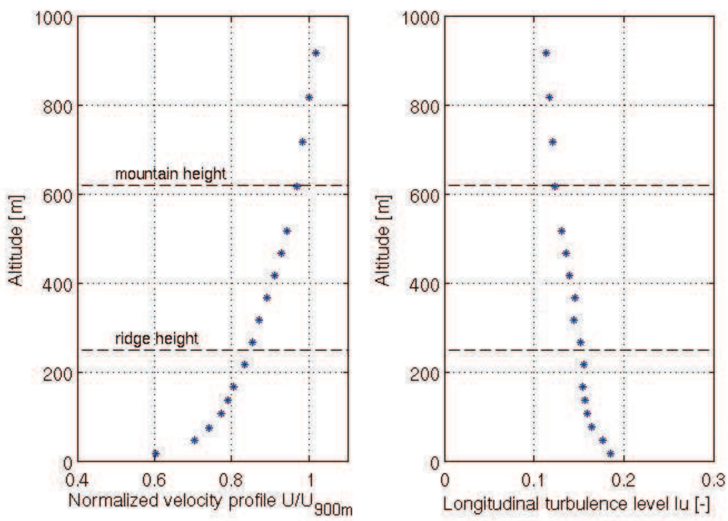

Figure 5.32.: Alaiz inlet conditions measured at position $R1$.

figure 5.28, to the North of Alaiz, apart from the *ridge*, the field is even, of a countryside type. More upstream, there is the city of Pamplona and other mountains. The inlet conditions tested, plotted in figure 5.32, is using a fence and a grid at the entrance of the test section and the test section floor is covered with cups. The ABL generation set-up is detailed in chapter 3, section 3.2.2 using "Cup 2" configuration in table 3.1. This is modelling a *moderately rough* to *rough conditions*.

5.5.4. Wind evaluation by sand erosion technique

Before using very precise, delicate and expensive measurement tools, the sand erosion technique is applied to the Alaiz mountain to have a general view of the wind repartition over the terrain. The goal is to get a rough idea of the location of the high wind zones over the model and to focus the use of traditional and time consuming measurements techniques only to necessary zones.
The sand erosion technique is a global technique that consists in covering the terrain mock-up with a thin layer of sand that contrasts with the color of the mock-up. The wind tunnel speed is then set to increasing velocity steps and a picture is taken for each step. A calibration allows to associate each velocity step to a speed-up ratio (FSR) compared to the incoming flow. The first zones to be eroded are those with the highest speed-up. The technique is omnidirectional with a repeatability scatter of less than 7% (see [26]).
The information extracted is mainly qualitative but an estimation by 10% of the velocity speed-up is performed compare to conventional HW or PIV measurements.

The technique is a very interesting tool for evaluating quickly an unknown terrain and helps in focusing the measurements to interesting areas. Figure 5.33 presents results on the Alaiz mock-up. The sand erodes first in high altitude locations.

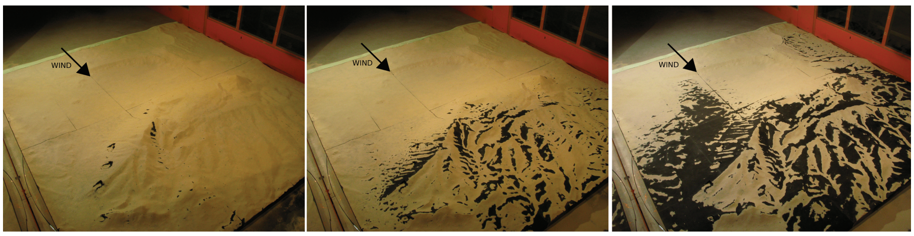

Figure 5.33.: Example of a model at the beginning of the test (left) after 1 min at 6 m/s (middle) and after 1 minute at 7 m/s (right).

When the quantitative estimation is applied, the FSR map gives an estimation of the high wind locations (in red in figure 5.34). As expected, two zones are predominant, the first and the second hill tops (near position P4 and P6).

The sand erosion is a very useful qualitative tool for highlighting the high wind potential areas ; an estimation of the speed-up is also possible. This technique

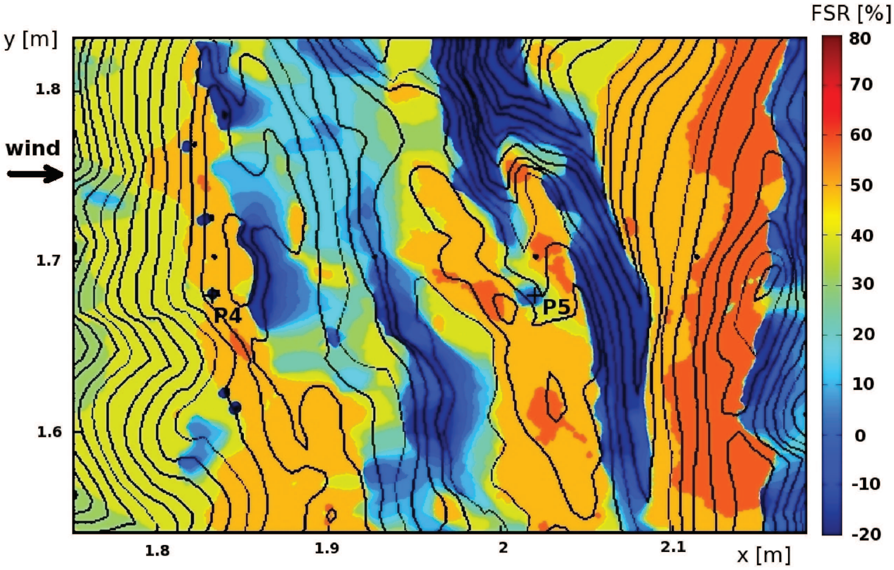

Figure 5.34.: Amplification factor map on Alaiz mountain, the dots are reference positions (masts). Axis are in meter at the wind tunnel scale (see figure 5.30)

allows the focusing of further advanced measurement techniques to interesting areas. The development and the implementation of this technique is detailed in Appendix C.

5.5.5. Flow over the Alaiz mountain

The behaviour of the flow over the Alaiz mountain is presented in figures 5.35 to 5.40. As expected, the mountain induces streamline convergence and velocity speed-up. This phenomena leads to a more homogeneous wind velocity profile at position $P4 = 4728000$m. After $P4$, the terrain reaches the *plateau* of the mountain and the velocity is decreasing. Then a second speed-up is observed at the second peak of the mountain next to the position $P6 = 4726000$m. The second peak is a little weaker.
The vertical velocity plot, figure 5.37, shows the high perturbation induced by the mountain. The two successive slopes of the wind side of the mountain, from $X = 4730000$ m to $X = 4729500$ m and from $X = 4729500$ m to $X = 4728000$ m are leading to vertical velocity maxima, short for the steeper slope and more extended for the second slope. At the top of the mountain, the vertical velocity is coming back to zero. At the mountain top ($P4$) it is almost back to horizontal, an angle of $+1.5°$ is recorded at 100 m a.g.l and $+2°$ at 200 m. The vertical velocity

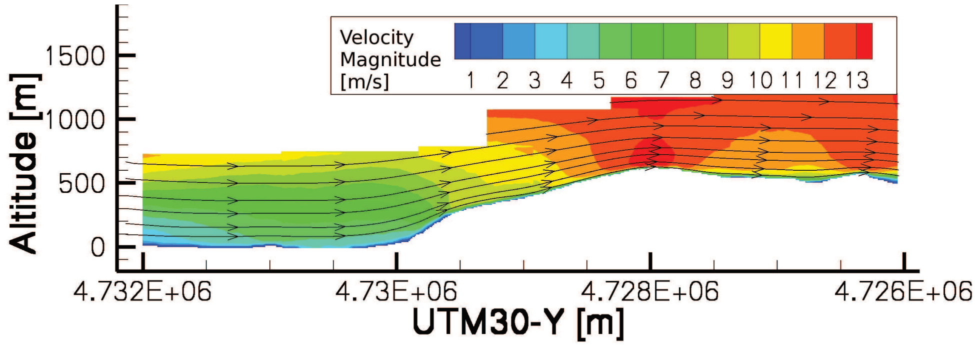

Figure 5.35.: Mean velocity magnitude field and velocity streamlines over Alaiz mountain at $Re = 110000$.

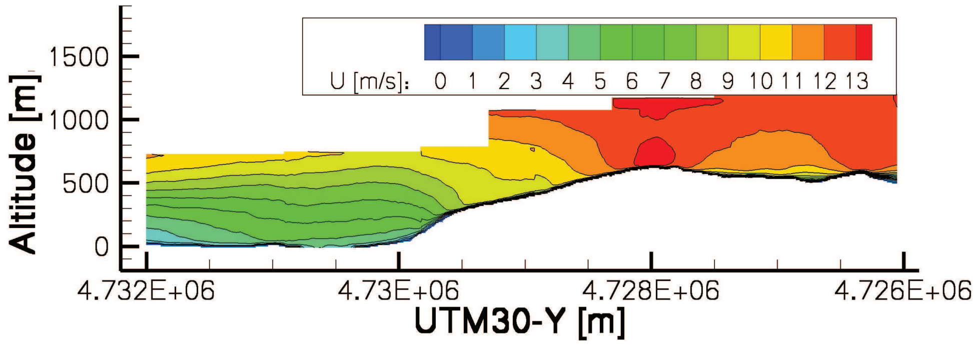

Figure 5.36.: Longitudinal velocity field over Alaiz terrain.

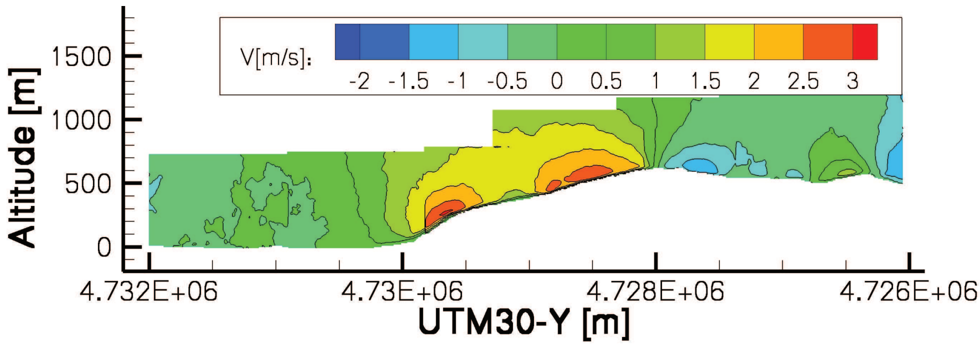

Figure 5.37.: Vertical velocity field over the Alaiz terrain.

is then negative in the *plateau* area. A second maxima is recorded at the second peak, near the position $P6$. The velocity vector inclination is also visible in figure

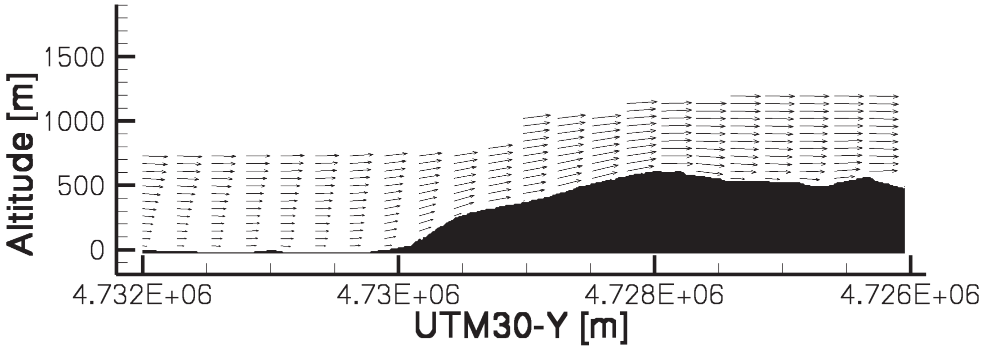

Figure 5.38.: Velocity vector field over Alaiz mountain at $Re = 110000$.

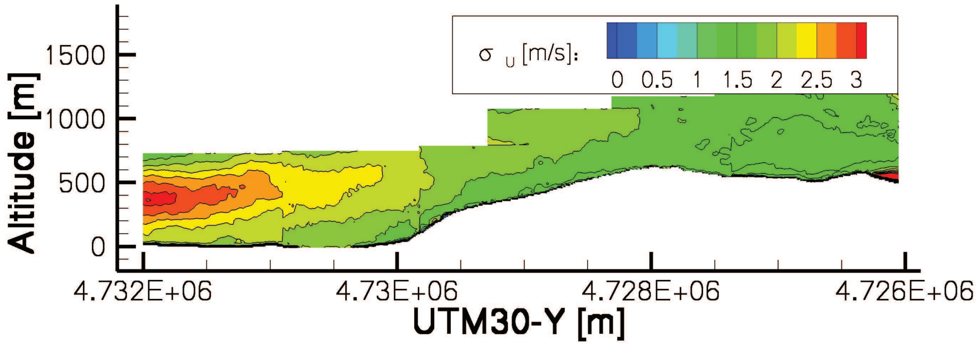

Figure 5.39.: Longitudinal velocity standard deviation field over Alaiz terrain.

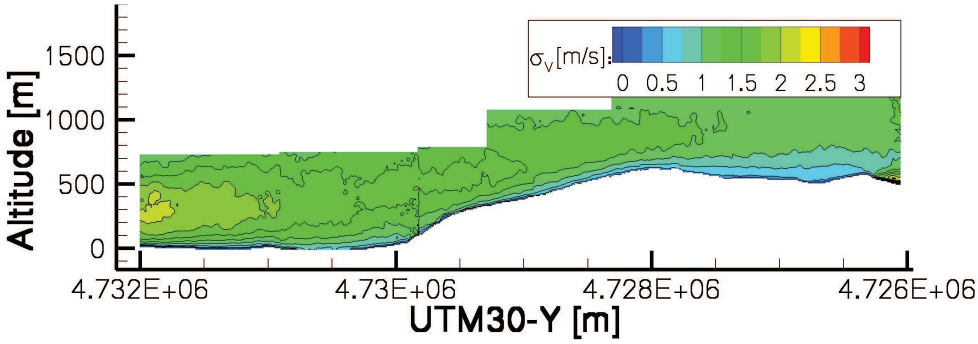

Figure 5.40.: Vertical velocity standard deviation field over the Alaiz terrain.

5.38 showing the velocity vector field.
On the same figure, before the mountain, around $X = 4732000$m, the velocity

is not presenting a ABL type profile, the velocity gradient is very steep. This resembles to a wake area like presented in figure 4.17 from chapter 4. At the same position, figure 5.39, presenting the standard deviation of the longitudinal velocity component, shows a peak of the standard deviation around an altitude of 350 m. Further downstream, the value is progressively deceasing. The observations support the hypothesis of the wake area coming from a separation region after the upstream *ridge* at $X = 4734000$ (not in the measurement area).
Contrary to the tests performed in chapter 4, the altitude of the maxima (350m)is higher than the *ridge* height ($h = 250$m). In [65], and in [27] the authors compare the wake of a bell shape and a triangle shape and finds that the recirculation after a triangle gives a stronger perturbation with a maximum velocity fluctuation situated higher that for the bell shape. The ridge has a triangle shape, therefore, it makes sense that the wake observed is higher than it could be expected from chapter 4.
From figure 5.39 and 5.40, the perturbation is still important at the mountain foot and even reaches its top. From the observations, the front *ridge* has an impact on the mountain situated $16h$ downstream. That supports the choice of including it in the test (see section 5.5.2).

5.5.6. Comparison of the measurement techniques

On the model, two kind of measurements are performed, Particle Image Velocimetry (PIV) and hot-wire anemometry with a single wire (HW). Figure 5.41 compares both techniques at the positions $P1$ and $P4$ with their respective error bars. Both techniques are giving very close results, at $P1$ there is 1% difference for average quantities and 2% for fluctuating quantities. The difference is of the same order of magnitude at $P4$.
The PIV technique is very useful to have a continuous dataset with the horizontal and vertical information. This is a non intrusive technique and a lot of information can be computed. A description of both techniques is presented in appendix A.

5.5.7. Comparison with field data

On the field, two instrumented masts are available near the position $P4$ (UTM30-X = 618 000m, UTM30-Y = 4 728 000m), the masts $MP5$ (UTM30-X = 618 240m, UTM30-Y = 4 728 189m) and $MP0$ (UTM30-X = 618 331m, UTM30-Y = 4 728 097m).
The data are provided by CENER from a 3 month period (March-June 2010) [69]. Five heights are available from 40 m to 120 m. Measurements are 10 min samples from cup anemometers and wind vanes, the data availability is 80% in this period. The ensemble average is performed for the North direction with a bin width of 10°. Measurements are filtered to have only neutral conditions, the hypothesis is to have $|Fr^{-1}| < 0.5$. All the filtering process leads to a high reduction of the number of samples, for mast $MP5$, 84 samples of 10 min are available.

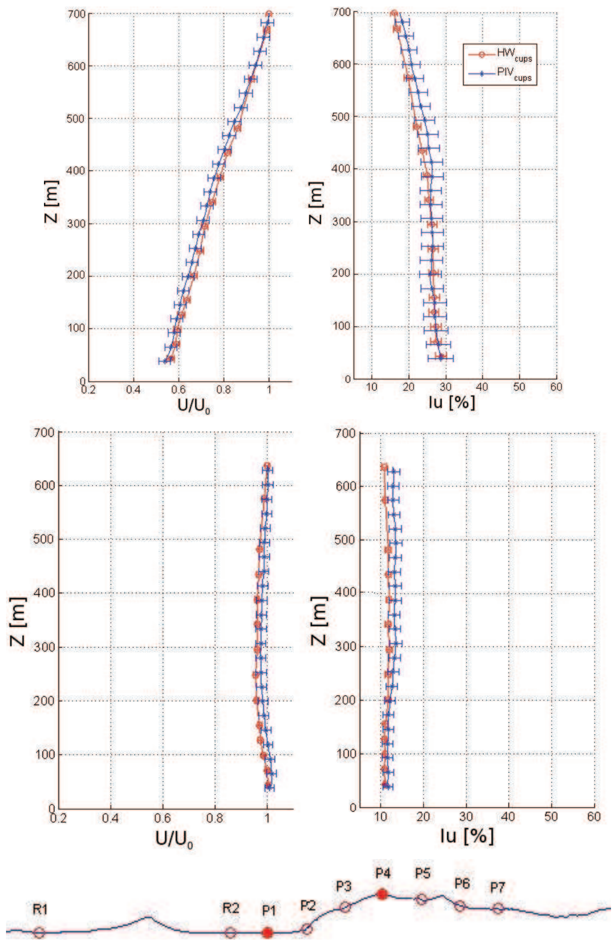

Figure 5.41.: Comparison of the normalized wind speed and the longitudinal turbulence intensity between PIV and HW profiles at positions $P1$ (top) and $P4$ (bottom). The reference speed U_0 is here defined at 100 m.

The error bars on the mast are computed from equation A.13 and A.14 in Annexe A.1.4. The question of the determination of the field measurement error is mentioned in section 5.3.1.
The experimental data are normalized at 120 m, at the same height as the field data.

Even if only profiles at almost the same position are available, the comparison between the wind tunnel measurements and the field gives satisfactory results.

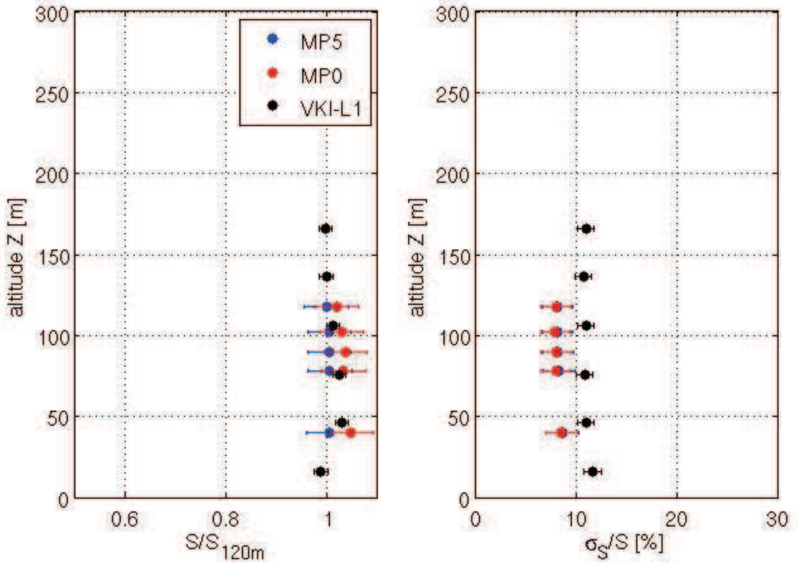

Figure 5.42.: Comparison of the velocity and turbulence profiles measured in the wind tunnel at position $P4$ with field data at $MP0$ and $MP5$.

The velocity profile from the wind tunnel falls between the two closest masts available for the comparison, in average, the experimental result is 1.7% above the $MP5$ mast and -1.5% below the $MP0$ velocity profile. The shape of the velocity profile is also very similar, the wind is almost constant with the altitude between 40 m and 160 m. The speed-up is here compensating the velocity gradient of a classical ABL profile. A slight increase of the speed is even recorded around 50 m altitude.

On the turbulent side, both field measurements and wind tunnel data are presenting a quasi constant turbulence level between 40 m and 160 m. A constant shift of around +2.6% turbulence intensity is recorded in the wind tunnel. Because no field measurement is available upstream the mountain, the shift may be due to a higher turbulence level simulated in the wind tunnel. Another explanation may be the overestimation of the effect of the ridge, in the wind tunnel, due to a Reynolds number effect, the ridge may present a stronger separation than in the field. Those hypothesis would need further measurements in the field, particularly of the inlet profile.

The velocity and turbulence intensity profiles at the position $P4$ are uniform between 40 m and 180 m and uniform. Theses conditions are very favourable for the installation of a 100 m hub height wind turbine because, in addition to the velocity speed-up and the turbulence intensity of 10 %, the turbine would be submitted to weak velocity and turbulence gradients.

5.5.8. Comparison with CFD computations

The comparison with mast measurement at one location ensures the right reproduction of the velocity profile, however, the velocity increase from the plain to the mountain's top is not verified. In absence of field data, a comparison of the experimental results is made against 2D and 3D CFD computations performed at VKI [63] and at CENER [17]. Both CFD simulations also include the front ridge. The 2D numerical simulation, realized using *OpenFoam*, is modelling, at the wind tunnel scale, a 2D profile of the Alaiz mountain corresponding to the measurement plane investigated experimentally (figure 5.30). The 2D simulation is justified by the fact that, from UTM30-X = 617 000 m to UTM30-X = 619 000 m, the mountain presents a nearly constant profile in the North-South direction.
The 3D simulation is performed using *CFDWind* from CENER using the same relief map as used for fabricating the wind tunnel mock-up. Figure 5.43 to 5.45 are presenting the velocity ratio $U/U_{R1}(90m) = \Delta U + 1$ from the two simulations and the experiment.
The overall distribution of the velocity ratio is very similar from one simulation to the other, however, some discrepancies can be noticed: the 2D simulation models higher speed-up than the experiment and the 3D CFD at tops of the mountain, around UTM30-X = 4 728 000 m and UTM30-X = 4 727 000 m. The velocity deficit upstream the hill is also lower.

To compare easily the simulations, the FSR ΔU at the height of a typical turbine, 90 m, is plotted in figure 5.46. The comparison metric (appendix B) is computed to quantify the difference between the simulations. The reference speed is the velocity at $R1$, at 90 m. For the FSR at 90 m, the three simulations are giving very similar results, the average correlation coefficient is close to 95 %. The two numerical simulations are also modelling the flow around the front *ridge*. The FSR is rising in the upwind slope of the *ridge* and suddenly drops in the downwind slope, down to around -40%. The two simulations are not reaching the same maximum at $X \approx 4728000$m, the 2D CFD finds a higher value (+20%) of the speed-up and the 3D CFD a lower value of the speed-down (-25%). The three dimensional nature of the ridge can explain this discrepancies, at the position of the 2D cut, the ridge is almost at its highest and sharpest point and the 2D simulation doesn't allow the flow to go around it leading to an over estimation of the speed-up. The higher speed down after the ridge of the 3D CFD case can be explained by the large scale shape of the ridge. Indeed, from wind tunnel observations of the flow behaviour around the ridge, it is likely that a side West wind is developing along the ridge and leading to an increase of the velocity drop and an increase of the turbulence level. The visualization of the side wind is presented in figure 5.47.

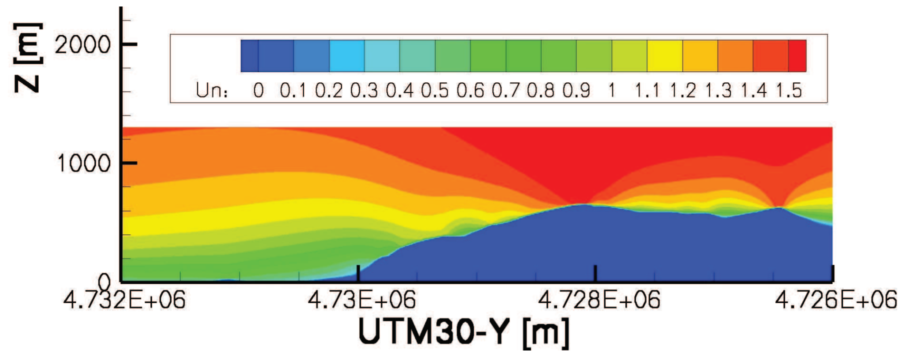

Figure 5.43.: Velocity ratio, $U/U_{R1}(90m)$, from the 2D CFD computation [63].

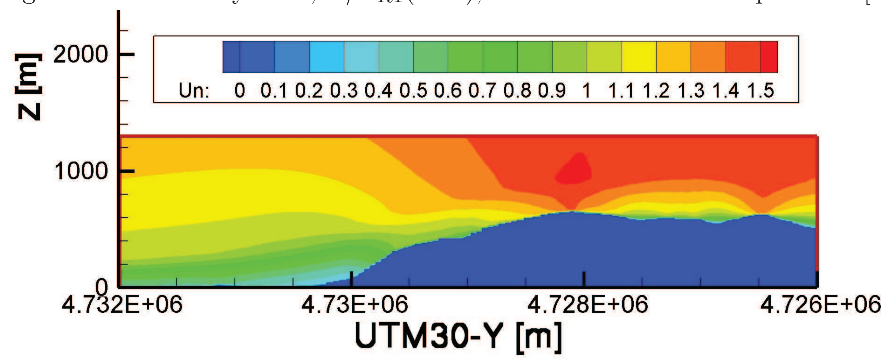

Figure 5.44.: Velocity ratio, $U/U_{R1}(90m)$, from the 3D CFD computation performed by CENER [17].

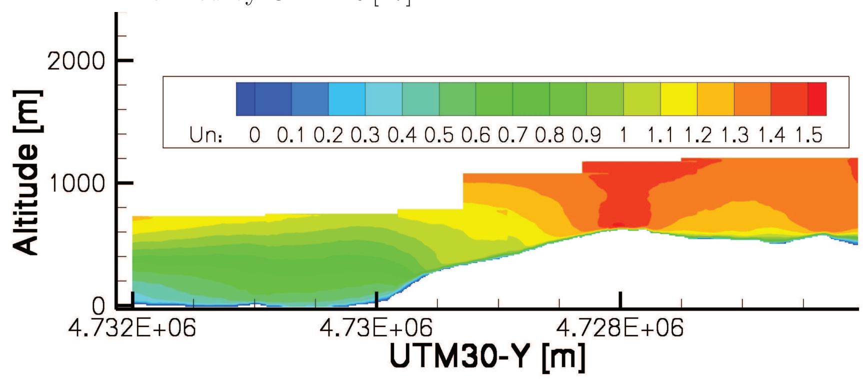

Figure 5.45.: Velocity ratio, $U/U_{R1}(90m)$, from VKI-L1 experiment.

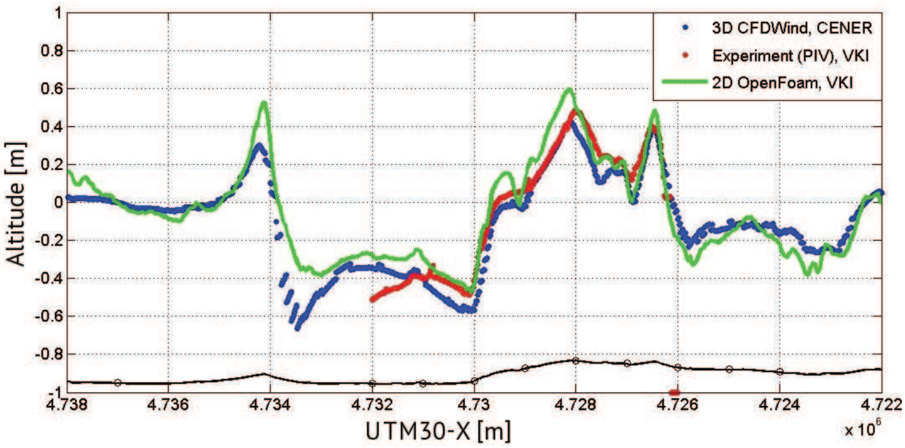

Figure 5.46.: Comparison of the FSR (ΔU) at 90 m by experiments and 2D and 3D CFD computations.

At the top of the hill, for the same reason as for the ridge, the 2D simulation found a higher speed-up: 60% instead of 42.5% for the 3D simulation and around 48% for the experiment. Along the mountain, the experimental result falls in between the two numerical simulations but closer to the 3D simulation. Details are plotted in figure 5.48 and quantitative value are presented in table 5.7. The bottom right plot of figure 5.48 gives the scatter plot of the entire common field between the experiment and the 3D CFD. Results are coherent but an important scatter of the data is observed. The average difference is nevertheless staying below 13%.

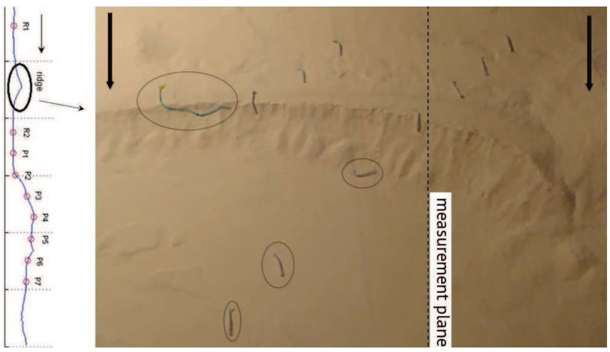

Figure 5.47.: 3D effect after the Alaiz front *ridge*, the North flow induces a secondary West flow blowing along the ridge. Visualization by tufts.

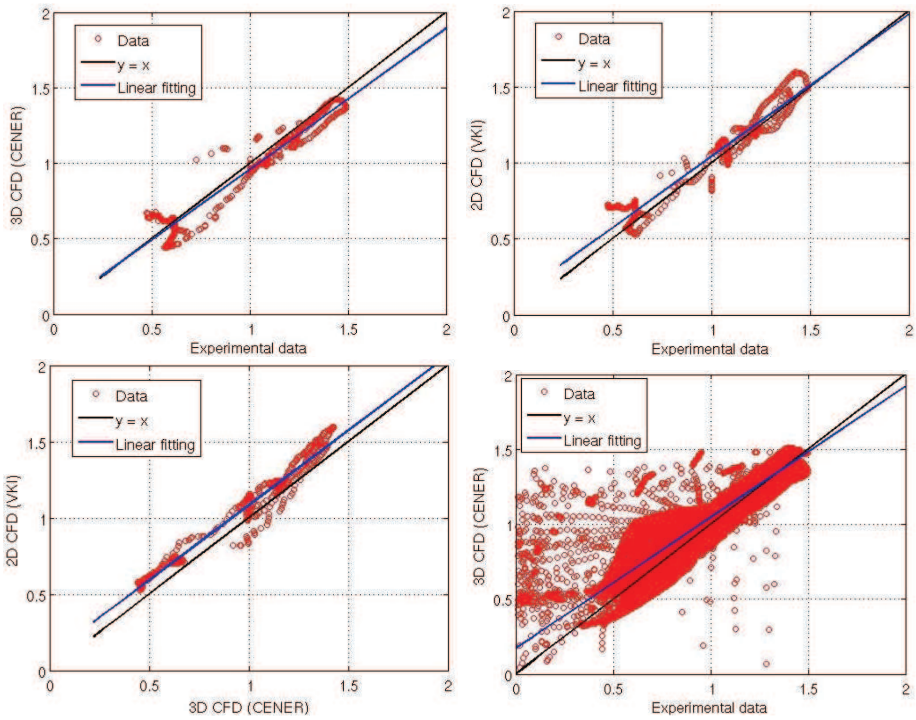

Figure 5.48.: Scatter plot for the comparison between experimental results and 2D and 3D CFD.

Comparison FSR	Exp / 3D CFD	Exp. / 2D CFD	Exp. / 3D CFD	Field	Perfect
Lin. coeff.	0.934	0.9360	0.982	0.875	1
Corr. coeff.	0.9662	0.965	0.9795	0.889	1
Frac. Bias	0.046	-0.042	-0.084	-0.038	0
N. Mean Sq. Err.	0.009	0.009	0.011	0.011	0
Geo. Mean	1.045	0.948	0.907	0.953	1
Geo. Variance	1.017	1.016	1.016	1.045	1
Avg Diff. [%]	9.8	9.3	11.8	12.7	0

Table 5.7.: Comparison between the wind tunnel experimental and CFD results for the FSR at 90 m and comparison between the 3D CFD and the experimental case on the common field.

The repartition of the difference between the experimental result and the 3D CFD is calculated by the equation,

$$Diff = \frac{FSR_{3D-CFD} - FSR_{EXP}}{FSR_{EXP}} \times 100 \tag{5.6}$$

and plotted in figure 5.49. The maximum difference is mainly in the *plain* between the ridge and the mountain, it is lower above the mountain. All over the distance, the maximum difference is at around 350 m above the local ground and decreasing with distance. The discrepancies are clearly coming from a different modelling of the ridge.

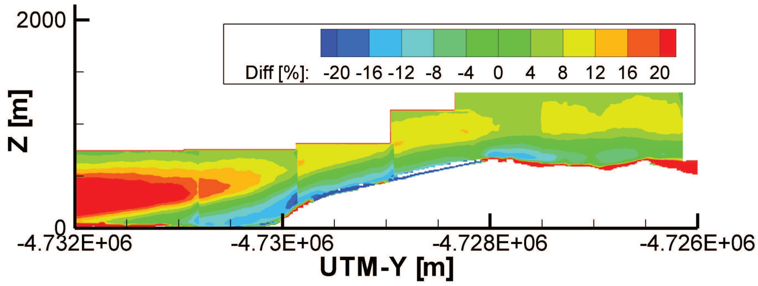

Figure 5.49.: Error plot of the discrepancy between the FSR from the experimental and from the numerical 3D simulations.

The flow around the Alaiz hill investigated in the VKI-L1 wind tunnel gives satisfactory results for the wind profile at its top (position $P4$), the speed-up falls between the two closest masts and the turbulence level is overestimated by 20% (3% in absolute value). A better knowledge of the real conditions may improve the results.
To estimate the relative influence of the inlet conditions and of the reproduction of the upstream *ridge* in the modelling, a parametric study is performed. This study, as in section 5.4, aims at pointing out the most important features to reproduce in the wind tunnel modelling.

5.6. Parametric study

To have an idea of the influence of the front *ridge* and the inlet flow conditions at the top of the Alaiz mountain, the goal is to change the position of the upstream *ridge* and to change the inlet wind profile in order to evaluate the effect at the mountain top. The parametric study is performed on a 2D model in the VKI-L2 wind tunnel (description in section 5.3.3). The choice of a 2D model is supported by the 2D CFD computation in section 5.5.8 that gives qualitatively acceptable results.

5.6.1. Experiments

In this study, a 2D shape of the Alaiz mountain extracted along UTM-Y = 6180 000m (figure 5.28) is tested in the VKI-L2 wind tunnel. The front *ridge* is simpli-

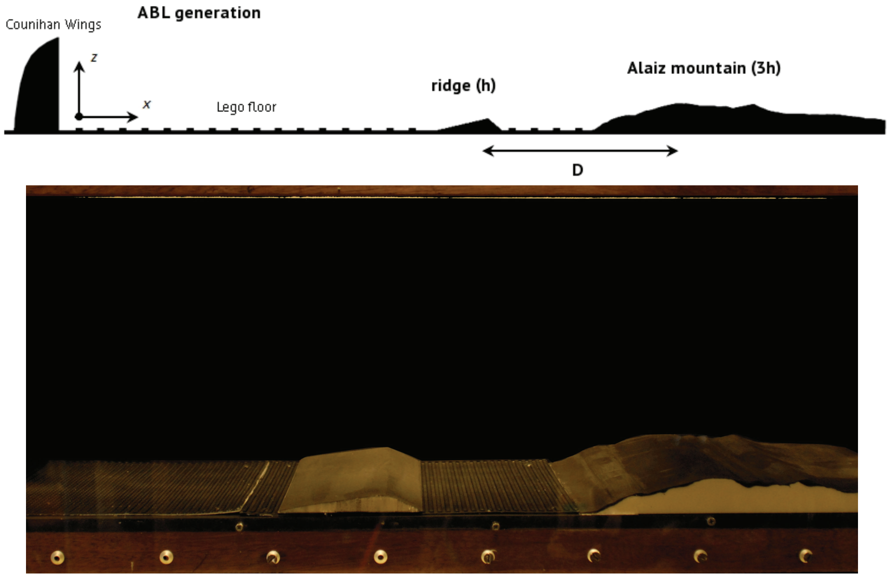

Figure 5.50.: Experimental set-up (top) and picture of the 2D model of Alaiz in the wind tunnel (bottom).

fied to a triangular shape and can be displaced from $D = 20h$ to $D = 90h$ with h the height of the *ridge* and D the distance between the *ridge* top and the mountain top (see figure 5.50). The original distance is $D = 24h$.
Giving the size of the test section (section 5.3.3), the scaling factor is set to approximately 1/19 000 to keep the blockage ratio below 10%. The mock-up is 33 mm high for the mountain and 13.5 mm for the *ridge*. The ratio between the *ridge* height and the mountain height is 2.5. The blockage in the test section is close to 9%, this is a limit value for the test but it can be acceptable for a parametric study. A schematic and a picture of the set-up are presented in figure 5.50. Tests are performed at $Re = 43000$, based on the mountain's height.
The model is two dimensional, the scaling factor is far from the academic range and the blockage ratio is high, however, the experimental set-up aims at performing a parametric study and the data gathered are expected to give, instead of a real quantification, an evaluation of the relative effect of the incoming BL and of the positioning of the upstream *ridge*.
Beside the high level of modelling, the FSR measured in the original configuration ($D = 24h$) compares well to the measurements performed in the VKI-L1 test section at 1/5357 scale (figure 5.51). The two speed-up maximum are well reproduced as well as the speed-down before the mountain. The wake of the ridge doesn't match with the 1/5357 scale. This may be a modelling effect of the *ridge*

that is approximated to sharp triangle and may induce a stronger flow separation. Additionally, the 2D state of the ridge may over estimate its real effect.

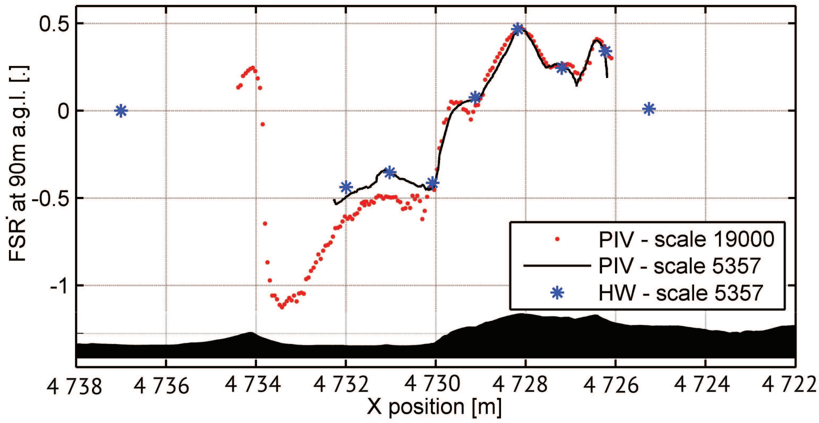

Figure 5.51.: FSR obtained over the Alaiz mountain from wind tunnel testing in VKI-L1 at 1/5357 scale and in VKI-L2 at 1/19 000 scale. The test performed in VKI-L2 wind tunnel uses the *Flate Plate* inlet conditions (FP).

In the parametric study detailed hereafter, the results focus only on the position $P4$ and its evolution with the change of inlet profile and of position of the upstream *ridge*. In all the parametric study, measurements are performed with PIV only at the position $P4$.

5.6.2. Influence of the distance of the ridge

To investigate its effect on the flow at the top of the mountain, the front *ridge* is displaced from $D = 20h$ to $D = 90h$. Figure 5.52 presents the velocity profile at the position $P4$ for the ridge at different positions and without the ridge. The velocity and turbulence intensity profiles are compared to the field data at masts $MP5$ and $MP0$ and to the VKI-L1 profile. All profiles are normalized by the velocity in the default configuration at 500 m.
As a first approach, it is clear that the ridge has an effect on the flow at the top of the mountain, at 100 m, it reduces the velocity profile by more than 4% in average and it increases the turbulence level by 55% in average (2% in absolute value) compared to the profile without the ridge. The velocity profiles with the ridge are very similar from one ridge position to the other, the scatter at 100 m is around 3%. At this height, the strongest influence of the ridge is found when it is the nearest to the mountain, at $D = 20h$, with 6% of velocity deficit. The

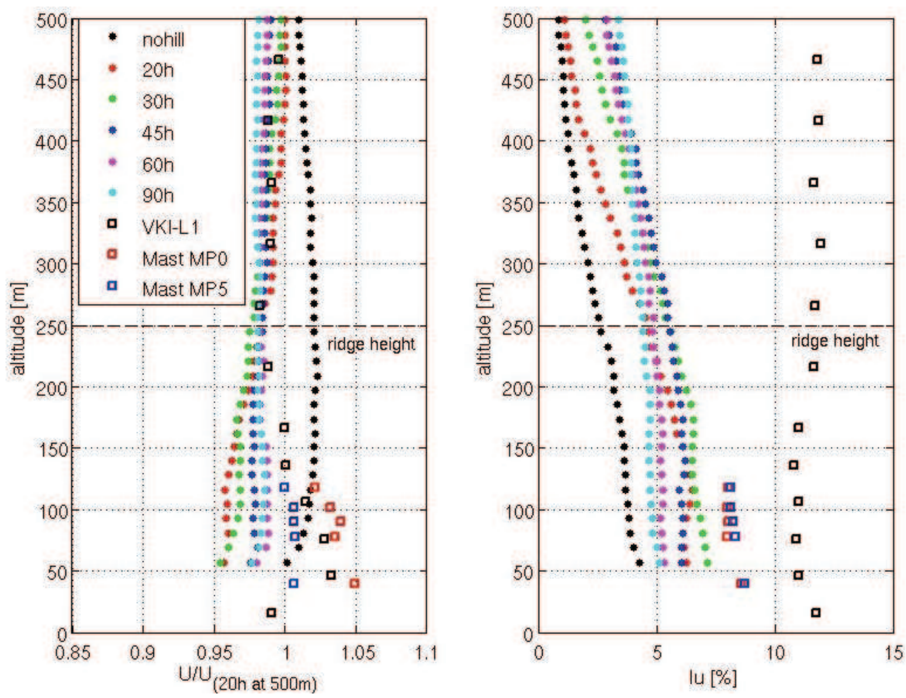

Figure 5.52.: Evolution of the velocity profile (left) and the longitudinal turbulence intensity (right) with increasing distance between the ridge and the mountain. Comparison with field data and experiment in VKI-L1 wind tunnel.

least influence is encountered for $D = 90h$ with 3% velocity deficit. As expected, the effect of the hill is weaker with increasing distance. Higher in altitude, the tendency is inverted, at 400 m, the higher velocity deficit is found for $D = 90h$ and the least velocity deficit for $D = 20h$. The limit is situated around 250 m, the height of the ridge.

At 100 m, the turbulence level is more dependent on the ridge position with 30% scatter. With no hill, the turbulence level is around 3.7%, and it reaches more than 6.5% for the two closest ridge positions, the turbulence level is almost doubling. Similarly to the velocity profiles, at a higher altitude the turbulence increase is inverted, a higher turbulence is found for the further distance.

This inversion phenomenon can be explained with diffusion and dissipation as described in chapter 4. At a height below the ridge, close to the ridge, the turbulence is the highest and then dissipates with distance following a 1/x law (section 4.6.5). Then, the further the ridge, the lower the turbulence and the lower the velocity deficit. Additionally to the dissipation process, the velocity deficit and the turbulence increase propagates to higher altitude. At a height above the ridge, the flow is not *seeing* the perturbation until it is diffused in altitude up to the given height. That gives a velocity deficit and a turbulence increase at a larger distance from the ridge. This is what happen over 250 m for the velocity profile and over 350 m for the turbulence intensity, the *ridge* effect is seen only after a large distance between the *ridge* and the mountain. Figure 4.29 in chapter 3 also enlighten this effect.

5.6.3. Influence of the inlet conditions

To assess the effect of the inlet conditions on the flow at the top of the mountain, three inlet conditions corresponding to different terrain roughness are tested by changing the BL generators. The *slightly rough* conditions are obtained with an empty test section (FP), the *moderately rough* conditions with a Lego floor (LF) and the *very rough conditions* with *Counihan wings* and a Lego floor (CW). The three BL are represented in figure 5.53.
A high scaling factor induces that the height of the viscous layer of the velocity profile in the wind tunnel can become significant when it is translated to the full scale height. In figure 5.53, the wind profile can be considered out of the viscous region above 50 m, results below that height are then not considered.

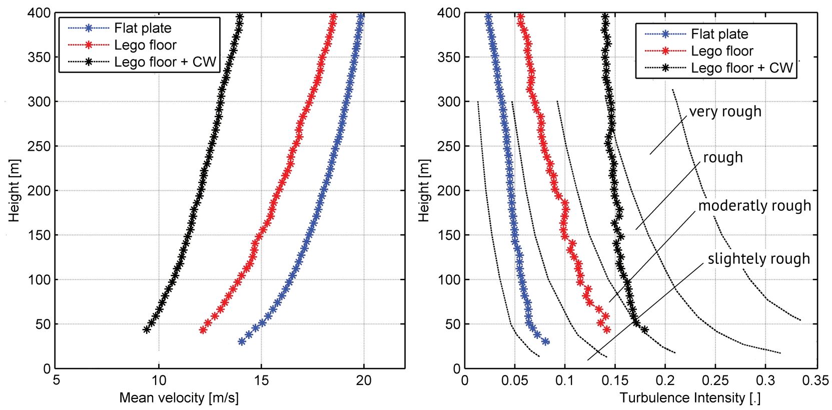

Figure 5.53.: Inlet profiles in the wind tunnel with VDI guidelines categories.

Figure 5.54 compares the FSR (ΔU) for the three inlet conditions. The reference position is taken at the position of the mountain but without any model. It is clear that the CW inlet condition (black) leads to higher speed-up ratio. At 100 m, the FSR is nearly 83% instead of 64% with the LF inlet profile and 40% with

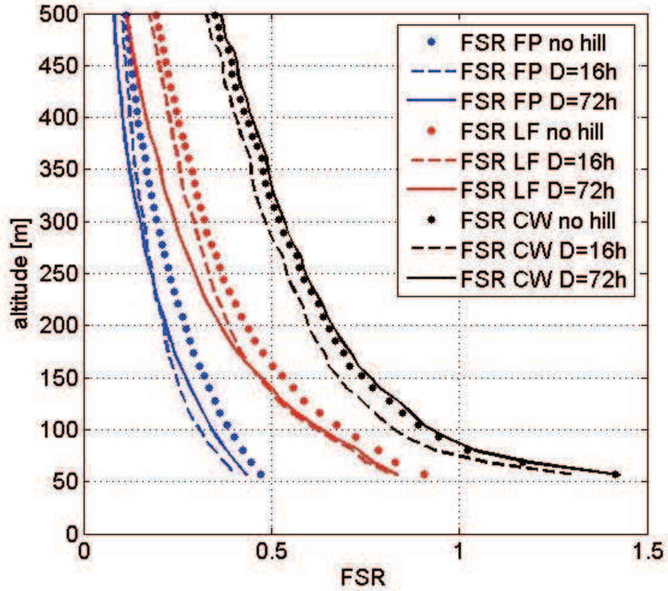

Figure 5.54.: FSR at the top of the mountain. Influence of the inlet conditions and of the position of the front ridge.

the FP inlet profile. Same thing at 400 m with 41% for the CW, 22% for the LF and 10% for the FP.
These observations are similar to the one made on the Bolund hill when changing the inlet profile (section 5.4.2), the most rough conditions give a higher speed-up ratio and the smoother inlet profile gives the lower speed-up.

On figure 5.54, the FSR is also plotted for the extremes ridge configurations: no ridge, $D = 16h$ and $D = 72h$. An influence of the ridge is visible but negligible compared to the influence of the inlet conditions. The ridge position is changing up to +10% the FSR but it remains very small compared to the difference between the inlet conditions, up to +50%.
In this study, the influence of the inlet conditions is by far more important compared to the position of the *ridge* to determine the FSR, table 5.8 summarises the results of the parametric study.

5.7. Conclusions

The two test cases studied in this chapter are different. The Bolund island is a very well instrumented hill with well defined boundary conditions and a small size

Configurations	Variation	FSR
Inlet profile	FP - LF - CW	50%
Ridge - mountain distance	16h - 72h	10%

Table 5.8.: Summary of the parametric study of the influence of the inlet conditions and the distance between the ridge and the mountain.

allowing to use an *academic* scale of 1/500. On the contrary, the Alaiz mountain is very extended and of a great complexity with only one area instrumented, unknown inflow conditions and complex surroundings leading to a scaling factor of more than 1/5 000. The Bolund hill is closer to an idealized test case and the Alaiz mountain is a *real* test case for wind turbine siting.
For both complex terrains, the comparison between the flow modelled in the wind tunnel and the measurements is giving results close to the available measurements for the velocity but more scatter is observed for the turbulence. For Bolund, the FSR is simulated with 8.8% difference in average but only one measurement point out of four has more than 4.5% of difference. The turbulence increase Δk is simulated with in average of 34% difference.
For the Alaiz test case, where only the wind profile at the top of the mountain is compared to field data, the velocity profile falls between the two nearest masts and the turbulence profile is overestimated by around 20%, that is only 3% in absolute value.

For both test cases, parametric studies are carried out in order to estimate which parameter is influencing the most the final result. For both studies, the reproduction of the inflow conditions appears to be affecting the most the final result. In the Bolund parametric study, the velocity and the turbulence profiles are affecting more the final result than the flow angle (+/- 15°), the Reynolds number and the reference height. In the Alaiz experiment, the inlet profiles are affecting more the flow at the mountain top than the position of the upstream ridge.
The two test cases are different but the conclusion is the same, the modelling of the inflow conditions is the main parameter that influences the velocity and the turbulence. Nevertheless, other parameters are affecting the flow field: the upstream topography that induces a velocity deficit and a turbulence increase depending on its distance from the main mountain, the flow angle that depends on the case geometry.

Chapter 6.

Conclusion and perspectives

6.1. Wind tunnel flow modelling in complex areas

In front of a complex site to assess, lots of parameters are to be considered, one of the goal of the work is to quantify them and to assess their importance. The main issues are on: the choice of the area to model around a site, the reproduction of the inflow conditions and the flow dependency on the Reynolds number. Secondary parameters like the effect of the averaging wind directions or the spatial accuracy of the measurement are also investigated.

The choice of the area around a site to model is especially of importance in the case of complex terrain. Indeed, the test section has limited dimensions and the choice of the area to model is a trade-off between having a large area to include the far surroundings that may affect the flow and keeping a reasonable scaling factor for a good flow reproduction.
This topic is tackled in the 4^{th} and 5^{th} chapters where a quantitative assessment of the downstream effect of a simple topography is performed on a simplified 2D model of the Alaiz mountain by testing different distances from the mountain to the ridge (see section 6.2).
The 3^{rd} chapter deals with the reproduction of the inflow conditions in the VKI wind tunnels. The BL generators used are a grid, a fence and roughness elements. Thanks to a parametric study, the intrinsic rule of each element is detailed. The fence height and the roughness element height are found to be the two main drivers compared to the number of fences, the roughness element density and the grid. The fence height determines the height of the boundary layer and sets the turbulence level in its upper part. The roughness element height affects the lower part of the BL by controlling the aerodynamic roughness length z_0 and the near wall turbulence. Both tools have to be combined to find the best fit to a known BL.

Two parametric studies are performed to assess the relative importance of the different parameters cited. On the Bolund hill, parametric studies are performed on the inflow conditions, the Reynolds number, the flow angle and the precision of the reference height. The goal is to quantify the effect of each parameter on the FSR and the turbulence increase. the most important for the modelling. The conclusion is that the change of the inflow conditions, although small, has the most important effect on the FSR. The second in the ranking, is the flow angle. This latter effect is case dependent as the geometry changes with the angle. Then, the Reynolds number is the next important parameter to take into account. The reference height has the least impact.

The conclusion of the first parametric test is confirmed by the parametric study of the Alaiz mountain. In this parametric study, a 2D model of the Alaiz mountain is tested with varying inflow conditions and different positions of the upstream *ridge*. In this test as well, the FSR is more influenced by the inflow conditions than by the location of the front *ridge*.

To summarise, the reproduction of the inlet conditions is found to have the most important influence on the speed-up on a complex terrain. The effect of an upstream topography can be estimated thanks to the work of chapter 4 that also helps the experimentalist in choosing the area to model.
For going further, a deeper systematic investigation could be set up to estimate the influence of each parameter of the ABL: BL height, turbulence level, velocity profile on the flow modelling. CFD would be a complementary tool to multiply the range of investigation after validating it against the already available wind tunnel test cases.

6.2. Wind turbines near complex topography

Hills, mountains or cliffs are creating higher winds that can be beneficial for wind turbines. As a consequence, wind turbines tend to be more and more placed in complex terrains. However complex topography implies complex flows, including recirculations and wakes. Moreover, a nearby hill can influence the local wind and affect the available wind power. This work quantifies the effect a single hill has on its near and far flow-field at a neutral stability of the ABL. This is of interest for a wise siting of wind turbines near hills.

In the 4^{th} chapter of this work, the flow around simple geometries is studied experimentally with 2D models of a simplified hill. The near and far influence of the hill is measured using PIV up to 50 times the hill height. The hill is a bell shape from ERCOFTAC. Different aspect ratios are tested and ERCOFTAC data are added to complete the experimental work.
Two types of hills are distinguished, the *low* hill (slope $< 15°$), and the *steep* hill (slope $> 18°$). Both types of hills present a velocity deficit and a turbulence increase that is visible up to tens of times the hill height. The distinction is justified by the difference in the nature of the wake. For a hill with a slope over 18°, a recirculation and a vortex shedding are present. That leads to a very high perturbation in the lee side of the hill much stronger than for the cases without flow separation.

The perturbed area is defined by the velocity speed-up ratio $\Delta S < -0.05$ for the mean velocity speed-up and by $Iu_w > 0.05$ for the turbulence. Its longitudinal and vertical extensions are defined as l_w and h_w respectively.
For *low* hills, l_w/H is increasing linearly with the L/H ratio (H is the hill height and L the hill *half* length and a steep slope is equivalent to a low L/H ratio). A conservative parameter is found to be $l_w = 2L$. The vertical extension of the wake is much smaller, below $h_w/H = 1.7$. It is also increasing with L/H (H the height of the hill). For *steep* hills, h_w is decreasing with L/H. An approximate coefficient of decrease is 5. The vertical extension of the wake is of the same order as for the *low* hill but it is decreasing with increasing L/H.
In general, the turbulence increase remains longer after the hill than the velocity deficit. At a given height, a x^{-1} function describes the turbulence decay over the distance.

In addition to the speed-up ratio that is commonly presented in the literature, this study also proposes to enlighten the unfavourable positioning of a wind turbine near a hill: before l_w and below h_w.

This study can be further completed with more hill shapes and the parameters influencing the wake extension can be determined and quantified: the initial turbulence level, boundary layer height...
In addition to guidelines giving the speed-up at a hill top, it can be useful for many applications to define guidelines for wakes. Although this task may be very demanding due to the complexity of wake flows.

6.3. Validation of the use of the wind tunnel approach

Another goal of the study is the validation of the use of wind tunnels for wind resource assessment.
In chapter 3, two VKI wind tunnels are deeply investigated for verifying the reliability and suitability to reproduce atmospheric flows. The requirements are verified one by one and quantified. The flow properties simulated are then successfully compared to field atmospheric data.

In the last chapter, two test campaigns on a complex hill (Bolund) and a very complex mountain (Alaiz) are performed and results are compared to available field data. The FSR is measured over the Bolund hill and matches the field data by 8% in average but in most of the measurements by less than 5%. This is a good result according to the results of the Bolund blind comparison that compares all kind of simulations. On the other side more scatter, up to 100% is find for the turbulence increase. Difficulties to properly model turbulence is also experienced in CFD.

In the Alaiz comparison between wind tunnel and field data, only field mast profiles are available but the wind tunnel measurement fall in between the velocity profile of the two nearest mast positions. The turbulence profile is very similar to the field measurements but results are shifted due to a higher prediction of the turbulence level in the wind tunnel.

The experiments performed for Bolund and Alaiz are giving good quality results (5-10%) for the prediction of the velocity. More work has to be performed to succeed in reproducing the right turbulence level. The study of the precise rule of the inlet conditions like the boundary layer height or the inlet turbulence quantities may give more information.
The test on the Alaiz mountain at 1/5300 scale proves the possibility to use high scaling factors. The test of the Bolund hill at 1/500 scale in a 0.35 x 0.35 x 2 m proves that correct and reliable experimentation can be carried out in a small wind tunnel. The test of the 1/19 000 scale tends to say that extreme scaling can still give qualitative informations for the velocity.
The understanding of the effect of the scaling factor, especially on the turbulence intensity, can be a subject for further studies. CFD computation can be a useful tool to further understand the effect of the scaling in the wind tunnel.

The comparison of the Alaiz results with more field data would be an additional validation of the wind tunnel technique. The measurement of the real inflow conditions will improve the reliability of the simulation. For a more detailed validation, the ideal would be to have field campaign based on Lidar measurements, like that, full wind profiles with three dimensional velocity and turbulent components can be compared.

Compared to the other approaches, wind tunnel modelling proves to be a reliable, rather inexpensive and versatile tool for the assessment of the wind resource in complex terrain.

Appendix A.

Measurement techniques and error analysis

This appendix describes the measurement techniques used during this work. Two main techniques are used to measure the flow in the wind tunnels: the hot-wire anemometry and the Particle Image Velocimetry (PIV). Both techniques are very common in fluid dynamics.

A.1. Particle Image Velocimetry

In different sections of the manuscript, the Particle Image Velocimetry (PIV) technique is used to measure the velocity field. Measurements are always carried out in a vertical plane using *2D2C-PIV* where the vertical and horizontal displacements are measured in a vertical 2D plane. The instantaneous informations are averaged over 500 or 1 000 images allowing to compute statistics like the average or the standard deviation of the velocity components.
The technique, emerged in the late 80's is now very commonly used for a large field of activity in fluid mechanics [67, 83]

A.1.1. Measurement Principle

The principle of the technique is to measure the displacement of particles tracers in a fluid by taking two successive pictures of the flow at two instants. The amplitude and the direction of the velocity vector can be computed simply by estimating the displacement in pixels d of the particles tracers from an image to the other: $U = d.M/t$. t is the separation time between the two frames and M the magnification factor of the image [mm/px].
The particles injected in the air are oil droplets with a typical diameter of 2 μm. A laser is used to provide a very short and bright light flash to "freeze" the particles. Optics are settled after the laser to produce a thin laser sheet. The laser sheet is then carefully aligned with the desired plane to measure in the area of interest. The alignment of the laser plane and its thickness have a direct impact on the precision of the measurement. For those measurements, a single camera is synchronised with the laser to take two images separated by t, typically a hundred micro-second. The area of interest is painted mat black and environment light is avoided to prevent spurious light in the frames of the camera. The PIV system is set to take couples of images at a repetition rate of 3 Hz. This is not enough

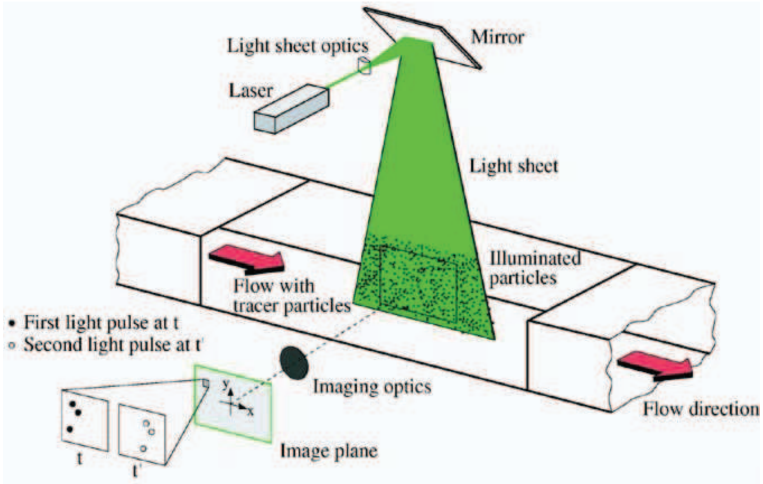

Figure A.1.: Principle of PIV. Image from [83]

to have time-resolved information. However, couples of images are statistically independents (separated by more than two times the integral time scale) so all frames can be used to calculate the time average flow.

A.1.2. Image processing

Each couple of image, separated by t, is processed to find the velocity field. For this, the images are divided in interrogation windows and a cross-correlation function is applied to each couple of windows to determine its statistical mean displacement. The interrogation windows number and size is determining the spatial resolution of the measurement, the smaller the window, the better the spatial resolution. However, to have a good correlation between the two images, most of the particles should remain from one image to the other. It is commonly accepted that the interrogation window should be at least four times the mean displacement (1/4 rule) in such a way that at least 75% of the particles remain in the second frame.

This rule is quite restrictive for the resolution, a way to overcome it is to apply so-called refinement steps: a first cross-correlation is applied following the 1/4 rule to determine the average velocity of the window. Then, a second correlation is performed after removing the mean displacement calculated in the first step. The remaining displacement being very small, the window can be refined several times, improving a lot the resolution.

The next restriction to increase the spatial resolution is due to the fact that the

cross-correlation is a statistical operation, then, a minimum number of particles has to be present in each window. It is commonly accepted that at least 10 particles should be present to apply the cross-correlation function.
To increase again the spatial resolution, an overlapping procedure can be applied to the last refinement step. It consists in multiplying for example by 4 the number of windows by overlapping them by half in the two directions instead of having them side-to-side.
All the processing of the images is performed with an in-house code (WIDIM) [70].

Before the processing, the images are pre-processed to improve the contrast and to remove spirituous light reflection by subtracting the mean image containing the background information from every single image, the correlation peak is greatly improved.

All instantaneous velocity fields computed can be averaged to have the time-averaged velocity field and statistics can be performed on the dataset.
In most of the experiments in this work, a series of successive planes is necessary to measure the flow over the entire area of interest. In this case, the fields are joined to each other after the time average is computed. Instantaneously, two joined images are not time correlated.

A.1.3. Estimation of differential quantities

From the instantaneous information, quantities can be computed such as the vorticity or the vortex detection criteria λ_2 [46].
The vorticity ω_Y, in the transversal direction, is defined by the curl (vector operator) of the velocity in the plane and detects high rotation area, a positive value means counter-clockwise vortex and a negative value clockwise vortex:

$$\omega_Y = \frac{dW}{dX} - \frac{dU}{dZ} \tag{A.1}$$

The vorticity, ω_Y, doesn't distinguish between a vortex and a shear layer, therefore, the λ_2 criteria is used to find vortex centres:

$$\lambda_2 = \frac{dU}{dX}^2 - 4\left(\frac{dU}{dX}\frac{dW}{dZ} - \frac{dU}{dZ}\frac{dW}{dX}\right) \tag{A.2}$$

The derivative along the X-axis of the function f with uniform ΔX intervals is defined at the i position as:

$$\left(\frac{df}{dX}\right)_i = \frac{2f_{i+2} + f_{i+1} - f_{i-1} - 2f_{i-2}}{10\Delta X} \tag{A.3}$$

A.1.4. Error analysis of the PIV technique

Like for the HW error, two types of errors are distinguished. The systematic error reveals the error made for every measurement, it is coming from the measurement bias: calibration, acquisition chain... The second error is the random error, due to the variability of the phenomena.
Then the total error is defined by the equation:

$$\epsilon_{tot} = \sqrt{\epsilon_{bias}{}^2 + \epsilon_{rand}{}^2} \tag{A.4}$$

The bias error

In PIV measurements, the bias error is coming from the different steps leading to the determination of the velocity:

$$U = \frac{M \times d}{t} \tag{A.5}$$

The bias error on the velocity can be written as

$$\epsilon_{bias} = \frac{\Delta U}{U} = \sqrt{\left(\frac{\Delta M}{M}\right)^2 + \left(\frac{\Delta d}{d}\right)^2 + \left(\frac{\Delta t}{t}\right)^2} \tag{A.6}$$

The magnification factor M is giving the size, in mm of a pixel to find the displacement in m, it is computed by:

$$M = \frac{\cos\theta_1 \times L_{mm}}{L_{pxl}} \tag{A.7}$$

with θ the angle between the calibration plane and the laser plane, L_{mm} the reference length of the calibration plate in mm and L_{pxl} the size in pixels of the reference length seen by the camera. The reference length is a distance between two reference points on the target. The target is a chessboard, this allows to have 1 pixel precision in determining the length in pixels (no line thickness). The error in the angle is converted to an error in the length due to the cosine: $\frac{\Delta L_{\theta_1}}{L_{\theta_1}}$, then we have,

$$\frac{\Delta M}{M} = \sqrt{\left(\frac{\Delta L_{mm}}{L_{mm}}\right)^2 + \left(\frac{\Delta L_{pxl}}{L_{pxl}}\right)^2 + \left(\frac{\Delta L_{\theta_1}}{L_{\theta_1}}\right)^2} \tag{A.8}$$

the angle θ_1 is supposed to be $0°$, a fluctuation of $\pm 2°$ is applied, converted to a distance it gives $\Delta L_{\theta_1} = 1.2 \times 10^{-3}$. Thanks to the chess board, $\Delta L_{pxl} \approx 1$ pixel and $\Delta L_{mm} \approx 1$ mm. The longer the length for the calculation of M the more precise will be the measurement. We have $L_{mm} \approx 100$mm and $L_{pxl} \approx 1000$. That gives, $\frac{\Delta M}{M} = 5.5 \times 10^{-3}$.

The separation time t is set around $t = 150\mu s$ with a *Standford* trigger precise at $\Delta t \approx \pm 1\mu s$. Then we have, $\Delta t/t = 6.67 \times 10^{-3}$.

The real displacement d of the particles can be different than the one measured by the camera x because it can be affected by a misalignment of the camera that should be at 90° of the measurement axis: $d = x/\cos\theta_2$, then,

$$\frac{\Delta d}{d} = \sqrt{\left(\frac{\Delta x}{x}\right)^2 + \left(\frac{\Delta L_{\theta_2}}{L_{\theta_2}}\right)^2} \tag{A.9}$$

A variation of $\pm 2°$ is applied and gives, $\Delta L_{\theta_2} = 1.2 \times 10^{-3}$. The error Δx is coming from the uncertainty of the processing software, from [70], it is around 0.1 pixel. The typical displacement in the free-stream is 8 pixels. Then we have $\Delta x/x = 0.0125$ and $\Delta L_{\theta_2}/L_{\theta_2} = 1.2 \times 10^{-3}$.

In total the bias error of the PIV measurements in the free-stream is,

$$\begin{aligned}
\frac{\Delta U}{U} &= \sqrt{\left(\frac{\Delta L_{mm}}{L_{mm}}\right)^2 + \left(\frac{\Delta L_{pxl}}{L_{pxl}}\right)^2 + \left(\frac{\Delta L_{\theta_1}}{L_{\theta_1}}\right)^2 + \left(\frac{\Delta x}{x}\right)^2} \\
&\overline{+\left(\frac{\Delta L_{\theta_2}}{L_{\theta_2}}\right)^2 + \left(\frac{\Delta t}{t}\right)^2} \\
&= \sqrt{(5 \times 10^{-3})^2 + (2 \times 10^{-3})^2 + (1.2 \times 10^{-3})^2 + (12.5 \times 10^{-3})^2} \\
&\overline{+ (1.2 \times 10^{-3})^2 + (6.67 \times 10^{-3})^2} \\
&= 0.01525 \\
&\approx 1.52\%
\end{aligned} \tag{A.10}$$

Like described, the bias error is function of the displacement between two images d (equation A.9), then the error due to the displacement can be written in function of the velocity:

$$\frac{\Delta x}{x} = \frac{\Delta x}{U \times t}.M \tag{A.11}$$

therefore, the velocity error can also be expressed in function of the velocity:

$$\frac{\Delta U}{U} = \sqrt{A + \left(\frac{B}{U}\right)^2} \tag{A.12}$$

with A and B constants: A contains all sources of error except from the displacement ($A = 7.64 \times 10^{-5}$) and B depends on the configuration used. An example is given in figure A.2 with typical values: $M = 0.1mm/pxl$, and $t = 100\mu s$. The bias error gives the error of the instantaneous flow field.

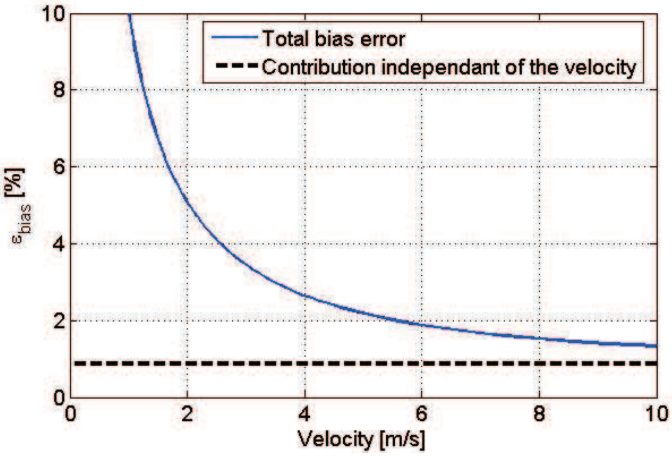

Figure A.2.: Example of the evolution of the bias error in function of the local speed (equation A.12).

The random error

The random error is not very linked to the measurement set-up but more to the variation of the phenomena. For a given flow, the statistical error can be reduced only by increasing the number of sample.
Each instantaneous PIV measurement is a snapshot of the flow at one moment, but from an instant to another, the characteristics of the flow varies (turbulence). The assumption is made that the variability of the flow at a given point is following a Gaussian distribution, then, an important number of image is necessary to converge to the average value. The random error is always an association of an error interval and a confidence level. The calculation of the random error follows mathematical rules. We have for a mean information μ:

$$\begin{aligned} \epsilon_\mu &= \frac{z_{\alpha/2}\sigma_\mu}{\mu\sqrt{N}} \\ &= \frac{z_{\alpha/2}I_\mu}{\sqrt{N}} \end{aligned} \tag{A.13}$$

with I_μ the local turbulence level, $z_{\alpha/2}$ a setting for the confidence level desired (table A.1) and N the number of independent samples recorded. Samples are independent if the time between them is more than 2 times the characteristic time of the flow. For the PIV set-up used in this work, at 3 Hz, this is always the case.

The random error of the mean value depends on the standard deviation (the turbulence level) of the variable, the error increases with increasing turbulence level.

At the contrary, the random error on the standard deviation depends only on the number of samples:

$$\epsilon_\sigma = \frac{z_{\alpha/2}}{\sqrt{N}} \tag{A.14}$$

The $z_{\alpha/2}$ coefficient depends on the confidence level desired, table A.1 gives the values associated to the confidence levels.

$z_{\alpha/2}$	Confidence level [%]
1.65	90
1.96	95
2.33	98
2.57	99

Table A.1.: The $z_{\alpha/2}$ associated to the confidence levels.

Summary of the PIV errors in the work

Here are summarized all the PIV experiments with the associated error A.2. The confidence level is set to 95%, the bias error is given for the free-stream and the random error for the highest standard deviation value.

Configuration	# of images	M [mm/pxl]	t [ms]	ϵ_{bias}	ϵ_{Rand_μ}	ϵ_{rand_σ}
Ch.3 - VKI-L2 ABL	500	0.1960	0.0784	1.8%	1.58%	8.7%
Ch.4 - VKI-L2	1 000	0.109	0.057	2.2%	1.55%	6.2%
Ch.5 - VKI-L1 Alaiz	500	0.2232	0.119	1.6%	2.19%	8.7%
Ch.5 - VKI-L2 Alaiz	500	0.1960	0.	1.8%	1.75%	8.7%
Ch.5 - VKI-L2 Bolund	1 000	0.122	0.065	2.0%	1.24%	6.2%

Table A.2.: Random and bias error on the PIV experiments, confidence level is set to 95%.

A.2. Hot-wire anemometry

The hot-wire anemometry is a very mature technique that had a second birth with the rise of PC and acquisition systems. It is a key tool daily used by experimentalists for the measurement of all kind of flows. The principle is to heat at a constant temperature a very thin wire hold between two supports. When it blows, the wind is cooling down the wire and a higher tension is needed to maintain the wire at a given temperature (often around 170°). To measure the wind velocity, a careful calibration is performed to link the wind velocity to the tension supplied to the wire to maintain its temperature.
The probe has a very short response time, this is its main advantage, the frequency response can typically be more than 50 kHz, this is a great advantage for studying high frequency turbulence. The technique also has some drawbacks, it depends on the air temperature, it is fragile (5-9 μm wire) and it is a punctual and intrusive technique.

A.2.1. Single hot-wire probe

For a single wire probe placed in a flow, the wire is cooled down by the flow velocity coming from all directions, it is called the effective cooling velocity U_{eff}. U_{eff} is related to the three velocity components relative to the probe: normal (aligned with the support), tangential (aligned with the wire), and bi-normal, that gives the Jørgensen law [49]:

$$U_{eff}{}^2 = U_N{}^2 + h^2.U_B{}^2 + k^2.U_T{}^2 \tag{A.15}$$

with U_N the velocity component aligned to the probe, U_T the velocity component aligned to the wire with k the yaw angle coefficient, usually around $k = 0.1$, and U_B the third velocity component normal to the two other wires with h the pitch angle coefficient, usually around $h = 1.1$ (Figure A.3).
For the calibration, the probe is placed in the core of a low-turbulent and uniform jet created by a nozzle and controlled by pressure difference. The output voltage of the probe is recorded as function of the velocity in the core of the jet. Because the hot-wire is very sensible at very low speed, several point have to be recorded in the lower part of the velocity range desired, that prevents interpolation problems when fitting the calibration to a high order polynomial.
The calibration curve is fitted with a 4^{th} degree polynomial function. This relation is the used to convert the instantaneous voltage measured to instantaneous wind velocity (Figure A.3).

When using a single-wire hot-wire, the component measured is not only the longitudinal one, but a combination of the three components (Eq. A.15).
This is not enough for the determination of the three components of the velocity necessary for a deep characterization of the flow, three equations are necessary to solve equation A.15. For this, a triple hot-wire probe can be used.

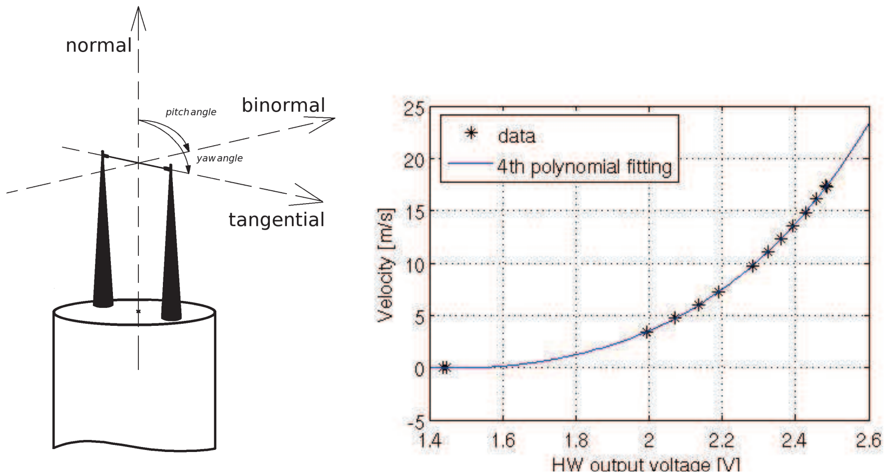

Figure A.3.: View of a single wire hot-wire (left). Example of a 4^{th} order polynomial fitting on calibration data (right).

A.2.2. Three component hot-wire probe

The characterization of the inlet wind profile modelled in the wind tunnel requires to record the three components of the velocity. The triple hot-wire, here a Dantec 55P91 [48], is suitable for these turbulent measurements.

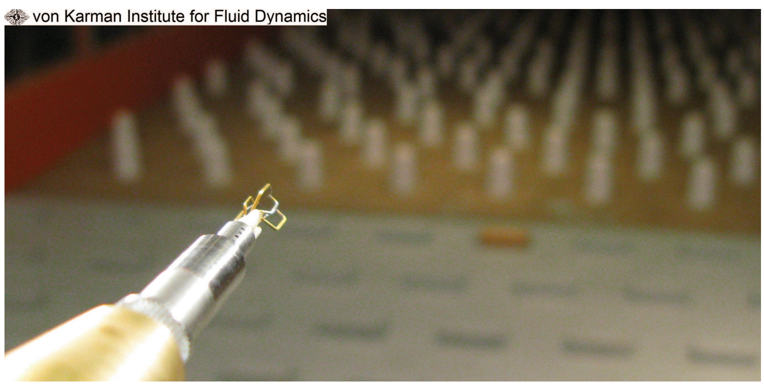

Figure A.4.: Picture of the 3C HWA probe measuring the ABL in L1 test section.

A.2.2.1. Description of the triple wire probe

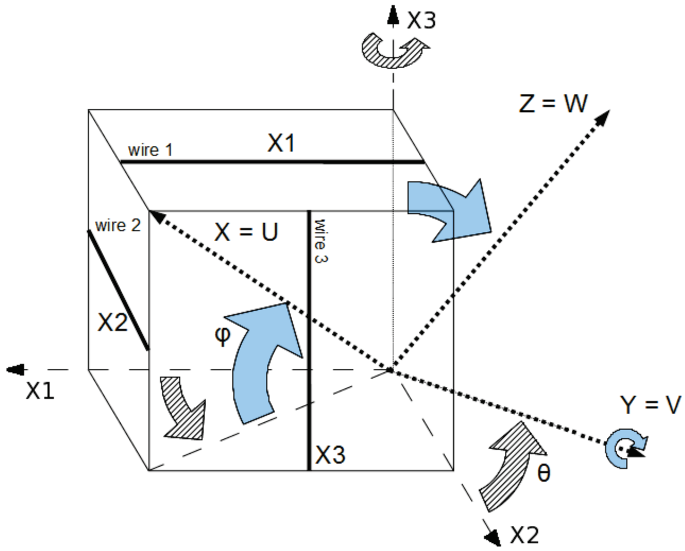

Figure A.5.: Wire frame $(X1, X2, X3)$ and probe frame (X, Y, Z) of the DANTEC 55P91 triple wire probe.

The three orthogonal wires of the probe are making a frame (X_1, X_2, X_3), the wire frame. This frame is rotated in two directions compared to the probe frame (X, Y, Z). The probe frame is also the wind tunnel frame with $(X, Y, Z) = (U, V, W)$, with X, the longitudinal stream-wise direction, Y, the transversal direction and Z, the vertical direction.
Two angles can be defined to go from one frame to the other: $\theta = 45°$ around $X3$ and $\varphi = 35.3°$ around Y. They are shown in (Fig. A.5). A rotation matrix can then be used to go from one frame to the other (Eq. A.16 and A.17).

$$\begin{pmatrix} U \\ V \\ W \end{pmatrix} = R. \begin{pmatrix} X_1 \\ X_2 \\ X_3 \end{pmatrix} \tag{A.16}$$

with,

$$R = \begin{pmatrix} cos\varphi.cos\theta & cos\varphi.sin\theta & sin\varphi \\ -sin\theta & cos\theta & 0 \\ -sin\varphi.cos\theta & -sin\varphi.sin\theta & -cos\varphi \end{pmatrix} = \begin{pmatrix} 1/\sqrt{3} & 1/\sqrt{3} & 1/\sqrt{3} \\ -1/\sqrt{2} & 1/\sqrt{2} & 0 \\ -1/\sqrt{6} & -1/\sqrt{6} & -2/\sqrt{6} \end{pmatrix} \tag{A.17}$$

A.2.2.2. Effective cooling velocity

The effective cooling velocity U_{eff} of a wire is commonly related to the output voltage E by a 4th polynomial (P) fitting (figure A.3). The uncertainty associated to this approach is close to 0.15 % in mean value [15].

$$U_{eff} = P_0 + P_1.E + P_2.E^2 + P_3.E^3 + P_4.E^4 \tag{A.18}$$

On the other side, the effective cooling velocity is linked to the three components of the velocity in the frame of the wire by the Jørgensen law [49]:

$$U_{eff}{}^2 = U_N^2 + U_B{}^2.h^2 + U_T{}^2.k^2 \tag{A.19}$$

with U_N : velocity component normal to the wire ; U_B : velocity component bi-normal to the wire ; U_T : velocity component tangential to the wire ; h: pitch angle coefficient ; k: yaw angle coefficient.

The Jørgensen law is applied to each wire giving three equations. In this particular case of three orthogonal wires, the normal direction of the first wire is as well the tangential direction of the second wire and the bi-normal direction of the third. This relationship between wires is maintained in a cyclic order. The resolution of the Jørgensen laws written for each wire is then simplified to a system with three equations and three unknowns without additional rotation:

$$\begin{pmatrix} U_{eff_1}{}^2 \\ U_{eff_2}{}^2 \\ U_{eff_3}{}^2 \end{pmatrix} = J\o . \begin{pmatrix} X_1{}^2 \\ X_2{}^2 \\ X_3{}^2 \end{pmatrix} \tag{A.20}$$

with $U_{eff(i)}$: effective cooling velocity of the wire (i) ; (X_i): velocity in the frame linked to the wires ; Jø: Jørgensen matrix defined with the pitching and yawing coefficients.

The Jørgensen matrix is defined as:

$$J\o = \begin{pmatrix} k_I{}^2 & 1 & h_I{}^2 \\ h_{II}{}^2 & k_{II}{}^2 & 1 \\ 1 & h_{III}{}^2 & k_{III}{}^2 \end{pmatrix} \tag{A.21}$$

with (h, k) coefficients must be measured by a directional calibration of the probe. In the literature, these coefficients are often taken as constant: $h_I = h_{II} = h_{III} = h$.

A.2.2.3. Directional calibration

The directional calibration is an aerodynamic calibration linked to the shape of the probe. The directional calibration is normally done only once. It consists in

determining the pitching and yawing coefficients h and k from the Jørgensen law [49] (Eq. A.21). The probe, submitted to a known calibration velocity, is tested for different angles. The procedure is to be performed wire by wire to determine the Jørgensen matrix. It is however commonly accepted that (k, h) are independents from the wire, $h_i = h$ and $k_i = k$.
For regular measurements, (k, h) coefficients given by the manufacturer can be a good option. In this experiment, the calibration performed by [39] is used.

A.2.2.4. Velocity calibration process

First, the dynamic response of the hot-wire is set in the conditions of the test and at the maximum wind speed. It is usually around 7 000 Hz. Then, the static velocity calibration can start.
During this process, a known velocity is applied to the probe, usually a velocity in X direction: $U = U, V = 0, W = 0$. The velocity imposed is decomposed in the (X_1, X_2, X_3) frame by the inverse of the rotation matrix (Eq. A.16 and A.17) (in this case: $X_1 = X_2 = X_3 = U/\sqrt{3}$). The effective cooling velocity can then be determined thanks to the Jørgensen equation (Eq. A.20).
For several values of U, from 2 to 25 m/s, voltage outputs are recorded and a 4^{th} polynomial (Eq. A.18) is fitted for each wire.
This calibration is repeated each time the hit-wire is turn off, at least every day.

A.2.2.5. Determination of the velocity

During the measurement, the three output voltages are recorded simultaneously and the following "measurement process" is followed (Fig. A.6). The polynomial fitting (P) is applied to the recorded voltage to get the effective cooling velocity. Then, the system (Eq. A.20) is solved to get the velocity components in the frame of the wires (X_1, X_2, X_3). The rotation matrix R (Eq. A.17) is finally applied to get the velocity in the frame of the wind tunnel.
For the uniqueness of the solution, the velocity measured has to stay in a 35.3 ° cone.

A.2.3. Measurement procedures

The acquisition parameters are details in table A.3. Generally speaking, the convergence of the mean and the standard deviation values is verified, the acquisition frequency is at least the double of the filter frequency.

Test	Acq. frequency [Hz]	filter frequency [Hz]	Acquisition time [s]
Ch.3 VKI-L1 ABL	3 000	1 000	120
Ch.3 VKI-L2 ABL	4 000	1 000	45
Ch.5 VKI L1 Alaiz	750	300	120

Table A.3.: Setting of the hot-wire acquisition for the tests.

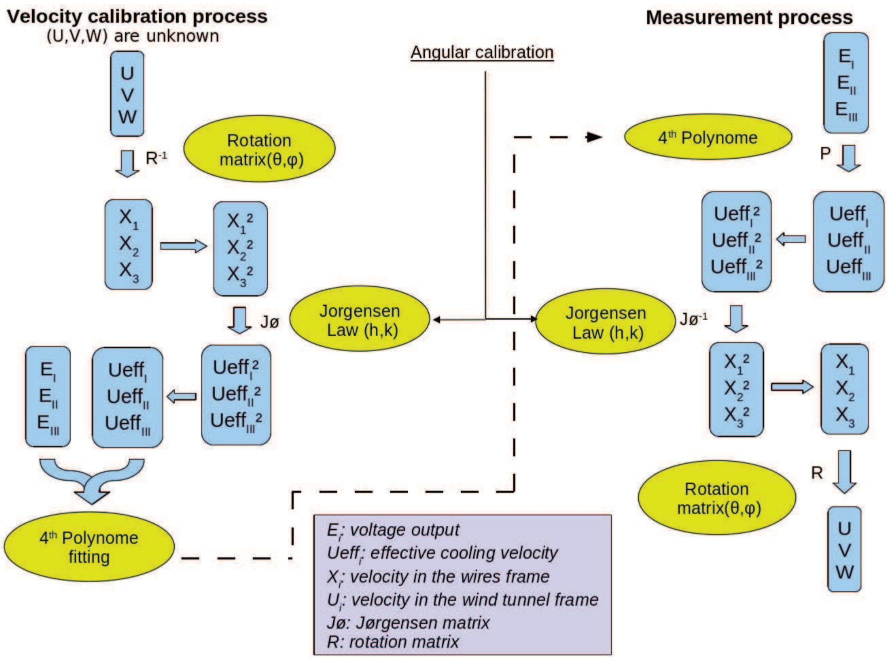

Figure A.6.: Summary of the calibration and the measurement procedure for three components HWA.

A.2.4. Error analysis

Two types of errors are distinguished. The systematic error, or bias error, reveals the error made for every measurement, it is coming from the measurement bias, mainly from the calibration procedure: accuracy of the separation time, estimation of the magnification factor... The second error is the random error, due to the variability of the phenomena.
Then the total error is defined by the equation A.4.

The bias error

For the calculation of the bias error of a single wire anemometer, the velocity calibration procedure is taken into account. The anemometer is placed in the core of a nozzle which velocity is calculated from the difference between the ambient pressure and the pressure in the settling chamber by the simplified Bernoulli equation:

$$U = \sqrt{\frac{2 \times P_{diff} \times R \times T_{amb.}}{P_{amb.}}} \tag{A.22}$$

with the pressure P_{diff} calibrated from a water manometer:

$$P_{diff} = g \times H_{mmH2O} \tag{A.23}$$

with P_{diff} the pressure difference between the settling chamber of the nozzle and the ambient pressure $P_{amb.}$, at the ambient temperature $T_{amb.}$, R the specific gas constant (dry air), g the gravitational acceleration, and H_{mmH2O} the water height in the water manometer given in mm.

From this, we can derive, assuming $\Delta g = 0$:

$$(\partial U)^2 = \left(\frac{\partial U}{\partial P_{diff}} \Delta P_{diff}\right)^2 + \left(\frac{\partial U}{\partial T_{amb.}} \Delta T_{amb.}\right)^2 + \left(\frac{\partial U}{\partial P_{amb.}} \Delta P_{amb.}\right)^2 \tag{A.24}$$

and,

$$(\partial P_{diff.})^2 = \left(\frac{\partial P_{diff.}}{\partial H_{mmH2O}} \Delta H_{mmH2O}\right)^2 \tag{A.25}$$

that gives,

$$\left(\frac{\Delta U}{U}\right)^2 = \left(\frac{1}{2}\frac{\Delta H_{mmH2O}}{H_{mmH2O}}\right)^2 + \left(\frac{1}{2}\frac{\Delta T_{amb.}}{T_{amb.}}\right)^2 + \left(\frac{1}{2}\frac{\Delta P_{amb.}}{P_{amb.}}\right)^2 \tag{A.26}$$

The bias error on the temperature and the ambient pressure are constant, the ambient pressure is given with 1 hPa resolution and the temperature with 1 °K. Then, as an example, $\frac{\Delta P_{amb.}}{P_{amb.}} = \frac{0.5}{1002} = 0.05\%$ and $\frac{\Delta T_{amb.}}{T_{amb.}} = \frac{0.5}{293} = 0.17\%$.

The water manometer has a resolution of 0.2 mmH2O, then $\Delta H_{mmH2O} = 0.1mm$. The height of water H_{mmH2O} depends on the velocity measured, then, the error is function of the velocity:

$$\frac{\Delta H_{mmH2O}}{H_{mmH2O}} = \frac{\Delta H_{mmH2O} \times 2 \times g \times R \times T_{amb.}}{U^2 \times P_{amb.}} \tag{A.27}$$

Then we have:

$$\left(\frac{\Delta U}{U}\right)^2 = \left(\frac{1}{2}\frac{1.64}{U^2}\right)^2 + \left(\frac{1}{2}0.0017\right)^2 + \left(\frac{1}{2}0.0005\right)^2 \tag{A.28}$$

Then the error due to the fitting by a 4^{th} order polynomial is added. It is estimated with the RMSE (Root Mean Square Error) of the fitting, 2.6% in this case.

Finally, figure A.7 presents a typical example of the bias error.

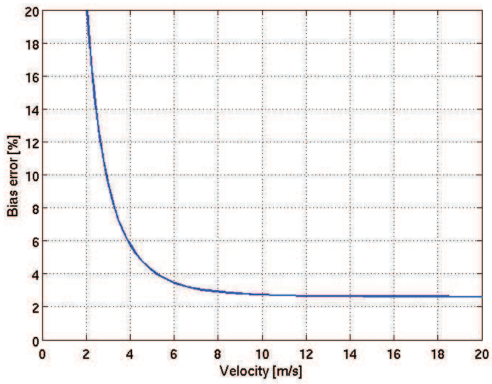

Figure A.7.: Typical bias error of hot-wire measurements in function of the local velocity.

The bias error of the triple HW

For the triple HW, the error calculated is valid for each wire (U_{eff}). Then, the error is transposed to the frame of the probe passing by the Jørgensen law and the rotation matrix (see figure A.6). Errors added are due to the angles θ and ϕ, estimated to 2° and the pitch and yaw angle coefficients h and k, estimated to 5%. The estimation of the final error on the velocity is given as the final variation obtained by varying the parameters in the code.
The coupled variation of 2° of the angles and 5% on the yaw and pitch parameters leads to a maximum error of roughly 8%.

The random error

The flow measured is varying with time, therefore, an error is made when calculating average quantities. This error depends on the variance of the phenomena and on the number of independent samples. Due to the high acquisition frequency, a large number of samples are available to compute an average. However, the statistical average is based on the mean of *independent* samples. To be statistically independent, two point must be separated by at least two times the characteristic time (integral time scale) T_u of the flow. The number of independent sample during the observation time is then $N = T_{obs}/(2 \times T_u)$.
The random error is calculated in the same way as the PIV random error by equations A.13 and A.14 as a consequence, the random error is lower than for PIV.

Summary of the HW errors in the work

Here are summarized all the HW experiments with the associated error (see table A.4). The confidence level is set to 95%, the random error is given for the highest standard deviation value.

Configuration	HW	Acq. time	L_i	N	ϵ_{Rand_μ}	ϵ_{rand_σ}
Ch.3 VKI-L1 ABL	3-C	120	0.45	1 800	0.88%	2.3%
Ch.3 VKI-L2 ABL	1-C	45	0.1	3 375	0.67%	1.7%
Ch.5 VKI L1 Alaiz	1-C	120	0.45	1 800	0.88%	2.3%

Table A.4.: Random and bias error on the HW experiments, confidence level is set to 95%.

Appendix B.

The comparison metrics

Comparison procedure taken from Waudit Guidance report [42]. (available in http://www.waudit-itn.eu/documents.php):
1- determination of quantities of interest
2- other considerations: averaging time, how many spacial locations needed
3- plot quantities of interest: first data comparison (initial comparison)
4- plot scatter plot: visualization of the comparison or correlation(qualitative comparison)
5- use metrics for statistical comparison: list of statistical quantities (quantitative comparison)

Correlation coefficient
$$R = \frac{\overline{(O-\bar{O})(P-\bar{P})}}{\sigma_P \sigma_O} \tag{B.1}$$

Fractionnal Bias
$$FB = \frac{\bar{O}-\bar{P}}{0.5(\bar{O}+\bar{P})} \tag{B.2}$$

Normalized Mean Square Error
$$NMSE = \frac{\overline{(O-P)^2}}{\bar{O}\bar{P}} \tag{B.3}$$

Geometric Mean
$$MG = exp\left[\overline{ln\ O} - \overline{ln\ P}\right] \tag{B.4}$$

Geometric Variance
$$VG = exp\left[\overline{(ln\ O - ln\ P)^2}\right] \tag{B.5}$$

Quantity	Interpretation	Perfect match
Fractional Bias (FB)	FB = +/- 0.67, factor of 2 under/over prediction	0
Normalized Mean Square Error (NMSE)	< 1, log normal distribution, NMSE = 1 typical error equals the mean, NMSE = 4, typical error equals 2 times the mean	0
Geometric Mean (MG)	MG = 0.5 or 2, factor of two bias, MG = 0.25 or 4, factor of four of bias	1
Geometric variance (VG)	VG = 1.6, factor of two scatter, VG = 6.8, factor of four scatter	1

Table B.1.: Calculation of the comparison matrics.

Appendix C.

The Sand Erosion technique

Text extracted from: Conan, B., van Beeck, J. and Aubrun, S., 2012 "Sand erosion technique applied to wind resource assessment", *Journal of Wind Engineering and Industrial Aerodynamics* 104, pp 322-329

C.1. Abstract

One of the major challenges of the wind energy sector is to accurately predict the wind potential. This task is especially difficult in mountainous terrains where the topography can imply complex relief-induced flows. Wind tunnel testing is one of the possibilities to simulate and predict the wind for wind turbine micro-siting. Most advanced quantitative measurement techniques can be used in the wind tunnel, however, measuring the whole terrain to find the highest wind potential zones is very time-consuming. This paper proposes to use a very simple, quick and cheap technique to detect and evaluate the high wind speed areas over an entire model. Commonly used for pedestrian wind comfort assessment, the sand erosion technique is here applied to wind resource assessment. The technique can provide valuable qualitative informations but can also give an order of magnitude of the local speed-up. It is first applied to a backward facing step flow and then on a mountainous terrain. An amplification factor and the fractional speed-up ratio (FSR) can be calculated over the entire mountain. For high speed positions results extracted from sand erosion appears to be comparable the one calculated by particle image velocimetry. The technique is repeatable, able to perform a detection of the high speed area, and capable of giving an estimation of the amplitude of the wind. The technique allows to restrict the use of quantitative measurements to the most interesting areas.

Keywords

sand erosion technique, PIV, wind energy, wind resource assessment, wind tunnel test

C.2. Introduction

In the fast development of wind energy, wind-farms tend to be more and more located in complex terrains. On a cliff, a hill or a mountain, the wind speed-up created at the top of the topography is an advantage for the wind farm productivity. However, the complexity of the terrain increases the difficulty of determining the wind characteristics (direction, mean speed, turbulence); therefore the prediction of the wind resource and the profitability of a wind farm becomes more challenging.

The wind resource assessment in complex terrain and the determination of the local effect of a topography on wind characteristics can be performed by physical modelling in the wind tunnel. To measure the flow in the wind tunnel, measurement techniques like hot-wire anemometry (HWA) and Particle Image Velocimetry (PIV) are used. The state-of-art PIV technique allows the determination of the mean wind speed and the turbulence level of the three velocity components in a volume (usually reduced to a few centimetres). However, for cost effective reasons, two velocity components in a two dimensional plane is the most common technique. Despite the very good spatial resolution, the frequency resolution of PIV is often a limitation for measuring the turbulence spectra ($>$ 10 kHz needed) that is an order of magnitude above the classical PIV possibilities. The hot-wire technique can complement the PIV measurements by a punctual measurement of the three velocity components with a very high frequency resolution ($>$ 10 kHz). This technique is used for computing the spectral density distribution and the turbulence length scales. Those two very accurate techniques can fully characterize the wind profile [23].

However, the installation and the use of these techniques require time, precision and a lot of precautions. A first estimation of the location of the speed-up areas is a very valuable information to save time by reducing the measurement zone. This paper presents a simple tool for a global approach of the wind over complex terrains: the sand erosion technique.

For the assessment of pedestrian-level wind in urban areas, where computational techniques remain very difficult to use, erosion tests are ordinary carried out in a wind tunnel to predict the wind comfort: see [78], [66], [33] and [84]. Simple, quick and cheap, erosion techniques are commonly performed for studying urban flows. Based on this experience, the sand erosion technique is here tested in another application: wind resource assessment in complex terrain.

The objective of this work is to evaluate the possibility of using the sand erosion technique as an initial qualitative vision of the potential wind park siting areas on a large domain. The technique allows to focus further investigations with more expensive quantitative measurement techniques. The study presents the technique, proposes a methodology to use it, assesses the reliability of the results, discusses its limitations and presents visualizations and quantitative measurements compared with proven techniques. Tests are performed first on a backward-facing step (BFS) and then on a mountainous terrain, the Alaiz mountain (Spain).

C.3. The sand erosion technique

C.3.1. Principle

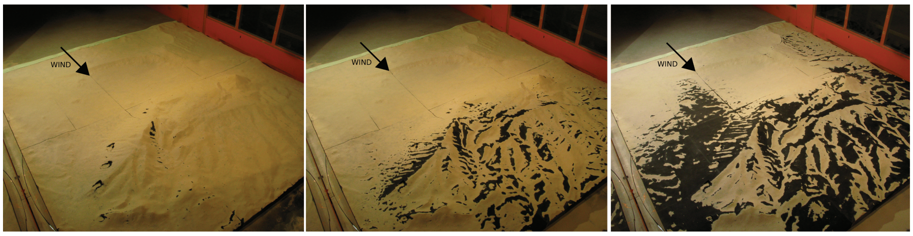

Figure C.1.: Example of a model at the beginning of the test (left) after 1 min at 6 m/s (middle) and after 1 minute at 7 m/s (right).

The sand erosion technique is commonly used for pedestrian-level wind assessment in urban area. It is based on the erosion of sand placed on a model. Different authors developed methodologies to use the technique for wind comfort assessment: [87, 89, 59, 10]; and [33].
In practice, the model is placed in a wind tunnel and covered with a thin layer of 1 mm to 1.5 mm of sieved sand. The surface of the model is usually painted black and the sand used is either white or coloured to contrast with the background. The sand placed on a surface has the property to erode at a given friction-velocity called here threshold friction-velocity, $U*_{th}$. The velocity of the wind tunnel is then increased step by step and a picture is taken after 1 min of exposition to a given free-stream velocity. At each velocity step, areas on the model are more and more eroded and contrast with the rest of the model still covered by the sand. Revealed sand contours are iso-friction-velocity contours and the friction-velocity is close to the threshold friction-velocity of the sand ($U*_{th}$). The relationship between the sand erosion patterns and the friction-velocity is still not completely understood, especially in detached zones. [34] showed that the eroded area contours are linked to the mean friction-velocity and the RMS. In regions with high turbulence level, the sand erodes for a lower mean friction-velocity due to large fluctuations around the mean that are higher than the threshold friction-velocity of the sand ($U*_{th}$). Another limitation of the technique is the easier entrainment of particles due to up-wind particle impacts, this is called "down-wind erosion" and discussed in section C.5.2.4.
Sand contours are evolving at each velocity step and give a visualization of the locations of the high velocity zones. Different techniques (section C.3.3) allow to compute an amplification factor map or to retrieve the velocity at a higher altitude. Figure C.1 presents an example of sand erosion patterns obtained on a large model of a mountain (details are given in section C.5).

C.3.2. Sand characteristics

The sand used is sieved and measured to be statistically mono-dispersed around a mean diameter of 400 μm. A friction velocity calibration is performed on a flat-smooth plate. To do so, a layer of sand is placed on a flat plate and the wind tunnel speed is raised step by step until the sand erodes, at that moment, the friction-velocity exceeds the threshold friction-velocity of the sand. For that speed, the velocity profile is measured by hot-wire anemometry (HWA), Particle Image Velocimetry (PIV) or Laser Doppler Velocimetry (LDV). The friction-velocity is deduced from Bradshaw's method [12]. For the sand employed in this study, $U*_{th}$ = 0.27 m/s. Because the threshold friction-velocity is a property of the sand, it has to be calibrated only once and then it can be used in different set-up with different configurations.

C.3.3. Methodology

To extract useful information from the sand erosion test, a specific methodology is followed. The model is first covered partially or completely with 1 mm sand layer as described in section C.3.1, the free-stream velocity of the wind tunnel, U_i, is then increased by steps of 0.5 m/s and an image is taken after 1 min of exposure to each velocity step. One minute is long enough so that sand contours are stable and do not depend much on the initial sand thickness non-uniformities, and short enough so that extreme gusts do not play an important role (see [84] and [33]). At each step, at the sand contour, the friction-velocity is $U*_{th}$. The free-stream velocity of every step (U_i) can be compared to the free-stream velocity (at the same height) for which the sand flies on a flat surface with an empty test section: U_{ref}. This allows to define an amplification factor, A, giving the speed-up or the speed-down due to the model (see [10]):

$$A = \frac{U_{ref}}{U_i} \tag{C.1}$$

Where the sand erodes for a free-stream velocity lower than the reference velocity ($U_i < U_{ref}$), the model creates a local speed-up ($A > 1$). At the contrary, if locations are not eroded for $U_i > U_{ref}$, it means that those locations are speed-down zones ($A < 1$). Thanks to the different velocity steps realized and an automatic detection of contours, a map of amplification factor can be drawn.
The well known Fractional Speed-up Ratio (FSR) can also be computed. In this case, (U_i) is varying at each step and U_{ref} is a constant:

$$FSR = \frac{U_{ref} - U_i}{U_i} = A - 1 \tag{C.2}$$

With this method, there is no need to know the threshold friction-velocity of the sand, however equations C.1 and C.2 are valid under some major hypothesis [10]: the flow is Reynolds number independent in the range of velocity used, the flow is

fully developed, the flow near the wall follows the logarithmic law profile and the sand erosion occurs always at the same ground-level wind speed.
Knowing the threshold friction-velocity allows to compute the velocity at a height, z, thanks to the universal log-law of the wall for turbulent flow over smooth wall [12]:

$$U(z) = U *_{th} . \left(5 + 2.5.ln\left(\frac{z.U*_{th}}{\nu}\right)\right) \tag{C.3}$$

With $U(z)$: velocity [m/s] at altitude z [m] and ν: kinetic viscosity of the air [m^2/s].

The applicability of equation C.3 is presented in section C.4. The methods presented allow to extract quantitative data like amplification factors or FSR.

C.3.4. Contour detection method

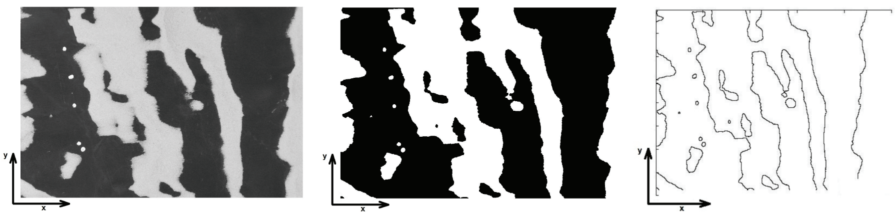

Figure C.2.: Post-processing steps: raw image (left), binary image (middle) and contours detection (right)

All images taken at the different velocity steps are processed with an in-house MatLab code detecting the sand contours. In the wind tunnel, the contrast is increased by using white sand on black-painted model. The code transforms the image in black and white and then in binary. The contours are then smoothed and finally detected (Fig. C.2). A full amplification factor or FSR map can be extracted.

C.4. Validation test: the backward facing step

For validation purposes, the technique is applied to a well-known case study, the Backward Facing Step (BFS). The aim is to perform a sand erosion test as described in section C.3.3 and to compare the results with quantitative measurements.

C.4.1. Experimental set-up and quantitative measurements

The experiment is conducted in a blowing type wind tunnel able to provide 20 m/s with 0.3 % free-stream turbulence intensity. The test section (0.2 x 0.2 m^2)

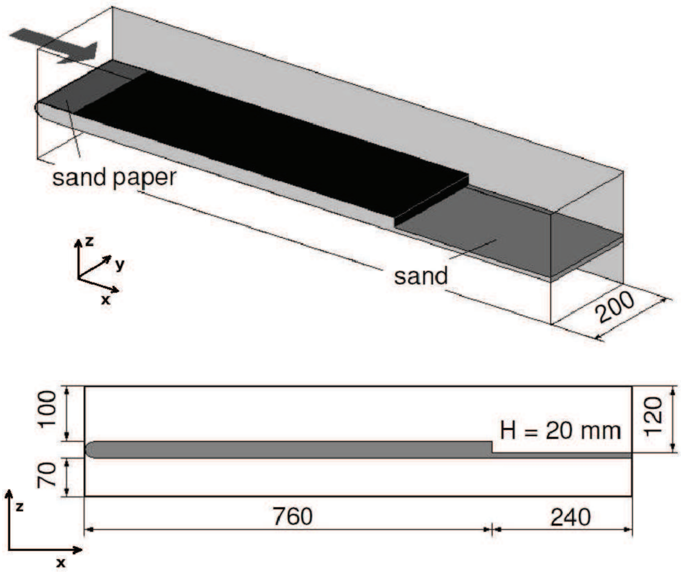

Figure C.3.: Wind tunnel set-up for the backward-facing step test case [33].

is equipped with a 1000 mm long wooden flat plate with a $H = 20$ mm height backward-facing step. A sand paper strip is placed at the start of the plate to trigger the development of a turbulent boundary layer (Fig. C.3). The Reynolds number based on the step height and the wind tunnel free-stream velocity ($U_\infty =$ 17.1 m/s) is: $Re_H = \frac{U_\infty . H}{\nu} = 21800$.
The flow downstream of the step is measured using Particle Image Velocimetry (PIV) and a set of 500 images is used for computing the time-averaged flow field. The statistical error on velocity in the free-stream is assessed to 2% at 98% confidence level. The single velocity measurement error is approximately $\pm$ 0.25 m/s. Presented in numerous literature papers like [71] or [57], the time-averaged flow field, shown in Figure C.4, is characterized by a clockwise recirculation area extending up to 5.5 H downstream of the step and a counter-clockwise corner vortex at the foot of the step.

C.4.2. Sand erosion tests and comparison of the results

The downstream part of the step is covered with a thin layer of sand (Fig. C.3). The amplification factor (A) and the FSR (Eq. C.1 and C.2) are computed at 5 free-stream velocities: 15.3 m/s, 16 m/s, 16.5 m/s, 17 m/s, and 17.6 m/s.
To be comparable with sand erosion, the mean velocity of the PIV data is calculated as $U = \overline{(|u|)}$. Figure C.5 presents the comparison of the FSR extracted from sand erosion (dots) with the PIV results (full lines). Two curves are plotted from

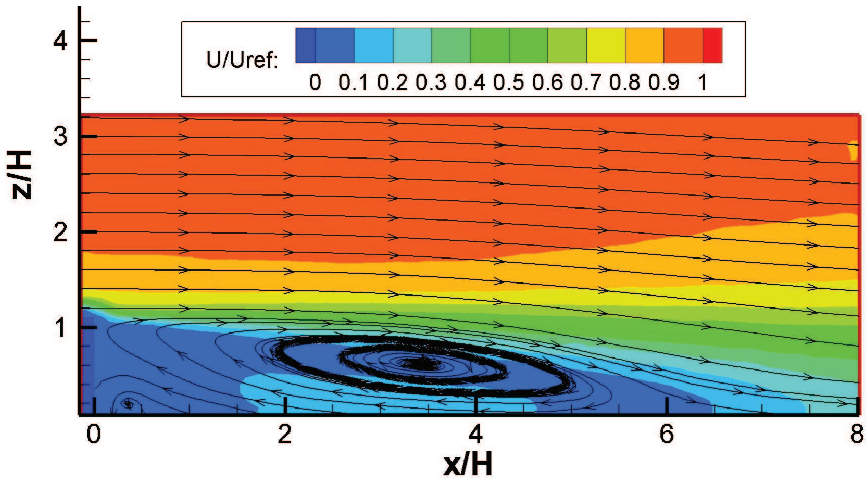

Figure C.4.: Time averaged velocity magnitude and velocity streamlines on the BFS at Re = 21800 [33].

the PIV results: the mean velocity, U (in red), and the mean velocity plus the RMS, $U + Urms$ (in blue).
The sand erosion result has the same trend and falls between the two curves extracted from PIV. For low turbulence ($x/H < 3$), the sand gives rather good agreement (2%) with quantitative measurement. However, at the re-attachment zone ($4 < x/H < 6$), the sand erosion gives values closer to $U + Urms$.
Sand erosion contours are thus overestimating the mean velocity in regions with high turbulence intensity. This is conservative for wind comfort studies because uncomfortable zones are never missed. However, for wind energy assessment this is less favourable because a soon erosion can be due to a high mean velocity or a high turbulence level (see section C.3.1). Consequently, for application of the sand erosion technique to the wind energy sector, the high speed locations are never missed but the level of turbulence has to be assessed by other means in order to establish confidence in the mean velocity prediction from sand contours.

C.5. Application to a complex terrain

In this section, experiments are performed on a model of a mountainous terrain situated next to Pamplona in the North of Spain, the Alaiz mountain. Wind farms already exist on site and field measurements are currently being performed. CFD computations by [17] and [63] as well as wind tunnel experiments [23] and [25] have already been carried out concerning this site.

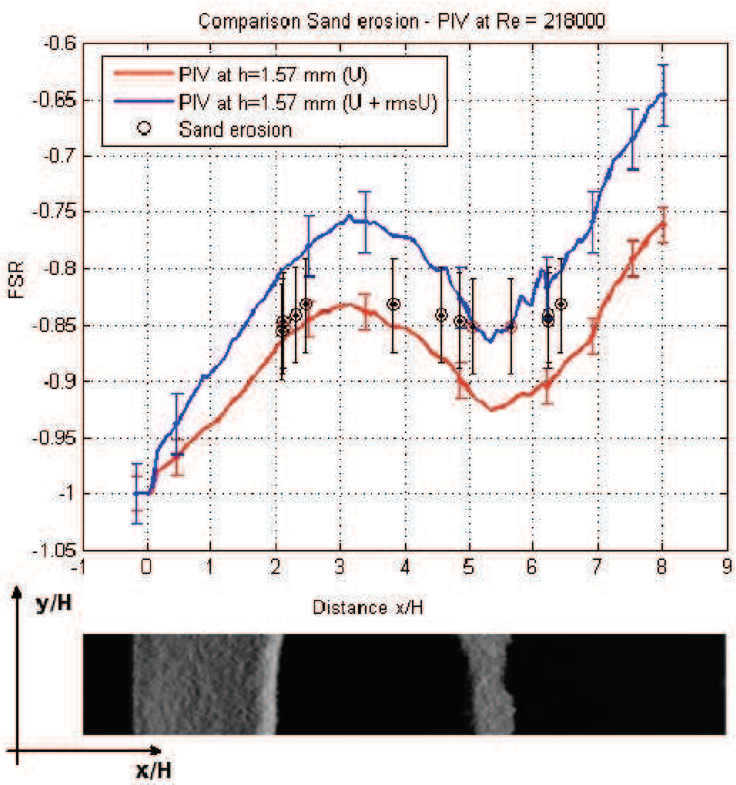

Figure C.5.: Comparison of the FSR computed from PIV measurements and from sand erosion tests (top). Top view of the sand erosion pattern after 1 min at 17 m/s (bottom).

C.5.1. Description of the experiment

C.5.1.1. The Alaiz mountain

The mountain is 1130 m high and is stretching over 10 km in the W-E direction and over 8 km in the N-S direction (Fig. C.6). The configuration tested in the wind tunnel is the dominant wind direction: North. Upstream the mountain, to the North, a 200 m high ridge is facing the incoming wind (X = 0.75 m in Fig. C.6) and the wind tunnel mock-up is designed to include it because it is expected to affect the incoming flow. The area modelled is 16 km x 15 km. Giving the test section constraints, the scaling factor is 5300. The mock-up is the one used by [23], which was directly drilled in Necuron® from the 3D topographic file with 1/10 mm precision. The finishing is of the order of 10 μm. As a first approach, the roughness of the terrain is not modelled.

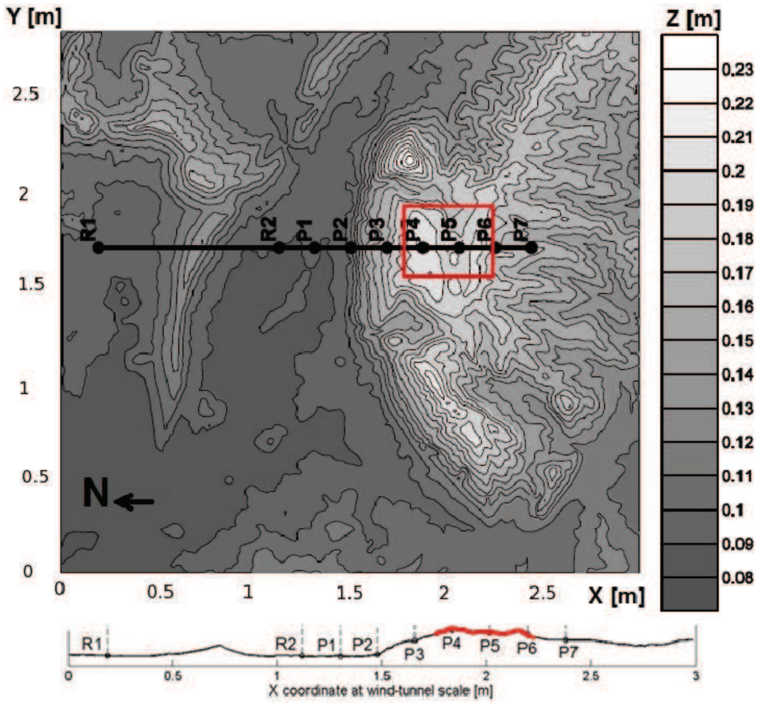

Figure C.6.: Alaiz model: top view and profile of the terrain following the measurement line. Red area: sand erosion zone. Points R1 and R2 are reference positions and points P1 to P7 are measurement position.

A line following the wind direction is defined to perform quantitative measurements (Fig. C.6). Two main crests can be defined on the mountain: a first one, the main crest, is at the position of P_4 and a second one just before the position P_6.

C.5.1.2. Atmospheric boundary layer modelling

Tests are performed in the VKI-L1 boundary layer wind tunnel. The test section is 15 m long, 3 m wide and 2 m high. This length allows the development of a neutral atmospheric boundary layer generated thanks to a grid and a step at the entrance of the test section, and roughness elements spread over 12 m on the floor. The boundary layer modelled represents both the velocity and the turbulence profile of a moderately rough to rough terrain with $z_0 = 2.2$ m at real scale (see [23, 85] and [36]).

C.5.1.3. Quantitative measurements: Particle Image Velocimetry and hot-wire anemometry

A quantitative assessment of the wind over the mountain is performed with Particle Image Velocimetry (PIV) [67] and hot-wire anemometry (HWA) [15]. Measurements are performed on the vertical plane presented in Figure C.6, between measurement points R_1 and P_7.
PIV is performed between R_2 and P_7 with a free-stream velocity at 1 m above the floor of 14 m/s. The mountain height based Reynolds number is $Re_M = 105000$. The average velocity vector field is computed in the vertical plane (U, W) over 500 images taken at a sampling frequency of 3 Hz. The statistical uncertainty associated is assessed to 1.5% at 95% confidence level for the mean speed and 8% for the RMS at the same confidence level.
Additionally, hot-wire measurements are performed at each of the positions at a sampling frequency of 5 kHz. The uncertainty is assessed to 1% for mean values and 5.7% from RMS at 95% confidence level. PIV and HWA profiles are in very good agreement, within less than 2%.
For the assessment of the wind characteristics, the combination of PIV and hot-wire anemometry is very powerful: the PIV gives the mean velocity profile and the turbulence intensity on a 2D field with a very high spatial resolution and the hot-wire provides a punctual time series leading to turbulence length scale and turbulent spectra.
The Fractional Speed-up Ratio (FSR) is computed at 90 m real scale (common hub height) as:

$$FSR(90m) = \frac{U(90m) - U_{ref}(90m)}{U_{ref}(90m)} \tag{C.4}$$

With U_{ref} the reference velocity at 90 m for the position R_1.
This parameter gives information on the ratio of change of the wind at a given location with reference to the inlet condition. Results in Figure C.11 (red curve for PIV and red dots for HWA) show a speed-down before the hill and two major areas of high wind speed situated next to positions P_4 and P_6.

C.5.2. Sand erosion on a mountainous terrain

C.5.2.1. Sand erosion tests

The sand erosion technique is tested on the Alaiz mountain in the area of interest indicated with a red square on Figure C.6. The reference velocity used for the FSR, ($U_{ref}(90m)$ in eq. C.4), is calculated at 90 m real scale in the wind tunnel from the threshold friction-velocity and the law of the wall (eq. C.3): $U_{ref}(90m) = 5.21 m/s$. To verify it, the velocity at 90 m (real scale) is measured in the wind tunnel when the sand erodes without the model. This measurement gives $U_{ref}(90m) = 5.28 m/s$. Both estimations of the reference velocity agree. The technique is verified for a log-law profile.

In this study, 13 velocity steps ($U_{ref}(90m)$) are performed in the range 3-7 m/s. Table C.1 lists the velocities used.

Velocity at 90m [m/s]	3.35	3.55	3.8	4.04	4.29	4.54	4.79
	5.04	5.28	5.53	5.78	6.03	6.28	

Table C.1.: Velocities, $U(90m)$, tested tested in the wind tunnel.

C.5.2.2. Visualization

Before trying to extract any quantitative values, the sand erosion is a very valuable technique for the visualization of the high wind speed areas, the observation of the erosion contours illustrates the repartition of the high and low speed areas. Figure C.7 presents a set of pictures taken at different increasing velocities. The sand is cleared step by step from the mock-up surface.
The technique allows a very quick visualization of the high-speed areas that are eroded first. The two crests are quickly appearing to be the highest wind speed positions. They are clearly good candidates for deeper analysis to state their suitability for wind turbine siting.

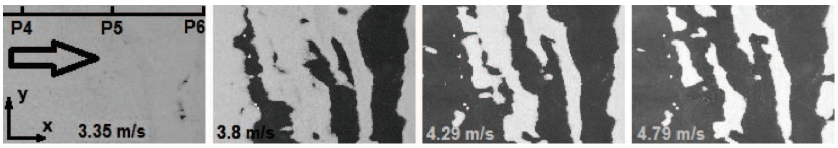

Figure C.7.: Example of an evolution of the erosion pattern with the free-stream velocity (red area on Figure C.6).

C.5.2.3. Repeatability study

To assess the repeatability of the method, a set of five runs is performed in the same conditions and with the same sand spread over the same area of the model. Tests are conducted at different days and the sand is spread on the model by different people. Figure C.8 presents the superposition of the sand contours for the five independent runs at two velocities together with the elevation map. Generally speaking, contours are very similar, at low speed, the up-wind contour of the sand area is very well reproducible but more scatter is observed at the down-wind contour. In general, low friction-velocity gradients lead to higher variability of the sand contours and introduce more uncertainty on the position of the sand contours, but after a certain velocity, sand contours match. A quantification of the repeatability is performed by comparing the eroded surfaces for the different runs. At 3.8 m/s, there is around 7% of scatter between independent tests, this value decreases rapidly with increasing speed, it goes lower than 3%, at 5 m/s. The repeatability study corroborates the observations of [34] that the repeatability of the technique is good.

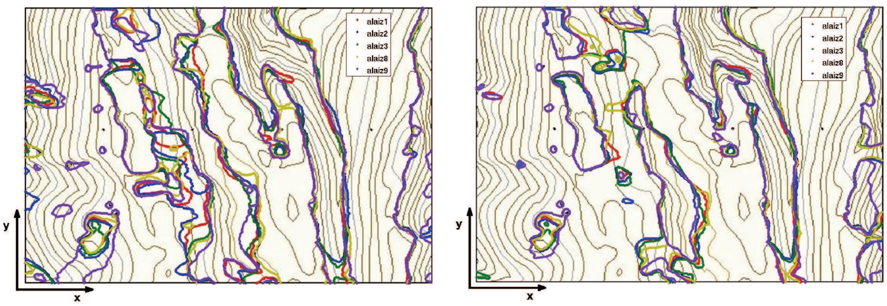

Figure C.8.: Superposition of the sand contours of five independent runs performed at two velocity steps 4.29 m/s (left) with 6.5% scatter and 4.79 m/s (right) with 5.5% scatter.

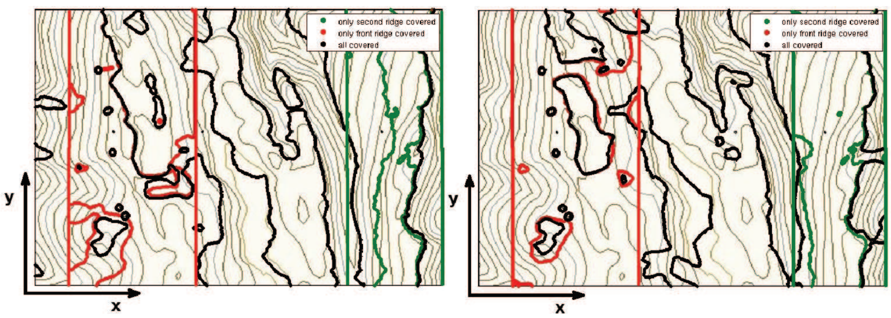

Figure C.9.: Effect of the area covered at two velocities: 4.29 m/s (left) and 4.79 m/s (right). Only first ridge covered (red), only second ridge covered (green) and all area covered (black).

C.5.2.4. "down-wind erosion" study

This phenomena, described by [34] and [89], is observed when an important area is covered with sand, in this case, the downstream sand is more likely to erode. The two main explanations brought forward are: an easier erosion due to upwind sand impacts and the increase of the wall turbulence due to the surface roughness of the sand.

To assess its importance in this particular case, tests are performed by covering partially the area of interest, first only the first ridge (area between the two red lines in Fig. C.9) and in another test only the second ridge (area between the two green lines in the same figure) are covered. Results are compared with the fully covered test (black contours in Fig. C.9).

From the observations, the erosion is generally weaker when the area is not completely covered. At 4.29 m/s, for the first ridge, the sand contours are at the lower limit (less erosion) of the 7% of repeatability error. For the second ridge, the sand area before the ridge crest (down-wind contour of the sand area) is much less eroded, however, the sand contour at the crest (up-wind sand contour) is the same as in the reference case. At 4.79 m/s all sand contours falls in the repeatability error of 5%.

The presence of sand upstream of the area of interest implies a sooner erosion upstream the second ridge crest, the data taken with local covering on the second ridge are the one used further in the paper to extract the velocity speed-up at that position. For the first ridge there is no difference. Generally speaking, the upstream sand effect decreases rapidly with increasing speed.

C.5.3. Sand erosion compared with PIV and HWA

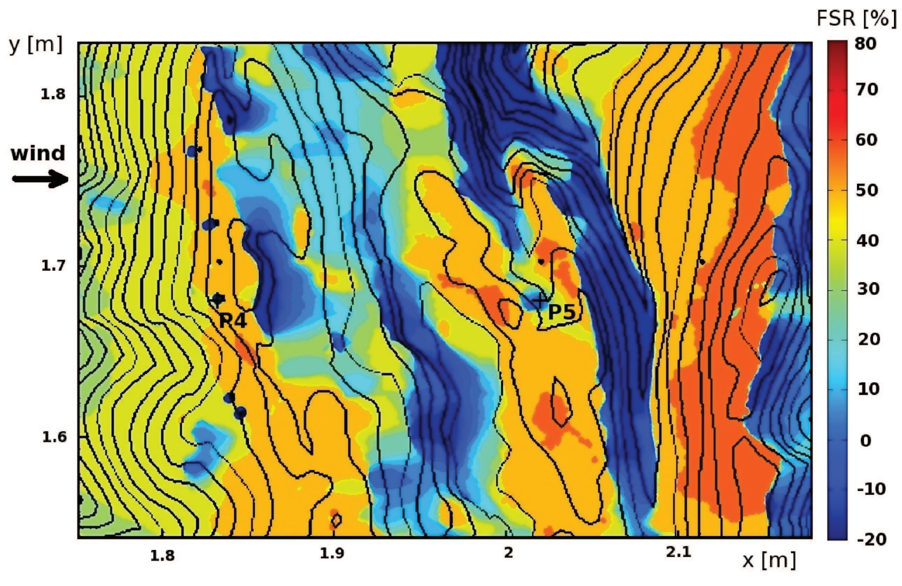

Figure C.10.: Amplification factor map on Alaiz mountain (eq. C.1), the white dots on the image are reference positions (masts). Axis are in meter at the wind tunnel scale.

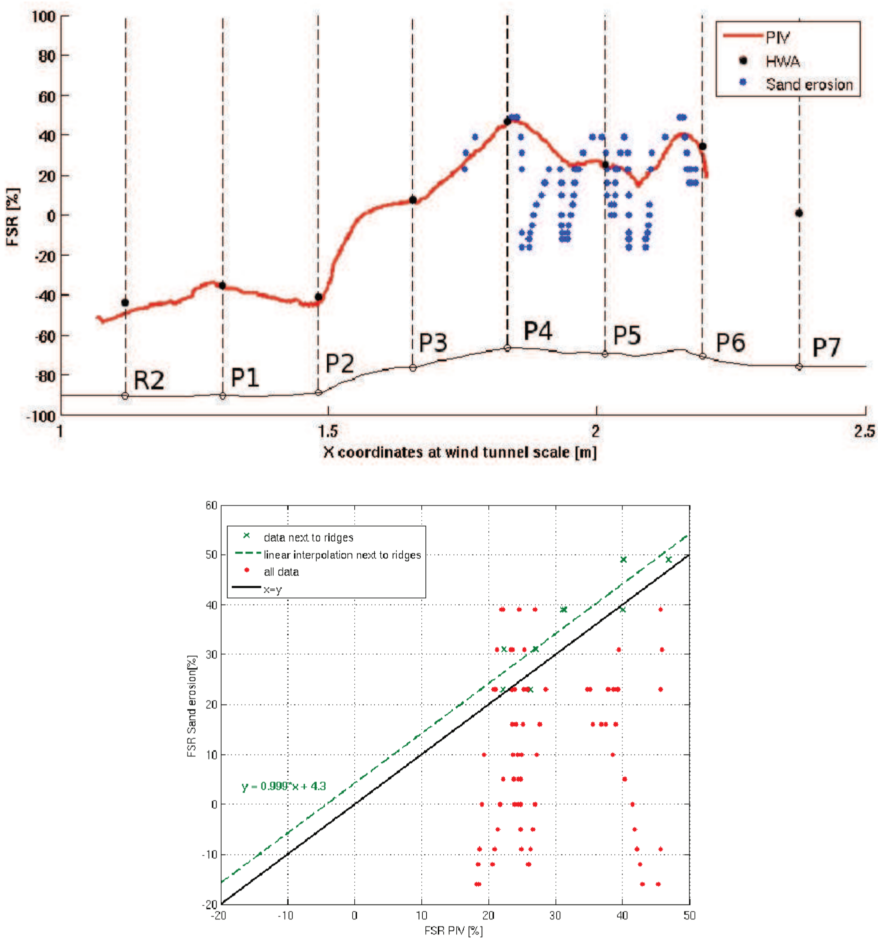

Figure C.11.: (top) Comparison between the fractional Speed-up Ratio calculated by PIV and extracted from the erosion technique. The FSR is plotted over the line described in Figure C.6. (bottom) Scatter plot between the PIV results and the sand erosion results.

More than a visualization, the methodology presented in section C.3.3 allows to go further and can give an estimation of the over-speed on mountain tops. Figure C.10 is the FSR (equ. C.2) map drawn on the elevation contours of the Alaiz mountain. All velocity steps tested are here superimposed. Red areas are related to high speeds and blue areas to low speeds. The map underlines the general speed-up created in a large part of the top of the mountain. Low winds are limited to the recirculation area (after to the second ridge $x > 2.15$ m) and to low

elevation zones ($x \approx 2.08$ m). At the first region cleaned, the second ridge, the FSR is the highest with more than 55 % ; the sand contour follows the crest line. The second region affected by erosion is the crest line close to the position P_4 ($x \approx 1.85$ m). The FSR at this position is close to 50%. Similarly to a recovery from a perturbation (even without separation), the FSR is the lowest right after crest tops and gradually increases after it. Other places with low friction-velocities are located in troughs of the relief like next to positions $x = 1.97$ m and $x = 2.09$ m.
To compensate the downstream erosion effect detailed in section C.5.2.4, the processing of the images with partial covering of the terrain is used for the calculation of the FSR at the top of the second ridge.
The FSR extracted from sand erosion is compared with the PIV data in Figure C.11 and a scatter plot is presented. The scatter plot generally shows important discrepancy between the PIV results and the quantitative sand erosion data ($R^2 = 0.04$). However, the two peaks are clearly appearing at a very similar position and with a comparable value, around 50%. A correlation coefficient of $R^2 = 0.81$ is determined in the region of the two ridges, the high-speed regions detected by sand erosion are confirmed by the comparison with quantitative data. Discrepancies appear mainly on the downwind slopes of the two ridges, speed-down calculated with the sand erosion technique is overestimated.
Unlike hot-wire and PIV, the sand erosion is a near wall evaluation of the velocity that is extrapolated upwards with a log-law. This assumption may not be fulfilled down-wind the ridges and can explain the discrepancies. If the near wall turbulence is high, the sand will erode earlier and that will lead to an over estimation of the speed at a higher altitude. Additionally, the technique is omnidirectional. These differences can explain the higher level of details given by the erosion technique in Figure C.11 and the bad correlation with PIV measurements. As PIV results are here given at 90 m above the surface, near-ground effects are smoothed.
The FSR based on the sand erosion method gives coherent results with quantitative measurements in high speed-up areas, the high speed zones are detected very easily and the FSR is of the same order of magnitude as a quantitative measurement. However, the way the technique is here used doesn't allows a right determination of the wind speed in the downwind part of the ridge. For wind resource assessment, only high wind speed area are of interest.

C.6. Conclusions

The sand erosion technique is an omni-directional tool able to detect high speed zones on a large area. It is used to evaluate high wind speed spots on an unknown terrain.
The implementation of the technique is very simple, fast and cheap. The image post-processing methodology is straight forward and does not require advanced tools. The repeatability error of the technique is below 7% and decreases with

speed. This is very reasonable regarding the manner to spread the sand.
One of the main limitations comes from the fact that the sand erodes more in the downstream part. This can be overcome by performing local sand erosion tests, i.e. putting sand only on hill tops.
Qualitative results are very interesting and high wind speed zones are detected very fast. When a terrain is investigated for the first time, this is a great advantage that enables to select the areas where deeper measurements have to be carried out.
For more qualitative data, the comparison with PIV and HWA measurements demonstrates that by a simple calibration, the technique can give meaningful estimations (by 10%) of the over-speed expected on a mountains top next to the surface as far as the log-law applies. Results obtained downstream the ridges are however far from reality.
While evaluating an unknown complex terrain, the technique appears to be a very valuable tool to give quickly a global approach of high wind speed locations. Included in a global methodology, the sand erosion technique is a very interesting tool as a first approach. Detailed investigations with more delicate and expensive measurement techniques, like PIV, can be performed at detected locations to get the wind profiles and to assess with accuracy the suitability of placing wind turbines at these positions.

Acknowledgements

This study has been realized with the financial support of the European Commission within the WAUDIT Initial Training Network (Wind resource assessment audit and standardization: www.waudit-itn.eu), a Marie-Curie action funded under FP7-People program.
The authors gratefully acknowledge the support of G. Dezső for providing experimental data for section C.4.

Appendix D.

Résumé en français

D.1. Introduction

D.1.1. Le secteur éolien et ses enjeux

Durant l'année 2011, le secteur éolien a augmenté sa capacité de production d'électricité de 94 GW. Cela représente 11% de plus par rapport à 2010. Depuis 2000, le secteur éolien connaît une croissance annuelle de 15% en moyenne pour atteindre en 2011, 10% de la capacité de production d'électricité en Europe au lieu de 2% en 2000. En 2011, la part de l'éolien dans la production d'énergie de l'UE est d'environ 6.3%. (Statistiques accessibles sur le site de l'EWEA : www.ewea.org)

Malgré une forte croissance, l'énergie extraite du vent demeure chère en comparaison aux autres sources de production classiques, ainsi, une montée en puissance du secteur est nécessaire pour diminuer les coûts de production, s'affranchir des subventions et être compétitif en comparaison à la filière gaz ou nucléaire. Un des aspects essentiels est la précision de l'évaluation du potentiel de vent et le choix du site d'implantation. En effet, de la prédiction du vent dépend directement la production d'électricité et donc la rentabilité du champ éolien. Il est primordial pour l'avenir du secteur que l'estimation du potentiel de vent soit la plus précise possible.

Pour bénéficier de vents plus forts et plus constants, les champs éoliens peuvent être placés en mer, proches des côtes. Cette pratique a de nombreux avantages mais fait aussi face des défis technologiques importants. L'émergence et la forte croissance de l'éolien offshore ces cinq dernières années ne doivent pas faire oublier qu'encore en 2011, plus de 90% des nouvelles installations éoliennes ont été érigées sur le continent. Ainsi, pour trouver des vents plus forts, un nombre croissant de champs éoliens sont placés sur des collines ou même des montagnes, le vent y est plus fort, mais la prédiction du potentiel de vent y est plus complexe. En effet, sur un site montagneux, le vent en un point dépend fortement du relief alentour et des phénomènes non-linéaires tels que des recirculations sont fréquants.

Les mesures sur site sont indispensables à la prédiction du vent mais dans le cas d'un terrain complexe, la variabilité spatiale du vent est telle que ces mesures sont insuffisantes. De plus, l'aspect tridimensionnel du vent, induit par de fortes pentes

et la complexité du relief, est un frein aux mesures sur site. Dans de telles conditions, les modèles classiques simplifiés d'évaluation du vent ne sont pas capables de donner une précision suffisante du potentiel de vent. Ainsi, la méthode la plus utilisée est la simulation numérique (CFD) qui utilise des modèles de turbulence. Cette méthode est capable de résoudre des écoulements complexes et focalise une grande partie de la recherche actuelle pour son développement, sa validation et la réduction du coût de calcul.
Une troisième approche, qui peut être complémentaires aux deux précédentes, est possible, c'est la modélisation en soufflerie et à échelle réduite du vent atmosphérique. L'avantage est que le vent n'est pas modélisé mais reproduit à une autre échelle, le niveau de modélisation est donc bien moindre comparé à la simulation numérique. Un autre avantage est que les conditions du test sont constantes et contrôlées. Cependant, la simulation en soufflerie reste une modélisation et doit être réalisée en tenant compte de nombreux paramètres.

D.1.2. La modélisation du vent atmosphérique en soufflerie

La soufflerie est communément utilisée en mécanique des fluides, pour l'aérodynamique des véhicules ou l'étude du vent et ses effets sur des bâtiments. Malgré l'essort de la simulation numérique, la soufflerie reste une référence pour la validation des modèles numériques.

La simulation en soufflerie est aussi appelée modélisation physique, en effet, un écoulement réel est simulé par un autre écoulement qui présente les mêmes caractéristiques mais à une échelle différente. Le niveau de modélisation est plus faible que la simulation numérique mais un certain nombre de vérifications sont néanmoins nécessaires à la validation, par exemple, les paramètres de similarité doivent être respectés (nombres sans dimension) et les conditions initiales doivent être reproduites le plus fidèlement possible. Une modélisation correcte des écoulements atmosphériques doit traiter des conditions suivantes :

- La reproduction des nombres sans dimension provenant des équations de Navier-Stokes

- La reproduction des conditions limites et particulièrement des conditions d'entrée

- Le choix de la zone reproduire autour du point d'intérêt et du facteur d'échelle : un terrain complexe peut nécessiter la reproduction d'un grand périmètre autour du point d'intérêt mais le facteur d'échelle doit rester "raisonnable"

- Les techniques de mesure doivent être adaptées et suffisamment précises et résolues dans le temps et dans l'espace

Ces paramètres d'étude sont développés dans les chapitres de la thèse. Le but est de quantifier leur relative importance dans la simulation et de contribuer à accroitre la connaissance de la simulation physique en soufflerie.

D.1.3. Objectifs et structure de la thèse

Deux principaux objectifs sont fixés : démontrer la capacité et les limites de la simulation en soufflerie pour l'évaluation du potentiel éolien en terrain complexe et quantifier les paramètres les plus importants la modélisation.

La thèse est structurée autour des objectifs en augmentant progressivement la complexité du relief, en passant d'un terrain plat à un terrain très complexe. Le premier chapitre introduit le contexte éolien et décrit les objectifs de la thèse. Le deuxième chapitre décrit les caractéristiques des écoulements atmosphériques et la manière de les simuler en soufflerie. Le chapitre 3 est dédié à la vérification précise de la possibilité de simuler les écoulements atmosphériques en terrain plat dans les deux souffleries disponibles. La paramétrisation de la reproduction des conditions d'entrée est aussi étudiée.
Le chapitre 4 est dédié à l'étude de reliefs bidimensionnels simples. Le but est de déterminer la zone d'influence en aval d'un relief pour orienter la décision de la zone à modéliser en soufflerie. Ce chapitre a aussi pour objectif de souligner les zones défavorables à l'installation d'éoliennes proches d'un relief.
Dans le chapitre 5, la complexité du terrain augmente avec l'étude de deux cas réels en soufflerie : l'île de Bolund au Danemark et la montagne Alaiz en Espagne. Les deux cas d'étude sont réalisés dans des souffleries différentes et les résultats sont comparés aux données terrain. Deux études paramétriques sont réalisées afin de quantifier l'influence des paramètres de modélisation comme le nombre de Reynolds, la reproduction des conditions d'entrée ou la direction du vent.

D.2. Conclusion

D.2.1. Modélisation en soufflerie du vent en terrain complexe

Face à un site complexe à évaluer, un grand nombre de paramètres entrent en considération pour sa modélisation en soufflerie. Les principaux sont : le choix de la zone à modéliser autour du point d'intérêt, la reproduction des conditions atmosphériques et la dépendance de l'écoulement au nombre de Reynolds.

Le choix de la zone à modéliser est particulièrement important dans le cas d'un terrain complexe, en effet, il résulte d'un compromis entre tenir compte des reliefs amonts pouvant avoir des effets lointains en aval et garder un facteur d'échelle raisonnable dans la soufflerie. L'étude présentée dans le chapitre 4 aide à cette décision en étudiant les effets avals de collines bidimensionnelles simplifiés : déficit

de vitesse et accroissement de la turbulence. Dans le cas d'un relief ne donnant pas lieu à une séparation de l'écoulement, l'influence de celui-ci augmente avec L, la demi-longueur de la colline. En première approche, elle peut être négligée après 2L. Pour un relief avec recirculation, la zone d'influence en aval augmente avec -L mais l'estimation n'obéit pas à une loi simple et doit être étudiée au cas par cas.
La reproduction des conditions d'entrée est le sujet du chapitre 3. La technique de reproduction de la couche limite atmosphérique utilise une barrière, une grille à l'entrée de la section d'essai et des éléments rugueux disposés sur le sol. L'étude paramétrique des éléments conclut que la hauteur des éléments de rugosité disposés et la hauteur de la barrière sont les principaux pilotes de la couche limite. En effet, la grille, le nombre de barrières et la densité des éléments de rugosité n'ont qu'un rôle secondaire dans les cas étudiés. La hauteur de la barrière est le principal paramètre déterminant la hauteur de la couche limite et contrôlant le niveau de turbulence dans la partie haute de la couche limite. La hauteur des éléments de rugosité agit en revanche sur la partie basse de la couche limite en contrôlant le niveau de turbulence en proche paroi et la longueur de rugosité (z_0). La bonne combinaison des éléments assure le développement d'une couche limite similaire au vent atmosphérique voulu.
Deux études paramétriques sont réalisées sur les deux cas test, l'île de Bolund et la montagne Alaiz. Les paramètres testés sont : le nombre de Reynolds, les conditions d'entrée, la direction du vent et la précision de la hauteur de référence. Les deux études convergent vers le fait que la reproduction des conditions d'entrée est l'élément principal influenąnt la modélisation (de 10% à 50%). La direction du vent vient comme seconde source d'erreur, celle-ci dépend bien entendu de la géométrie du relief. Dans le cas étudié, la présence d'un relief amont est un ordre de grandeur moins important que la reproduction du profil d'entrée mais peut néanmoins représenter jusqu'à 10% de différence.

D.2.2. Le positionnement d'éoliennes proches de reliefs

Les éoliennes sont placées en terrain complexe pour bénéficier de vent plus fort qu'en plaine, l'avantage qu'apporte une colline ou une montagne de faible pente est le plus souvent documenté dans les normes comme l'EUROCODE. En revanche, les inconvénients liés à la complexité des écoulements induits par les reliefs sont peu documentés. Dans le chapitre 4, le sillage proche et lointaine générée par des reliefs simplifiés est étudiée à partir de modèles de collines bidimensionnelles.

Des collines de différentes pentes, générant ou non une séparation de l'écoulement sont étudiées. Il est généralement admis que les faibles pentes, moins de 15°, n'entraînent jamais de séparation de l'écoulement alors que les fortes pentes, de plus de 18°, en génèrent toujours. Les essais en soufflerie sont complétés par la base de données ERCOFTAC. L'étude souligne la différence de nature entre le sillage d'une colline de faible et de forte pente. Les deux cas entraînent un déficit de vitesse et une augmentation de la turbulence mais, pour les fortes pentes, un

détachement tourbillonnaire se déclare et entraîne une recirculation, dans ce cas, l'effet est plus prononcé et est visible plus loin en aval.
La région aval perturbée est localisée comme étant la zone avec un déficit de vitesse de 5% ($\Delta S < -0.05$) et un une augmentation de la turbulence de 5% par rapport au niveau amont. ΔS est la fraction de sur-vitesse par rapport aux conditions amont. Les variables h_w et l_w sont définies comme les dimensions verticale et horizontale de la zone perturbée.
Pour les collines de faible pente, l_w/H augmente linéairement avec le rapport L/H (demi longueur L et hauteur H). L'approximation $l_w = 2$ L est correcte pour les faibles pentes (L/H grand). La hauteur de la zone perturbée est toujours en dessous de hw/H=1.7. Pour les collines de forte pente, la distance l_w augmente fortement avec un L/H décroissant. La hauteur de la perturbation est du même ordre que pour les collines de faible pente.

La perturbation en turbulence persiste en général plus longtemps que la perturbation de la vitesse. A hauteur constante, la turbulence décroît en suivant une fonction x^{-1}.

Cette étude donne des indications quant à l'influence néfaste des terrains complexes pour le positionnement d'éoliennes. Elle pourrait être poursuivie par une étude sur d'autres types de collines et en faisant fluctuer des paramètres tels que le niveau de turbulence amont ou la hauteur de la couche limite...

D.2.3. Validation de l'approche expérimentale en soufflerie

Un autre objectif de ce travail est l'évaluation de l'outil soufflerie pour la simulation du vent en terrain complexe. Dans ce travail, le chapitre 3 est dédié à la validation de la reproduction des conditions atmosphériques : les conditions de simulation sont vérifiées rigoureusement et les propriétés de l'écoulement sont comparées aux données terrain.

Dans le dernier chapitre (5), deux campagnes d'essais sont réalisées en soufflerie pour reproduire le vent sur des reliefs réels. Le vent autour de l'ile de Bolund et de la montagne Alaiz est modélisé et comparé aux données terrain disponibles. Les résultats en soufflerie montrent une différence de seulement 8% en moyenne, et de seulement 5% pour les $\frac{3}{4}$ des points pour l'estimation de la vitesse du vent à différents endroits autour de l'île de Bolund. C'est un bon résultat comparé aux estimations réalisées par des simulations numériques et d'autres mesures en soufflerie. En revanche, la simulation de la turbulence est plus complexe, en effet, l'estimation de l'augmentation de turbulence due à l'île de Bolund est parfois estimée avec une erreur de 100%. Cette erreur est du même ordre ou inférieure à l'erreur faite avec une simulation numérique.

Une quantité plus limitée de données terrain sont disponibles sur la montagne

d'Alaiz, mais la mesure en soufflerie donne un résultat situé entre les données terrain des deux mâts de mesure les plus proches et les profiles sont semblables. Le profil de turbulence est aussi semblable, et les niveaux de turbulence mesurés en soufflerie sont proches (3% en différence absolue).
Les résultats obtenus sont satisfaisants en ce qui concerne la prédiction de la vitesse, la prédiction de la turbulence s'avère plus difficile, des études plus approfondies de l'influence de la hauteur de couche limite et de l'influence du niveau de turbulence amont peuvent apporter des pistes de réponse.

Différents tests ont été réalisés avec de très petites échelles et dans des petites souffleries (0.35x0.35x2m). Ces tests donnent un résultat acceptable pour la simulation de la vitesse, entre 5 et 10%.
Les données disponibles sont très comparables aux tests en soufflerie, cependant, un plus grand nombre de données terrain serait nécessaire pour une validation plus approfondie, notamment des conditions d'entrée.

Comparée aux autres approches, la simulation en soufflerie s'avère être un outil valide pour l'estimation du vent en terrain complexe.

Nomenclature

Abbreviations

ABL Atmospheric Boundary Layer

BL Boundary Layer

FSR Fractional Speed-up Ratio or ΔS

HW Hot-wire

PIV Particle Image Velocimetry

RMS Root Mean Square 4.12

TKE Turbulent Kinetic Energy

TR Turbulent Ratio

a.g.l. Above ground level

Greek Symbols

α	Power law coefficient	[-]
δ_{i3}	Kronecker's delta	[-]
ϵ_{ijk}	Alternative tensor	[-]
κ	von Karman constante (0.4)	[-]
λ	Latitude	$[degree]$
λ	Roughness density	[-]
λ_2	Vortex detection criteria	[-]
λ_f	Frontal roughness density	[-]
ν	Kinematic viscosity of the air	$[m^2.s^{-1}]$
Ω	Angular rotation of the Earth	$[rad.s^{-1}]$
ω_i	Vorticity in the i direction	$[s^{-1}]$
ϕ	Dissipation function	$[kg/(m.s^3)]$

ρ	Air density	$[kg.m^3]$
σ_i	Standard deviation of the i component	[-]
τ	Shear stress	$[Pa]$
θ'	Instantaneous temperature	$[K]$

Roman Symbols

ΔS	Speed-up ratio or fractional speed-up ratio (FSR)	[-]
ΔT	Time average temperature difference	$[K]$
A_f	Projected frontal area of the roughness elements	$[m^2]$
A_g	Projected area of the roughness elements	$[m^2]$
C_p	Specific heat of the air	$[J/(kg.K)]$
D	Dist. betw. the main and secondary topo/ Base of the cups	$[m]$
d	Diameter of the top of the cup	$[m]$
f	Frequency	$[Hz]$
f_c	Coriolis parameter	$[rad.s^{-1}]$
g	Acceleration of gravity	$[m.s^{-1}]$
H	Height of the main topography	$[m]$
h	Height of the secondary topography / vertical dimension of the cups	$[m]$
H_F	Height of the fence	$[m]$
h_m	Height of the middle layer above a hill	$[m]$
H_R	Height of the roughness elements	$[m]$
h_w	Depth of the wake	$[m]$
I_i	Turbulence intensity of the i component	[-]
Ii_w	Turbulence intensity increase in the i component	[-]
k	Turbulence Kinetic Energy (TKE)	$[m^2/s^2]$
k_0	Thermal conductivity	$[W/(m.K)]$
L_i	Hill length at H/2	[m]
L_i	Integral length scale of the i component in the longitudinal direction	$[m]$

l_i or l^*	Height of the inner layer above a hill	$[m]$
l_w	Length of the wake	$[m]$
n	Dimensionless frequency	$[m]$
P	Time average pressure difference compare to the atmosphere	$[Pa]$
P_W	Wind power	$[W]$
R	Surface roughness height	$[m]$
S_R	Wind turbine swept area	$[m^2]$
S_i	Spectra in the i direction	[-]
T	Time average temperature	$[K]$
t	Time	$[s]$
T_i	Integral time scale of the i component in the longitudinal direction	$[m]$
U, V, W	Time average velocity	$[m/s]$
u, v, w	Instantaneous velocity components	$[m/s]$
u', v', w'	Velocity fluctuation	$[m/s]$
u_*	Friction velocity	$[m/s]$
U_w	Velocity deficit	$[m/s]$
x, y, z	Longitudinal, transversal and vertical direction	[-]
z	Height above local ground	$[m]$
z_0	Aerodynamic roughness length	$[m]$
Z_r	roughness sub-layer height	$[m]$

Sub- and Superscripts

$*$	Dimensionless number
0	Reference quantities given by boundary conditions
δ	Property at the boundary layer height
amb	Related to the ambient conditions
$field$	Value measured in the field
hub	Values at hub height

i Component: longitudinal, transversal and vertical (u,v,w)

ref Refers to the reference value

$wall$ Limit value at the wall

wt Value measured in the wind tunnel

Bibliography

Each reference is followed by the list of the pages where it is cited.

[1] E.W. Adams and J.P. Johnston. Effects of the separating shear layer on the reattachment flow structure part 1: Pressure and turbulence quantities. *Experiments in fluids*, 6(6):400–408, 1988. 72

[2] E.W. Adams and J.P. Johnston. Effects of the separating shear layer on the reattachment flow structure part 2: Reattachment length and wall shear stress. *Experiments in Fluids*, 6(7):493–499, 1988. 72

[3] G.P. Almeida, D.F.G. Durao, and M.V. Heitor. Wake flows behind two-dimensional model hills. *Experimental Thermal and Fluid Science*, 7(1):87–101, 1993. 16, 63

[4] S.P.S. Arya, M.E Capuano, and L.C. Fagen. Some fluid modeling studies of flow and dispersion over two-dimensional low hills. *Atmospheric Environment (1967)*, 21(4):753–764, 1987. 79, 80, 84

[5] K.W. Ayotte, R.J. Davy, and P.A. Coppin. A simple temporal and spatial analysis of flow in complex terrain in the context of wind energy modelling. *Boundary-Layer Meteorology*, 98(2):275–295, 2001. 62

[6] K.W. Ayotte and D.E. Hughes. Observations of boundary-layer wind-tunnel flow over isolated ridges of varying steepness and roughness. *Boundary-Layer Meteorology*, 112(3):525–556, 2004. 61

[7] A. Bechmann, J. Berg, M.S. Courtney, H. Jørgensen, J. Mann, and N. Sørensen. The bolund experiment: overview and background. *Risø DTU report Risø Risø-R-1658(EN)*, pages 1–50, 2009. 91, 92, 93

[8] A. Bechmann, N.N. Sørensen, J. Berg, J. Mann, and P.E. Réthoré. The bolund experiment, part 2: blind comparison of microscale flow models. *Boundary-Layer Meteorology*, 141(2):245–271, 2011. 91, 93, 94, 95

[9] J. Berg, J. Mann, A. Bechmann, MS Courtney, and HE Jørgensen. The bolund experiment, part 1: flow over a steep, three-dimensional hill. *Boundary-Layer Meteorology*, 141(2):219–243, 2011. 91, 96

[10] B. Blocken and J. Carmeliet. Pedestrian wind environment around buildings: Literature review and practical examples. *J. Thermal Env. & Bldg. Sci*, 28(2):107, 2004. 163, 164

[11] AJ Bowen. Modelling of strong wind flows over complex terrain at small geometric scales. *Journal of Wind Engineering and Industrial Aerodynamics*, 91(12):1859–1871, 2003. 90

[12] P. Bradshaw and G.P. Huang. The law of the wall in turbulent flow. *Proc. Roy. Soc. London A*, 451(1941):165, 1995. 164, 165

[13] P. Bradshaw and F.Y.F. Wong. The reattachment and relaxation of a turbulent shear layer. *Journal of Fluid Mechanics*, 52(01):113–135, 1972. 79

[14] R.E. Britter, J.C.R. Hunt, and K.J. Richards. Air flow over a two-dimensional hill: Studies of velocity speed-up, roughness effects and turbulence. *Quarterly Journal of the Royal Meteorological Society*, 107(451):91–110, 1981. 60, 61

[15] H.H. Bruun. *Hot-wire Anemometry - Principle and Signal Analysis*. Oxford University Press, 1995. 153, 170

[16] D. Cabezón, A. Iniesta, E. Ferrer, and I. Marui. Comparing linear and nonlinear flow models. In *Proceedings of EWEC*, 2006. 113

[17] D. Cabezón, J. Sanz, and J. Van Beeck. Sensitivity analysis on turbulence models for the abl in complex terrain. In *Proceedings of the EWEC*, 2007. 113, 127, 128, 167

[18] S. Cao and T. Tamura. Experimental study on roughness effects on turbulent boundary layer flow over a two-dimensional steep hill. *Journal of Wind Engineering and Industrial Aerodynamics*, 94(1):1–19, 2006. 63, 80, 112

[19] S. Cao and T. Tamura. Effects of roughness blocks on atmospheric boundary layer flow over a two-dimensional low hill with/without sudden roughness change. *Journal of Wind Engineering and Industrial Aerodynamics*, 95(8):679–695, 2007. 112

[20] J.E. Cermak. Laboratory simulation of the atmospheric boundary layer. Technical report, DTIC Document, 1970. 13

[21] JE Cermak. Physical modelling of flow and dispersion over complex terrain. *Boundary-Layer Meteorology*, 30(1):261–292, 1984. 90

[22] G.Y.K. Chock and L. Cochran. Modeling of topographic wind speed effects in hawaii. *Journal of Wind Engineering and Industrial Aerodynamics*, 93(8):623–638, 2005. 90

[23] B. Conan, S. Buckingham, , J. Van Beeck, S. Aubrun, and J. Sanz. Feasibility of micro-siting in mountainous terrain by wind tunnel physical modelling. In *In: Sc. Proc. European Wind Energy Conf., March 2011, Brussels*, pages 136–140, 2011. 162, 167, 168, 169

[24] B. Conan, S. Buckingham, J. van Beeck, S. Aunbrun, and J. Sanz. Feasibility of micro-siting in mountainous terrain by wind tunnel physical modelling. In *EWEA 2011, Brussels, Belgium*, 2012. 113

[25] B. Conan, F. Carbajo, , J. Van Beeck, and S. Aubrun. Experimental parametric study of the influence of an idealized upstream ridge on the flow characteristics over alaiz mountain. In *In: Proc. PHYSMOD2011, August 2011, Hamburg, Germany*, pages 272–279, 2011. 167

[26] B. Conan, J. van Beeck, and S. Aubrun. Sand erosion technique applied to wind resource assessment. *Journal of Wind Engineering and Industrial Aerodynamics*, 104:322–329, 2012. 113, 120

[27] M.J. Costa. *Simulação física do Escoamento Atmosférico e Dispersão sobre Colinas Bidimensionais*. PhD thesis, von Karman Institute for Fluid Dynamics - Universidad de Aveiro, 1996. 63, 116, 124

[28] J. Counihan. An improved method of simulating an atmospheric boundary layer in a wind tunnel. *Atmospheric Environment (1967)*, 3(2):197–214, 1969. 23

[29] J. Counihan. Adiabatic atmospheric boundary layers: a review and analysis of data from the period 1880–1972. *Atmospheric Environment (1967)*, 9(10):871–905, 1975. 10, 11, 35, 36, 37, 38

[30] P.A. Davidson. *Turbulence: an introduction for scientists and engineers*. Oxford University Press, USA, 2004. 12

[31] de Volder. étude expérimentale et numérique du développement de couches limites atmosphériques dans la soufflerie l1-b de l'institut von karman. Master's thesis, UCL - U-VKI-2007-01, 2007. 43

[32] R.G. Derickson and Peterka J.A. Development of a powerful hybrid tool for evaluating wind power in complex terrain: Atmospheric numerical models and wind tunnels. *AIAA-2004-1005*, 2004. 90

[33] G. Dezső. On assessment of wind comfort by sand erosion. *PhD thesis, Technidche Universiteit Eindhoven & von Karman Institute for Fluid Dynamics - ISBN 2-930389-22-2*, 2006. 162, 163, 164, 166, 167

[34] G. Dezső-Weidinger, M. Massini, and J. van Beeck. Pedestrian wind comfort–approached by piv and sand erosion. *Proc. of PHYSMOD2003, Firenze*, 2003. 163, 172

[35] ESDU. Characteristics of atmospheric turbulence near the ground. part ii: single point data for strong winds (neutral atmosphere). *ESDU International, London*, 1985. 8, 9, 17, 38

[36] Eurocode. En 1991-1-42: Actions on structures part 1-4: Wind actions. *Comit Europen de Normalisation, Bruxelles*, 2004. 8, 169

[37] C. Farell and A.K.S. Iyengar. Experiments on the wind tunnel simulation of atmospheric boundary layers. *Journal of Wind Engineering and Industrial Aerodynamics*, 79(1):11–35, 1999. 21, 32, 33, 35, 36

[38] J.J. Finnigan. *Air flow over complex terrain*. Springer-Verlag, 1988. 61, 62, 78

[39] P-A Fruytier. Conception, experimentation, amelioration d'un logiciel de mesure anemometrique tridimentionnelles pour des sondes a trois fils chauds. Master's thesis, von Karman Institute U-VKI 1993-12, 1993. 154

[40] J.R. Garratt. *The atmospheric boundary layer*. Cambridge university press, 1994. 7

[41] F.R. Hama. *Boundary-layer characteristics for smooth and rough surfaces*. SNAME, 1954. 32

[42] H.A. Holmes. Waudit guidance report -wp6 deliverable d24 - quality assurance of wind energy assessment models. Technical report, Meteorological Institute, University of Hamburg, 2011. 159

[43] J.C.R. Hunt, S. Leibovich, and K.J. Richards. Turbulent shear flows over low hills. *Quarterly Journal of the Royal Meteorological Society*, 114(484):1435–1470, 1988. 60, 61

[44] A.K.S. Iyengar and C. Farell. Experimental issues in atmospheric boundary layer simulations: roughness length and integral length scale determination. *Journal of Wind Engineering and Industrial Aerodynamics*, 89(11):1059–1080, 2001. 32, 33, 34, 35

[45] P.S. Jackson and J.C.R. Hunt. Turbulent wind flow over a low hill. *Quarterly Journal of the Royal Meteorological Society*, 101(430):929–955, 1975. 60

[46] J. Jeong and F. Hussain. On the identification of a vortex. *Journal of Fluid Mechanics*, 285(69):69–94, 1995. 71, 145

[47] J. Jiménez. Turbulent flows over rough walls. *Annu. Rev. Fluid Mech.*, 36:173–196, 2004. 34, 35

[48] F.E. Jø rgensen. How to measure turbulence with hot-wire anemometers - a practical guide. Technical report, Dantec Dynamics, 2002. 151

[49] F.E. Jorgensen. *Directional sensitivity of wire and fibre-film probes.* DISA Inform 11: 3137, 1971. 150, 153, 154

[50] S. Jovic and D. Driver. Reynolds number effect on the skin friction in separated flows behind a backward-facing step. *Experiments in fluids*, 18(6):464–467, 1995. 79

[51] J.C. Kaimal and J.J. Finnigan. *Atmospheric boundary layer flows: their structure and measurement*. Oxford University Press, USA, 1994. 7, 39

[52] J.C. Kaimal, J.C. Wyngaard, Y. Izumi, and O.R. Cote. Spectral characteristics of surface-layer turbulence. *Quarterly Journal of the Royal Meteorological Society*, 98(417):563–589, 1972. 11, 12, 39, 40

[53] A. Karimpour, N.B. Kaye, and Z. Baratain. Modeling the neutrally stable atmospheric boundary layer for laboratory scale studies of the built environment. *Building and Environment*, 2011. 32, 33, 34, 35

[54] LH Khurshudyan, WH Snyder, and IV Nekrasov. Flow and dispersion of pollutants over two-dimensional hills. *Environment Protection Agency Report no EPA-600/4-81-067. Research Triangle Park*, 1981. 64, 65

[55] H.G. Kim, C.M. Lee, H.C. Lim, and N.H. Kyong. An experimental and numerical study on the flow over two-dimensional hills. *Journal of Wind Engineering and Industrial Aerodynamics*, 66(1):17–33, 1997. 63, 77, 78, 79, 80

[56] J. Kostas, J. Soria, and M. Chong. Particle image velocimetry measurements of a backward-facing step flow. *Experiments in Fluids*, 33(6):838–853, 2002. 72

[57] H. Le, P. Moin, and J. Kim. Direct numerical simulation of turbulent flow over a backward-facing step. *J. Fluid Mech.*, 330(1):349–374, 1997. 166

[58] D.R. Lemelin, D. Surry, and A.G. Davenport. Simple approximations for wind speed-up over hills. *Journal of Wind Engineering and Industrial Aerodynamics*, 28(1):117–127, 1988. 60

[59] F. Livesey, D. Morrish, M. Mikitiuk, and N. Isyumov. Enhanced scour tests to evaluate pedestrian level winds. *J. Wind Eng. and Ind. Aerodyn.*, 44(1-3):2265–2276, 1992. 163

[60] PJ Mason and R.I. Sykes. Flow over an isolated hill of moderate slope. *Quarterly Journal of the Royal Meteorological Society*, 105(444):383–395, 1979. 60, 61, 62, 63, 78

[61] B.R. McAuliffe and G.L. Larose. An experimental approach to wind resource assessment of wind farms in complex terrain. In *Proceedings of the ICWE 13, Amsterdam, The Netherlands*, 2011. 90, 112

[62] R.N. Meroney. Wind-tunnel simulation of the flow over hills and complex terrain. *Journal of Wind Engineering and Industrial Aerodynamics*, 5(3):297–321, 1980. 60, 89

[63] D. Muñoz Esparza, B. Conan, E. Croonenborgs, A. Parente, J. van Beeck, and J. Sanz. Sensitivity to inlelt conditions of wind resource assessment over complex terrain using three cfd solvers and wind tunnel data. In *Proceedings of the EWEA 2011, Brussels, Belgium*, 2012. 127, 128, 167

[64] D. Neal and D.C. Stevenson. A wind tunnel boundary layer simulation of wind over complex terrain: effect of terrain and model construction. *Boundary-Layer Meteorology*, 21:271–293, 1981. 90

[65] JR Pearse, D. Lindley, and DC Stevenson. Wind flow over ridges in simulated atmospheric boundary layers. *Boundary-Layer Meteorology*, 21(1):77–92, 1981. 63, 116, 124

[66] E.J. Plate. Methods of investigating urban wind fields–physical models. *Atmos. Environ.*, 33(24-25):3981–3989, 1999. 162

[67] M. Raffel, C.E. Willert, and J. Kompenhans. *Particle image velocimetry: a practical guide*. Springer Verlag, 1998. 71, 143, 170

[68] M.R. Raupach, R.A. Antonia, and S. Rajagopalan. Rough-wall turbulent boundary layers. *Appl. Mechanics Revs.*, 44:1–25, 1991. 33, 35, 36

[69] J. Sanz, Borbón F., P. Gómez, M.S. Courtney, R. Wagner, and E. Dupont. Multi-scale testing and evaluation of remote sensing instruments for wind resource assessment. In *proceedings of EWEA 2012, Copenhagen Denmark*, 2012. 124

[70] F. Scarano. *Particle Image Velocimetry - Development and Application*. PhD thesis, von Karman Institute for Fluid Dynamics, 2000. 72, 145, 147

[71] F. Scarano, C. Benocci, and ML Riethmuller. Pattern recognition analysis of the turbulent flow past a backward facing step. *Phys. Fluids*, 11:3808, 1999. 166

[72] F. Scarano and ML Riethmuller. Iterative multigrid approach in piv image processing with discrete window offset. *Experiments in Fluids*, 26(6):513–523, 1999. 118

[73] M. Sherry, D. Lo Jacono, and J. Sheridan. An experimental investigation of the recirculation zone formed downstream of a forward facing step. *Journal of Wind Engineering and Industrial Aerodynamics*, 98(12):888–894, 2010. 108

[74] B.S. Shiau and B.J. Tsai. Wind tunnel measurement of flow and dispersion of power plant emission on the coastal region with complex terrain. In *Proceedings of the EAWE 5 Florence, Italy*, 2009. 90

[75] K. Siddiqui, H. Hangan, and A. Rasouli. Piv technique implementation for wind mapping in complex topographies. *Measurement Science and Technology*, 19(6):065403, 2008. 90

[76] W.H. Snyder. Guidelines for fluid modelling of atmospheric diffusion. epa office of air quality, planning and standards, research triangle park, usa. Technical report, EPA-600/8-81-009, 1981. 13, 16

[77] P.G. Spazzini, G. Iuso, M. Onorato, N. Zurlo, and G.M. Di Cicca. Unsteady behavior of back-facing step flow. *Experiments in Fluids*, 30(5):551–561, 2001. 72

[78] T. Stathopoulos. Pedestrian level winds and outdoor human comfort. *J. Wind Eng. and Ind. Aerodyn.*, 94(11):769–780, 2006. 162

[79] P.A. Taylor. Some numerical studies of surface boundary-layer flow above gentle topography. *Boundary-Layer Meteorology*, 11(4):439–465, 1977. 60

[80] P.A. Taylor and R.J. Lee. Simple guidelines for estimating wind speed variations due to small scale topographic features. *Climatol. Bull*, 18(2):3–32, 1984. 62

[81] P.A. Taylor and H.W. Teunissen. The askervein hill project: overview and background data. *Boundary-Layer Meteorology*, 39(1):15–39, 1987. 60

[82] H.W. Teunissen, M.E. Shokr, A.J. Bowen, C.J. Wood, and D.W.R. Green. The askervein hill project: wind-tunnel simulations at three length scales. *Boundary-Layer Meteorology*, 40(1):1–29, 1987. 60, 90

[83] C. Tropea, A.L. Yarin, and J.F. Foss. *Springer handbook of experimental fluid mechanics*, volume 1. Springer, 2007. 143, 144

[84] J. van Beeck, G. Dezső, and P. Planquart. Microclimate assessment by sand erosion and irwin probes for atmospheric boundary layer wind tunnels. *In: Proc. PHYSMOD2009, Rhode-Saint-Genése*, 2009. 162, 164

[85] Guideline VDI. 3783/12, 2000. environmental meteorology, physical modelling of flow and dispersion processes in the atmospheric boundary layer–applications of wind tunnels. 8, 16, 17, 30, 38, 105, 169

[86] C.A. Veiga Rodrigues. Analysis of the atmospheric boundary layer flow over mountainous terrain. Master's thesis, von Karman Institute for Fluid Dynamics, 2005. 90, 112

[87] DX Viegas and AR Borges. An erosion technique for the measurement of the shear stress field on a flat plate. *J. Physics E: Sc. Instruments*, 19:625, 1986. 163

[88] W. Weng, P.A. Taylor, and J.L. Walmsley. Guidelines for airflow over complex terrain: model developments. *Journal of Wind Engineering and Industrial Aerodynamics*, 86(2):169–186, 2000. 60, 61

[89] J.J. Williams. Aeolian entrainment thresholds in a developing boundary layer. *PhD thesis, Department of Geography and Earth Science Queen Mary College University of London*, 1986. 163, 172

[90] J.C. Wyngaard. *Turbulence in the Atmosphere*. Cambridge University Press, 2010. 7

[91] E. Yee, R.M. Gailis, A. Hill, T. Hilderman, and D. Kiel. Comparison of wind-tunnel and water-channel simulations of plume dispersion through a large array of obstacles with a scaled field experiment. *Boundary-Layer Meteorology*, 121(3):389–432, 2006. 16

[92] T.S. Yeow, A. Cuerva, Boris Conan, and J. Peréz-Alvaréz. Wind tunnel analysis of the detachment bubble on bolund island. In *Proceedings of: The Science of Making Torque from Wind, Oldenburg, Germany*, 2012. 97

[93] T.S. Yeow, A. Cuerva, and J. Peréz-Alvaréz. Pressure measurement of the detachment bubble on bolund island. In *Proceedings of the EWEA 2012, Copenhagen Denmark*, 2012. 97

Boris CONAN

Modélisation en soufflerie du vent en terrain complexe pour l'évaluation du potentiel éolien

Résumé :
Afin de bénéficier de vents importants, un nombre croissant d'éoliennes est installé en terrain complexe. Cependant, un terrain complexe accroit la complexité de l'écoulement et donc la prédiction du potentiel éolien. Dans ce travail, le vent en terrain complexe est simulé en soufflerie. L'objectif est d'étudier la capacité de la modélisation en soufflerie.
La partie basse de l'atmosphère, appelée couche limite atmosphérique, est le siège d'important gradients de vitesse et de turbulence. Dans la soufflerie, ils sont reproduits grâce à des obstacles placés dans la section d'essai. Leurs tailles varient en fonction du type de terrain à modéliser. Cette approche expérimentale est validée par des données terrain. La reproduction des conditions atmosphériques est le paramètre crucial pour une bonne modélisation.
Pour évaluer le vent en terrain complexe, le choix de la zone à reproduire autour du site d'intérêt est une question centrale : elle doit tenir compte de l'effet des reliefs environnants mais doit être assez réduite pour préserver un facteur d'échelle raisonnable dans la soufflerie. Une série d'études sur des collines simplifiées est ainsi réalisé afin de déterminer l'étendue spatiale du sillage en aval d'un relief simplifié afin de rationaliser le choix de la zone d'étude. Deux cas réels sont ensuite traités, l'ile de Bolund au Danemark et la montagne Alaiz en Espagne. Les résultats sont bons pour l'estimation de la vitesse du vent, entre 5 et 10% mais la modélisation de la turbulence est plus difficile, des écarts jusqu'à 100% sont enregistrés comparés aux données terrain.
Mots clés : écoulement atmosphérique, terrain complexe, énergie éolienne, soufflerie, collines bidimensionnelles, silage, Bolund, Alaiz, PIV

Wind resources assessment in complex terrain by wind tunnel modelling

Abstract :
To benefit from strong winds, an increasing number of wind turbines are placed in complex terrains. But complex terrains means complex flows and difficult wind resource assessment. This study proposed to use wind tunnel modelling to evaluate the wind in a complex topography.
The goal of this study is to evaluate the possibilities of wind resources assessment by wind tunnel modelling and to quantify the important modelling parameters.
The lower part of the atmosphere, the atmospheric boundary layer (ABL) is defined by a velocity and a turbulence gradient. The ABL is reproduced in the wind tunnel by placing obstacles and roughness elements of different size representative to the type of terrain desired. The flow produced in the wind tunnel is validated against field data and a wise choice of the obstacles is discussed to reproduce the desired wind profile. The right reproduction of the inflow conditions is found to be the most important parameter to reproduce.
The choice of the area to reproduce around a site in usually difficult to make in order to keep a low scaling factor and to account for the surrounding topography. A series of tests on simplified hills helps the experimentalist in this choice by enlightening the longitudinal and vertical extension of the wake downstream different hills shapes.
Finally, two complex topographies are studied in two wind tunnels, the Bolund hill in Denmark and the Alaiz mountain in Spain. The results are giving good results, 5 to 10%, for predicting the wind speed but more scatter is observed for the modelling of the turbulence, up to 100%.
The laboratory simulation of atmospheric flows proves to be a demanding but reliable tool for the prediction of the mean wind speed in complex terrain.
Keywords: atmospheric flows, complex terrain, wind energy, wind tunnel, 2D hills, Bolund, Alaiz, PIV

UNIVERSITE D'ORLEANS

Laboratoire PRISME - Institut von Karman